



HAL
open science

pH-induced valence inversion in bio-inspired diiron complexes

Ramachandran Balasubramanian

► **To cite this version:**

Ramachandran Balasubramanian. pH-induced valence inversion in bio-inspired diiron complexes. Inorganic chemistry. Université de Grenoble, 2013. English. NNT : 2013GRENV080 . tel-01555350

HAL Id: tel-01555350

<https://theses.hal.science/tel-01555350>

Submitted on 4 Jul 2017

HAL is a multi-disciplinary open access archive for the deposit and dissemination of scientific research documents, whether they are published or not. The documents may come from teaching and research institutions in France or abroad, or from public or private research centers.

L'archive ouverte pluridisciplinaire **HAL**, est destinée au dépôt et à la diffusion de documents scientifiques de niveau recherche, publiés ou non, émanant des établissements d'enseignement et de recherche français ou étrangers, des laboratoires publics ou privés.

THÈSE

Pour obtenir le grade de

DOCTEUR DE L'UNIVERSITÉ DE GRENOBLE

Spécialité : **CHIMIE**

Arrêté ministériel : 7 août 2006

Présentée par

Ramachandran BALASUBRAMANIAN

Thèse dirigée par **Dr. Geneviève BLONDIN**

préparée au sein du **Laboratoire de Chimie et Biologie des Métaux**

dans l'**École Doctorale de Chimie et Sciences du Vivant**

Inversion de valence induite par le pH dans des complexes à deux fer

Thèse soutenue publiquement le **22 octobre 2013**,
devant le jury composé de :

Mr Bruno ANDRIOLETTI

Professeur, Université Claude Bernard, Lyon, Rapporteur

Mr Yves LE MEST

Directeur de Recherches CNRS, Université de Bretagne Occidentale, Brest,
Rapporteur

Mme Carole DUBOC

Directrice de Recherches CNRS, Université Joseph Fourier, Grenoble,
Présidente

Mr Cyrille COSTENTIN

Professeur, Université Paris Diderot – Paris 7, Paris, Examineur

Mr Jean-Marc LATOUR

Directeur de Recherches CEA, CEA, Grenoble, Examineur

Mme Geneviève BLONDIN

Directrice de Recherches CNRS, CEA, Grenoble, Directrice de thèse



Acknowledgement

Foremost, I would like to express my sincere gratitude to my advisor **Dr. Geneviève BLONDIN** for the continuous support of my Ph.D study and research, for her patience, motivation, enthusiasm, and immense knowledge. Her guidance helped me in all the time of research and writing of this thesis. I could not have imagined having a better advisor and mentor for my Ph.D study.

Besides my advisor, I would like to thank the rest of my thesis committee: Dr. Carole DUBOC, Dr. Lionel DUBOIS, and Dr. Jean-Marc LATOUR, for their encouragement and insightful comments over the project.

My sincere thanks go to Prof. Cyrille COSTENTIN, Prof. Marc ROBERT and Prof. Jean-Michel SAVEANT of LEM group in Université Paris 7 for offering me an opportunity to perform electrochemical experiments in collaboration to the current project.

I would like to thank my fellow lab mates in PMB group, CEA, Grenoble: Nathalie GON for teaching and helping me in chemical synthesis, Patrick DUBOURDEAUX for guiding me in chemical synthesis, NMR and UV-vis measurements, Eric GOURE for getting along with me and the project by sharing immense ideas and extensive support, Dr. Martin CLEMANCEY and Dr. Ricardo GARCIA-SERRRES for Mössbauer, Colette LEBRUN for mass spectroscopy, Pierre-Alain BAYLE for NMR spectroscopy, In particular, I am grateful to **Dr. Jean-Marc LATOUR** for holding the team PMB together on all occasion and discussing science with each and everybody enthusiastically.

I would also like to thank the other members in my lab that includes, Dr. Victor DUARTE and his cute family (Mme. Isabelle DUARTE, Quentin and Alisée), Dr. Olivier SENEQUE, Christelle CAUX-THANG, Vincent LEBRUN (PhD student), Aurélie JACQUES (PhD student), Manon ISAAC (PhD student), Alexandra SEVE (M2 student-UJF), Patricia SCHNEIDER (M2 student-UJF) for making each and every day lively and most I am going to miss will be the Group presentations, Friday breakfast, Christmas lunch, Birthdays parties, etc. My thanks also extend to all the staffs and members in CEA, Grenoble; CNRS-Délégation Alpes who made life simpler by providing resources and funds. A special thanks to head Mr. Stéphane MENAGE, LCBM, CEA-Grenoble and other members for their active participation in the development of science.

A special thanks to all the Indian colleagues in CEA, Grenoble: Dr. Ashok Kumar NANJUNDAN (Post-Doc) and his family, Dr. Senthilnathan DHURAIRAJAN (Post-Doc) and his family, Dr. Ramakrishnan SETHU (Post-Doc) and his family, Dr. Velavan KATHIRVELU (Post-Doc) and his family, Dr. Sabareesh VELU and his family, Dr. Govindh PRAJAPATHI (Post-Doc), Dr. Manikandan KARUPASAMY (Post-Doc) and his

family, Dr. Saravanan RENGARJAN (Post-Doc) and his family, for sharing all the good will, trust, faith and made me to feel better at hard times.. Also my gratitude extends to fellow Indians inside and outside CEA (the list continues...), for your great support and participation in activities like weekend crickets, group lunch parties etc

On the whole, my hearty wishes for each and every other mentioned above, to succeed in any future endeavors they come across and I pray god to shower you good health and wealth...

*Last but not the least; I would like to thank my family: my parents **Mr. Balasubramanian NAGARAJAN** and **Mrs. Girija BALASUBRAMANIAN**, for giving birth to me at the first place and supporting me throughout my life, my brother **Mr. Kalyanaraman BALASUBRAMANIAN** for giving me immense support on everything and everyday.*

Thank you

Ramachandran BALASUBRAMANIAN

LIST OF ABBREVIATIONS iv**INTRODUCTION 1**

1	Electron Transfer – The Example of the Blue Copper Proteins	3
2	Proton Liability and Metal Redox Potential.....	4
2.1	Fe- and Mn-Superoxide Dismutases.....	4
2.2	Iron and Manganese Hexa-aqua Complexes	7
3	Proton-Coupled Electron Transfer Reactions	7
4	Two Examples of PCET in Diiron Proteins.....	10
4.1	Ribonucleotide Reductases	10
4.2	Hemerythrin	12
5	Work Developed in the PhD	14
6	References.....	17

PART 1. A Proton-Coupled Electron Transfer: Discovery of the Phenomena 21

1	Mixed Valence Complexes.....	23
1.1	X-Ray Characterization	25
1.2	Spectroscopic Characterizations.....	26
1.2.1	UV-Visible Absorption Spectroscopy	27
1.2.2	¹ H-NMR Spectroscopy	28
1.2.3	Mössbauer Spectroscopy	31
1.3	Electrochemical Characterization.....	35
2	pH-Driven Valence Inversion	37
2.1	X-Ray Structure.....	38
2.2	Mössbauer Characterization	39
2.3	UV-Visible Characterization.....	40
2.4	¹ H-NMR Characterization	41
2.5	Demonstration of the Valence Inversion.....	42

2.5.1	UV-Visible Absorption Spectroscopy	42
2.5.2	¹ H-NMR Spectroscopy	44
2.5.3	Mössbauer Spectroscopy	44
3	Isomerization Reaction	46
3.1	Manuscript submitted to Chemistry – A European Journal.....	46
3.2	Discussion	68
4	Studies of the proton-coupled electron transfer reaction	76
4.1	Published work	77
4.2	Strategy developed.....	86
5	References	90
 PART 2. A Proton-Coupled Electron Transfer: How it is influenced by the redox potential and acid strength of the partners		93
1	Overview.....	95
2	Draft n°1	97
3	Draft n°2	122
 CONCLUSION		159
 ANNEX 1. Ligand syntheses.....		163
1	2-hydroxymethyl-6-carboxaldehyde-p-cresol (2)	165
2	2-chloromethyl-6-carboxaldehyde-p-cresol (3).....	165
3	bis-(2-picolyl) amine (4)	166
4	2-(<i>N,N</i> -bis(2-picolyl)-aminomethyl)-6-carboxaldehyde-p-cresol (5)	166
5	2-(<i>N,N</i> -bis(2-picolyl)-aminomethyl)-6-hydroxymethyl-p-cresol (6).....	169
6	2-(<i>N,N</i> -bis(2-picolyl)-aminomethyl)-6-chloromethyl-p-cresol (7)	169
7	<i>N</i> -(2-nitro) benzyl- <i>N</i> -(2-picolyl) amine (8)	170
8	2-(bis(2-picolyl)-aminomethyl)-6-(<i>N</i> -(2-nitro)benzyl- <i>N</i> -(2-picolyl)-aminomethyl-p-cresol (9).....	170

9	2-(bis(2-picolyl)-aminomethyl)-6-(<i>N</i> -(2-amino)benzyl- <i>N</i> -(2-picolyl)-aminomethyl- <i>p</i> -cresol, HL-BnNH ₂ (10)	171
10	bis((1-methyl-benzoimidazol-2-yl)methyl)amine, HN(CH ₂ BzImMe) ₂ (11)	172
11	2-((bis((1-methyl-benzimidazol-2-yl)methyl)amino)methyl)-6-((bis((pyridyl-2-yl)methyl)amino)methyl)-4-methylphenol, HL-(BzImMe) ₂ (Py) ₂ (12)	173
12	2,6-bis((bis((1-methyl-benzoimidazol-2-yl)methyl)amino)methyl)-4-methylphenol, HL-(BzImMe) ₄ (13)	174
13	2-((bis((1-methyl-benzimidazol-2-yl)methyl)amino)methyl)-4-methyl-6-(((2-nitrobenzyl)(pyridilmethyl)amino)methyl)phenol, HL-(MeBzIm) ₂ (Py)(NO ₂) (14)	174
14	2-(((2-aminobenzyl)(pyridin-2-yl-methyl)amino)methyl)-6-((bis((1-methyl-benzimidazol-2-yl)methyl)amino)methyl)-4-methylphenol, HL-(MeBzIm) ₂ (Py)(NH ₂) (15)	175
15	2-(bis(2-picolyl)-aminomethyl)-6-(bis(2-benzimidazole)-aminomethyl- <i>p</i> -cresol, HL-(BzImH) ₂ (Py) ₂ (17)	175

ANNEX 2. Complex syntheses 177

1	[Fe ^{III} (μ ₂ -mpdp)Fe ^{II} (H ₂ NBn-L)](ClO ₄) ₂	179
2	[(L-(BzImH) ₂ (Py) ₂)Fe ^{III} (μ ₂ -mpdp)Fe ^{II}](ClO ₄) ₂	180
3	[(L-(BzImMe) ₄)Fe ^{III} (μ ₂ -mpdp)Fe ^{II}](ClO ₄) ₂	180
4	[(L-(BzImMe) ₂ (Py) ₂)Fe ^{III} (μ ₂ -mpdp)Fe ^{II}](ClO ₄) ₂	181
5	[(L-(BzImMe) ₂ (Py)(BnNH ₂)Fe ^{III} (μ ₂ -mpdp)Fe ^{II}](ClO ₄) ₂	182

SUMMARY IN FRENCH 185

SUMMARY IN ENGLISH 186

List of abbreviations

AcO ⁻	Acetate
Ar	Argon gas
ar	Aromatic
BPA	bis(2-picoyl)amine
BDE	Bond Dissociation Energy
CH ₂ Cl ₂	Dichloromethane
CO	Carbon monoxide
CH ₃ CN	Acetonitrile
CT	Charge Transfer
CPET	Concerted Proton-Electron Transfer
d, s, t, m	Doublet, Singlet, Triplet, Multiplet observed in ¹ H-NMR spectra
DMF	Dimethyl formamide
EPT	Electron-Proton Transfer
Eq.	Equation
equiv.	Equivalent
¹ H-NMR	Proton Nuclear Magnetic Resonance
IVCT	InterValence Charge Transfer
KIE	Kinetic Isotope Effect
L	Ligand
MW or M	Molecular weight (g/mol)
m	Mass of the substance
MMO	Methane Mono Oxygenase
mpdp ²⁻	<i>m</i> -phenylenedipropionate
Na ₂ SO ₄	Sodium sulphate
NaBH ₄	Sodium borohydride
NaHCO ₃	Sodium bicarbonate
NEt ₃	Triethylamine
NHE	Normal Hydrogen Electrode

PF ₆ ⁻	Hexafluorophosphate
PCET	Proton-Coupled Electron Transfer
PET	Proton-Electron Transfer
PAP	Purple Acid Phosphatase
PrO ⁻	Propionate
RNR	Ribo Nucleotide Reductase
ppm	parts per million
rpm	revolutions per minute
SOCl ₂	Thionyl chloride
SOD	Super Oxide Dismutase
SCE	Standard Calomel Electrode
TLC	Thin Layer Chromatography
THF	Tetrahydrofuran
TBAP	Tetra- <i>n</i> -butylammonium perchlorate
UV	Ultra-Violet
w.r.t	With respect to



INTRODUCTION

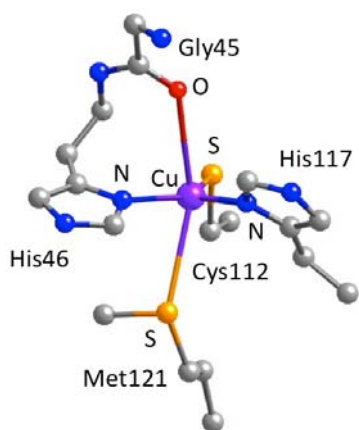


A fundamental concept of coordination chemistry is that ligand type may favor one oxidation state of a metal over another. Thus π -acceptor ligands such as CO and PF₃ stabilize low oxidation states, whereas high oxidation states are favored by π -donor ligands such as fluoride or anionic oxygen donors. Implicit in this concept is the idea that chemical modification of the ligand may change its ligating properties, and thereby modify the reduction potential of the metal to which it is coordinated. Protonation or deprotonation of the ligand at a site near or remote from the metal–ligand bond is a simple, reversible method of modification, and can influence dramatically the redox potential of metal bound to the ligand as well as influencing the spin state.

The change of metal redox state is central to inorganic chemistry being involved in wide range of domains of chemistry starting from catalysis to corrosion and from materials to biology. So for the ease of understanding the effects on the redox potentials, few literature illustrations on different metalloproteins are presented briefly in the following sub divisions viz. the electron transfer in blue copper proteins, pK_a dependency in Fe/Mn superoxide dismutases, and proton-coupled electron transfers.

1 Electron Transfer – The Example of the Blue Copper Proteins

Important processes in biology are redox reactions. One can quote for example respiration and photosynthesis. To be achieved, these redox reactions require the setup of an electron transport chain and specific proteins are devoted to this task. A well-known example of this class of proteins that carry out electron transport is the blue copper proteins⁽¹⁾. The T1-type contains a single copper ion. They are named cupredoxins by analogy with ferredoxins that are iron proteins also assuming electron transfers. Examples of cupredoxins are azurins and stellacyanins. The active site of the azurin from *Pseudomonas aeruginosa* is shown in Figure 1.1.



	Cu ^I -L distance in Å	Cu ^{II} -L distance in Å
Cu-N _{His46}	2.14	2.09
Cu-N _{His117}	2.15	2.04
Cu-S _{Cys112}	2.27	2.26
Cu-S _{Met121}	3.17	3.12
Cu-O _{Gly45}	3.10	2.95

Figure 1.1. Active site of the *Pseudomonas aeruginosa* azurin (drawn from PDB 4AZU). Metal–ligand distances are those measured at pH = 9.9⁽²⁾.

The copper ion is in a trigonal bipyramidal environment. In the equatorial plane, the metal is coordinated by two histidines, namely His46 and His117, and one cysteine, Cys112. The two axial positions are occupied by more remote atoms, the sulfur atom of the methionine 121 and the backbone carbonyl oxygen atom of a glycine residue (Gly45). This strong coordination by three ligands in the equatorial plane and the presence of one weaker axial coordination are common features of cupredoxins⁽³⁾.

The active site shuffles between Cu^{II} and Cu^I oxidation states. The structure depicted above is neither optimized for the oxidized state nor for the reduced one. In addition, hydrogen bond network makes the structure quite rigid, with only small changes upon redox interconversion (see Figure 1.1 for the Cu-ligand distances in azurin). This makes the active site well adapted for electron transfer.

2 Proton Liability and Metal Redox Potential

2.1 Fe- and Mn-Superoxide Dismutases

SuperOxide Dismutases (SODs) catalyze the disproportionation of the superoxide radical anion O₂^{•-} into dioxygen and hydrogen peroxide. One out of the three families of SODs is Fe- or Mn-dependent. These proteins share structural and amino-acid sequence homology. While some members of this family are only active with Fe (FeSODs) or Mn (MnSODs), others display significant activity with both metals (cambialistic Fe/MnSODs). These differences have been nicely

rationalized by the group of Anne-Frances Miller that has evidenced the crucial role of the coordinated water molecule⁽⁴⁾.

The left part of Figure 2.1 shows the active site of Fe- or MnSODs. The metal ion is in a trigonal bipyramidal environment with two histidine and one aspartate ligands in the equatorial plane. The two axial positions are occupied by one histidine and a water molecule. It has to be noticed that the coordinated water molecule interacts with a nearby residue, glutamine or histidine, through hydrogen bonding. The position and orientation of the glutamine residue are the main structural differences between the active site of Fe(Fe)SOD (that is the FeSOD filled with Fe) and that of Fe(Mn)SOD (that is MnSOD filled with Fe) (see right part of Figure 2.1)¹.

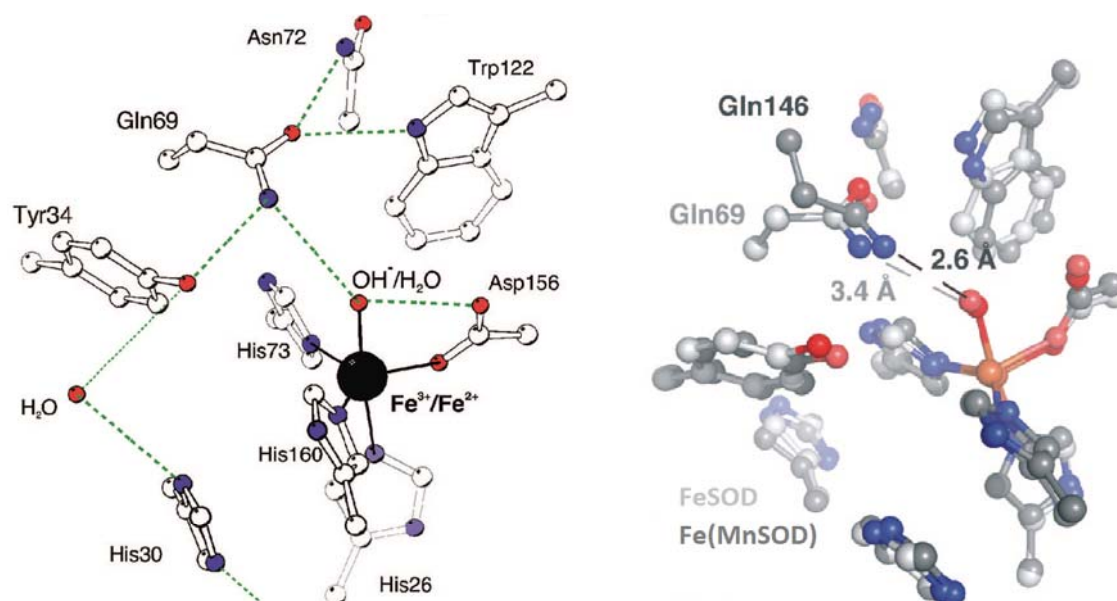
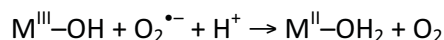
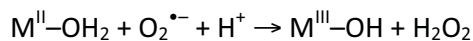


Figure 2.1. Left : Cartoon of the active site of FeSOD. The green dashed lines indicate the hydrogen bond network present at least in some FeSOD variants. Right : Comparison between the active sites of *Echerichia Coli* Fe(Fe)SOD (in light gray) and Fe(Mn)SOD (in drack gray)⁽⁴⁾.

During catalysis, the metal ion cycles between the +II and +III oxidation states. More precisely, it is proposed that the active site goes back and forth between M^{II}-OH₂ and M^{III}-OH according to the following reactions:



¹ The metal in parenthesis is the physiological one. The metal indicated first is the one that has been incorporated in the protein. So M₁(M₂)SOD stands for the specific M₂SOD filled with M₁.

The redox potentials at pH = 7 for the oxidation and the reduction of the superoxide ion are equal to 0.89 and -0.16 V vs NHE, respectively⁽⁵⁾. These values are indicated on Figure 2.2 as blue lines. To be efficient, the active site of SODs must present a redox potential lying between these values. Indeed, the values for Mn(Mn)SOD and Fe(Fe)SOD were determined close to 0.3 and 0.1 V vs NHE, respectively.

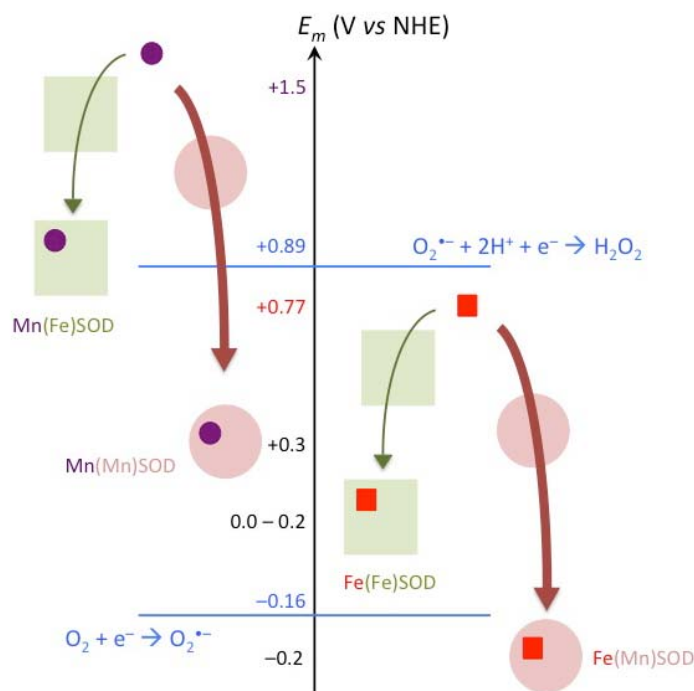


Figure 2.2. Metal ion reduction midpoint potentials for FeSODs (large green square) and MnSODs (large pink disk) when filled with Fe (red small square) or Mn (violet small disk). The redox potentials for the oxidation and the reduction of the superoxide ion are also indicated (adapted from ref (4)).

The hexa-aqua complexes, namely $[\text{Mn}(\text{OH}_2)_6]^{3+/2+}$ and $[\text{Fe}(\text{OH}_2)_6]^{3+/2+}$, present reduction midpoint potentials (E_m) of 1.5 and 0.77 V vs NHE, respectively (see Figure 2.2). Similar differences between $\text{Mn}^{\text{III/II}}$ and $\text{Fe}^{\text{III/II}}$ were observed in other complexes. A similar difference is thus anticipated for the same protein substituted by either Mn or Fe. According to the measured midpoint potentials, one can deduce that the Mn-specific SOD proteins decrease E_m by hundreds of millivolts, much more than the Fe-specific SOD proteins (compare in Figure 2.2 the thick brown and thin green arrows for Mn and Fe, respectively). Anne-Frances Miller further hypothesized that these depressions will lead to a too low E_m value for Fe(Mn)SOD and a too high one for Mn(Fe)SOD (see Figure 2.2). The group of A.-F. Miller nicely demonstrates through a combination of mutations by NMR and EPR studies, that the modulation of the redox potential is due to the hydrogen bond interaction between the coordinated solvent molecule and the glutamine residue that indeed

controls the ability to protonate the coordinated hydroxide ion issued from the coordinated water molecule.

2.2 Iron and Manganese Hexa-aqua Complexes

According to the values reported in Figure 2.2, $[\text{Fe}(\text{OH}_2)_6]^{2+}$ is easier to oxidized than the analogous $[\text{Mn}(\text{OH}_2)_6]^{2+}$ complex.

Differences in the pK_a values are also observed between these four complexes. The values associated to the reaction given in Eq. 1.1 are listed in Table 2.1⁽⁶⁾.



Table 2.1. pK_a values associated to the $[\text{M}(\text{OH}_2)_6]^{n+} / [\text{M}(\text{OH}_2)_5(\text{OH})]^{(n-1)+}$ couples (M = Mn, Fe ; n = 2, 3).

n ↓ M →	Mn	Fe
2	10.6	9.5
3	0.1	2.2

These values indicate that the 3+ hexa-aqua complexes are more acidic than the 2+ complexes, as can be anticipated from the metal charges. While the Mn^{III} complex is more acidic than the ferric one, the Mn^{II} complex is less than the ferrous one.

So the ability of releasing a proton from a coordinated water molecule depends both on the nature of the metal and its oxidation state.

We have seen one example of electron transfer and one example of the role of proton transfer. These can be intimately coupled in biological processes. They are usually named proton-coupled electron transfer (PCET) reactions.

3 Proton-Coupled Electron Transfer Reactions

Transferring electrons automatically leads to a change in the charges of the involved species. The system accepting additional electron(s) will become more difficult to reduce, and on the reverse, when releasing electron(s), oxidation will be harder. Proton motion is a simple way to compensate the charge generated by the electron transfer. Coupling proton and electron transfers allows avoiding high-energy intermediates but may have a kinetic cost to pay. It also leads to a

redox potential leveling, thus rendering high-oxidation states accessible. Proton-coupled electron transfer (PCET) reactions are the heart of important biological processes such as respiration, photosynthesis or nitrogen fixation⁽⁷⁾. It should also be noticed that pH changes may induce electron transfer and reciprocally, electron transfer may induce proton translocation.

We will focus in this section on PCET reactions where one electron and one proton are transferred. In Section 4, an example of a reaction involving two electrons and one proton will be given but other stoichiometries are also observed. When the electron and the proton originate from or are directed toward the same chemical bond, the reaction corresponds to a hydrogen atom transfer (HAT). Otherwise, the term PCET is used. The question of the sequence order of the electron and the proton transfers automatically rises. Conceptually three kinds of situations can be envisioned: electron transfer followed by proton transfer (EPT), the reverse that is first proton and then electron (PET) or a concerted process (CPET). The following example will illustrate that considerations on the thermodynamics may allow discriminating between these three mechanisms.

The group of James M. Mayer has investigated the oxidation of dihydroanthracene (DHA) to anthracene by the mononuclear Fe^{III} complex $[\text{Fe}(\text{H}_2\text{bim})_2(\text{Hbim})]^{2+}$ where H₂bim = 2,2'-biimidazoline⁽⁸⁾. Mechanistic studies suggest the formation of the monoanthracenyl radical HA[•] on the first step (see Figure 3.1).

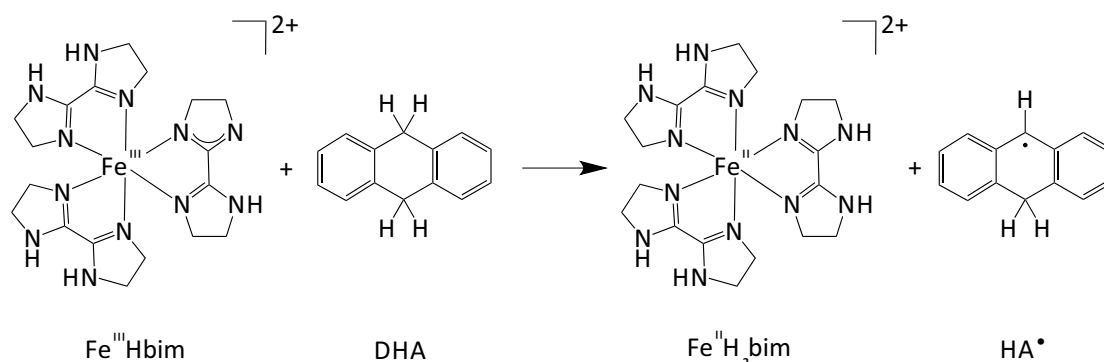


Figure 3.1. First step of the oxidation of dihydroanthracene (DHA) by the mononuclear Fe^{III} complex $[\text{Fe}^{\text{III}}(\text{H}_2\text{bim})_2(\text{Hbim})]^{2+}$ (denoted Fe^{III}Hbim).

The following graphs summarize the thermodynamic data.

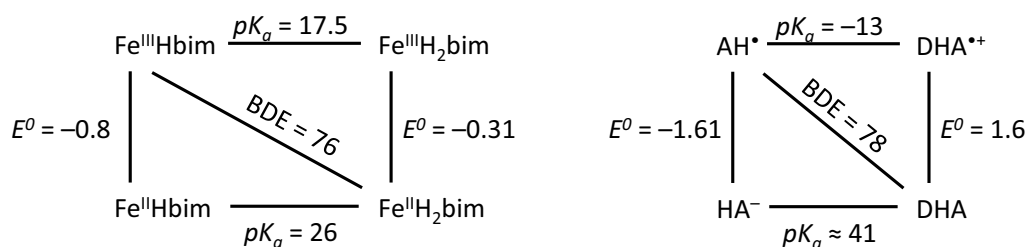


Figure 3.2. pK_a , redox potential (in V vs ferrocenium/ferrocene) and bond dissociation energies (in kcal.mol⁻¹) for the iron complexes and dihydroanthracene.

The values for ΔG^0 can be calculated for the three mechanisms according to the above thermodynamic data (see Figure 3.3). They have to be compared with the activation energy $\Delta G^0 = 22$ kcal.mol⁻¹ (8). Since the values for ΔG^0 determined for the ET and PT mechanisms are larger than the activation barrier, these processes can be discarded. So this PCET occurs within a concerted process.

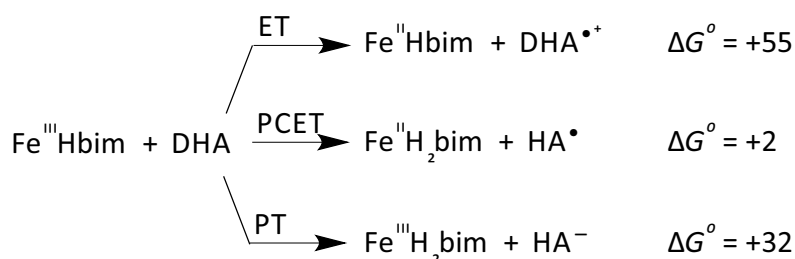


Figure 3.3. ΔG^0 values (in kcal.mol⁻¹) for the three mechanisms.

These considerations can't always been done and the intrinsic process is often difficult to determine. Two sequential PET mechanisms have been demonstrated for the release of the hydroquinone H₂Q_B in the photosynthetic reaction center of *Rhodobacter sphaeroides* (see Figure 3.4)^(9,10).

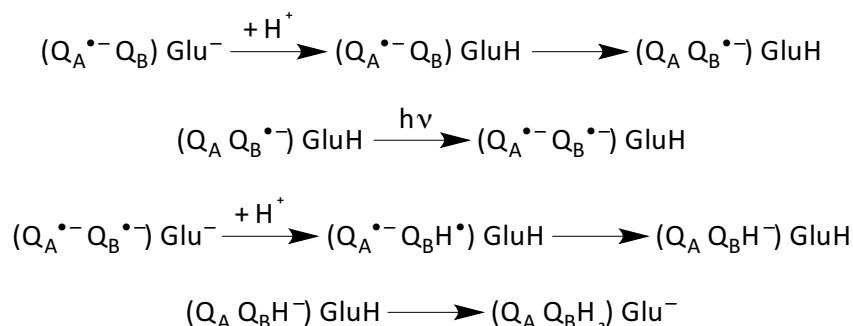


Figure 3.4. Summary of the reaction sequence in the photosynthetic reaction center of *Rhodobacter sphaeroides* evidencing two sequential PET processes (1st and 3rd lines). The hydroquinone H₂Q_B is released after protonation by the nearby carboxylic acid Glu₂₁₂. Protons originate from the cytoplasm and recent studies evidenced a key role for the nearby His₁₂₆ and His₁₂₈.

An EPT mechanism has been identified for the reaction between a Ru^{IV} and a Os^{II} complexes⁽⁷⁾. This is due to the high acidity of *cis*-[Ru^{IV}(bpy)₂(py)(OH)]³⁺ that prevents a PET mechanism⁽¹¹⁾.

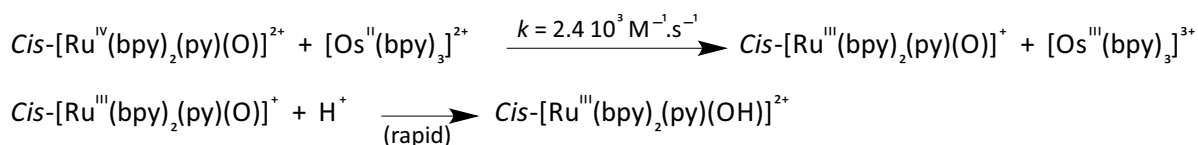


Figure 3.5. Sequential EPT mechanism identified in acidic medium (pH < 6.2).

The two examples given above indeed reflect the two major types of systems that have been investigated: (i) organic systems such as quinones but also phenols and (ii) metal complexes mainly based on second (such as ruthenium) or third (such as osmium) row transition metals. More recently, the role of hydrogen bond in the oxidation of phenols has also been investigated, in relation with the oxidation of the Tyrosine_z residue in the photosystem II⁽¹²⁾.

4 Two Examples of PCET in Diiron Proteins

4.1 Ribonucleotide Reductases

Ribonucleotide Reductases (RNRs) catalyze one of the most important reactions in Nature, the reduction of nucleoside 5'-di- or triphosphates to deoxynucleoside 5'-di- or triphosphates, which is the kinetic limiting step in DNA synthesis. In the first step, a thiyl radical originating from a conserved cysteine performs the abstraction of the H atom in the 3' position (see Figure 4.1).

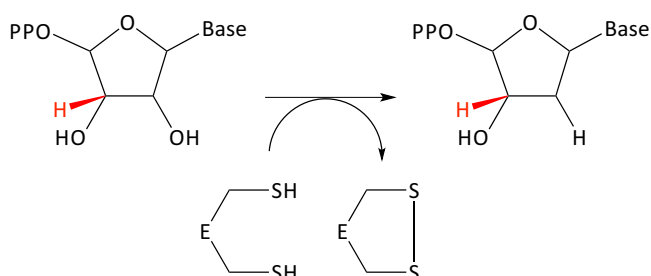


Figure 4.1. Reaction catalysed by RNRs. PPO stands for the polyphosphate group. The base can be either an adenine, a guanine, a cytosine or a uracil. The reaction starts by the abstraction of the H atom drawn in red, located in 3' position.

RNRs have been divided in three classes, according to the metal cofactor used for nucleotide reduction⁽¹³⁾. Class I RNRs present similar folding, two subunits, denoted α and β , and contain a dinuclear metal cluster for catalysis. Class II RNRs require Ado-cobalamine while Class III

RNRs contain a Fe_4S_4 cluster. Class I is further divided in three subclasses. RNRs of class Ia contain a diiron cluster, class Ib a dimanganese one, and class Ic a hetero iron-manganese system. In classes Ia and Ib, a tyrosine is associated to the dimetallic cluster.

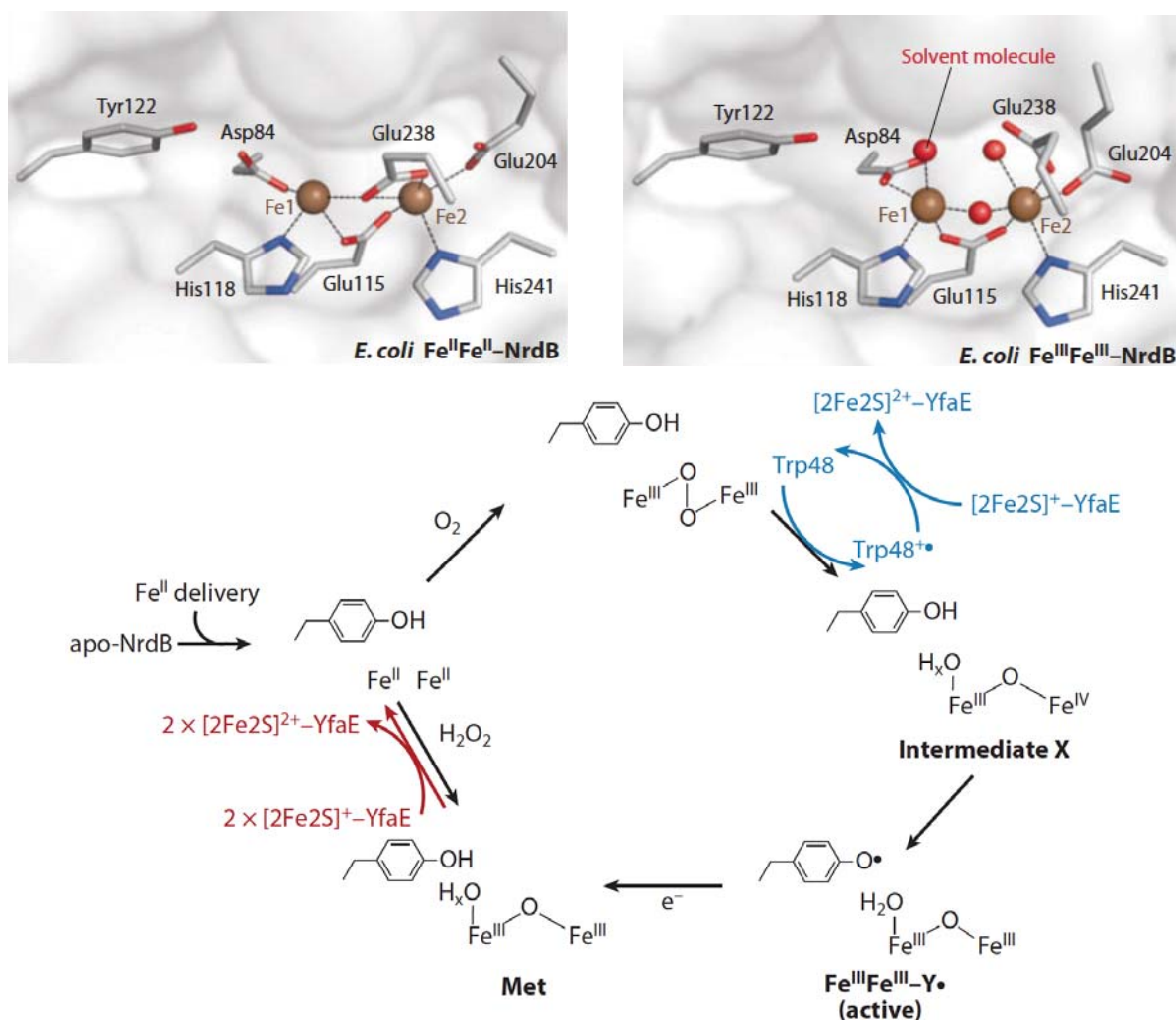


Figure 4.2. Top: X-ray structure of the reduced (left) and oxidized (right) diiron site of class Ia RNRs. Bottom: Proposed mechanism for the generation of the tyrosyl radical in class Ia RNRs. Proposed maintenance of the cofactors is written in red while the extra reducing agents are indicated in blue. NrdB and YfaE designate the β subunit and the assembly cofactor, respectively⁽¹⁴⁾.

The diiron cluster in RNR class Ia is located in the β subunit and its main role is to generate upon oxygen activation and stabilize a tyrosine radical ($\text{Y}_{122}\cdot$). The radical initially located on the tyrosine 122 in the β subunit is then translocated to the cysteine 439 of the α subunit by a multistep of hole/electron hopping mechanism over a ≈ 35 Å distance. Proton transfer reactions are coupled to this radical migration (see Figure 4.3).

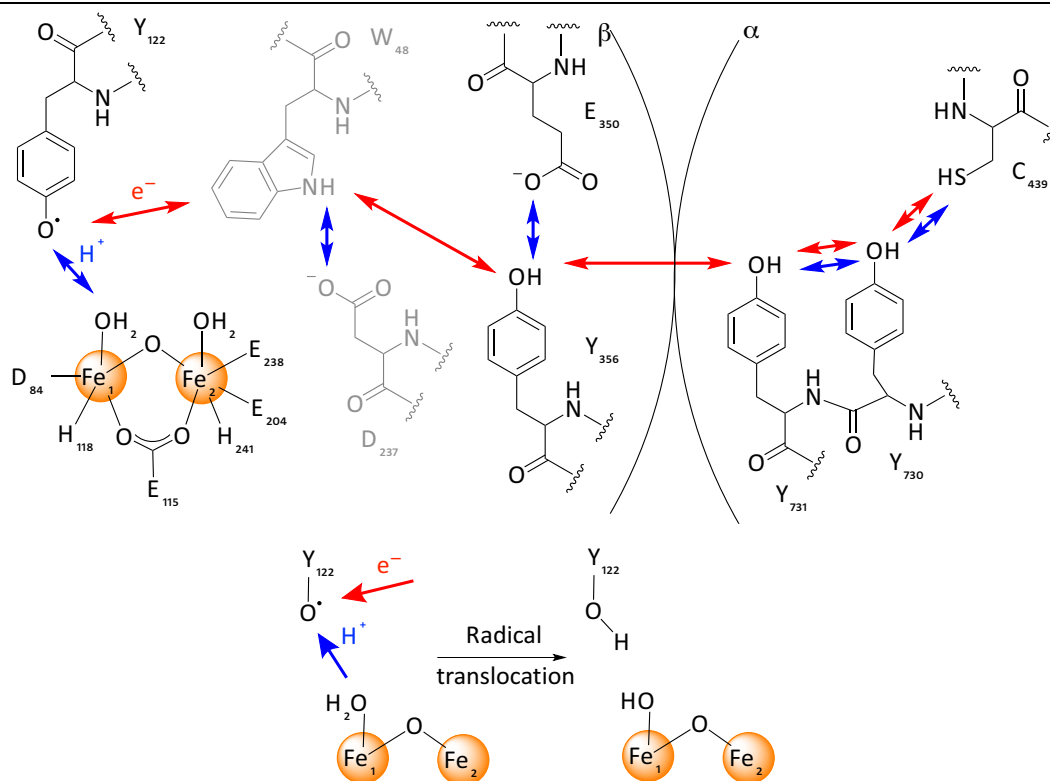


Figure 4.3. Top: Proposed radical translocation pathway from the Y_{122}^{\bullet} in the β subunit to C_{439} in the α subunit. Since there is no direct evidence for the involvement of W_{48} and D_{237} in this pathway, they are shown in gray. Bottom: Radical translocation. The resting state of the cofactor in the β subunit is shown on the left⁽¹⁵⁾.

JoAnne Stubbe, J. Martin Bollinger, Carsten Krebs and coworkers have nicely demonstrated in a very recent paper⁽¹⁵⁾ that, in the key first step of the reduction of Y_{122}^{\bullet} , the water molecule coordinated to the Fe_1 site that is the closest iron site to the tyrosine residue, indeed transfers one proton to yield the neutral tyrosine residue. The sequence order is still unknown.

4.2 Hemerythrin

Hemerythrin is an oxygen carrier found in several invertebrates. Its active site contains two iron centers bridged by one aspartate and one glutamate. In the deoxy form, the two iron ions are in the +II redox state and bridged by an extra hydroxide. One of the iron centers is pentacoordinated with two coordinated histidines while the other iron center is hexacoordinated with three histidines (see left part of Figure 4.4). The fixation of dioxygen leads to the formation of the oxy form where the two iron atoms have been oxidized to the +III oxidation state and are bridged by an oxo group (see right part of Figure 4.4). A hydroperoxo anion is end-on coordinated to the iron site bearing two histidines. The hydroperoxo ligand is hydrogen bonded to the oxo bridge⁽¹⁶⁾.

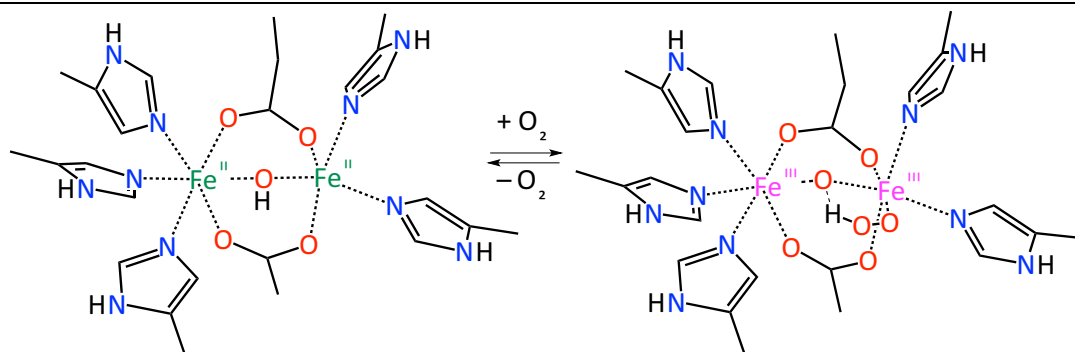


Figure 4.4. Conversion upon dioxygen fixation/release between the deoxy (left) and oxy (right) forms of hemerythrin.

This oxygen fixation reaction can be viewed as a proton-coupled electron transfer involving two electrons and one proton.

It should be noticed that two mixed valent non-physiological forms of hemerythrin have been characterized. One (semimet_R) is obtained from the one electron reduction by dithionite of the met form, that results from the oxidation to the diferric state of the deoxy-hemerythrin by ferricyanide, and the other (semimet_O) from the one electron oxidation by $[\text{Fe}(\text{CN})_6]^{3-}$ of the deoxy form (see Figure 4.5). These two semimet forms present distinct UV-visible and EPR signatures reflecting different electronic structures⁽¹⁷⁾. Indeed, one main difference is the location of the iron valences. It has been demonstrated that a change in pH above and below 7 induces this valence inversion⁽¹⁸⁾.

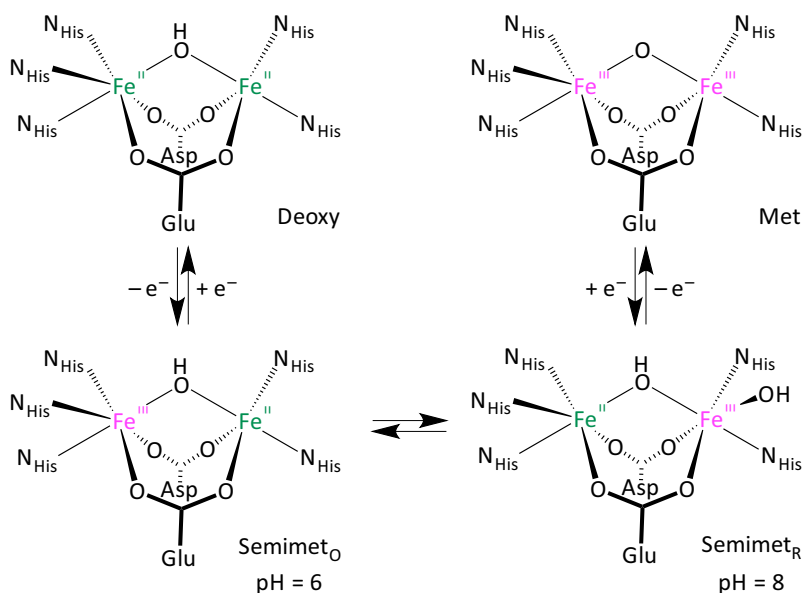


Figure 4.5. The different forms of hemerythrin and the interconversion between the semimet forms upon pH variations.

5 Work Developed in the PhD

The group of Jean-Marc Latour has long been interested in diiron complexes as models of proteins such as hemerythrin⁽¹⁹⁾ or purple acid phosphatases⁽²⁰⁾ but also as catalysts for oxygen atom insertion^(21,22). More recently, new diiron systems were synthesized and their reactivity toward amine transfer reactions investigated^(23,24).

In the course of these studies, a ditopic ligand L-BnNH₂ bearing an aniline group was designed and the corresponding mixed valent diiron complex [Fe^{III}(μ₂-mpdp)Fe^{II}(H₂NBn-L)]²⁺ isolated where the aniline is coordinated to the Fe^{II} site. Before my PhD, it was demonstrated that this complex can be reversibly deprotonated to the mixed valent complex [Fe^{II}(μ₂-mpdp)Fe^{III}(HNBn-L)]⁺ where the anilide is coordinated to the Fe^{III} site. Thus, a valence inversion is observed upon deprotonation. This was the first example of a pH-driven valence inversion within a dinuclear system that is based on a first-row transition metal. It should be noticed that this reaction can be reversed, that is the addition of acid on the anilide complex [Fe^{II}(μ₂-mpdp)Fe^{III}(HNBn-L)]⁺ gives back the starting aniline system [Fe^{III}(μ₂-mpdp)Fe^{II}(H₂NBn-L)]²⁺ ⁽²⁵⁾.

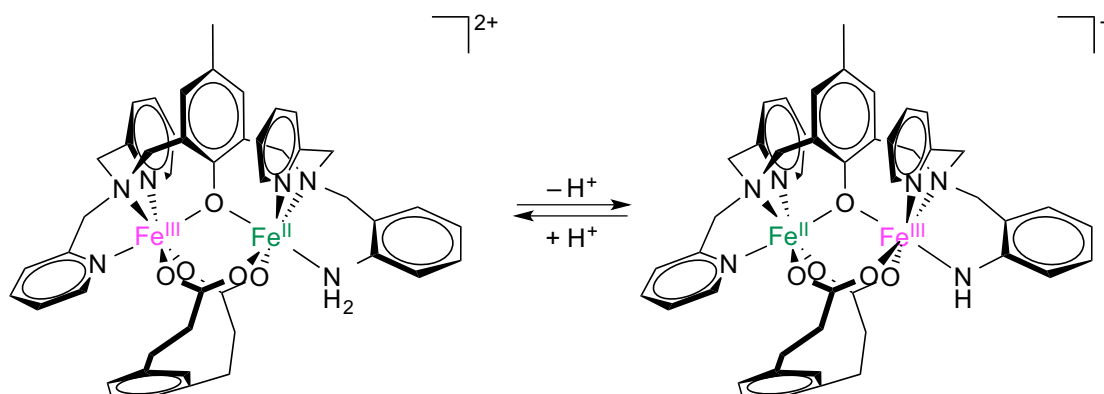


Figure 5.1. Reversible intervalence charge transfer triggered by (de)protonation of the terminal aniline (anilide) ligand.

This reaction is similar to that observed between the two semimet forms of hemerythrin (see section 4.2). This is to my knowledge the single example of a valence inversion triggered by pH variations in biological systems. As synthetic complexes are concerned, a similar reaction has been observed for a single hetero dinuclear ruthenium-osmium complex⁽²⁶⁾.

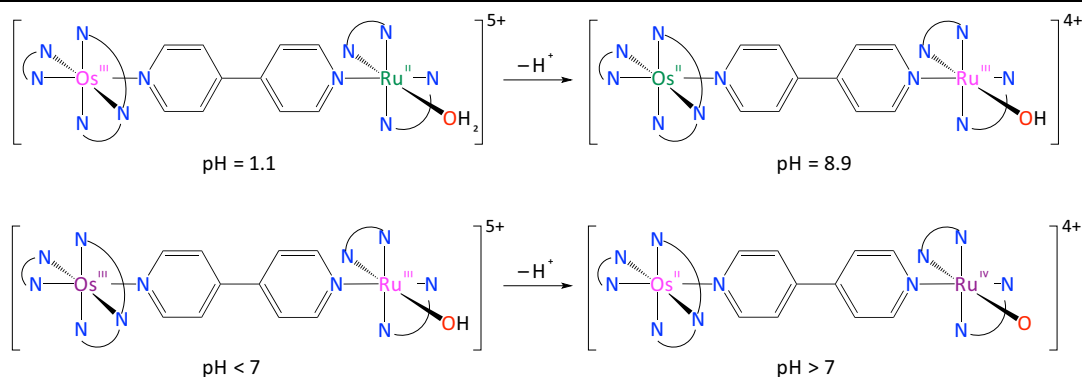


Figure 5.2. Valence inversion induced by pH increase when starting from $[(\text{tpy})(\text{bpy})\text{Os}^{\text{III}}(\mu\text{-}4,4'\text{-bpy})\text{Ru}^{\text{II}}(\text{bpy})_2(\text{OH}_2)]^{5+}$ (1st line) or from the one-electron oxidized species $[(\text{tpy})(\text{bpy})\text{Os}^{\text{III}}(\mu\text{-}4,4'\text{-bpy})\text{Ru}^{\text{III}}(\text{bpy})_2(\text{OH})]^{5+}$ (2nd line). tpy = 2,2':6,2''-terpyridine, bpy = 2,2'-bipyridine, 4,4'-bpy = 4,4'-bipyridine.

It should be noticed that a proton-coupled electron transfer involving an aniline/anilide complex has been investigated in great details by James M. Mayer and coworkers⁽²⁷⁾. The reaction is a hydrogen atom transfer between the complexes $[(\text{Tp})(\text{Cl})_2\text{Os}^{\text{III}}(\text{H}_2\text{NPh})]$ and $[(\text{Tp})(\text{Cl})_2\text{Os}^{\text{IV}}(\text{HNPh})]$ (Tp^- = hydrotris(1-pyrazolyl)borate). This study is remarkable in that all the five related self-exchange rate constants have been determined as the thermochemical data.

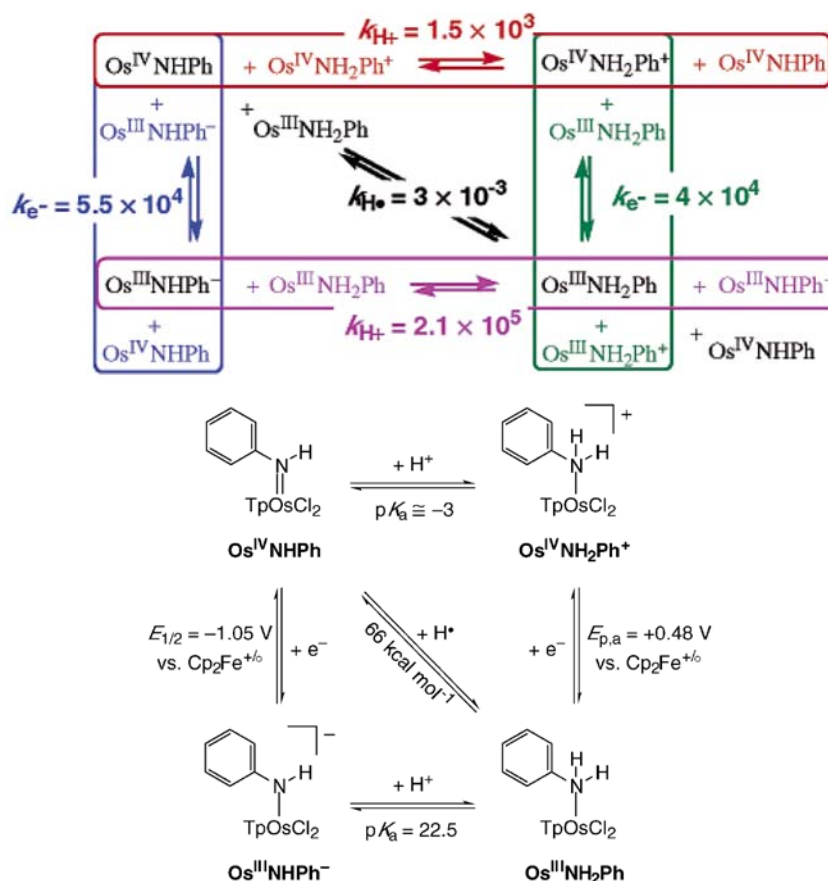


Figure 5.3. Rate constants and thermodynamic data for the HAT reaction between $[(\text{Tp})(\text{Cl})_2\text{Os}^{\text{IV}}(\text{HNPh})]$ and $[(\text{Tp})(\text{Cl})_2\text{Os}^{\text{III}}(\text{H}_2\text{NPh})]$. Taken from ref (27).

It was concluded that the reaction proceeds via a concerted process except if traces of acid or base are present where the sequential pathway EPT or PET prevails.

In 2011, the Agence National de la Recherche funded Jean-Marc Latour's team for the three-year project Bi3Pro (Proton-triggered bistable bimetallic bio-inspired systems). The main objective of this project is (i) to identify the critical parameters that control proton-coupled electron transfer reactions in mixed valent diiron complexes and (ii) to decipher the PCET mechanisms. The complex presented above is the prototype of the study. The critical parameters that are anticipated are (i) the acid strength of the ligand bearing the exchangeable proton, (ii) the redox potentials of the Fe^{II} and Fe^{III} sites, and (iii) the communication between the two iron sites. These parameters can indeed be varied according to the flexibility of the ditopic ligand. The para position of the central phenol ring can be substituted by groups differing in the electrodonating (–NO₂) or withdrawing character (–NMe₂). The coordinating groups of the two tertiary amines linked in ortho positions can be changed in order to stabilize either the +III or the +II states. In addition, the dicarboxylate bridge can be changed (into a bis-diphenylphosphate for instance) in order to modify the separation between the two metal ions. Characterization of the mixed valent complexes relies on spectroscopic techniques such as Mössbauer, UV-visible and ¹H-NMR. The distinct signatures of the protonated and deprotonated forms allow a rigorous characterization of the complexes and the unambiguous determination of the valence locations. The work of my PhD fully falls within this project.

The first part of this manuscript deals with the mixed valent complex schemed in Figure 5.1, namely [Fe^{III}(μ₂-mpdp)Fe^{II}(H₂NBn-L)]²⁺. In a first section, I present the properties of similar mixed valent diiron complexes as observed by the spectroscopic techniques used through this PhD work that is UV-visible, ¹H-NMR and Mössbauer. Cyclic voltammetry studies are also summarized. In the second section, I present in more details the investigated aniline complex and summarized the spectroscopic evidence for the pH-induced valence inversion. Sections 3 and 4 are devoted to the specific studies performed during my PhD.

My first task was to decipher the PCET reaction associated to the deprotonation of [Fe^{III}(μ₂-mpdp)Fe^{II}(H₂NBn-L)]²⁺. This work was performed by the group of Pr. Cyrille Costentin of the

Laboratoire d'Electrochimie Moléculaire (UMR 7591, Université Paris Diderot – Paris 7) who is a partner of the Bi3Pro project. I've spent three months in Paris and investigated in details by cyclovoltammetry the behavior of this complex in presence of triethylamine. All the studies conducted in the LEM converged to conclude for a concerted transfer of the proton and of the electron. These results are presented in Section 3.

Before the start of my PhD, it was observed that the aniline complex $[\text{Fe}^{\text{III}}(\mu_2\text{-mpdp})\text{Fe}^{\text{II}}(\text{H}_2\text{NBn-L})]^{2+}$ spontaneously evolves in acetonitrile solution. To identify the generated complex, UV-visible, $^1\text{H-NMR}$ and Mössbauer spectra were recorded both on the aniline complex and on the deprotonated form $[\text{Fe}^{\text{II}}(\mu_2\text{-mpdp})\text{Fe}^{\text{III}}(\text{HNBn-L})]^+$. All these studies, reported in Section 4, led to the conclusion that the reaction is an isomerization process involving the aniline and the pyridine ligands connected to the same tertiary amine.

As mentioned above, the main objective of the ANR project was to synthesize new mixed valent diiron complexes bearing a ligand with an exchangeable proton and to investigate the associated PCET reaction. The objective was to vary the acid strength of the ligand and to modulate the redox potentials of the iron centers. Two modifications of the ditopic ligand were achieved. The first one relies in the introduction of two *N*-methylbenzimidazole groups in place of the two pyridines coordinating to the Fe^{III} site in $[\text{Fe}^{\text{III}}(\mu_2\text{-mpdp})\text{Fe}^{\text{II}}(\text{H}_2\text{NBn-L})]^{2+}$. The second modification was the replacement of the aniline ring by a benzimidazole ligand. The originality was to investigate the PCET reaction when the exchangeable proton is on a nitrogen atom that is not bond to the iron site. All these studies are presented in the second part of this manuscript.

Lastly, some concluding remarks and perspectives are given.

6 References

- [1] O. Farver, I. Pecht: Electron transfer in blue copper proteins. *Coord. Chem. Rev.* **2011**, *255*, 757-773.
- [2] B. R. Crane, A. J. Di Bilio, J. R. Winkler, H. B. Gray: Electron tunneling in single crystals of *Pseudomonas aeruginosa* azurins. *J. Am. Chem. Soc.* **2001**, *123*, 11623-11631.
- [3] C. Dennison: Investigating the structure and function of cupredoxins. *Coord. Chem. Rev.* **2005**, *249*, 3025-3054.
- [4] A.-F. Miller: Redox tuning over almost 1 V in a structurally conserved active site: Lessons from Fe-containing superoxide dismutase. *Acc. Chem. Res.* **2008**, *41*, 501-510.

- [5] D. T. Sawyer, J. S. Valentine: How super is superoxide? *Acc. Chem. Res.* **1981**, *14*, 393-400.
- [6] J. Li, C. L. Fischer, J. L. Chen, D. Bashford, L. Noodleman: Calculation of redox potentials and pK_a values of hydrated transition metal cations by a combined density functional and continuum dielectric theory. *Inorg. Chem.* **1996**, *35*, 4694-4702.
- [7] M. H. V. Huynh, T. J. Meyer: Proton-coupled electron transfer. *Chem. Rev.* **2007**, *107*, 5004-5064.
- [8] J. M. Mayer: Proton-coupled electron transfer: A reaction chemist's view. *Annu. Rev. Phys. Chem.* **2004**, *55*, 363-390.
- [9] M. Y. Okamura, M. L. Paddock, M. S. Graige, G. Feher: Proton and electron transfer in bacterial reaction centers. *Biochim. Biophys. Acta* **2000**, *1458*, 148-163.
- [10] M. L. Paddock, L. Sagle, A. Tehrani, J. T. Beatty, G. Feher, M. Y. Okamura: Mechanism of proton transfer inhibition by Cd^{2+} binding to bacterial reaction centers: Determination of the pK_A of functionally important histidine residues. *Biochemistry* **2003**, *42*, 9626-9632.
- [11] E. L. Lebeau, R. A. Binstead, T. J. Meyer: Mechanistic implications of proton transfer coupled to electron transfer. *J. Am. Chem. Soc.* **2001**, *123*, 10535-10544.
- [12] J. Bonin, C. Costentin, M. Robert, J.-M. Savéant, C. Tard: Hydrogen-bond relays in concerted proton-electron transfers. *Acc. Chem. Res.* **2012**, *45*, 372-381.
- [13] D. T. Logan: Closing the circle on ribonucleotide reductases. *Nat. Struct. Mol. Biol.* **2011**, *18*, 251-253.
- [14] J. A. Cotruvo Jr., J. Stubbe: Class I ribonucleotide reductases: Metallocofactor assembly and repair in vitro and in vivo. *Annu. Rev. Biochem.* **2011**, *80*, 733-767.
- [15] B. Wörsdörfer, D. A. Conner, K. Yokoyama, J. Livada, M. Seyedsayamdost, W. Jiang, A. Silakov, J. Stubbe, J. M. Bollinger Jr., C. Krebs: Function of the diiron cluster of *Escherichia coli* class Ia ribonucleotide reductase in proton-coupled electron transfer. *J. Am. Chem. Soc.* **2013**, *135*, 8585-8593.
- [16] R. E. Stenkamp: Dioxygen and hemerythrin. *Chem. Rev.* **1994**, *94*, 715-726.
- [17] L. M. Babcock, Z. Bradic, P. C. Harrington, R. G. Wilkins, G. S. Yoneda: Preparation, disproportionation, and reactions of two semi-met forms of hemerythrin. *J. Am. Chem. Soc.* **1980**, *102*, 2849-2850.
- [18] J. M. McCormick, R. C. Reem, E. I. Solomon: Chemical and spectroscopic studies of the mixed-valent derivatives of the non-heme iron protein hemerythrin. *J. Am. Chem. Soc.* **1991**, *113*, 9066-9079.
- [19] W. Kanda, W. Moneta, M. Bardet, E. Bernard, N. Debaecker, J. Laugier, A. Bousseksou, S. Chardon-Noblat, J.-M. Latour: A model of semimet hemerythrin; NMR spectroscopic evidence of valence localization in bis(μ -carboxylato)(μ -phenolato)diiron(II,III) complexes in solution. *Angew. Chem., Int. Ed. Engl.* **1995**, *34*, 588-590.
- [20] E. Bernard, W. Moneta, J. Laugier, S. Chardon-Noblat, A. Deronzier, J.-P. Tuchagues, J.-M. Latour: A mixed-valent Fe(II)Fe(III) complex with an unsymmetrical terminal phenoxo ligand as model for the active site of purple acid phosphatases. *Angew. Chem., Int. Ed. Engl.* **1994**, *33*, 887-889.

-
- [21] F. Avenier, L. Dubois, P. Dubourdeaux, J.-M. Latour: A diiron complex mediates an intramolecular aliphatic hydroxylation by various oxygen donors. *Chem. Commun.* **2005**, 480-482.
- [22] F. Avenier, L. Dubois, J.-M. Latour: Intermolecular aromatic hydroxylation mediated by a dinuclear iron complex: an oxo-Fe^{IV} Fe^{IV} active intermediate is suggested. *New. J. Chem.* **2004**, *28*, 782-784.
- [23] F. Avenier, J.-M. Latour: Catalytic aziridination of olefins and amidation of thioanisole by a non-heme iron complex. *Chem. Commun.* **2004**, 1544-1545.
- [24] F. Avenier, E. Gouré, P. Dubourdeaux, O. Sénèque, J.-L. Oddou, J. Pécaut, S. Chardon-Noblat, A. Deronzier, J.-M. Latour: Multiple Aromatic Amination Mediated by a Diiron Complex. *Angew. Chem. Int. Ed.* **2008**, *47*, 715-717.
- [25] E. Gouré, G. Thiabaud, M. Carboni, N. Gon, P. Dubourdeaux, R. Garcia-Serres, M. Clémancey, J.-L. Oddou, A. Y. Robin, L. Jacquamet, L. Dubois, G. Blondin, J.-M. Latour: Reversible (De)protonation-Induced Valence Inversion in Mixed-Valent Diiron(II,III) Complexes. *Inorg. Chem.* **2011**, *50*, 6408-6410.
- [26] G. A. Neyhart, T. J. Meyer: pH-induced intramolecular electron transfer. *Inorg. Chem.* **1986**, *25*, 4807-4808.
- [27] J. D. Soper, J. M. Mayer: Slow hydrogen atom self-exchange between Os(IV) anilide and Os(III) aniline complexes: Relationships with electron and proton transfer self-exchange. *J. Am. Chem. Soc.* **2003**, *125*, 12217-12229.



PART 1



A Proton-coupled electron transfer:
Discovery of the phenomena

Much work has been devoted towards the synthesis and structural characterization of diiron complexes as models of proteins such as hemerythrin⁽¹⁾ and purple acid phosphatases⁽²⁾ by Jean-Marc Latour's group. Before the presentation of the specific system that is investigated in this section, I would like to brief some of the mixed valent diiron complexes bearing dissymmetric ligands and their characterizations. After a description of the ligands used, spectroscopic properties will be detailed (UV-visible, ¹H-NMR, Mössbauer). Electrochemical characterizations will also be presented.

1 Mixed Valence Complexes

This section is devoted to summarize the literature data on mixed-valent diiron complexes synthesized with a binucleating ligand derived from the well known Hbpmp ligand (Hbpmp = 2,6-bis[[bis(2-pyridylmethyl)amino)methyl]-4-methylphenol). A major part of these results were obtained in Jean-Marc Latour's group. Scheme 1.1 shows the Hbpmp ligand as the dissymmetric ones synthesized in different groups. In one of the ligand synthesized by Lambert *et al.*⁽³⁾, further denoted HL-PhOH, a second phenol was introduced to act as a terminal phenoxide on one iron ion in order to mimic the binding of a single terminal tyrosinate at the diiron center of the purple acid phosphatase enzyme (PAP). Earlier, a quite similar ligand and the corresponding diiron(II,III) complex were synthesized by Neves *et al.* with one hydroxybenzyl group (HL-BnOH)⁽⁴⁾. These two ligands differ by the presence (in HL-BnOH) or absence (in HL-PhOH) of the methylene group between the tertiary amine and the phenol ring. Also in 2004, Chardon-Noblat *et al.*, two dissymmetric ligands bear a non coordinating group (R = -Bn and -BnCl₂)⁽⁵⁾.

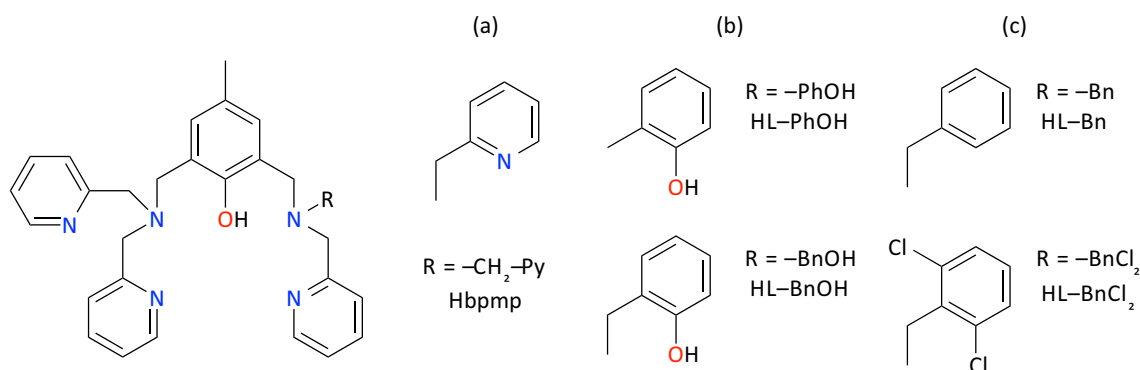


Figure 1.1. Representation of the ligands derived from Hbpmp ((a) R = CH₂Py) with (b) terminal phenol (R = -PhOH or -BnOH) and (c) non coordinating groups (R = -Bn or -BnCl₂).

Since HL-Bn group introduction does not saturate the coordination of one iron of the pair, the corresponding mixed valent complex possesses a coordinated solvent molecule (water in crystals). These modifications had served as a continuation in the preparation of dissymmetrical diiron(II,III) complexes, which mimic the coordination of the tyrosinate at the PAP active site⁽²⁾. Table 1.1 lists the complexes reported in the literature synthesized with the ligands shown in Figure 1.1.

Table 1.1. List of the diiron complexes of interest reported in the literature.

Complex	Chemical formula	Ref.	X-Ray
1a	$[(\text{bpmp})\text{Fe}_2(\mu\text{-OPr})_2]^{2+}$	(6,7)	Yes
1b	$[(\text{bpmp})\text{Fe}_2(\mu\text{-OAc})_2]^{2+}$	(8)	
2a	$[(\text{L-BnO})\text{Fe}_2(\mu\text{-OAc})_2]^+$	(4,9)	Yes
2b	$[(\text{L-BnO})\text{Fe}_2(\mu\text{-O}_2\text{P}(\text{OPh})_2)_2]^+$	(3)	
3a	$[(\text{L-Bn})\text{Fe}_2(\mu_2\text{-mpdp})(\text{OH}_2)]^{2+}$	(1)	Yes
3a'	$[(\text{L-Bn})\text{Fe}_2(\mu_2\text{-mpdp})(\text{CH}_3\text{CN})]^{2+}$	(5)	
3b	$[(\text{L-BnCl}_2)\text{Fe}_2(\mu_2\text{-mpdp})(\text{CH}_3\text{OH})]^{2+}$	(5)	Yes
3b'	$[(\text{L-BnCl}_2)\text{Fe}_2(\mu_2\text{-mpdp})(\text{CH}_3\text{CN})]^{2+}$	(5)	
4	$[(\text{L-PhO})\text{Fe}_2(\mu_2\text{-mpdp})]^+$	(3)	Yes

The additional bridging ligands are either two identical carboxylates (acetate = AcO^- , propionate = PrO^-) or phosphates (diphenylphosphate = $(\text{PhO})_2\text{PO}_2^-$) or a bis-carboxylate (*m*-phenylenedipropionate = mpdp^{2-}). They are drawn in Figure 1.2.

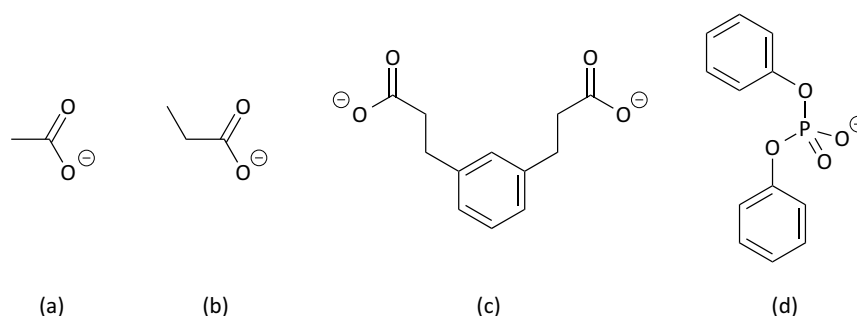


Figure 1.2. Extra bridges in the diiron complexes listed in Table 1.1: a) acetate; b) propionate; c) *meta*-phenylenedipropionate; d) diphenylphosphate.

The dissymmetry introduced by a single terminal phenoxide influences drastically the redox properties of the diiron site: the strong destabilization of the diferrous state and the less pronounced stabilization of the diferric state lead to an enlarged stability domain for the mixed valent state (see below). The purpose of briefing about the characterization of above mentioned diiron complexes acts as a reference for the mixed-valent complexes developed before and in the due course of the PhD work.

1.1 X-Ray Characterization

Complexes **1a** $[(\text{bpmp})\text{Fe}_2(\mu\text{-OPr})_2]^{2+}$ ^(6,7), **2a** $[(\text{L-BnO})\text{Fe}_2(\mu\text{-OAc})_2]^+$ ⁽⁹⁾, **3a** $[(\text{L-Bn})\text{Fe}_2(\mu_2\text{-mpdp})(\text{OH}_2)]^{2+}$ ⁽¹⁾ and **4** $[(\text{L-PhO})\text{Fe}_2(\mu_2\text{-mpdp})]^+$ ⁽³⁾ have been structurally characterized using X-ray crystallography by different groups and their X-ray structures are shown in Figure 1.3. The X-ray structure of complex **3b** $[(\text{L-BnCl}_2)\text{Fe}_2(\mu_2\text{-mpdp})(\text{CH}_3\text{OH})]^{2+}$ ⁽⁵⁾ is analogous to that of complex **3a** with methanol in the place of water.

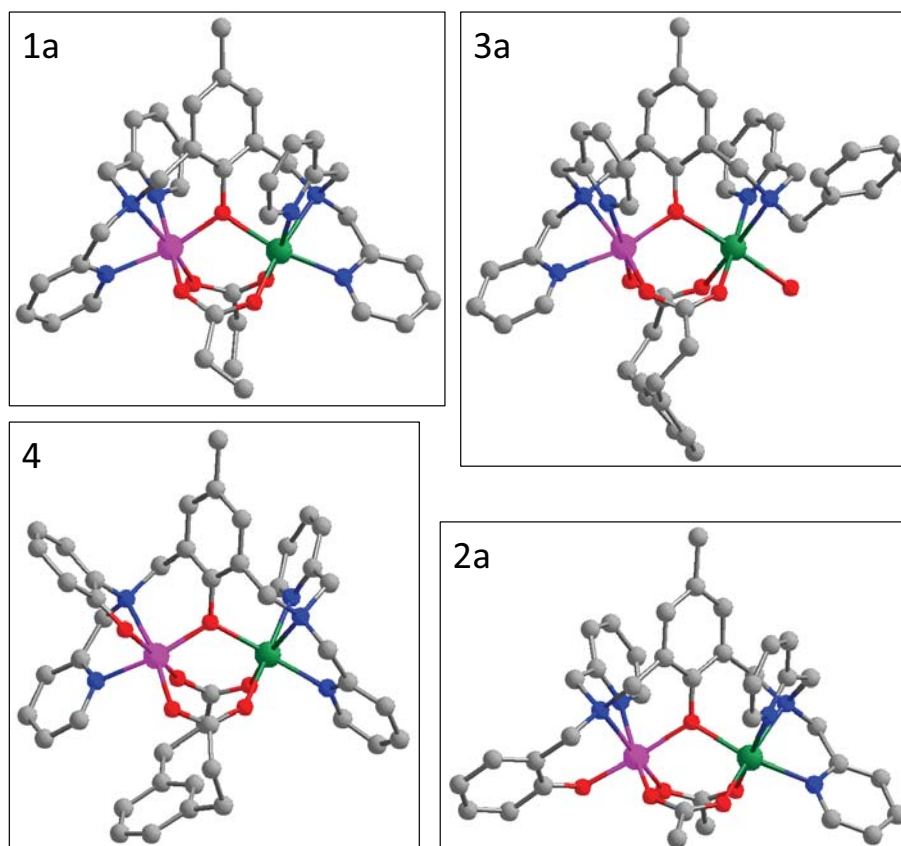


Figure 1.3. X-ray structures of the mixed valent complexes $[(\text{bpmp})\text{Fe}_2(\mu\text{-OPr})_2]^{2+}$ (1a, top left)⁶, $[(\text{L-Bn})\text{Fe}_2(\mu_2\text{-mpdp})(\text{OH}_2)]^{2+}$ (3a, top right)¹, $[(\text{L-PhO})\text{Fe}_2(\mu_2\text{-mpdp})]^+$ (4, bottom left)³ and $[(\text{L-BnO})\text{Fe}_2(\mu\text{-OAc})_2]^+$ (2a, bottom right)⁴. The Fe^{II} ion is always schemed in green on the left hand side while the Fe^{III} is drawn in pink on the right side.

The two Fe ions in complex **1a** $[(\text{bpmp})\text{Fe}_2(\mu\text{-OPr})_2]^{2+}$ possess a N_3O_3 environment. The metal centers are bridged by the phenoxide oxygen atom of bpmp^- and by two propionate ligands leading to a triply bridged core similar to that found in hemerythrin. The overall N_3O_3 coordination is best described as a rhombically distorted octahedron for the two iron atoms. This is indeed observed in all the other structures mentioned in Figure 1.3. Crystals of complex **4** consist in discrete cations $[\text{Fe}_2(\text{L-PhO})(\text{mpdp})]^+$ and complex **2a** consist in $[(\text{L-BnO})\text{Fe}_2(\mu\text{-OAc})_2]^+$. Both show a N_2O_4 coordination for Fe^{III} with the terminal phenoxide and a N_3O_3 environment for the Fe^{II} . It is noteworthy that in complex **2a** one pyridine coordinated to the Fe^{III} is in *cis* position to the bridging phenoxide whereas in complex **4** it is in *trans* position, the Fe^{II} ion being in the bispicolylamine site in both the cases. In complexes **3a** and **3b** the coordination sphere of the Fe^{II} ion is not fulfilled by the binucleating ligand and coordination of a solvent molecule (water or methanol) makes it to N_2O_4 environment. The exchange of this exogenous molecule by the solvent (CH_3CN) was studied in the complexes **3a** and **3b** forming **3a'** and **3b'** (refer Table 1.1)⁽⁵⁾.

Table 1.2 summarizes the average bond distances of the two iron ions w.r.t. the neighboring atoms for the X-ray characterized complexes. The valence localization is in agreement with the Fe^{III} ion associated to the smaller average M–L distance and the Fe^{II} ion to the larger one.

Table 1.2. Average M–L bond distances (Å) for the complexes **1a**, **2a**, **3a**, **3b** and **4**.

Complex	Fe^{II}	Fe^{III}
1a $[(\text{bpmp})\text{Fe}_2(\mu\text{-OPr})_2]^{2+}$	2.131	2.056
2a $[(\text{L-BnO})\text{Fe}_2(\mu\text{-OAc})_2]^+$	2.140	2.051
3a $[(\text{L-Bn})\text{Fe}_2(\mu_2\text{-mpdp})(\text{OH}_2)]^{2+}$	2.154	2.073
3b $[(\text{L-BnCl}_2)\text{Fe}_2(\mu_2\text{-mpdp})(\text{CH}_3\text{OH})]^{2+}$	2.134	2.061
4 $[(\text{L-PhO})\text{Fe}_2(\mu_2\text{-mpdp})]^+$	2.134	2.061

1.2 Spectroscopic Characterizations

Upon determining the crystal structure, the complexes were subjected to a study by UV-visible absorption spectroscopy, Mössbauer spectroscopy, $^1\text{H-NMR}$ spectroscopy and electrochemical techniques. This section will be oriented for the briefing of the characterizations of few complexes listed in Table 1.1 performed by the different groups.

1.2.1 UV-Visible Absorption Spectroscopy

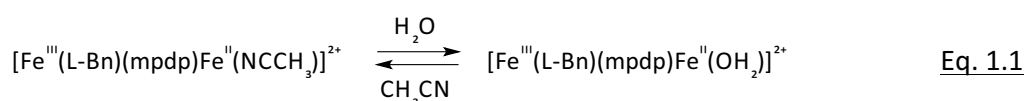
The absorption maxima and extinction coefficient values for acetonitrile solutions of the complexes are summarized in Table 1.3. It is noteworthy that the spectrum of the mixed valent complexes is dominated in the visible range by a band in the 500 – 600 nm domain. In addition the complexes exhibit a strong band at higher energy, $\lambda \approx 330\text{-}370$ nm, and a low intensity band at $\lambda \approx 1050$ nm in acetonitrile⁽³⁾. For instance, the Fe^{II}Fe^{III} derivatives of the tetrapyridyl ligand⁽⁸⁾ which exhibit (i) a band around 550 nm which has been assigned to a charge transfer from the bridging phenoxide to the ferric ion (LMCT), (ii) a transition at higher energy ($\lambda \approx 330$ nm) attributed to a charge transfer from the ferrous ion to the pyridyl groups (MLCT), and (iii) a band at lower energy ($\lambda \approx 1200$ nm) assigned to the intervalence charge transition (IVCT). Alternatively the latter absorption could originate from a d-d transition of the ferrous ion; such transitions have been shown to appear in this domain in semimet hemerythrins⁽¹⁰⁾. In complexes **2a**⁽⁶⁾, **2b**⁽³⁾ and **4**⁽³⁾ bearing a terminal phenoxide in addition to the bridging one, a single band is detected in the 400-600 nm range with an increased intensity compared to that in complex **1a**^(6,7) (see Table 1.3), suggesting that two phenoxide-to-Fe^{III} charge transfer bands cannot be distinguished. It has also been noticed that these CT transitions are sensitive to the nature of the additional bridges (e.g., mpdp²⁻, benzoate, diphenylphosphate).

Table 1.3. Maximum wavelengths (λ_{max} in nm) and molar extinction coefficients (ϵ in $\text{M}^{-1}\cdot\text{cm}^{-1}$) of mixed valent complexes in acetonitrile.

Complex	PhO ⁻ → Fe ^{III} λ_{max} (ϵ)	IVCT λ_{max} (ϵ)	Ref
1a	554 (950)	1348 (310)	(6)
1b	556 (900)	1364 (290)	(6)
2a	556 (4560)	1050 (60)	(4)
2b	580 (3300)	1050 (90)	(1)
3a', 3b'	578 (1300)	Not described	(5)
3a	569 (1050)		
4	548 (1900)	1050 (160)	(3)

Upon dissolution in acetonitrile, the exogenous aqua/methanol ligand of **3a** and **3b** respectively is substituted by an acetonitrile molecule leading to the formation of the complex **3a'**

$[\text{Fe}^{\text{III}}(\text{L-Bn})(\text{mpdp})\text{Fe}^{\text{II}}(\text{NCCH}_3)]^{2+}$ (**3b'**) $[\text{Fe}^{\text{III}}(\text{L-BnCl}_2)(\text{mpdp})\text{Fe}^{\text{II}}(\text{NCCH}_3)]^{2+}$ for the methanol substituted starting complex **3b**)⁽⁵⁾. It has been also shown that when the binucleating ligand is HL-Bn (complex **3a**), the progressive addition of water causes the band at 578 nm to shift to 569 nm ($\epsilon = 1050 \text{ mol}^{-1} \cdot \text{L} \cdot \text{cm}^{-1}$) with a slight loss in the intensity (see Table 1.3). This transformation is quantitative after an addition of ≈ 1500 molar equiv. of water and occurs with an isosbestic point at 947 nm evidencing the back formation of **3a** from **3a'**^(1,5). It has been concluded that, after initial replacement of the exogenous ligand present in the solid state (H_2O or CH_3OH) by acetonitrile, the complex of the form $[\text{Fe}^{\text{III}}(\text{L-Bn})(\text{mpdp})\text{Fe}^{\text{II}}(\text{CH}_3\text{CN})]^{2+}$ is transformed into the aqua derivative of the form $[\text{Fe}^{\text{III}}(\text{L-Bn})(\text{mpdp})\text{Fe}^{\text{II}}(\text{H}_2\text{O})]^{2+}$ (Eq. 1.1):



1.2.2 ¹H-NMR Spectroscopy

This kind of complexes presents a high spin Fe^{II} and a high spin Fe^{III} ions in weak antiferromagnetic exchange interaction. At room temperature, the compounds are thus paramagnetic. The ¹H-NMR spectra feature sharp downfield shifted signals in a very wide frequency range extending to ≈ 600 ppm. The narrow line widths of the signals are consistent with the presence of a high spin ferrous ion that relaxes faster than the ferric one⁽⁶⁾. In the case of complex **1a** the ¹H-NMR spectrum (Figure 1.4) consists of relatively sharp resonances, which extend to 400 ppm in chemical shifts with no signal at negative values. The number of resonances reveals a fast electron exchange between the $\text{Fe}^{\text{II}}\text{Fe}^{\text{III}}$ and $\text{Fe}^{\text{III}}\text{Fe}^{\text{II}}$ forms on the NMR time scale (in other words, the iron valences are delocalized on the NMR time scale).

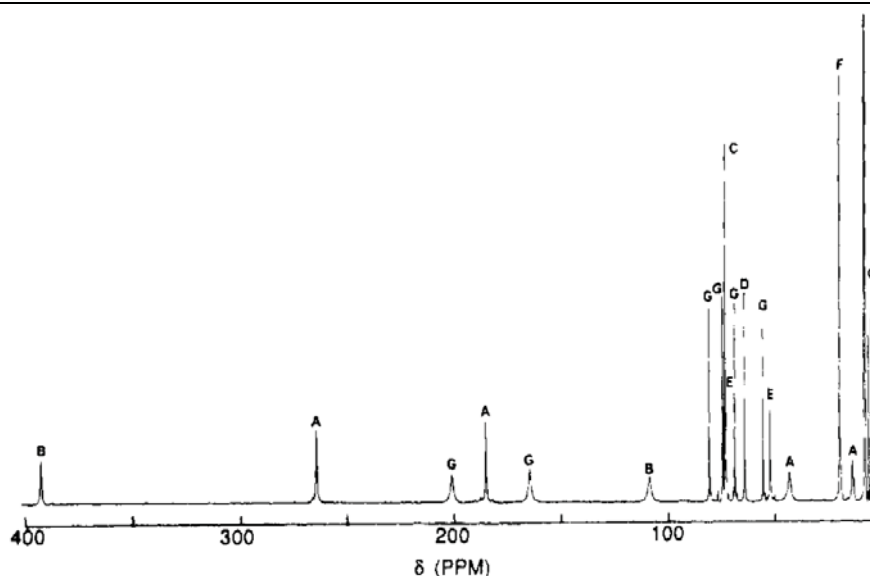


Figure 1.4. $^1\text{H-NMR}$ spectra of the complex **1a** : $[(\text{bpmp})\text{Fe}_2(\mu\text{-OPr})_2]^{2+}$.

In the case of complex **4**⁽³⁾, the $^1\text{H-NMR}$ spectrum (Figure 1.5) bears a strong resemblance in having a wide spectral range extending from 540 to -50 ppm unlike the tetrapyrrolyl complex **1a**. The even wider range and the presence of negatively shifted peaks evidence iron valence location on the NMR time scale. It is worth noting that in this series of compounds, negative chemical shifts are associated to methylenic protons close to a ferrous center. Through NOE experiments, the authors of ref.⁽³⁾ were able to show a correlation between the peak at -33 ppm and the one at 90 ppm assigned to the axial¹ methylenic proton of the picolyl group coordinating the Fe^{II} ion and another correlation between the peak at 70 ppm and the one at 206 ppm assigned to the σ -pyridyl proton of the same picolyl group (on the Fe^{II} side). Correlations do exist between the meta, para, and meta' protons of two pyridyl groups in the sequences $59 \leftrightarrow 10 \leftrightarrow 35$ ppm and $75 \leftrightarrow 5 \leftrightarrow 85$ ppm. The former is associated to one pyridyl group coordinated to Fe^{II} while the latter corresponds to one pyridyl bound to the Fe^{III} . The protons of the second pyridyl of the bis-picolylamine branch have not been assigned specifically because their signals overlap with that of mpdp^{2-} . However they have been observed when the experiments are performed at low temperature.

¹ Axial and equatorial methylenic protons are defined by analogy with those of cyclohexane.

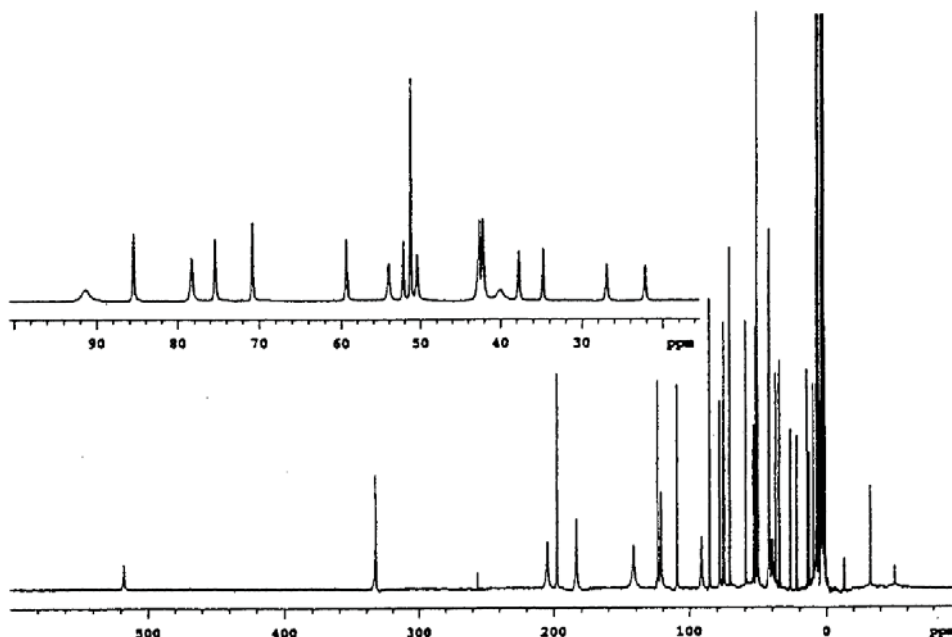


Figure 1.5. $^1\text{H-NMR}$ spectrum of the complex **4** $[(\text{L-PhO})\text{Fe}_2(\mu_2\text{-mpdp})]^+$ (solvent = CD_3CN).

Similarly the $^1\text{H-NMR}$ spectrum of the complex **3a'** (Figure 1.6) shows three extreme downfield resonances at 555, 375, and 265 ppm that were quite confidently assigned to the equatorial methylenic protons of the branch bound to the Fe^{III} ion⁽¹¹⁾.

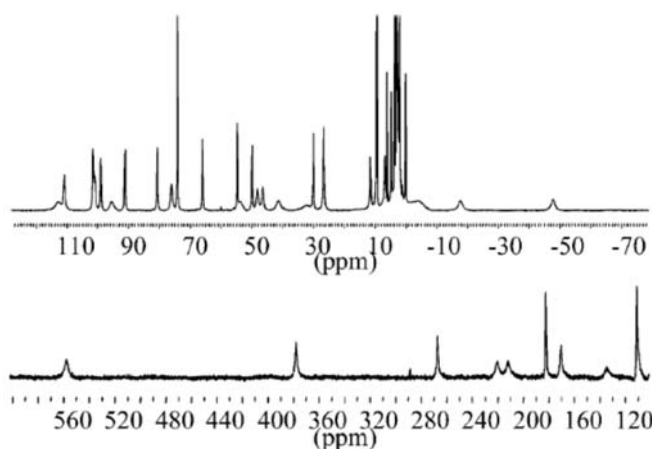


Figure 1.6. $^1\text{H-NMR}$ spectrum of the complex **3a'** $[(\text{L-Bn})\text{Fe}_2(\mu_2\text{-mpdp})(\text{CD}_3\text{CN})]^+$ (solvent = CD_3CN)

The three very wide resonances at 219, 210, and 137 ppm correspond to the *ortho*-pyridyl protons: Their short distances to the metal ions are responsible for their short T_2 . The observation of two resonances more downfield shifted than the third one indicates that the Fe^{III} ion with the larger spin is bound in the branch possessing two pyridines (bispicolylamine site), thereby confirming the valence localization observed in the solid state. The peculiar upfield shifted resonance at -48 ppm is assigned to the equatorial methylenic proton of the third picolyl group

bound to the Fe^{II} ion. Thus ¹H-NMR acts as a probe to clearly define the location of the iron centers in the mixed valence systems according to the groups coordinated to them.

1.2.3 Mössbauer Spectroscopy

Mössbauer spectroscopy relies on the recoilless nuclear resonance absorption of γ -rays.⁽¹²⁾ The energy of the nuclear transition between the ground state and a low-excited state of a nucleus is quite high, on the order of tens of keV. For a free nucleus, the absorption or the emission of a γ -photon induces important recoil. This leads in turn to a significant shift of the energy of the absorbed or emitted photon compared to the separation of the two levels for the nucleus in the resting state. This shift amounts to 5-6 orders of magnitude of the intrinsic line width that is directly related to the lifetime of the excited state of the nucleus. Consequently, the overlap between the emission and the absorption lines is not possible, preventing resonant absorption to occur. The great discovery of Rudolf Mössbauer in 1958 during his PhD in Heidelberg (he received the Nobel price in 1961) was that when embedded in a solid lattice, there is a non-zero proportion of the nuclei able to absorb or emit γ -photons without any recoil. The resonant absorption of γ -rays can then be observed. Only ≈ 40 elements of the periodic table are susceptible to be investigated by Mössbauer spectroscopy, the most common being the 57 isotope of iron (2.5 % natural abundance, energy of the γ -rays = 14.4 keV, intrinsic line width = 4.55 neV). Note that the ratio between the intrinsic line width and the energy of the γ -photon makes the Mössbauer spectroscopy one of the most precise spectroscopy in energy.

The nuclear transitions are sensitive to the electrons that surround the nucleus. Therefore, by probing the nucleus (⁵⁷Fe in what will follow), information on the electronic structure can be deduced. It is included in three parameters, namely the isomer shift (δ), the quadrupole splitting (ΔE_Q) and the hyperfine constants (a).

Because the ⁵⁷Fe nuclei in an investigated sample (that is the nuclei that absorb the γ -photon) present a different environment compared to that of the emitting ⁵⁷Fe nuclei in the source, the energy of the emitting photons must be tuned in order to match resonance. This tuning is obtained by moving back and forth the source up to few mm/s (Doppler effect). Accordingly, a Mössbauer spectrum corresponds to the transmission of the γ -photons (in %) as a function of the velocity of the source.

The required energy for resonance is generally referred to that of metallic iron at room temperature. This difference corresponds to the isomer shift (expressed in mm/s, see Figure 1.7). The value is sensitive to the oxidation state, the spin state and the coordination sphere of the iron ion (chemical nature of the ligands, their number and the covalency of the Fe–L bonds). For instance, δ decreases with increasing oxidation state.

The two nuclear states of ^{57}Fe involved in the Mössbauer transition present a non-zero nuclear spin: $I = 1/2$ for the ground state, $I = 3/2$ for the excited one. The non-spherical distribution of the electrons generates an electric field gradient at the nucleus that splits the $I = 3/2$ level in two sub-levels. Consequently, two nuclear transitions are possible: the quadrupole splitting is a direct measure of the separation in energy of these two transitions (unit = mm/s). This parameter gives also information about the oxidation state, the spin state and the site symmetry of the Fe. For example $\Delta E_Q = 0$ for the low-spin Fe^{II} ion in $[\text{Fe}(\text{CN})_6]^{4-}$ while a large $\Delta E_Q \approx 3$ mm/s is observed for the high-spin Fe^{II} ion in $[\text{Fe}(\text{OH}_2)_6]^{2+}$.

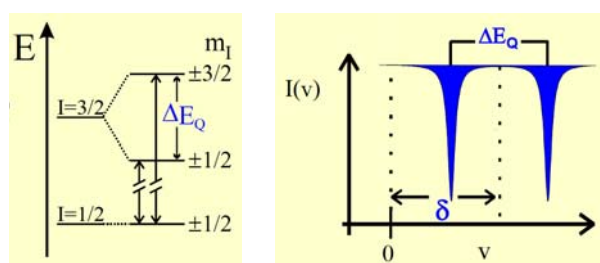


Figure 1.7. Energy diagram of the nuclear sub-levels of ^{57}Fe (left) and definition of the isomer shift and of the quadrupole splitting (right)⁽¹³⁾.

Lastly, the unpaired electrons generate large magnetic field at the nucleus. Interaction with the magnetic moment of both the $I = 1/2$ and $I = 3/2$ states leads to a total removing of the degeneracy of these levels and up to six nuclear transitions are thus detected. The hyperfine constants that can be deduced give information on the detailed magnetic structure of the Fe site. In addition, an external magnetic field can be applied in order to compete with the internal magnetic field produced by the unpaired electrons (Figure 1.8).

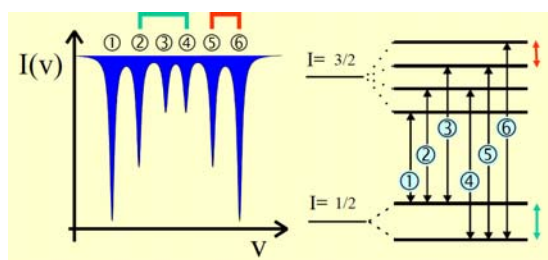


Figure 1.8. Mössbauer spectrum with hyperfine interactions (left) and assignment of the six Mössbauer transitions according to the energy diagram (right)⁽¹³⁾.

When investigating a sample containing ^{57}Fe , the recorded Mössbauer spectrum is the superimposition of the different contributions originating from the ^{57}Fe nuclei. The relative areas of the individual spectra correspond to the relative proportions of the Fe sites in the sample. For instance, a localized mixed-valent $\text{Fe}^{\text{II}}\text{Fe}^{\text{III}}$ species gives in zero field two quadrupole doublets of equal area, the doublets differing in the δ and ΔE_Q parameters.

Mössbauer spectroscopy concurs to probe, that the valences of the mixed valent compounds are trapped both in solution as well as in the solid state. We have gathered in Table 1.4 the reported values of the isomer shift and the quadrupole splitting for the complexes **1a**, **1b**, **2a**, **2b**, **4**, **3a'** and **3a** in solid state and in frozen acetonitrile solutions. This could serve for the assessment of the favorable coordination preferred by the Fe^{II} and Fe^{III} sites in the above mentioned mixed valent diiron systems.

Table 1.4. Mössbauer data of the complexes listed in Table 1.1.

Complex	Sample state	T (K)	High spin Fe^{III}			High spin Fe^{II}			Ref
			δ (mm/s)	ΔE_Q (mm/s)	%	δ (mm/s)	ΔE_Q (mm/s)	%	
1a	Solid	55	0.48	0.54	52	1.13	2.91	48	(6)
	CH_3CN	55	0.48	0.49	50	1.12 1.10	2.85 2.39	25 25	
1b	Solid	77	0.47	0.51	51	1.16	2.42	49	(8)
1 with $\mu_2\text{-mpdp}^{2-}$	Solid	80	0.42	0.41	50	1.05	2.58	50	
2a	Solid	115	0.522	1.096	50	1.132	2.544	50	(4)
2b	Solid	80	0.550	1.220	50	1.183	3.358	50	(3)
4	Solid	80	0.490	0.594	50	1.124	2.376	50	(3)
3a'	CH_3CN	77	0.48	0.39	50	1.20	3.14	50	(5)
3a	Solid	77	0.475	0.329	50	1.196	2.657	50	(5)
	CH_3CN	77	0.47	0.36	50	1.19	2.41	50	

The 77 K and zero-field Mössbauer spectra of complex **3a'** (Figure 1.9 left) and **4** (Figure 1.9 right) consist of two quadrupole doublets with equivalent absorption areas. On the left part of Figure 1.9, the spectrum has been deconvoluted into the individual contributions (solid lines above the experimental spectrum). The two quadrupole doublets (traces A1 and A2) have equal relative areas with isomer shifts $\delta_{\text{Fe}} = 1.20(1)$ and $0.48(1)$ mm/s and quadrupole splittings $\Delta E_Q = 3.14(1)$ and $0.39(1)$ mm/s. The first doublet (trace A1) is attributed to the high-spin Fe^{II} center, while the second one (trace A2) corresponds to the high-spin Fe^{III} center of the mixed-valent complex. A high-spin Fe^{III} impurity (trace A3, $\delta_{\text{Fe}} = 0.64(2)$ mm/s, $\Delta E_Q = 1.0(1)$ mm/s) is also present.

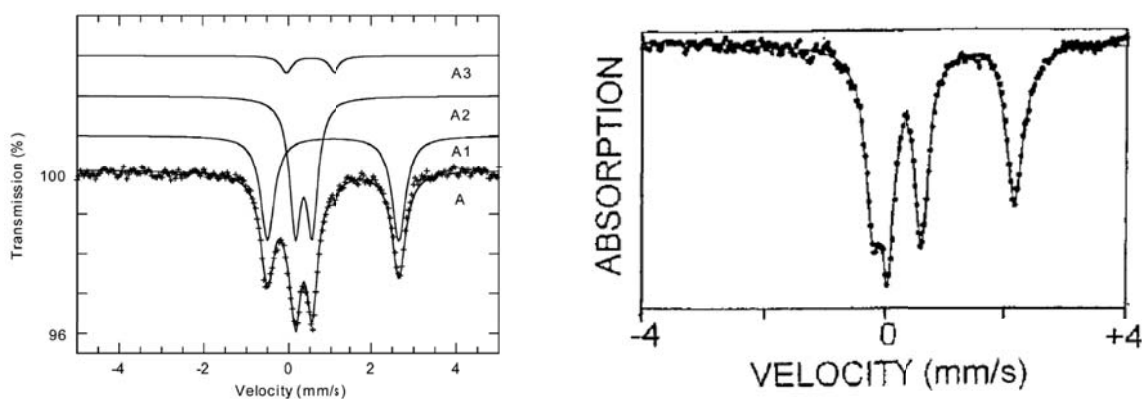


Figure 1.9. Zero-field Mossbauer spectra at 77 K of acetonitrile solution of **3a'** [$\text{Fe}^{\text{III}}(\text{L-Bn})(\mu_2\text{-mpdp})\text{Fe}^{\text{II}}(\text{NCCH}_3)_2$]²⁺ (left) and **4** [$\text{Fe}^{\text{III}}(\text{L-PhO})(\mu_2\text{-mpdp})\text{Fe}^{\text{II}}_2$]²⁺ (right).

The Mössbauer parameter values for four bis-ferric complexes synthesized with a dissymmetric ligand derived from Hbpmp are listed in Table 1.5.

Table 1.5. Mössbauer parameters for bis-ferric complexes in frozen solutions⁽⁵⁾.

Diferric complexes	Site 1 ($\text{Fe}^{\text{III}}\text{N}_3\text{O}_3$)		Site 2	
	δ (mm/s)	ΔE_Q (mm/s)	δ (mm/s)	ΔE_Q (mm/s)
$[\text{Fe}_2(\text{L-Bn})(\text{mpdp})(\text{NCCH}_3)_2]^{3+}$	0.47(1)	0.40(1)	0.40(1)	0.25(1)
$[\text{Fe}_2(\text{L-Bn})(\text{mpdp})(\text{OH}_2)_2]^{3+}$	0.48(1)	0.44(1)	0.55(1)	0.60(1)
$[\text{Fe}_2(\text{L-Bn})(\text{mpdp})(\text{OH})_2]^{2+}$	0.48(1)	0.44(1)	0.55(1)	1.51(1)
$[\text{Fe}_2(\text{L-BnO})(\mu\text{-O}_2\text{P}(\text{OPh})_2)_2](\text{PF}_6)_2$	0.447(5)	0.31(2)	0.57(2)	0.99(2)

The Mössbauer spectrum was recorded at 77 K for the electrochemically oxidized acetonitrile solution of complex **3a'** (mixed valent form) which therefore contains the bis-ferric

species $[\text{Fe}^{\text{III}}(\text{L-Bn})(\text{mpdp})\text{Fe}^{\text{III}}(\text{NCCH}_3)]^{3+}$. The obtained Mössbauer parameter values look very similar to those of the Fe^{III} site in complex **3a'** (Tables 1.5 and 1.4). Addition of water was then performed. Two bis-ferric complexes are generated in a 90:10 ratio. The minor species presents Mössbauer parameters similar to those of $[\text{Fe}^{\text{III}}_2(\text{L-Bn})(\text{mpdp})(\text{OH}_2)]^{3+}$, that can be independently generated from the one electron oxidation of **3a** in dichloromethane. One of the Fe^{III} centers of the major species is characterized by $\delta = 0.48(1)$ mm/s and $\Delta E_Q = 0.44(1)$ mm/s. These values are close to those obtained for one of the Fe^{III} centers in complexes $[\text{Fe}^{\text{III}}(\text{L-Bn})(\text{mpdp})\text{Fe}^{\text{III}}(\text{NCCH}_3)]^{3+}$ and $[\text{Fe}^{\text{III}}_2(\text{L-Bn})(\text{mpdp})(\text{OH}_2)]^{3+}$ as listed in Table 1.5. Consequently this Fe^{III} ion is likely to be associated to N_3O_3 site. We observe a significant increase in the ΔE_Q for the other Fe^{III} site which is the reminiscent of the parameters observed for the Fe^{III} center linked to the terminal phenoxide ligand in complex $[\text{Fe}^{\text{III}}_2(\text{L-BnO})(\mu\text{-O}_2\text{P}(\text{OPh})_2)_2](\text{PF}_6)_2^{(3)}$. Such a large quadrupole splitting is consistent with the presence of an anionic ligand on the Fe^{III} site. Consequently, the major species is the hydroxo complex $[\text{Fe}_2(\text{L-Bn})(\text{mpdp})(\text{OH})]^{2+}$.

Similarly the spectrum shown in the right part of Figure 1.9 can be reproduced with two doublets of equal area, one with isomer shift and quadrupole splitting values of $\delta = 0.490$ mm/s and $\Delta E_Q = 0.594$ mm/s, clearly indicating the presence of a high spin iron (III) site, the other with $\delta = 1.124$ mm/s and $\Delta E_Q = 2.376$ mm/s that are typical of a high-spin Fe^{II} site ^[13].

From the values tabulated in Table 1.4, we observe that the ΔE_Q values for the high spin Fe^{II} is sensitive to the coordination group which is evident from the values obtained both in solid state and CH_3CN solution for the complexes **3a** and **3a'**. These two complexes don't show any significant difference for the isomer shift values but a significant increase is observed in the ΔE_Q by +0.5 mm/s.

The values obtained for the high spin Fe^{III} site bearing an anionic ligand in the mixed valent systems observed in complexes **2b** and **4** show a large ΔE_Q value (≥ 0.95 mm/s) when the anionic group is in *trans* position while a $\Delta E_Q \approx 0.60$ mm/s is determined when it is in *cis*. For the complexes bearing neutral ligands, the ΔE_Q ranges from 0.3 to 0.54 mm/s. These values are of great importance as they could serve as references in the determination of the valence localization in the mixed valent diiron systems which have been developed during my Ph.D.

1.3 Electrochemical Characterization

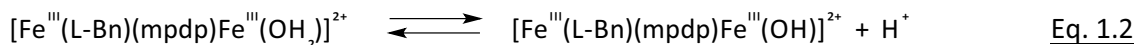
Through electrochemistry, oxidation and reduction of these mixed valence complexes have been studied and reported in the literature in detail. Table 1.6 lists the redox potentials associated to both the reduction $\text{Fe}^{\text{II}}\text{Fe}^{\text{III}} \rightarrow \text{Fe}^{\text{II}}\text{Fe}^{\text{II}}$ and the oxidation $\text{Fe}^{\text{II}}\text{Fe}^{\text{III}} \rightarrow \text{Fe}^{\text{III}}\text{Fe}^{\text{III}}$ processes, as measured from the anodic and cathodic peaks of the reversible waves observed on the recorded cyclic-voltammograms.

Table 1.6. Electrochemical data of mixed-valent diiron complexes from the literature.

Complex	$\text{Fe}^{\text{II}}\text{Fe}^{\text{III}} \rightarrow \text{Fe}^{\text{III}}\text{Fe}^{\text{III}}$ $E_{1/2}$ in V_{NHE} (in V_{SCE})*	$\text{Fe}^{\text{II}}\text{Fe}^{\text{III}} \rightarrow \text{Fe}^{\text{II}}\text{Fe}^{\text{II}}$ $E_{1/2}$ in V_{NHE} (in V_{SCE})*	ΔE (V)	K_{com}	Ref
1a	+0.94 (0.692)	+0.24 (-0.010)	0.702	7.5×10^{11}	(6)
1b	+0.93 (0.680)	+0.22 (-0.030)	0.710	1.6×10^{12}	(8)
2a	+0.38 (0.13)	-0.49 (-0.74)	0.87	5.0×10^{14}	(4)
2b	+0.68 (0.43)	-0.23 (-0.48)	0.91	2.5×10^{15}	(3)
3a'	+1.08 (0.83)	+0.20 (-0.05)	0.88	7.6×10^{14}	(5)
3a	+0.86 (0.61)	+0.18 (-0.07)	0.68	3.1×10^{11}	(5)
4	+0.63 (0.38)	-0.35 (-0.60)	0.98	3.8×10^{16}	(3)

* Reference electrode for the potentials is given in subscribes (NHE or SCE). The SCE reference potential is equal to $0.250 V_{\text{NHE}}$.

For the complex **3a**, a clean demonstration has been reported for the ligand exchange in the aqua complex⁽⁵⁾. It has been shown that the corresponding di-ferric aqua complex is not stable and spontaneously deprotonates to form a hydroxo species as summarized in Eq. 1.2:



For complex **4**, it is noteworthy that, a second reduction wave is detected at -0.22 V versus NHE ⁽³⁾. Due to the *cis* coordination of the terminal phenoxide with respect to the bridging phenoxide, one of the bridging carboxylate is in *trans* position of the terminal phenoxide. Hence, it was proposed that the second reduction wave originates from a complex where one of the carboxylate is decoordinated.

From the results listed in Table 1.6, the authors state that the potential difference between the oxidation and the first reduction of the mixed valent species strongly depends upon the

organic ligand used and less so on the bridging carboxylate/phosphate anion^(3,5). They quantified the stability domain of the mixed valent form through the equilibrium constant (K_{com}) of the comproportionation reaction by the Eq. 1.3:

$$K_{com} = e^{\Delta E(F/RT)} \quad \text{Eq. 1.3}$$

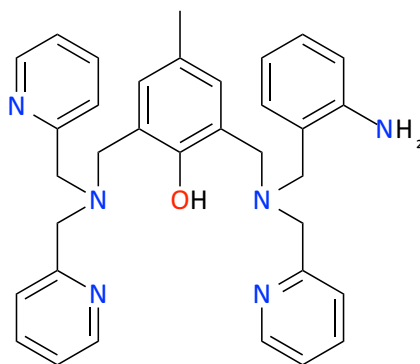
This relationship establishes that larger the potential difference the more stable the mixed-valent species. With this relation, Lambert *et al.* obtained values of K_{com} would range between 1–4 x 10¹⁶ for the dissymmetric complexes that resemble [Fe₂(L-PhO)(μ₂-mpdp)](BPh₄) while a much lower value (maximum few 10¹²) is observed for symmetric systems such as [(bpmp)Fe₂(μ-O₂CR)₂]²⁺ (RCO₂⁻ stands for a carboxylate)⁽³⁾.

In accordance with that, Chardon *et al.*⁽⁵⁾ have shown on an analogous system possessing a terminal phenoxide on one iron of the pair, that the dissymmetry of the charge distribution was the major contribution to the stability of the mixed-valent species⁽³⁾. In this respect, it is noteworthy that K_{com} for the aqua complex is in the range observed for the mixed-valent complexes of the tetrapyrrolyl ligands ($K_{com} \approx 10^{12}$)⁽⁶⁾.

These detailed characterization results segregated from the literature for the different mixed-valent diiron complexes form a basic reference for the analysis of complex of the form [Fe^{III}(μ₂-mpdp)Fe^{II}(H₂NBn-L)]²⁺⁽¹⁴⁾ whose characterizations will be explained in details in the coming sections of this manuscript.

2 pH-Driven Valence Inversion

Till this part of the manuscript, we have put forward some of the work that has been carried out by different groups on the preparation of mimicking complexes for biological enzymes like Purple Acid Phosphatases (PAP), Methane Mono-Oxygenase (MMO) or RiboNucleotide Reductases (RNR). Those model compounds were very well analyzed and the variety of techniques used allows the authors to show the functional relevancy in biological aspects. In this stream, Latour *et al.* have designed a ditopic ligand HL-BnNH₂ (see Scheme 2.1), bearing an aniline group and the corresponding mixed valent complex [Fe^{III}(μ₂-mpdp)Fe^{II}(H₂NBn-L)]²⁺ has been isolated (the extra bridge is the dicarboxylate mpdp²⁻ that is the *m*-phenylenedipropionate).



Scheme 2.1. Drawing of the ligand L-BnNH₂ bearing an aminobenzyl arm.

Aniline is among the least coordination nitrogen ligands and only a few aniline iron complexes have been structurally characterized due to the weak bonding⁽¹⁴⁾. Also the reversible (de)protonation-induced valence inversion in this system has been demonstrated with evidences obtained by Mössbauer, UV-Vis and ¹H-NMR spectroscopies⁽¹⁴⁾. This section is thus devoted to describe the mixed valence complex and to present the spectroscopic evidences for the valence inversion induced by the deprotonation of the aminobenzyl arm. These results were published in 2011 before I started my PhD and were the starting point of the ANR project mentioned in the Introduction of this manuscript.

When these characterizations of the mixed valent complex [Fe^{III}(μ₂-mpdp)Fe^{II}(H₂NBn-L)]²⁺ were performed, it was evidence that this system spontaneously evolves in solution. This will be the subject of the next section (Section 3). In all the characterization studies and the demonstration of valence inversions presented here, the experiments were performed either in solid state or in CH₃CN solution. For instance, the Mössbauer spectra were recorded on a CH₃CN solution frozen immediately after dissolution of the complex.

2.1 X-Ray Structure

The synthesis of the aniline ligand HL-BnNH₂ (Scheme 2.1) was adapted as in the case reported previously⁽³⁾ and the mixed-valent diiron complex was obtained by the reaction of the ligand with ferrous perchlorate and subsequent air oxidation⁽⁵⁾. Crystals were grown from an acetonitrile solution by slow evaporation, and the X-ray crystallographic structure of the complex is shown in Figure 2.1 along with the Table 2.1 listing out the bond distances of the Fe₁ and Fe₂ to the neighboring atoms.

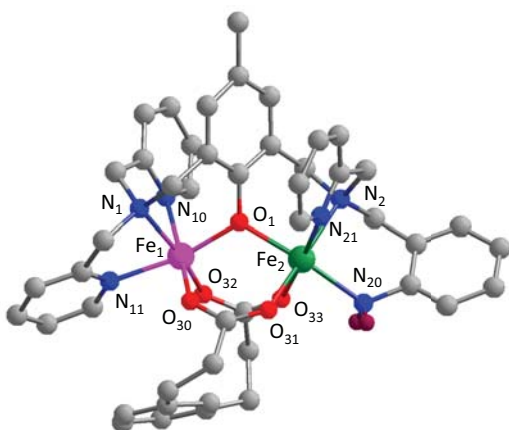


Figure 2.1. X-ray structure of the complex $[\text{Fe}^{\text{III}}(\mu_2\text{-mpdp})\text{Fe}^{\text{II}}(\text{H}_2\text{NBn-L})]^{2+}$.

Table 2.1. Selected interatomic distances (Å) and angle (deg) for the complex $[\text{Fe}^{\text{III}}(\mu_2\text{-mpdp})\text{Fe}^{\text{II}}(\text{H}_2\text{NBn-L})]^{2+}$.

Fe ₁ –O ₁	1.956(8)	Fe ₂ –O ₁	2.057(8)
Fe ₁ –O ₃₀	1.949(8)	Fe ₂ –O ₃₁	2.073(8)
Fe ₁ –O ₃₂	1.949(8)	Fe ₂ –O ₃₃	2.208(9)
Fe ₁ –N ₁	2.192(9)	Fe ₂ –N ₂	2.229(10)
Fe ₁ –N ₁₁	2.120(9)	Fe ₂ –N ₂₁	2.135(10)
Fe ₁ –N ₁₀	2.162(10)	Fe ₂ –N ₂₀	2.162(11)
Fe ₁ ...Fe ₂	3.473(3)	Fe ₁ –O ₁ –Fe ₂	119.8(4)

From the X-ray structure, the two pyridines are coordinated to Fe₁ ion and one pyridine and aniline are coordinated to Fe₂ ion with the help of a phenoxide bridge. The bond distances listed in the Table 2.1 allow us to get the average bond distance for the two iron ions to the neighboring atoms. Upon doing so, the bond distances of Fe₁ average significantly shorter (2.054 Å) than those of Fe₂ whose average bond distance accounts for 2.144 Å. This difference in the bond length clearly allows to identify as a mixed valent system with the valence localization as Fe₁ = Fe^{III} and Fe₂ = Fe^{II}. It is also noteworthy that the aminobenzyl group is bound to Fe₂ in a *trans* position to the phenoxo oxygen O₁ with a bond distance between Fe₂–N₂₀ as 2.162 Å. This is close to the Fe–O_{water} distance (2.156 Å) of the aqua complex $[\text{Fe}_2(\text{L-Bn})(\mu_2\text{-mpdp})(\text{OH}_2)](\text{BPh}_4)_2$ ⁽¹⁾, which shows the same valence localization. The coordination of aniline to the Fe₂ is favored by chelation. This is supported by the fact that the Fe–N_{aniline} distances in hexacoordinate high spin Fe^{II} complexes average 2.26 Å when the aniline is unsupported and 2.19 Å when it is chelating. Since the coordination is favored by chelation a question may arise for the replacement of aniline by solvent molecule upon dissolution of the complex but the Mössbauer spectroscopy answers the question.

2.2 Mössbauer Characterization

To have an in-depth confirmation about the valence of the two iron ions and the coordination of the aniline to the Fe^{II}, the Mössbauer spectrum of an acetonitrile solution of ⁵⁷Fe-

enriched $[\text{Fe}^{\text{III}}(\mu_2\text{-mpdp})\text{Fe}^{\text{II}}(\text{H}_2\text{NBn-L})]^{2+}$ complex has been recorded at 77 K. The zero-field Mössbauer spectrum is shown in Figure 2.2.

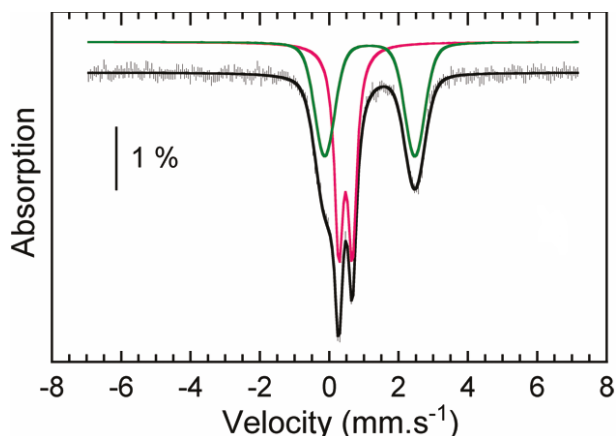


Figure 2.2. 77 K Mössbauer spectrum of an acetonitrile solution of the complex $[\text{Fe}^{\text{III}}(\mu_2\text{-mpdp})\text{Fe}^{\text{II}}(\text{H}_2\text{NBn-L})]^{2+}$ (experimental – hatched marks; simulated – solid lines). The colored solid lines correspond to the contributions of the Fe^{III} (pink) and the Fe^{II} (green) sites, respectively.

From the spectra in Figure 2.2, one can see two intense quadrupole doublets as expected for the mixed-valent diiron systems with the parameters $\delta = 0.47(1)$ mm/s, $\Delta E_Q = 0.39(2)$ mm/s and $\delta = 1.17(1)$ mm/s, $\Delta E_Q = 2.60(2)$ mm/s corresponding respectively to the high-spin Fe^{III} and high-spin Fe^{II} ions. The values of the high-spin Fe^{III} ion look similar to the values that have been tabulated in Table 1.4 for other mixed valent complexes and the quadrupole splitting of the ferrous site, which is very sensitive to its coordination sphere. Similar values have been obtained in solid state that is: $(\delta/\Delta E_Q)$ Fe^{III} 0.44/0.35 and Fe^{II} 1.17/2.49 mm/s. The values obtained both in solid state and in solution differ significantly from that of the complex **3a'** with a coordinated acetonitrile molecule ($\Delta E_Q = 3.14$ mm/s, see Table 1.4). This rules out the possibility of aniline replacement by the solvent and thereby strongly confirms that the aniline remains coordinated to the Fe^{II} in solution.

2.3 UV-Visible Characterization

Like the other mixed-valent diiron complexes reported in the earlier sections, the absorption spectrum of the complex $[\text{Fe}^{\text{III}}(\mu_2\text{-mpdp})\text{Fe}^{\text{II}}(\text{H}_2\text{NBn-L})]^{2+}$ is also dominated by the $\text{PhO}^- \rightarrow \text{Fe}^{\text{III}}$ charge transfer transition in the visible region. The UV-Visible recordings on an acetonitrile solution of the complex $[\text{Fe}^{\text{III}}(\mu_2\text{-mpdp})\text{Fe}^{\text{II}}(\text{H}_2\text{NBn-L})]^{2+}$ shows the absorption maximum at 586 nm leading to an extinction coefficient value $\epsilon \approx 1000 \text{ M}^{-1}\cdot\text{cm}^{-1}$. Similar absorption maximum at 578 nm ($\epsilon = 1300 \text{ M}^{-1}\cdot\text{cm}^{-1}$, see Table 1.3), was observed for the complex $[\text{Fe}^{\text{III}}(\text{L-Bn})(\text{mpdp})\text{Fe}^{\text{II}}(\text{NCCH}_3)]^{2+}$. In addition, the $\text{Fe}^{\text{II}}\text{Fe}^{\text{III}}$ derivatives of the tetrapyrrolyl ligand⁽⁴⁾ exhibit a

band around 550 nm, which has been assigned to a charge transfer (CT) from the bridging phenoxide to the ferric ion, which is in our case coordinated to the two pyridine arms thereby paving the way for the Fe^{II} to the aniline side.

2.4 ¹H-NMR Characterization

As we saw few examples of the ¹H-NMR characterization of mixed-valent diiron complexes in the previous section we get to know, that the spectra of these types of diiron complexes shows a distinctively large spectral range. For complexes of the benzyl ligand (HL-Bn)⁽¹⁾, it extends from +600 ppm to -50 ppm and from +600 ppm to -100 ppm for those of the 2-hydroxybenzyl ligand (HL-BnOH)⁽³⁾.

The NMR spectrum of the complex [Fe^{III}(μ₂-mpdp)Fe^{II}(H₂NBn-L)]²⁺ shown in Figure 2.3 shares a strong similarity to the spectra shown in the previous section for the benzyl ligand⁽⁵⁾. The three downfield resonances at 525, 370 and 270 ppm could be assigned to the equatorial methylenic protons of the branch bound to the Fe^{III} ion⁽¹¹⁾. This similarity in the peaks allows confirming the same valence distribution in the complex [Fe^{III}(μ₂-mpdp)Fe^{II}(H₂NBn-L)]²⁺.

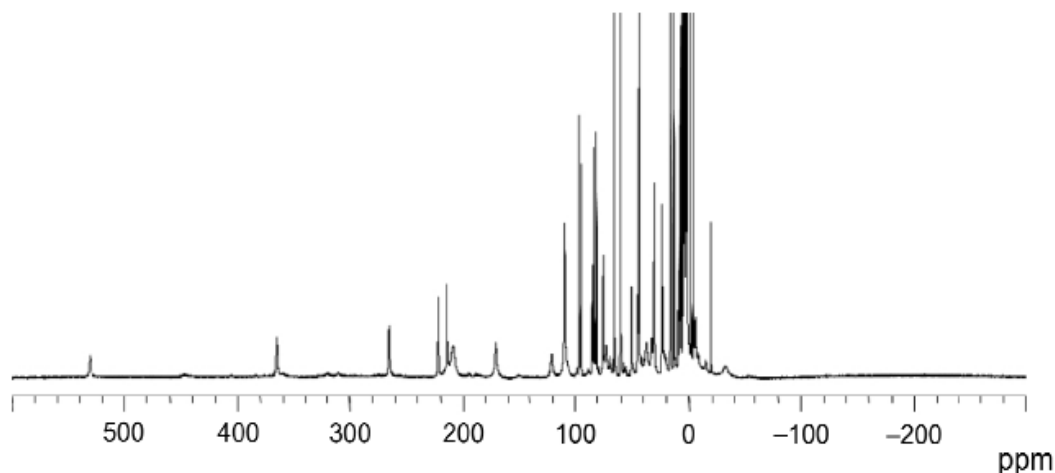
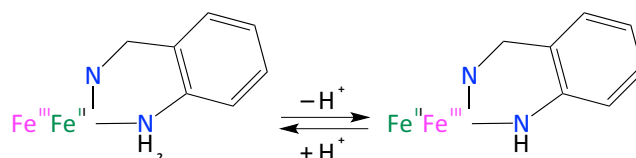


Figure 2.3. ¹H-NMR of the complex [Fe^{III}(μ₂-mpdp)Fe^{II}(H₂NBn-L)]²⁺ in CD₃CN.

So the analysis discussed so far clearly states that the mixed-valent complex [Fe^{III}(μ₂-mpdp)Fe^{II}(H₂NBn-L)]²⁺ presents an aniline coordinated to the Fe^{II} ion both in solid state and in solution. In the following, I would like to demonstrate the valence inversion upon deprotonation of the aniline group attached to the Fe^{II}. The deprotonation is achieved by the addition of a nitrogenous base, namely triethylamine (NEt₃), to the solution of the complex in acetonitrile. This leads to the formation of an anilide complex of the form [Fe^{II}(μ₂-mpdp)Fe^{III}(HNBn-L)]⁺ featuring an

inversion of the iron valences i.e. anilide is coordinated to Fe^{III}. This entire conversion can be reversed upon addition of acid on the anilide complex. The reaction outline of this conversion can be summarized as in the Scheme 2.2.



Scheme 2.2. Reversible valence inversion triggered by (de)protonation of the terminal anilide (aniline) ligand. Only the three partners within the complexes (the two iron sites and the aniline/anilide ligand) are shown.

2.5 Demonstration of the Valence Inversion

2.5.1 UV-Visible Absorption Spectroscopy

To find out the valence inversion by deprotonation, a titration of the complex $[\text{Fe}^{\text{III}}(\mu_2\text{-mpdp})\text{Fe}^{\text{II}}(\text{H}_2\text{NBn-L})]^{2+}$ in acetonitrile was performed using *N,N*-diisopropylethylamine. This addition of base leads to the appearance of a new intense absorption at 729 nm with an extinction coefficient $\epsilon = 3370 \text{ M}^{-1}\cdot\text{cm}^{-1}$. This transformation occurs at one isosbestic point at 543 nm, which features a simple transformation between two chromophores. The evolution of the UV-Visible spectrum of the complex $[\text{Fe}^{\text{III}}(\mu_2\text{-mpdp})\text{Fe}^{\text{II}}(\text{H}_2\text{NBn-L})]^{2+}$ upon addition of *iPr*₂EtN is shown in Figure 2.4.

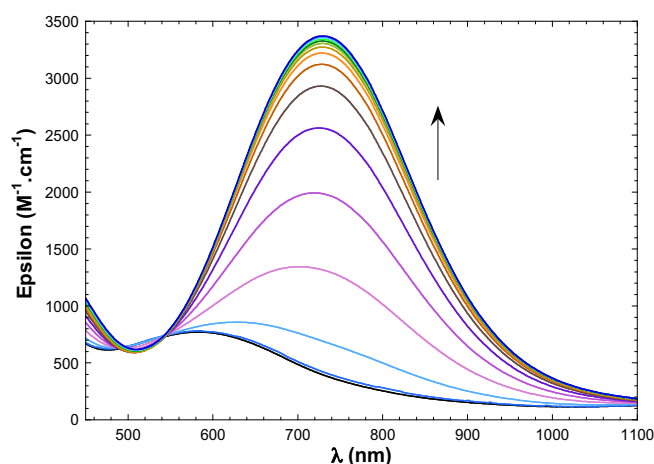
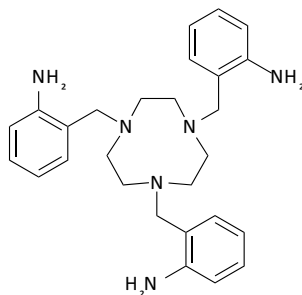


Figure 2.4. Evolution of UV-Visible spectrum of the a 0.3 mM acetonitrile solution of the complex $[\text{Fe}^{\text{III}}(\mu_2\text{-mpdp})\text{Fe}^{\text{II}}(\text{H}_2\text{NBn-L})]^{2+}$ (black trace) upon addition of *iPr*₂EtN by 0.2 equiv. aliquots up to 3 equiv. (colored traces).

This intense transition that occurred during the titration is in coherence with the complex $[\{\text{tacn}-(\text{BnNH})_3\}\text{Fe}^{\text{III}}]^{0}$ where three anilides are coordinated to the Fe^{III} (see Scheme 2.3). In this

complex the transition at 587 nm has been assigned to an anilide-to-Fe^{III} ligand-to-metal charge transfer⁽¹⁵⁾.



Scheme 2.3. Drawing of the ligand tacn-(BnNH₂)₃ used by Schlager et al. in 1995⁽¹⁵⁾.

To evaluate the pK_a of the diiron complex, titration was performed by monitoring the absorption at 729 nm in the presence of various bases exhibiting pK_a ranging from 4 – 12 in water. Assuming the presence of two chromophores i.e. both aniline and anilide complexes, the addition of one equivalent of base leads to the following relation (Eq. 2.1) between the absorption and the pK_a value of the complex:

$$\frac{A - A_0}{A_\infty - A_0} = \frac{1}{1 + 10^{\frac{pK_a - x}{2}}} \quad \text{Eq. 2.1}$$

where, “ pK_a ” stands for the pK_a value of the diiron couple,

“ x ” for the pK_a value of the added base and

“ A_0 ” (resp. A_∞) is the absorption of the starting aniline complex (resp. anilide complex).

In the plot shown in Figure 2.5, the best fit drawn as the solid (red) curve was obtained using Eq. 2.1 with a pK_a in water for the bound aniline of 8.4 that is ≈ 16 in acetonitrile⁽¹⁶⁾.

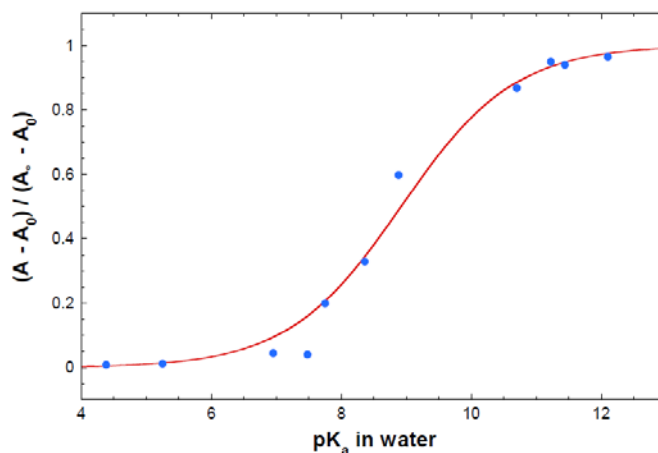


Figure 2.5. Evolution of the absorption at 729 nm of a 0.3 mM acetonitrile solution of $[\text{Fe}^{\text{III}}(\mu_2\text{-mpdp})\text{Fe}^{\text{II}}(\text{H}_2\text{NBn-L})]^{2+}$ upon addition of 1 equiv. of base (blue dots). Bases used are (pK_a in water): *o*-Toluidine (4.38), Pyridine (5.25), Imidazole (6.95), Collidine (7.48), 1,2-Methylimidazole (7.75), Morpholine (8.36), Diethanolamine (8.88), Diisopropylethylamine (11.44), Triethylamine (10.7), Piperidine (11.22), Proton sponge (12.1).

2.5.2 $^1\text{H-NMR}$ Spectroscopy

After obtaining the transformation through UV-Vis experiments, the changes in the NMR signature of the aniline complex were investigated. The NMR spectrum was recorded after adding 1.5 equiv of NEt_3 to the aniline complex in solution in acetonitrile. Significant changes are observed as seen from Figure 2.6.

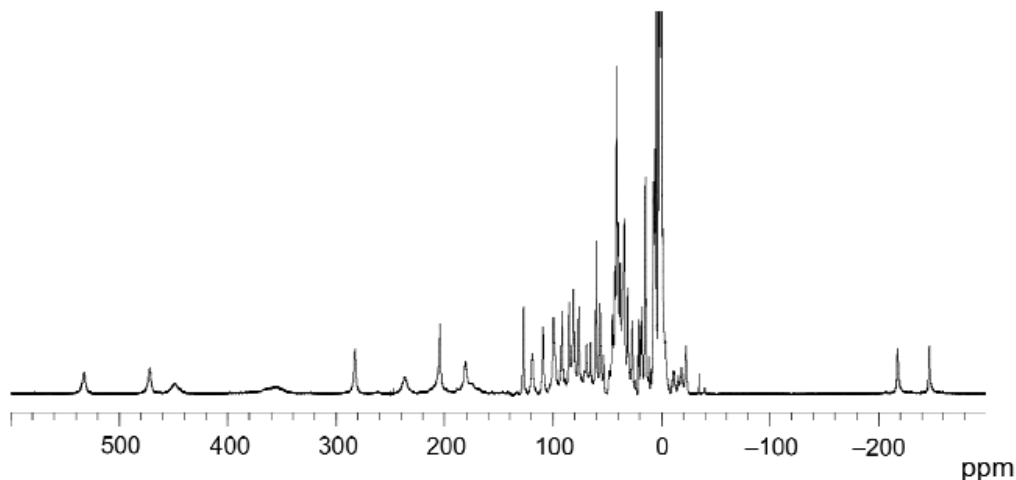


Figure 2.6. $^1\text{H-NMR}$ of the complex $[\text{Fe}^{\text{II}}(\mu_2\text{-mpdp})\text{Fe}^{\text{III}}(\text{HNBn-L})]^+$ in CD_3CN .

This spectrum resembles that of the complex with 2-hydroxybenzyl (complex **2b**⁽³⁾) with a spectral range extending over more than 700 ppm. The peaks with the more negative chemical shifts in the NMR spectrum are an important characteristic observed for the protons in *ortho* and *para* position for the PhO^- (around -80 to -110 ppm)⁽³⁾ or PhNH^- (around -200 ppm, see Figure 2.6)⁽¹⁴⁾ rings coordinated to Fe^{III} . The reason behind the occurrence of these negative chemical shifts has been attributed to the delocalization of the spin density of the high spin Fe^{III} ion coordinated to the anionic group. Upon evidencing the Fe^{III} coordination to the anionic side (anilide arm), this in turn shows that Fe^{II} lies in the bis-picolylamine site. The valence inversion is further supported by the Mössbauer experiments.

2.5.3 Mössbauer Spectroscopy

To probe further in the conversion, a Mössbauer spectrum was recorded at 77 K on an acetonitrile solution of ^{57}Fe enriched aniline complex after the addition of 1.5 equiv. of NEt_3 .

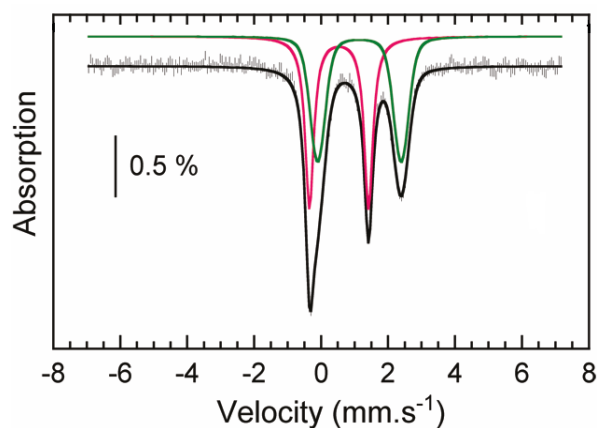


Figure 2.7. Mössbauer spectrum of an acetonitrile solution of the complex $[\text{Fe}^{\text{III}}(\mu_2\text{-mpdp})\text{Fe}^{\text{II}}(\text{H}_2\text{NBn-L})]^{2+}$ after the addition of 1.5 equiv. NEt_3 (experimental – hatched marks; simulated – solid lines). The colored solid lines correspond to the contributions of the Fe^{III} (pink) and the Fe^{II} (green) sites, respectively.

The spectrum shown in Figure 2.7 can be deconvoluted into two equally intense quadrupole doublets with parameters $\delta = 0.54(1)$ mm/s, $\Delta E_Q = 1.77(2)$ mm/s and $\delta = 1.14(1)$ mm/s, $\Delta E_Q = 2.49(2)$ mm/s corresponding to high-spin Fe^{III} and high-spin Fe^{II} , respectively. When compared to the ΔE_Q values obtained for the complex before the addition of NEt_3 , one can see an extreme increase in the value for the ferric iron, which shows that the site is highly distorted. Also it is worth noting that, similar high values have been reported for ferric iron in the case of the di-ferric complex with a terminal hydroxo⁽⁵⁾ (1.51 mm/s, see Table 1.5) where the anion is in *trans* position to the bridging phenoxide as well as for the ferric site of mixed valent $\text{Fe}^{\text{II}}\text{Fe}^{\text{III}}$ ⁽³⁾ (1.22 mm/s) and $\text{Fe}^{\text{III}}\text{Mn}^{\text{II}}$ ⁽¹⁷⁾ (1.04 mm/s) complexes bearing a Fe^{III} -coordinated 2-hydroxybenzyl. By contrast, when the ferric ion is bound to the bispicolylamine branch, only small ΔE_Q values (< 0.5 mm/s) are observed like in the case of the aniline complex. Thus, these high quadrupole splitting values for Fe^{III} appear to be characteristic of complexes in which the ferric site possesses an anionic ligand in *trans* position to the bridging phenoxide. This combination of anionic ligands in mutual *trans* positions generates a strong axial anisotropy of the charge distribution, giving rise to higher ΔE_Q values. Why the anionic ligand should not be in *cis* position? If that is the case, then the quadrupole splitting values will not be very high; it will be limited between 0.5 – 0.6 mm/s^(2,18).

Thus $^1\text{H-NMR}$ and Mössbauer spectroscopies clearly demonstrate that, upon deprotonation of the aniline ligand, the valences of the two iron ions are inverted as shown in Scheme 2.2. It is worth noting that the conversion is reversible upon adding acid to the anilide complex solution.

During the due course of the studies on these mixed valent diiron complexes, it was evidenced that the aniline complex $[\text{Fe}^{\text{III}}(\mu_2\text{-mpdp})\text{Fe}^{\text{II}}(\text{H}_2\text{NBn-L})]^{2+}$ transforms spontaneously over

2 h into another species of the same formula. In order to identify this new species, in-depth analysis with Mössbauer monitoring, NMR and UV-Visible kinetic studies were performed. This is the point of the next Section.

3 Isomerization Reaction

In the previous section, all the spectroscopic signatures that were presented for the aniline complex $[\text{Fe}^{\text{III}}(\mu_2\text{-mpdp})\text{Fe}^{\text{II}}(\text{H}_2\text{NBn-L})]^{2+}$ in acetonitrile were recorded on freshly prepared solutions. If one let these acetonitrile solutions and record the spectra after a while, significant differences are detected indicating that $[\text{Fe}^{\text{III}}(\mu_2\text{-mpdp})\text{Fe}^{\text{II}}(\text{H}_2\text{NBn-L})]^{2+}$ spontaneously evolves in solution at room temperature. All these modifications observed in ^1H -NMR, Mössbauer and UV-visible absorption spectroscopies are detailed in the manuscript submitted to *Chemistry – A European Journal* (a revised version has been sent the 18th of July 2013). The aim in this Section is not to rewrite the characterizations presented in this manuscript but rather to insist on how it was concluded that the spontaneous evolution is an isomerization reaction.

3.1 Manuscript submitted to Chemistry – A European Journal

Here after in the main text along with the Supporting Information.

Cis-trans isomerisations in diiron complexes involving aniline or anilide ligands

Eric Gouré,^[a] Michaël Carboni,^[a] Patrick Dubourdeaux,^[a] Martin Clémancey,^[a] Ramachandran Balasubramanian,^[a] Colette Lebrun,^[b] Pierre-Alain Bayle,^[c] Geneviève Blondin,^{*[a]} and Jean-Marc Latour^{*[a]}

Abstract: We have recently reported a deprotonation induced valence inversion within a phenoxido-bridged mixed-valent diiron(II,III) complex. The initial aniline coordinated to the Fe^{II} site reacts with triethylamine and the resulting complex contains an anilide ligand coordinated to the Fe^{III} ion. The behaviour of these complexes in acetonitrile is indeed more intricate. Owing to the very distinctive spectroscopic signatures of the complexes, the conjunction of NMR,

Mössbauer and UV-visible absorption spectroscopies allows evidencing two isomerisation reactions, one involving the aniline linked to the Fe^{II}, the other the anilide on the Fe^{III}. Aniline in *cis* position versus the bridging phenoxide is shown to be the most stable isomer while the anilide *trans* to the phenoxido bridge is favoured. The *trans* isomer of the aniline complex is more acidic than the *cis* one by one pK_a unit. Isomerisation of the anilide complex is six times faster than the analogous

isomerisation of the aniline complex. Both reactions are proposed to proceed through a unique mechanism. This is the first time that such isomerisation reactions are evidenced in dinuclear complexes.

Keywords: cis-trans isomerisation • iron complexes • aniline ligand • anilide ligand • Mössbauer spectroscopy

Introduction

Aniline is among the least coordinating nitrogen ligands and only a few aniline iron complexes have been structurally characterised. Most of these complexes involve chelating anilines, the formation of the chelate assisting the binding of aniline. This view is supported by the fact that the Fe-N_{aniline} distances in hexacoordinate high-spin Fe^{II} complexes average 2.29 Å when the aniline is unsupported^[1] and 2.20 Å when it is chelating.^[1c, 2] With the goal to obtain

potential biomimetic models of arylamine oxygenases^[3] we prepared a diiron complex of a binucleating aniline ligand [Fe₂(L-BnNH₂)(mpdp)](ClO₄)₂·H₂O (**1**).^[4] The X-ray structure revealed that **1** possesses a triply-bridged core [Fe^{II}(μ-OPh)(μ₂-mpdp)Fe^{II}(NH₂Bn)] (mpdp²⁻ = *m*-phenylenedipropionate) and bears a terminal aminobenzyl ligand in *trans* position with respect to the bridging phenoxide (Scheme 1). Interestingly we found that, upon addition of a nitrogenous base (e.g. triethylamine), the aminobenzyl ligand can be reversibly deprotonated to the anilide complex **2**, whose core [Fe^{II}(μ-OPh)(μ₂-mpdp)Fe^{III}(NHBn)] features an inversion of the iron valences. This was the first example of a (de)protonation-induced valence inversion for both a homodinuclear complex and first-row transition metals. A thorough electrochemical study indicated that the electron transfer and the proton exchange are concerted events.^[5] In order to gain more insight into the deprotonation induced valence inversion, we investigated further the solution behaviour of **1** and **2** and discovered that in acetonitrile solution the aniline complex **1** transforms spontaneously over 2h into another species of the same formula. Similarly **2** transforms into another species over a shorter time scale of 20 min. This article describes an in-depth study of these transformations using Mössbauer monitoring and NMR and UV-visible kinetic studies. Indeed both **1** and **2** possess very rich and distinctive spectroscopic properties that allow to monitor and quantitate their transformations. These studies strongly suggest that the transformations under consideration are most probably the same isomerisation of the ligand within the two complexes, the aniline or anilide and pyridine arms exchanging their respective positions *cis* and *trans* to the

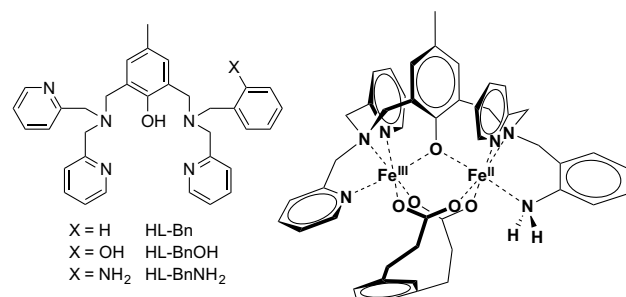
[a] Dr. E. Gouré, Dr. M. Carboni, P. Dubourdeaux, Dr. M. Clémancey, R. Balasubramanian, Dr. G. Blondin, Dr. J.-M. Latour
Univ. Grenoble Alpes, LCBM, F-38054 Grenoble, France
CEA, DSV, iRTSV, CBM, PMB, F-38054 Grenoble, France
CNRS UMR 5249, LCBM, F-38054 Grenoble, France
E-mail: genevieve.blondin@cea.fr, jean-marc.latour@cea.fr

[b] C. Lebrun
Univ. Grenoble Alpes, UMR-E 3, LRICC, F-38054 Grenoble, France
CEA, DSM, INAC, SCIB, RICC, F-38054 Grenoble, France

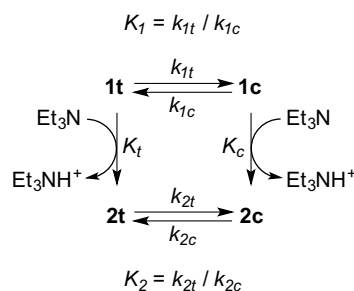
[c] P.-A. Bayle
Univ. Grenoble Alpes, UMR-E 3, LRM, F-38054 Grenoble, France
CEA, DSM, INAC, SCIB, RM, F-38054 Grenoble, France

Supporting information for this article is available on the WWW under <http://www.chemeurj.org/> or from the author.

bridging phenoxide. Accordingly, we note **1t** the initial form of **1** obtained upon dissolution of the solid into acetonitrile and **1c** the one after transformation. Similarly, we note **2t** the major deprotonated form obtained after equilibration and **2c** the other one. The transformations are summarised in Scheme 2.



Scheme 1. The ditopic ligand HL-BnNH₂ and related ones (left) and structure of complex **1** [Fe^{III}(μ₂-mpdp)Fe^{II}(NH₂Bn-L)]²⁺ according to the published X-ray diffraction studies (right).^[4] Only the two hydrogen atoms of the aniline group are indicated.



Scheme 2. Interconversion between the forms **1t** and **1c** of complex **1** on one hand and **2t** and **2c** of complex **2** on the other with the equilibrium constant K_1 and K_2 expressed as a function of the kinetic constants. The deprotonation of complexes **1t** and **1c** by NEt₃ is associated with the acidic constants K_t and K_c , respectively.

Results

The aniline and anilide complexes were obtained as previously described.^[4] The evolution of **1** was followed by NMR and UV-visible absorption spectroscopy. Kinetic analyses of the changes in these signatures allowed the rate of the transformation to be estimated. This transformation was also investigated by Mössbauer spectroscopy and mass spectrometry. The same techniques were then used to study the deprotonation and investigate the resulting two forms of **2**.

Spontaneous evolution of complex 1: ¹H-NMR spectroscopy: A first evidence of the spontaneous evolution of complex **1** is given by ¹H-NMR spectroscopy. The trace (a) of Figure 1 reproduces the low and high field ranges of the spectrum recorded immediately after complex **1** was dissolved in deuterated acetonitrile. The full spectrum is shown in the Supporting Information (Figure S1). This spectrum changes with time as shown by those obtained 20 and 120 minutes after dissolution (traces (b) and (c), respectively). Indeed, upon time, the initial resonances decreased in intensity and new ones appeared and grew. Spectra were recorded every 5 minutes during 2 hours after which no further modification of the ¹H-NMR spectrum was observed. This suggests that complex **1** exists under a

single form immediately after dissolution, denoted hereafter **1t**, and that a second form, denoted **1c**, is spontaneously generated from **1t**.

Trace (a) is reminiscent of the spectrum recorded for the complex [Fe^{III}(μ₂-mpdp)Fe^{II}(NCCH₃)(Bn-L)]²⁺ (see Scheme 1), indicating that the Fe^{III} is in the bis-picolylamine site.^[6] It is thus reasonable to assume that the structure of **1t** is identical to the X-ray structure with the aniline ligand coordinated to the Fe^{II} ion in *trans* position with respect to the bridging phenoxide. When the evolution is complete, both forms coexist. The ¹H-NMR spectrum associated to **1c** indicates that it is a mixed valent diiron species, as **1t**. This will be further confirmed by Mössbauer spectroscopy (see below).

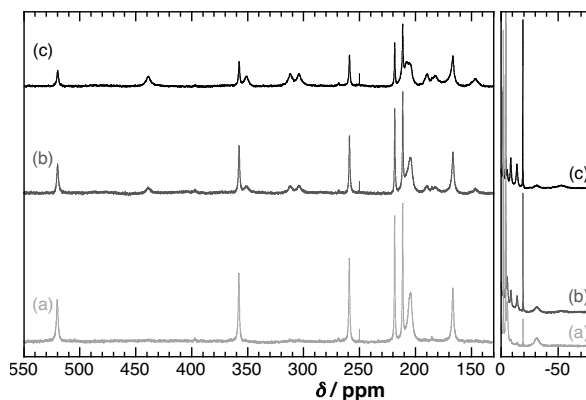


Figure 1. 550 to 130 and 0 to -80 ppm domains of the ¹H-NMR spectra recorded immediately (trace a, light grey line), 20 minutes (trace b, dark grey line) and 120 minutes (trace c, black line) after complex **1** was dissolved in CD₃CN. A vertical shift was operated on the right part to evidence the increasing intensity of the -19 ppm signal.

To demonstrate that the two forms **1t** and **1c** are in equilibrium, we recorded ¹H-NMR spectra between 258 and 313 K. The spectra are shown in the Supporting Information (Figure S2). The first spectrum within this series was recorded at room temperature and corresponds to spectrum (c) in Figure 1. It is remarkable to see that the spectrum was recovered after the temperature had been decreased down to 258 or increased up to 313 K. Such behaviour strongly suggests that **1t** and **1c** interconvert. Upon increasing temperatures, the spectrum range narrowed. The temperature dependence of the peak positions is close to the Curie law in agreement with the expected weak antiferromagnetic exchange interaction between the high-spin Fe^{II} and Fe^{III} ions that is mediated by the phenoxido bridge.^[7] Varying the temperature not only led to shifts in the peak positions but also to drastic broadening of many resonances, the latter effect precluding a reliable quantitative analysis of the equilibrium.

Assuming that equilibrium occurs between the two forms **1t** and **1c** (see top of Scheme 2), we considered the spectra recorded at 293 K to analyse the kinetics of the transformation. To determine the proportion of **1c**, we selected the peak at -19 ppm that increases upon time. The choice was governed by the small linewidth and the important separation with the other resonances. We then looked for **1t** for a peak in the same spectral range. Three resonances exist at -2, -4 and -5.5 ppm. Due to their close proximity, we chose to consider these three peaks all together. From previous work, we assumed that each of these four observed resonances is associated to a single

proton. The time dependence of proportion of **1c** is shown in Figure 2. It continuously increases to reach a plateau at ≈ 0.65 . Therefore, when the spontaneous evolution of complex **1** is complete, the resulting solution is a mixture of **1t** and **1c** in a $\approx 35:65$ ratio. The same conclusion was reached when we looked at the behaviour of the peaks located at 438, 310 and 304 ppm on one hand *versus* those at 520 and 258 ppm on the other, these sets being characteristic of **1c** and **1t**, respectively (see Supporting Information, Figure S3). A value of 1.8 ± 0.3 is thus obtained for the equilibrium constant K_I . Assuming that the forms **1t** and **1c** interconvert with kinetic constants k_{It} and k_{Ic} , respectively (see top part of Scheme 2) and that only **1t** is present initially, the proportion of **1c** is given by Eq. 1, where t stands for the time elapsed since dissolution of complex **1**:

$$\frac{|\mathbf{1c}|}{|\mathbf{1t}| + |\mathbf{1c}|} = \frac{k_{It}}{k_{It} + k_{Ic}} \left\{ 1 - \exp[-(k_{It} + k_{Ic})t] \right\} \quad (\text{Eq. 1})$$

The fit of the data leads to $(k_{It} + k_{Ic}) = 0.03(1) \text{ min}^{-1}$. Owing to the relation between K_I , k_{It} and k_{Ic} , one gets $k_{It} = 0.02(1) \text{ min}^{-1}$ and $k_{Ic} = 0.01(1) \text{ min}^{-1}$.

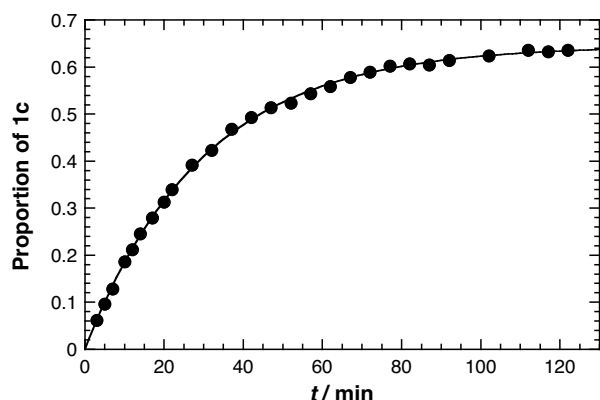


Figure 2. Time dependence of the proportion of form **1c** since dissolution of complex **1** in acetonitrile (black dots). The solid line corresponds to the best fit according to Eq. 1 (see text for parameters).

Mössbauer spectroscopy: Mössbauer spectroscopy is the most appropriate tool to characterize iron species and we used it to monitor the changes of the iron sites associated to the evolution of complex **1**. Figure 3 reproduces the spectra recorded at 80 K and zero-field on a freshly prepared (spectrum (a)) and an equilibrated (spectrum (b)) CH_3CN solutions of complex **1**. The two spectra are very similar. However, the shoulder at -0.36 mm.s^{-1} in spectrum (a) is clearly better resolved in spectrum (b) and superposition of the two spectra scaled to the same area reveal that the two central lines at 0.26 and 0.65 mm.s^{-1} are more intense in spectrum (a).

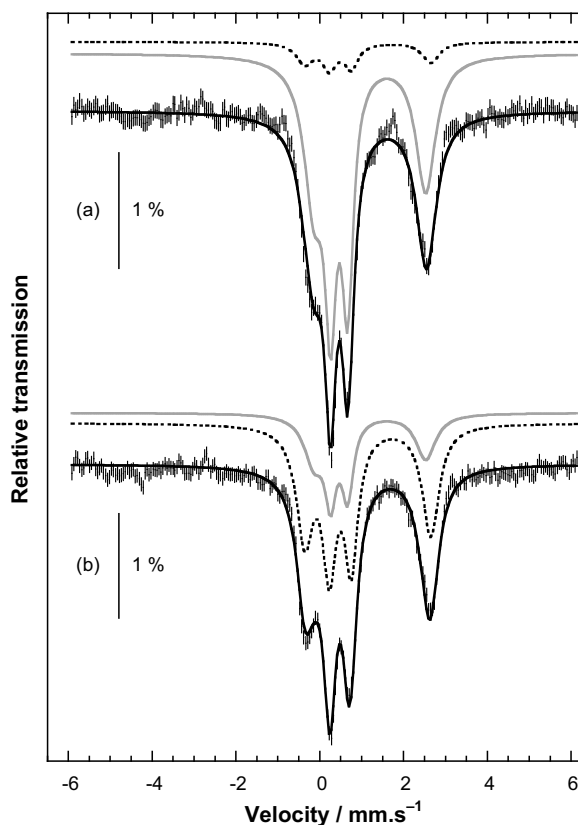


Figure 3. Zero-field Mössbauer spectra scaled to the same area recorded at 80 K (hashed lines) on an acetonitrile solution of complex **1** frozen either briefly or 4 hours after dissolution. The black solid lines correspond to the theoretical spectra calculated according to the parameters listed in Table 1. Contributions of complexes **1t** and **1c** are shown as solid grey and dotted black lines, respectively.

The analysis of the spectra was conducted in two sequential steps. As a first approach in agreement with the results of $^1\text{H-NMR}$ spectroscopy, it was assumed that a single species is responsible for spectrum (a) and that it contributes to 35% to spectrum (b). The signature of the resulting 65% in (b) was found to be composed of two equally intense quadrupole doublets characteristic of a mixed valent $\text{Fe}^{\text{II}}\text{Fe}^{\text{III}}$ complex (see Supporting Information, Figure S4). This confirms the dinuclear structure of complex **1c** as well as the oxidation states of the two iron ions. To improve the determination of the nuclear parameters of the iron nuclei in complexes **1t** and **1c** we then assumed that both species contribute also to spectra (a) (see Table 1). Indeed, freezing the sample induced a delay that allowed the initial solution to evolve. Eventually simulation of both spectra with the same set of nuclear parameters gave relative contributions in perfect agreement with the solution compositions issued from $^1\text{H-NMR}$ investigations. The isomer shift values ($\delta = 0.46(1)$ and $1.19(1) \text{ mm.s}^{-1}$ for **1t** and $0.49(1)$ and $1.14(1) \text{ mm.s}^{-1}$ for **1c**) are characteristic of high-spin Fe^{III} and high-spin Fe^{II} ions in N/O environment. The quadrupole splittings determined for the ferric centre of **1t** and **1c** ($\Delta E_Q = 0.41(2) \text{ mm.s}^{-1}$ and $0.52(2) \text{ mm.s}^{-1}$, respectively) are similar and in the range of those measured for a Fe^{III} ion in the bis-pycolylamine site in analogous complexes.^[6, 8] In contrast, the ΔE_Q values of the Fe^{II} sites ($\Delta E_Q = 2.67(2) \text{ mm.s}^{-1}$ for **1t** and $3.00(2) \text{ mm.s}^{-1}$ for **1c**) differ significantly.

Table 1. Mössbauer parameters for complexes **1t**, **1c**, **2t** and **2c** in acetonitrile solution.

		δ (mm.s ⁻¹)	ΔE_Q (mm.s ⁻¹)	% in spectrum (a) [a]	% in spectrum (b) [a]
1t	Fe ^{III}	0.46(1)	0.41(2)	89	33
	Fe ^{II}	1.19(1)	2.67(2)		
1c	Fe ^{III}	0.49(1)	0.52(2)	11	67
	Fe ^{II}	1.14(1)	3.00(2)		
2t	Fe ^{III}	0.56(1)	1.75(2)	44	77
	Fe ^{II}	1.15(1)	2.55(2)		
2c	Fe ^{III}	0.39(1)	0.80(2)	56	23
	Fe ^{II}	1.16(1)	3.15(2)		

[a] Labels of Mössbauer spectra refer to Figure 3 for complexes **1t** and **1c** and to Figure 8 for complexes **2t** and **2c**.

Mössbauer spectroscopy thus confirms the presence of two mixed valent species in a $\approx 35:65$ ratio in the equilibrated acetonitrile solution of **1**. In addition, the differences of the ΔE_Q values strongly suggest that the transformation involves the Fe^{II} site rather than the Fe^{III} ion.

ESI-Mass spectrometry: To get further insights into the chemical nature of **1t** we resorted to ElectroSpray Ionisation Mass Spectrometry. ESI-MS spectra were recorded immediately and 4 hours after complex **1** was dissolved in CH₃CN. The two spectra, reproduced in the Supporting Information (see Figure S5), are undistinguishable and dominated by the 437.6 *m/z* peak corresponding to the dicationic [Fe^{III}(μ_2 -mpdp)Fe^{II}(NH₂Bn-L)]²⁺ complex. Consequently, the two complexes **1t** and **1c** must present the same chemical formula except for coordinated solvent molecules if any.

UV-visible absorption spectroscopy: Phenoxido-bridged mixed valent Fe^{II}Fe^{III} complexes present a moderately intense absorption in the visible domain (500-600 nm) that corresponds to a phenoxido-to-Fe^{III} charge transfer.^[7a] Investigation of its time dependence allows getting insight in the kinetics of the spontaneous evolution of complex **1**. Figure 4 reproduces the evolution of the UV-visible spectra recorded during 2.5 hours. The starting spectrum presents a maximum at 564 nm with $\epsilon_{564} = 875 \text{ M}^{-1} \cdot \text{cm}^{-1}$ that shifts to 574 nm with $\epsilon_{574} = 950 \text{ M}^{-1} \cdot \text{cm}^{-1}$ when the conversion of **1t** into **1c** is complete. These variations (see inset of Figure 4) can be reproduced within the frame of the top part of Scheme 2 using the derived equations (see Eq. 2a-c). The best fit of the absorption at 565 nm leads to $(k_{It} + k_{Ic}) = 0.02(1) \text{ min}^{-1}$, in agreement with the value deduced from ¹H-NMR spectroscopy. Similar values are obtained whatever the wavelength.

$$\epsilon(\lambda, t) = \epsilon(\lambda, t \rightarrow \infty) + \{\epsilon(\lambda, t = 0) - \epsilon(\lambda, t \rightarrow \infty)\} \times \exp[-(k_{It} + k_{Ic})t] \quad (\text{Eq. 2a})$$

$$\epsilon(\lambda, t = 0) = \epsilon_{It}(\lambda) \quad (\text{Eq. 2b})$$

$$\epsilon(\lambda, t \rightarrow \infty) = \frac{k_{Ic}}{k_{It} + k_{Ic}} \epsilon_{It}(\lambda) + \frac{k_{It}}{k_{It} + k_{Ic}} \epsilon_{Ic}(\lambda) \quad (\text{Eq. 2c})$$

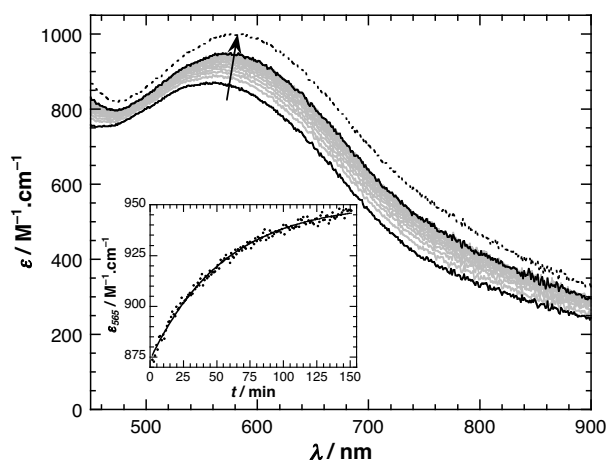


Figure 4. Evolution of the UV-visible absorption spectrum of complex **1** upon dissolution in CH₃CN. A selection of 16 spectra recorded each 10 minutes during 2.5 hours are reproduced (the first and last spectra are shown as black solid lines). The signature of **1c** is shown as the black dotted line. The arrow is a guide to indicate the increase in intensity. The inset reproduces the time dependence of the extinction molar coefficient at 565 nm. Experimental data are drawn as full dots while the best fit corresponds to the solid black line.

The spectrum of **1t** coincides with the first recorded spectrum. However, the determination of the UV-visible signature of complex **1c** requires the additional knowledge of at least one of the kinetic constants or their ratio K_I . The spectrum of **1c** is reproduced in Figure 4 as the black dotted line, assuming $K_I = 1.8$ as deduced from ¹H-NMR. The signatures of **1t** and **1c** are quite similar. Nevertheless, it may be noticed that **1c** presents a less energetic phenoxido-to-Fe^{III} charge transfer transition with an increased intensity compared to **1t** (**1t**: $\lambda_{max} = 564 \text{ nm}$, $\epsilon_{564} = 875 \text{ M}^{-1} \cdot \text{cm}^{-1}$; **1c**: $\lambda_{max} = 583 \text{ nm}$, $\epsilon_{583} = 1000 \text{ M}^{-1} \cdot \text{cm}^{-1}$). Since the observed absorption involves the Fe^{III} site, such small variations are perfectly consistent with the transformation occurring on the Fe^{II} site that was suggested by Mössbauer investigations (see above).

The above studies evidenced that the form **1t** obtained immediately after dissolution of complex **1** retains the structure revealed by crystallography. This structure is altered in **1c** in spite of the fact that it has a similar chemical composition and is also a mixed valent compound. To identify its nature, we took advantage of the acidic character of the aniline ligand and investigated the behaviour of acetonitrile solutions of complex **1** upon addition of NEt₃.

Deprotonated complexes: *¹H-NMR spectroscopy:* A first evidence of the generation of two different complexes upon deprotonation of complexes **1t** and **1c** is given by ¹H-NMR. Spectra were recorded after the addition of 1.5 equivalents of NEt₃ on a CD₃CN solution of complex **1** that was left to evolve for 4 hours. This solution is indeed composed of the two complexes **1t** and **1c** in a 35:65 ratio. The full-scale spectra are shown in the Supporting Information (see Figure S6) and two domains are enlarged in Figure 5. Firstly, it should be noticed that no resonances originating from complexes **1t** or **1c** are detected. Owing to the paramagnetic nature of the complexes that contributes to broaden the resonances, this suggests that the action of NEt₃ is almost quantitative and that no more than 5 to 10% of complex **1**, whatever the form, remains in solution. Secondly, the recorded spectra reveal that the species present in solution are mixed

valent diiron complexes. Thirdly, a close inspection of the series of spectra reveals the progressive disappearance of a set of resonances (see the dotted lines in Figure 5). The other set of peaks present in the first recorded spectrum concomitantly increases. This behaviour reveals that NEt_3 reacts on the two complexes **1t** and **1c** present in solution leading to the generation of two new complexes that will be further denoted **2t** and **2c** (see bottom part of Scheme 2). One of these complexes spontaneously evolves into the other and completion is reached after ≈ 20 minutes at room temperature. The major species that remains in solution is characterised by two signals at very negative chemical shifts, namely at -214 and -243 ppm (see Figure S6). They are indeed the signature of the anilide coordinated to the Fe^{III} site *trans* to the phenoxido bridge (see below).

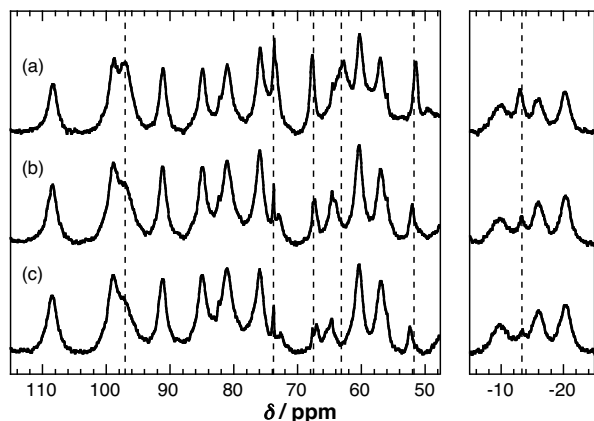


Figure 5. $^1\text{H-NMR}$ spectra recorded immediately (trace a), 1 minute (trace b) and 17 minutes (trace c) after addition of 1.5 eq of NEt_3 to a CD_3CN solution of complexes **1t** and **1c** in a 35:65 ratio. The dotted lines indicate the decreasing resonances.

UV-visible absorption spectroscopy: As previously published, deprotonation of complex **1** induced an intense absorption around 700 nm.^[4] To confirm that complex **2** indeed exists in two forms, namely **2t** and **2c**, we took advantage of the slow evolution of complex **1** to add base on solutions that differ in their **1t:1c** ratio. As it will be demonstrated, these experiments allowed the determination of the signatures of both forms and the kinetics of the **2t** \rightleftharpoons **2c** conversion. In addition, a difference in the acidic strength of complexes **1t** and **1c** is evidenced.

Aliquots of 1.5 eq of NEt_3 were added to CH_3CN solutions of complex **1** that were allowed to evolve for a time period from 50 s to 120 min after dissolution of complex **1**. Figure 6 presents the evolution of the absorption when the addition of base is performed on a **1t:1c** 35:65 mixture (grey solid lines). The analogous series of spectra recorded on solutions with larger **1t:1c** starting ratios are reproduced in the Supporting Information (see Figure S7). The last spectra within each series, recorded 18 minutes after the addition of NEt_3 are superimposable. This indicates that all final solutions have the same composition. The chromophore is characterised by a strong absorption at 730 nm with an ϵ value of $4715 \text{ M}^{-1}\cdot\text{cm}^{-1}$. Such an intense transition is reminiscent of that assigned to an anilide-to- Fe^{III} LMCT in a mononuclear trianilinetriazacyclononane Fe^{III} complex.^[9] This strongly suggests that NEt_3 indeed deprotonates the aniline group in both species leading to complexes bearing an anilide group coordinated to the Fe^{III} ion. By contrast, the first

spectra recorded within each series are different (see Figure S8). This reflects the different compositions of the **1t:1c** starting mixtures.

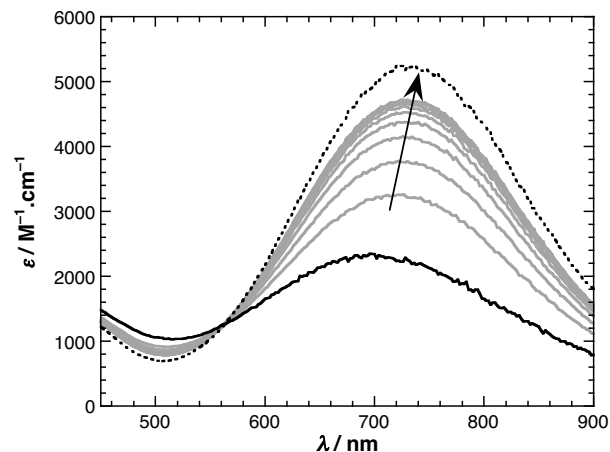


Figure 6. Evolution of the UV-visible absorption spectra when 1.5 eq of NEt_3 are added on **1t:1c** 35:65 solution (grey solid lines). The arrow is a guide to indicate the increase in intensity. The spectra of complexes **2t** and **2c** are shown as black dotted and black solid lines, respectively.

All these data sets can be fully accounted for upon assuming that the two starting complexes have been converted to **2t** and **2c** that further interconvert (see bottom of Scheme 2). The evolution of the absorption spectra after deprotonation on NEt_3 addition can be reproduced by using equations analogous to the set of Eq. 2 reflecting the conversion between species **1t** and **1c** (see Eq. 3a-c). In these equations, t is the time in the course of the evolution of complex **1** when NEt_3 is added while t' stands for the time evolved since the addition of the base. Previous electrochemical studies demonstrated that the rate of the deprotonation of complex **1** by NEt_3 is fast with a second order constant of $\approx 2 \cdot 10^7 \text{ M}^{-1}\cdot\text{min}^{-1}$.^[5] Therefore, in the present UV-visible investigations performed on 0.18 mM solutions, deprotonation is not the rate-limiting step. The absorption measured just immediately after the addition of the base is thus due to a **2t:2c** mixture with the composition of the initial **1t:1c** mixture (see Eq. 3b). The fits of the time dependence of the ϵ values at a given wavelength lead to $(k_{2t} + k_{2c}) = 0.30(2) \text{ min}^{-1}$, whatever the composition of the starting solution and whatever the wavelength. The fits for $\lambda = 720 \text{ nm}$ are reproduced in the Supporting Information (see Figure S9). Moreover, the variations of the absorbance of the solutions immediately after deprotonation lead to $(k_{1t} + k_{1c}) = 0.03(1) \text{ min}^{-1}$, in perfect agreement with the studies presented above (see Supporting Information, Figure S10). This allows the determination of the absorption spectra of **2t** and **2c** (see black traces in Figure 6). At last, these signatures lead to the determination of the composition of the solution once the interconversion between species **2t** and **2c** is complete: the two species **2t** and **2c** are present in an $\approx 83:17$ ratio. Consequently, the equilibrium constant K_2 is equal to 0.20(5) and the two kinetic constants k_{2t} and k_{2c} are equal to 0.05(2) and 0.25(2) min^{-1} , respectively.

$$\begin{aligned} \epsilon(\lambda, t, t') &= \epsilon(\lambda, t' \rightarrow \infty) \\ &+ \{ \epsilon(\lambda, t, t' = 0) - \epsilon(\lambda, t' \rightarrow \infty) \} \times \exp[-(k_{2t} + k_{2c})t'] \end{aligned} \quad (\text{Eq. 3a})$$

$$\begin{aligned} \varepsilon(\lambda, t, t' = 0) &= \frac{k_{1c}}{k_{1t} + k_{1c}} \varepsilon_{2t}(\lambda) + \frac{k_{1t}}{k_{1t} + k_{1c}} \varepsilon_{2c}(\lambda) \\ &+ \left\{ \varepsilon_{2t}(\lambda) - \varepsilon_{2c}(\lambda) \right\} \frac{k_{1t}}{k_{1t} + k_{1c}} \exp[-(k_{1t} + k_{1c})t] \end{aligned} \quad (\text{Eq. 3b})$$

$$\varepsilon(\lambda, t' \rightarrow \infty) = \frac{k_{2c}}{k_{2t} + k_{2c}} \varepsilon_{2t}(\lambda) + \frac{k_{2t}}{k_{2t} + k_{2c}} \varepsilon_{2c}(\lambda) \quad (\text{Eq. 3c})$$

The spectroscopic signatures of species **2t** and **2c** differ slightly in the wavelength of the absorption maximum, 730 nm for **2t** vs 700 nm for **2c**, and mostly by the associated value of the molar extinction coefficient, $\varepsilon_{730} = 5240 \text{ M}^{-1} \cdot \text{cm}^{-1}$ for **2t** vs $\varepsilon_{700} = 2175 \text{ M}^{-1} \cdot \text{cm}^{-1}$ for **2c**. Since these transitions involve the ferric site, such large variations in the intensity strongly suggest that the change between the two forms occurs on the Fe^{III} centre.

To determine the acidic strength of complexes **1t** and **1c**, increasing aliquots of NEt_3 were added to **1t:1c** 35:65 mixtures. Absorption spectra were regularly recorded during 20 minutes after the addition of the base. A plateau is reached after ≈ 14 min. Figure 7 reproduces the spectra recorded 17 minutes after the addition of up to 4 equivalents of NEt_3 . Two isosbestic points are observed at 485 and 547 nm, indicating that two chromophores coexist in solution. At first glance, isosbestic points are not expected due to the presence of four mixed valent diiron complexes, namely **1t**, **1c**, **2t** and **2c**. However, these spectra have been recorded at a time where a plateau had been reached, attesting the completion of the evolution of the solutions. This plateau certifies that the equilibria between species **1t** and **1c** on one hand and species **2t** and **2c** on the other are reached. Consequently the two chromophores that are evidenced here are the **1t:1c** 35:65 and the **2t:2c** 83:17 mixtures. The insert in Figure 7 shows the variations of the molar extinction coefficient at 720 nm as a function of the number of added equivalents of NEt_3 . These data can be satisfyingly reproduced by considering the deprotonation of the **1t:1c** 35:65 chromophore by NEt_3 leading to the **2t:2c** 83:17 chromophore in addition to Et_3NH^+ . A $K_{\text{app}} = 34(3)$ is determined for the equilibrium constant associated to this reaction (see Eq. 4a). Such a value indicates that 95% of complex **1** is deprotonated upon the addition of 1.5 eq. of NEt_3 , thus validating the previous analyses.

$$\begin{aligned} \varepsilon(\lambda, n_{\text{eq}}) &= \varepsilon_{1t,1c}(\lambda) + \left\{ \varepsilon_{2t,2c}(\lambda) - \varepsilon_{1t,1c}(\lambda) \right\} \\ &\times \frac{(n_{\text{eq}} + 1)K_{\text{app}} - \sqrt{(n_{\text{eq}} - 1)^2 K_{\text{app}}^2 + 4n_{\text{eq}} K_{\text{app}}}}{2(K_{\text{app}} - 1)} \end{aligned} \quad (\text{Eq. 4a})$$

$$K_t = K_{\text{app}} \times \frac{1 + K_1}{1 + K_2} \quad (\text{Eq. 4b})$$

$$K_c = K_{\text{app}} \times \frac{1 + K_1}{K_1} \times \frac{K_2}{1 + K_2} \quad (\text{Eq. 4c})$$

The above analysis shows that base addition to the mixture of aniline complexes causes a complete reequilibration of the two mixtures of aniline and anilide complexes. In this respect, the relative short time period (< 20 min) required for reaching equilibrium contrast with the large one (2h) necessary for equilibration of the mixture of aniline complexes in the absence of base. This apparent contradiction can be explained by calculating

the time dependence of the contribution of the four complexes to the total absorption of the solution for a fixed NEt_3 addition. Figure S11 in the Supporting Information illustrates these variations at 720 nm when 0.5 eq of NEt_3 are added. Less than 10% of the total variation is indeed detected after 15 min, attesting the validity of the previous analyses. This calculation shows that the interconversion between complexes **1t** and **1c** is indeed controlled by the conversion between the deprotonated complexes **2t** and **2c** and the fast acido-basic equilibria. Moreover, in conjunction with the two other equilibrium constants K_1 and K_2 , the acidic strengths K_t and K_c of the two aniline complexes **1t** and **1c** can be determined (see Scheme 2 and Eq. 4b-c). One gets $K_t = 83(10)$ and $K_c = 9(3)$, indicating that the form **1t** is *ca* one order of magnitude more acidic than the form **1c**.

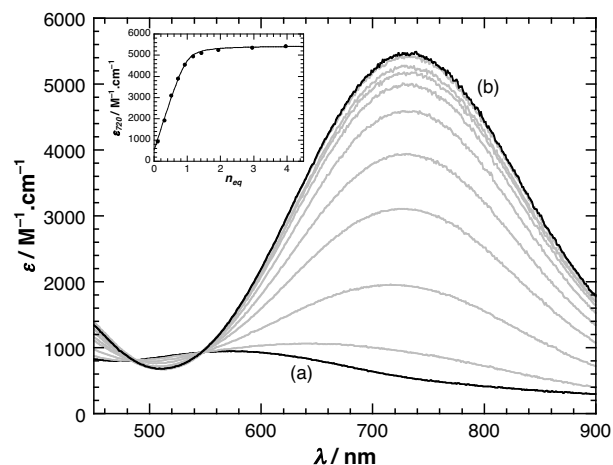


Figure 7. Evolution of the UV-visible absorption spectrum of an CH_3CN solution of complexes **1t:1c** in a 35:65 ratio upon addition of 0 (curve (a)) to 4 eq (curve (b)) of NEt_3 . The inset reproduces the evolution at 720 nm as a function of the number of added equivalents of NEt_3 (full circles). The black solid line corresponds to the best fit according to Eq. 4a.

Mössbauer spectroscopy: As already mentioned, Mössbauer spectroscopy is appropriate to evidence changes on the iron sites and was thus used to investigate the **2t:2c** mixtures. 1.5 eq. of NEt_3 were added to an CH_3CN solution of complexes **1t** and **1c** in a 35:65 ratio and the solutions were frozen shortly to maximize the proportion of species **2c** and at different times. Figure 8 reproduces the spectra recorded at zero-field and 80 K on solutions frozen shortly after the addition of the base (spectrum (a)) or 10 minutes after (spectrum (b)). Two additional spectra are shown in the Supporting Information (see Figure S12). Spectra in Figure 8 clearly evidence a change upon time in the solution composition. The line detected at $0.77 \text{ mm} \cdot \text{s}^{-1}$ in spectrum (a) has almost vanished in spectrum (b). In concert, the line at $1.40 \text{ mm} \cdot \text{s}^{-1}$ increases. The relative intensities of the two lines detected at 2.40 and $2.70 \text{ mm} \cdot \text{s}^{-1}$ are also reversed and the shoulder observed at $-0.04 \text{ mm} \cdot \text{s}^{-1}$ is less pronounced in spectrum (b) compared to spectrum (a). These spectra can be well reproduced by assuming the presence of two diiron complexes in different proportions (see Table 1). The isomer shift values (**2t**: $0.56(1)$ and $1.15(1) \text{ mm} \cdot \text{s}^{-1}$; **2c**: $0.39(1)$ and $1.16(1) \text{ mm} \cdot \text{s}^{-1}$) are consistent with mixed valent $\text{Fe}^{\text{II}}\text{Fe}^{\text{III}}$ species with high-spin ions, in agreement with the $^1\text{H-NMR}$ data. Since the UV-visible studies have demonstrated that species **2t** becomes the major species, this guided

us to attribute the Mössbauer nuclear parameters to the two complexes **2t** and **2c**. It must be underlined that the ΔE_Q values of the Fe^{III} ion are very large in both complexes, and even larger in **2t** than in **2c** (1.75(2) vs 0.80 $\text{mm}\cdot\text{s}^{-1}$, respectively). This large variation sustains a change on the ferric centre between the two forms **2t** and **2c**.

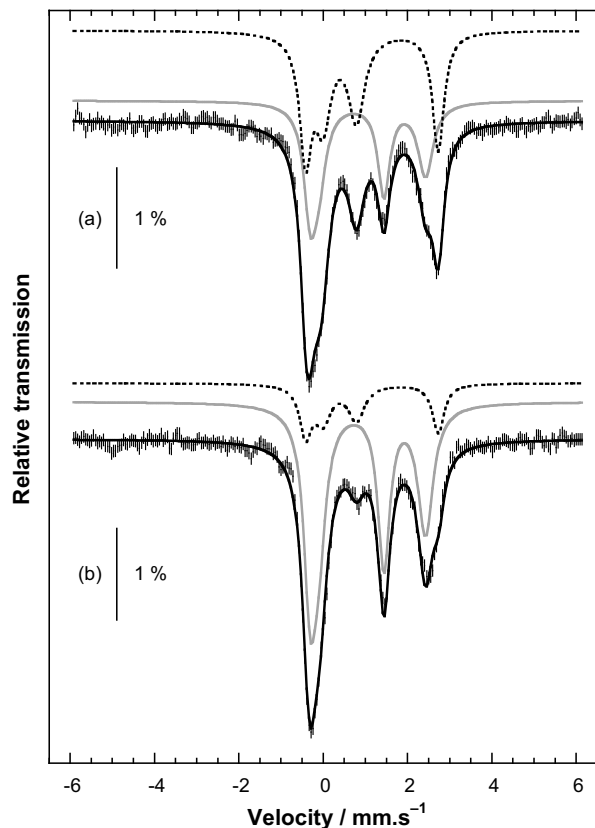


Figure 8. Zero-field Mössbauer spectra recorded at 80 K after the addition of 1.5 eq. of NEt_3 on a CH_3CN **1t:1c** 35:65 solution (hashed marks) that was frozen shortly (top part, spectrum (a)) or 10 minutes (bottom part, spectrum (b)) after the addition of the base. The black solid lines correspond to the theoretical spectra calculated according to the parameters listed in Table 1. Contributions of complexes **2t** and **2c** are shown as solid grey and dotted black lines, respectively.

It is worth noticing that the relative proportions of complexes **2t** and **2c** determined from the four recorded Mössbauer spectra (full dots in Figure 9) are perfectly in agreement with the theoretical evolutions calculated according to the values of k_{2t} and k_{2c} determined from UV-visible investigations (solid and dotted lines in Figure 9).

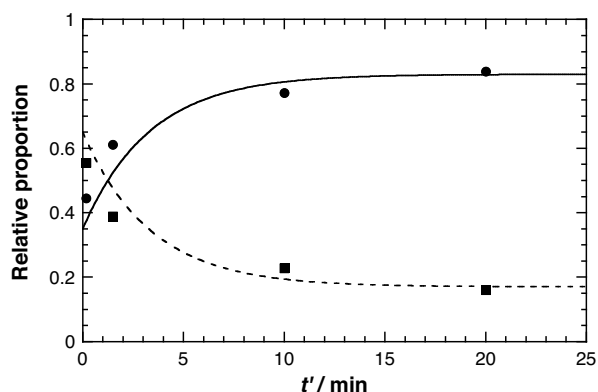


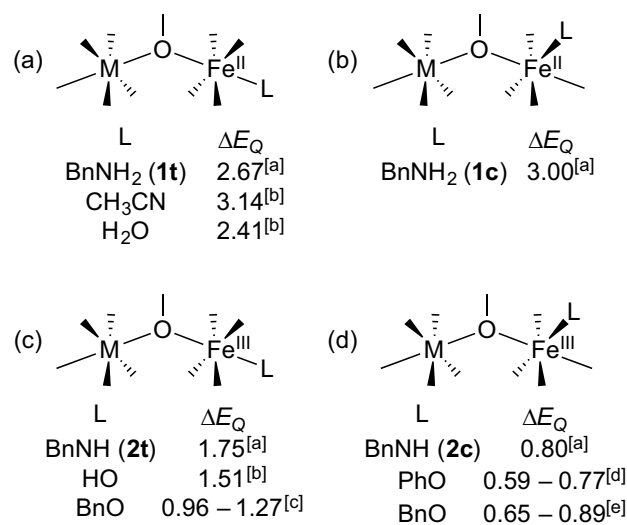
Figure 9. Time dependence of the relative proportions of complexes **2t** (full circles) and **2c** (full squares) as obtained from simulations of Mössbauer spectra (see caption of Figure S12). t' stands for the time since the addition of 1.5 eq of NEt_3 on a **1t:1c** 35:65 solution. The solid and dotted lines correspond respectively to the theoretical distribution of complexes **2t** and **2c** calculated by assuming $k_{2t} = 0.05 \text{ min}^{-1}$ and $k_{2c} = 0.25 \text{ min}^{-1}$ as determined from UV-visible absorption experiments.

Discussion

The above results have revealed that both the aniline and anilide complexes exist in two different forms that interconvert between them (**1t** \rightleftharpoons **1c** and **2t** \rightleftharpoons **2c**) and through (de)protonation (**1c,t** \rightleftharpoons **2c,t**). The form **1t** has been previously characterised in the solid state and shown to have the aniline group bound to the ferrous ion in *trans* position with respect to the bridging phenoxide^[4] but the coordination of **1c** must be assessed. Similarly, the binding of the anilide group to the ferric ion *trans* to the phenoxido bridge has been previously substantiated in **2t** by NMR and Mössbauer spectroscopies^[4] but the coordination of **2c** must be assessed. Once the nature of **1c** and **2c** has been found, the mechanism for the interconversions (**1t** \rightleftharpoons **1c** and **2t** \rightleftharpoons **2c**) and the difference in the properties of the two forms will be addressed.

Structure of 1t and 1c complexes: ESI-MS data reveal that complexes **1t** and **1c** contain the same dicationic species $[\text{Fe}^{\text{III}}(\mu_2\text{-mpdp})\text{Fe}^{\text{II}}(\text{NH}_2\text{Bn-L})]^{2+}$. However, the presence of additional coordinated solvent molecules cannot be excluded if the aniline group is not bound since these molecules dissociate in the ESI-MS experiments. Three hypotheses can thus be envisioned for the structure of **1c**: (i) a valence isomer $[\text{Fe}^{\text{II}}(\mu_2\text{-mpdp})\text{Fe}^{\text{III}}(\text{NH}_2\text{Bn-L})]^{2+}$ where the Fe^{II} and Fe^{III} sites are interchanged, (ii) a coordination isomer where the aniline and pyridine have interchanged position, the pyridine being *trans* and the aniline *cis* to the bridging phenoxide, (iii) an acetonitrile complex $[\text{Fe}^{\text{III}}(\mu_2\text{-mpdp})\text{Fe}^{\text{II}}(\text{NCCH}_3)(\text{L-BnNH}_2)]^{2+}$ where the solvent has replaced the aniline that is not bound anymore, and (iv) an aqua complex $[\text{Fe}^{\text{III}}(\mu_2\text{-mpdp})\text{Fe}^{\text{II}}(\text{OH}_2)(\text{L-BnNH}_2)]^{2+}$ where water binding is assisted by an H-bond from unbound aniline. We believe that hypothesis (i) is not likely since in all $\text{M}^{\text{III}}\text{M}^{\text{II}}$ complexes of these ligands with $\text{M} = \text{Fe}$ or Mn , the M^{III} ion is always bound in the bis-picolylamine site.^[6, 10] Moreover, in the $\text{Fe}^{\text{III}}\text{Fe}^{\text{II}}$ complexes the intervalence transition was observed at ca 9000 cm^{-1} (1100 nm), too high in energy to consider that the two valence forms can easily coexist. Hypotheses (iii) and (iv) can be probed by spectroscopy. Indeed, we showed earlier that the Mössbauer quadrupole splitting is sensitive to the coordination of the Fe^{II} ion in complexes of the

ligand bearing a benzyl group in place of the aniline. The complex is isolated in the solid state with a water molecule bound to Fe^{II} *trans* to the bridging phenoxide ([Fe^{III}(μ₂-mpdp)Fe^{II}(OH₂)(L-Bn)]²⁺),^[10a] but in acetonitrile solution the solvent is coordinated ([Fe^{III}(μ₂-mpdp)Fe^{II}(NCCH₃)(L-Bn)]²⁺).^[6] Replacement of the acetonitrile ligand by an aqua ligand requires addition of 1000 eq of water. These studies provide benchmarks of the coordination of ligands as illustrated in Scheme 3 (part a). The quadrupole splitting determined for **1c** ($\Delta E_Q = 3.00(2) \text{ mm.s}^{-1}$) does not match those for either the acetonitrile or the aqua complex ($\Delta E_Q = 3.14(1) \text{ mm.s}^{-1}$ and $\Delta E_Q = 2.41(2) \text{ mm.s}^{-1}$, respectively).^[6] Note that the difference is significant since it exceeds 4 times the standard deviation. Accordingly, these hypotheses are disfavoured. This conclusion is further supported by consideration of NMR spectra. Firstly, the observed signatures of complexes **1t** and **1c** are significantly different from that of [Fe^{III}(μ₂-mpdp)Fe^{II}(S)(L-Bn)]²⁺ with S = CD₃CN or D₂O.^[6] However, since the signature of the water adduct can be altered by H-bonding, we checked the consequences of the addition of D₂O on an equilibrated solution **1t:1c**. No change was indeed observed (see Figure S13 in the Supporting Information). Accordingly hypotheses (iii) and (iv) were rejected. We are thus left with hypothesis (ii) considering that **1c** is a geometrical isomer of **1t** with the aniline *cis* and the pyridine *trans* to the bridging phenoxide (see Scheme 4). Several X-ray structures of complexes with a pyridine bound in this position indicate that such a coordination is feasible.^[7a, 11]



Scheme 3. ΔE_Q values determined for relevant ferrous and ferric sites within dinuclear complexes. Classification is made to compare to complexes **1t** (part (a)), **1c** (part (b)), **2t** (part (c)) and **2c** (part (d)). Details on the complexes are given in the Supporting Information (see Table S1) [a] This work. [b] See ref [6]. [c] See refs [7a, 7c, 12]. [d] See refs [7a, 13]. [e] See refs [12b, 12c].

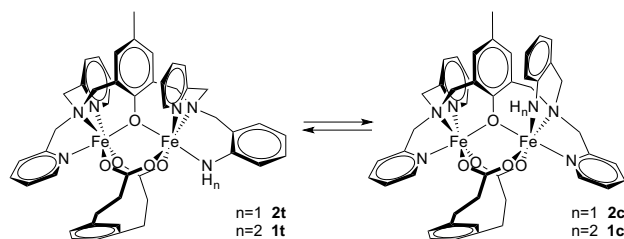
Structure of **2t and **2c** complexes:** Spectroscopic studies evidenced that the action of NEt₃ on **1t:1c** solutions leads to the generation of two different complexes, **2t** and **2c**. In these complexes the valence of the two Fe ions are inverted, the Fe^{II} ion being bound in the bis-picolylamine site. Complex **2t** is the major species that exists in solution 20 minutes after the addition of the base. Two particular spectroscopic features lead to assign the coordination of the anilide to the Fe^{III} ion *trans* to the bridging phenoxide. The first feature is the presence of two characteristic ¹H-NMR upfield resonances at – 214 and –243 ppm. Such negative values are very peculiar and

reminiscent of those observed at –100 and –105 ppm on the mixed valent complex [Fe^{II}(μ-O₂P(OPh)₂)₂Fe^{III}(OBn-L)]²⁺ where HL-BnOH is analogous to HL-BnNH₂ with a 2-hydroxybenzyl group in place of the 2-aminobenzyl arm (see Scheme 1).^[7a] They have been respectively attributed to the *para* and *ortho* protons of the phenoxido ring that is coordinated to the Fe^{III} ion in *trans* position with respect to the bridging phenoxide. The second feature is the unusually large Mössbauer quadrupole splitting determined for the Fe^{III} ion $\Delta E_Q = 1.75(2) \text{ mm.s}^{-1}$. In general, values lying between 0.30 and 0.55 mm.s⁻¹ are observed for ferric ions in similar environments.^[6, 7c, 11] In contrast, values higher than 0.95 mm.s⁻¹ have been previously observed for Fe^{III} sites in similar systems exclusively when an anionic ligand is coordinated *trans* to the phenoxido bridge as summarised in Scheme 3 (part c) and are reminiscent of those of μ-oxo-diferric entities.^[14]

The quadrupole splitting of the Fe^{III} site in **2c** is also large ($\Delta E_Q = 0.80(2) \text{ mm.s}^{-1}$), but not as large as in **2t** ($\Delta E_Q = 1.75(2) \text{ mm.s}^{-1}$). A similar difference in the ΔE_Q values of the ferric centre has been previously observed in the bisferric complexes [Fe^{III}(BBPPNOL)(μ-X)₂Fe^{III}]⁺ (0.89 and 1.27 mm.s⁻¹ for X=AcO⁻^[12e], 0.65 and 1.17 mm.s⁻¹ for X=(PhO)₂PO₂⁻^[12b]) where H₃BBPPNOL stands for *N,N',N',N'*-bis[(2-hydroxybenzyl)(2-pyridylmethyl)]-2-hydroxy-1,3-propanediamine. Neves *et al.* suggest that it could be due to the different coordination of the two terminal phenoxido ligands *vs* the bridging alkoxide, namely a *cis* position on one iron and a *trans* on the other.^[12e] This was confirmed by the X-ray structure of the bis-diphenylphosphato bridged complex.^[12b] Since the larger ΔE_Q value indeed originates from the site with a *trans* coordination of the terminal phenoxide, the lower one is attributed to the *cis*. Therefore, the ΔE_Q value of 0.80(2) mm.s⁻¹ found for **2c** is consistent with a *cis* coordination of the anilide on the Fe^{III} ion *vs* the bridging phenoxide. This assignment is supported by the observation that for related complexes in this series of ligands ΔE_Q values in the range of 0.5–0.6 mm.s⁻¹ are associated with the binding of anionic ligands in *cis* position to the bridging phenoxide (Scheme 3, part d).^[7a, 11]

Significant differences were also evidenced in the UV-visible absorption properties of the **2t** and **2c** complexes: $\lambda_{max} = 730$ and 700 nm with $\epsilon = 5240$ and 2175 M⁻¹.cm⁻¹, respectively. Whereas the change in energy of the absorption maximum is only modest ca 600 cm⁻¹, the change in absorption coefficient by ca 3000 M⁻¹.cm⁻¹ is quite substantial. This difference is reminiscent of that observed between the two bis-ferric complexes [Fe^{III}(BBPPNOL)(μ-OAc)₂Fe^{III}]⁺ and [Fe^{III}(BBPMP)(μ-OAc)₂Fe^{III}]⁺ (H₂BBPMP = 2,6-bis[(2-hydroxybenzyl)(2-pyridylmethyl)-aminomethyl]-4-methylphenol). Both binucleating ligands indeed present two terminal phenoxides but while both phenoxides are *trans* to the bridge in the latter complex, the former contains one *trans* and one *cis* phenoxide. In CH₃CN, the former complex is characterised by an intense absorption band at 540 nm with $\epsilon = 4400 \text{ M}^{-1}.\text{cm}^{-1}$ ^[12e] while the latter presents a more intense transition at 601 nm with $\epsilon = 7700 \text{ M}^{-1}.\text{cm}^{-1}$.^[12d] The two complexes differ also by the nature of the bridge: an alkoxide in the former and a phenoxide in the latter. Whereas the bridging alkoxide does not contribute to any absorption in the visible, a phenoxide→Fe^{III} LMCT absorption is associated to the bridging phenoxide at ca 575 nm with an extinction coefficient of 970 M⁻¹.cm⁻¹. Accordingly the difference in the bridge may contribute only a third of the extinction coefficient change between the two complexes and therefore the main difference is due to the change from a *cis* to a *trans* coordination of the terminal phenoxides. This observation is quite in line with the difference noted for **2t** and

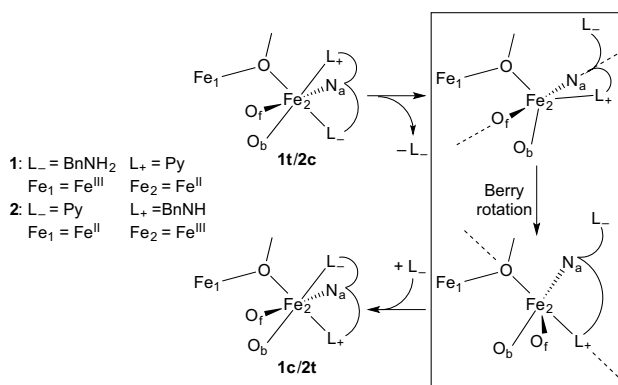
2c and in turn further supports that they differ by the *cis* vs *trans* coordination of the anilide (see Scheme 4).



Scheme 4. Isomerisation reactions of the aniline (complex **1**, $n=2$) or anilide (complex **2**, $n=1$) from a *trans* to a *cis* position with respect to the bridging phenoxide. The aniline (resp. anilide) is coordinated to the Fe^{II} (resp. Fe^{III}) ion in **1** (resp. **2**).

It is interesting to note that **1c** and **2t** are the preponderant isomers once equilibrations are reached. Since pyridine is a better ligand than aniline but weaker than anilide, the major isomer presents in both cases the better ligand in *trans* position to the phenoxido bridge.

Isomerisation processes: All the spectroscopic data accumulated on the solution changes of the aniline and anilide complexes can thus be accounted for by *cis/trans* isomerisation processes (see Scheme 4). The most common isomerisation mechanism of hexacoordinated metal complexes involves a twist of two opposite faces of the octahedron.^[15] Such a Bailar type mechanism cannot be envisaged in the present case owing to the structural rigidity brought about by the binucleating ligand and the presence of the three bridges. By contrast, a dissociative mechanism is more likely due to the presence of weak or labile ligands in the iron coordination sphere. Since dissociation of a ligand will give a pentacoordinate complex, a mechanism involving a Berry rotation appears attractive.^[15] Dissociation of a carboxylate cannot explain the aniline(anilide)/pyridine interconversion because the Berry rotation followed by the recoordination of the carboxylate will not generate the desired isomer but its enantiomer. However, dissociation of either the aniline or the pyridine can account for **1t**→**1c** and **2c**→**2t** transformations as illustrated in Scheme 5 where L_+ stands for the pyridine in complex **1** or for the anilide in complex **2** while L_- represents the aniline ligand in **1** or the pyridine in **2**. Dissociation of the weaker ligand L_- occurs in the first step. The resulting square-based pyramid can rearrange in two trigonal bipyramid (TBP) that differ on the axial ligands, either the tertiary amine N_a and the oxygen O_f of the mpdp^{2-} bridge or the nitrogen atom of the L_+ ligand and the oxygen O_b of mpdp^{2-} . In the first case, the Berry rotation that maintains the ligand O_b leads to a new TBP with the axis now along the L_+ -Fe direction that encompasses the bridging phenoxide. Reoordination of the L_- ligand *trans* to the oxygen O_b of the mpdp^{2-} gives the desired isomer (see Scheme 5). In the second case, the Berry rotation that puts O_f and N_a in axial positions and re-entry of L_- *trans* to O_b reform the desired octahedron (see Supporting Information, Scheme S1). This latter mechanism is however disfavoured because the bridging phenoxide and the tertiary amine would then belong to the equatorial plane of the starting TBP with a corresponding O-Fe- N_a angle approaching 120° , a value difficult to attain in the ligand framework. By contrast, the O-Fe- N_a angle remain at $\approx 90^\circ$ in the mechanism depicted in Scheme 5.



Scheme 5. **1t**→**1c** and **2c**→**2t** favoured isomerisation mechanisms through Berry rotation. N_a stands for the tertiary amine. O_f and O_b are the carboxylate oxygen atoms of mpdp^{2-} coordinated in front and in back of the plane formed by the two iron atoms and the bridging oxygen, respectively.

To validate this mechanistic proposal, we have attempted to measure the kinetics of both isomerisation processes in other solvents. The too low solubility if any of complex **1t** limited the choice for solvents. For instance methanol and dichloromethane were prohibited. $^1\text{H-NMR}$ spectra recorded on DMF or acetone solutions of complex **1** do not reveal any significant change in the **1t**:**1c** ratio at equilibrium. In addition, the UV-visible absorption measurements at room temperature lead to values for $(k_{1t} + k_{1c})$ and $(k_{2t} + k_{2c})$ that differ from that obtained in acetonitrile by less than one order of magnitude. Such small variations may originate from differences in the solvation of the proposed intermediates.

The two isomerisation processes **1t**→**1c** and **2c**→**2t** can be thus rationalised by a similar mechanism. We propose that the leaving ligand is the aniline in the case of complex **1** while it is the pyridine in complex **2**. In addition the two processes involve the iron centres in two different oxidation states: Fe^{II} in **1** and Fe^{III} in **2**. These differences may explain the factor 10 observed in the isomerisation rates ($k_{1t} = 0.02(1) \text{ min}^{-1}$ vs $k_{2c} = 0.25(5) \text{ min}^{-1}$). A slow process for complex **1** is compatible with the common neutral charge of the pyridine and aniline ligands that are indeed coordinated to the Fe^{II} ion. This contrasts with the higher rates measured for complex **2** where a negatively charge anilide ligand and a neutral pyridine are involved, both being linked to the ferric ion. A possible explanation for these differences lies in the strong and more covalent bonding of the ferric site with respect to the softer ferrous one.

Conclusion

The present study has revealed a number of interesting features related to the intrinsic properties of position isomers of metal complexes. To the best of our knowledge such a detailed study is unprecedented and was achievable only owing to the very rich and distinctive properties of the systems investigated. *Cis/trans* isomerisation processes within the coordination sphere of a metal have been scarcely reported in the literature. The most investigated ones concern complexes with monodentate ligands such as CO ,^[16] H^- ^[17] or Cl^- .^[18] *Cis* and *trans* isomers involving aniline or anilide ligands have been previously reported in square planar $[\text{PtL}_2]$ complexes where the chelating ligand L is the (*o*-aminophenyl)diphenylphosphine or its deprotonated form.^[19] More relevant to the present work are Carrano's studies of homoleptic complexes $[\text{ML}_2]$ of tridentate ligands containing two pyrazole and

one phenol groups. NMR spectroscopy indicates that the sandwich complexes $[ML_2]$ ($M=Co^{II}, Ni^{II}$) can exist in the *cis* and *trans* forms, the rate of the conversion being strongly dependent on the steric bulk of the ligand.^[20] In addition, when the two pyrazoles are methylated in 3 and 5 positions, it has been shown that the *cis* isomer is more stable for the ferrous complex $[FeL_2]$ while the *trans* isomer is favoured for the ferric species $[FeL_2]^+$.^[21] A similar dependence has been noted for molybdenum complexes of the same ligands: the Mo^{VI} complex $[LMoO_2Cl]$ favours the *cis* isomer whereas the Mo^V complex $[LMoOCl_2]$ favours the *trans*.^[22] Interestingly a structure dependence was observed in oxygen atom transfer reaction by the Mo^{VI} complexes, the *trans* isomer reacting 20 times faster than its *cis* counterpart. So these isomerisations are non-innocent in terms of electronic structure and associated properties and reactivities. The present work indeed substantiates these observations. For the anilides **2t/2c** the two isomers differ in several spectroscopic features: extinction coefficient of the UV-visible absorption, Mössbauer quadrupole splitting and NMR properties. Indeed, the spectral range of the NMR spectrum of the *trans* isomer **2t** extends to ca -250 ppm with the two resonances corresponding to the *ortho*- and *para*-anilide protons occurring at -214 and -243 ppm. By contrast those of the *cis* isomer **2c** appear in the range 0 to -15 ppm. This illustrates a very strong spin delocalisation over the anilide when it is *trans* to the bridging phenoxide. Similarly the very large quadrupole splitting observed for **2t** ($\Delta E_Q = 1.75 \text{ mm.s}^{-1}$) with respect to **2c** ($\Delta E_Q = 0.80 \text{ mm.s}^{-1}$) reflects a very strong covalency of the anilide bonding. It is thus of interest that this interaction manifests itself also in the different acidities of the aniline complex isomers: **1t** being more ca one order of magnitude more acidic than **1c** ($K_t = 83$ and $K_c = 9$). Work is currently underway in our laboratory to further assess the influence of the isomerisation of the ligand on the acidic and redox properties of the complexes.

Experimental Section

Materials: Complex **1** was prepared according to the published procedure.^[4] Acetonitrile for spectroscopic measurements was distilled under argon over CaH_2 and stored within an inert-atmosphere glovebox. All other reagents were reagent grade quality and used as received.

Physicochemical studies: 1H -NMR spectra were recorded in deuterated acetonitrile on a Bruker AC 200 with a 5 mm indirect detection as described previously.^[7a] Mass spectra were obtained in the electrospray ionisation mode on a LCQ-Finnigan Thermoquest spectrometer equipped with an octupolar analyser and an ion trap. Electronic absorption spectra were recorded in acetonitrile (0.18 mM solution with 1 cm optical length cuvettes) on a Varian Cary® 50 spectrometer. A Peltier device was used for temperature control (298 K). Mössbauer spectra were recorded on 2-4 mM solutions of ^{57}Fe -fully enriched complexes. The experiments were performed using a horizontal transmission cryostat (Oxford Instruments) and a 50 mCi source of ^{57}Co (Rh) as previously described.^[4] All velocity scales and isomer shifts are referred to the metallic iron standard.

Acknowledgements

The Agence Nationale de la Recherche (Grants ANR 2010 BLAN 703 and ANR-11-LABX-0003-01) and the Région Rhône-Alpes

(Grants CIBLE 07 016335 and CIBLE 08 019180) are gratefully acknowledged for their financial support.

- [1] a) M. H. Dickman, *Acta Cryst.* **2000**, *C56*, 58-60; b) W.-D. Song, J.-B. Yan, L.-L. Ji and H. Wang, *Acta Cryst.* **2008**, *E64*, m549; c) M. A. Kiskin, G. G. Aleksandrov, Z. V. Dobrokhotova, V. M. Novotortsev, Y. G. Shvedenkov and I. L. Eremenko, *Russ. Chem. Bull., Int. Ed.* **2006**, *55*, 806-820.
- [2] a) C. Genre, E. Jeanneau, A. Bousseksou, D. Luneau, S. A. Borshch and G. S. Matouzenko, *Chem. Eur. J.* **2008**, *14*, 697-705; b) A. Malassa, H. Görls, A. Buchholz, W. Plass and M. Westerhausen, *Z. Anorg. Allg. Chem.* **2006**, *632*, 2355-2362; c) C. Genre, G. S. Matouzenko, E. Jeanneau and D. Luneau, *New J. Chem.* **2006**, *30*, 1669-1674.
- [3] M. Carboni and J.-M. Latour, *Coord. Chem. Rev.* **2011**, *255*, 186-202.
- [4] E. Gouré, G. Thiabaud, M. Carboni, N. Gon, P. Dubourdeaux, R. Garcia-Serres, M. Clémancey, J.-L. Oddou, A. Y. Robin, L. Jacquamet, L. Dubois, G. Blondin and J.-M. Latour, *Inorg. Chem.* **2011**, *50*, 6408-6410.
- [5] R. Balasubramanian, G. Blondin, J. C. Canales, C. Costentin, J.-M. Latour, M. Robert and J.-M. Savéant, *J. Am. Chem. Soc.* **2012**, *134*, 1906-1909.
- [6] S. Chardon-Noblat, O. Horner, B. Chabut, F. Avenier, N. Debaecker, P. Jones, J. Pécaut, L. Dubois, C. Jeandey, J.-L. Oddou, A. Deronzier and J.-M. Latour, *Inorg. Chem.* **2004**, *43*, 1638-1648.
- [7] a) E. Lambert, B. Chabut, S. Chardon-Noblat, A. Deronzier, G. Chottard, A. Bousseksou, J.-P. Tuchagues, J. Laugier, M. Bardet and J.-M. Latour, *J. Am. Chem. Soc.* **1997**, *119*, 9424-9437; b) M. S. Mashuta, R. J. Webb, J. K. McCusker, E. A. Schmitt, K. J. Oberhausen, J. F. Richardson, R. M. Buchanan and D. N. Hendrickson, *J. Am. Chem. Soc.* **1992**, *114*, 3815-3827; c) A. Neves, M. A. de Brito, I. Vencato, V. Drago, K. Griesar and W. Haase, *Inorg. Chem.* **1996**, *35*, 2360-2368; d) M. Suzuki, A. Uehara, H. Oshio, K. Endo, M. Yanaga, S. Kida and K. Saito, *Bull. Chem. Soc. Jpn.* **1987**, *60*, 3547-3555.
- [8] A. S. Borovik, V. Papaefthymiou, L. F. Taylor, O. P. Anderson and L. Que Jr., *J. Am. Chem. Soc.* **1989**, *111*, 6183-6195.
- [9] O. Schlager, K. Wiegardt and B. Nuber, *Inorg. Chem.* **1995**, *34*, 6456-6462.
- [10] a) W. Kanda, W. Moneta, M. Bardet, E. Bernard, N. Debaecker, J. Laugier, A. Bousseksou, S. Chardon-Noblat and J.-M. Latour, *Angew. Chem., Int. Ed. Engl.* **1995**, *34*, 588-590; b) L. Dubois, D.-F. Xiang, X.-S. Tan, J. Pécaut, P. Jones, S. Baudron, L. Le Pape, J.-M. Latour, C. Baffert, S. Chardon-Noblat, M.-N. Collomb and A. Deronzier, *Inorg. Chem.* **2003**, *42*, 750-760.
- [11] F. Avenier, E. Gouré, P. Dubourdeaux, O. Sénéque, J.-L. Oddou, J. Pécaut, S. Chardon-Noblat, A. Deronzier and J.-M. Latour, *Angew. Chem. Int. Ed.* **2008**, *47*, 715-717.
- [12] a) P. Karsten, A. Neves, A. J. Bortoluzzi, M. Lanznaster and V. Drago, *Inorg. Chem.* **2002**, *41*, 4624-4626; b) B. Krebs, K. Shepers, B. Bremer, G. Henkel, E. Althaus, W. Müller-Warmuth, K. Griesar and W. Haase, *Inorg. Chem.* **1994**, *33*, 1907-1914; c) A. Neves, M. A. de Brito, V. Drago, K. Griesar and W. Haase, *Inorg. Chim. Acta* **1995**, *237*, 131-135; d) A. Neves, M. A. de Brito, I. Vencato, V. Drago, K. Griesar, W. Haase and Y. P. Mascarenhas, *Inorg. Chim. Acta* **1993**, *214*, 5-8; e) A. Neves, S. M. D. Erthal, V. Drago, K. Griesar and W. Haase, *Inorg. Chim. Acta* **1992**, *197*, 121-124; f) H. Nie, S. M. J. Aubin, M. S. Mashuta, C.-C. Wu, J. F. Richardson, D. N. Hendrickson and R. M. Buchanan, *Inorg. Chem.* **1995**, *34*, 2382-2388.
- [13] V. D. Campbell, E. J. Parsons and W. T. Pennington, *Inorg. Chem.* **1993**, *32*, 1773-1778.
- [14] D. M. Kurtz Jr., *Chem. Rev.* **1990**, *90*, 585-606.
- [15] K. F. Purcell and J. C. Kotz, *Inorganic Chemistry*, W. B. Saunders Company, Philadelphia, **1977**, p.
- [16] D. J. Darensbourg, *Inorg. Chem.* **1979**, *18*, 14-17.
- [17] a) D. L. Packett, C. M. Jensen, R. L. Cowan, C. E. Strouse and W. C. Trogler, *Inorg. Chem.* **1985**, *24*, 3578-3583; b) B. Rytchinski, Y. Ben-David and D. Milstein, *Organometallics* **1997**, *16*, 3786-3793.
- [18] B. P. Sullivan and T. J. Meyer, *Inorg. Chem.* **1982**, *21*, 1037-1040.
- [19] M. K. Cooper and J. M. Downes, *Inorg. Chem.* **1978**, *17*, 880-884.
- [20] T. C. Higgs, N. S. Dean and C. J. Carrano, *Inorg. Chem.* **1998**, *37*, 1473-1482.
- [21] T. C. Higgs, D. Ji, R. S. Czernusewicz and C. J. Carrano, *Inorg. Chim. Acta* **1999**, *286*, 80-92.
- [22] J. T. Hoffman, S. Einwaechter, B. S. Chohan, P. Basu and C. J. Carrano, *Inorg. Chem.* **2004**, *43*, 7573-7575.

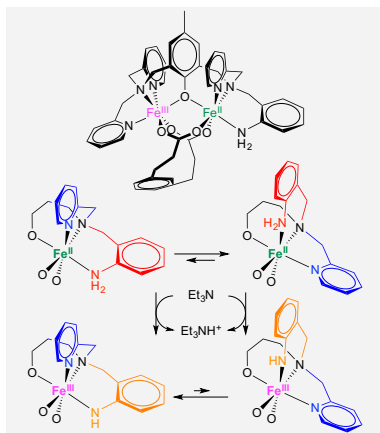
Entry for the Table of Contents (Please choose one layout only)

Layout 1:

Cis-trans isomerisation

Eric Gouré, Michaël Carboni,
Patrick Dubourdeaux, Martin
Clémancey, Ramachandran
Balasubramanian, Colette Lebrun,
Pierre-Alain Bayle, Geneviève
Blondin*, Jean-Marc Latour*
..... Page – Page

**Cis-trans isomerisations in diiron
complexes involving aniline or
anilide ligands**



Cis-trans isomerisation is evidenced in two mixed-valent diiron(II,III) complexes. Pyridine and aniline ligands are shown to exchange their positions on the Fe^{II} site, the *cis* isomer being favoured. In contrast, anilide *trans* to the bridging phenoxide is the more stable isomer for the deprotonated complex.

Supplementary information for the manuscript

Cis-trans isomerisations in diiron complexes involving aniline or anilide ligands

Eric Gouré,^[a] Michaël Carboni,^[a] Patrick Dubourdeaux,^[a] Martin Clémancey,^[a]
 Ramachandran Balasubramanian,^[a] Colette Lebrun,^[b] Pierre-Alain Bayle,^[c] Geneviève
 Blondin,^[a] and Jean-Marc Latour,^[a][a]

List of supplementary figures, comments, tables and schemes

S-3	Figure S1. Full-range ¹ H-NMR spectra recorded immediately (trace a, light grey line), 20 minutes (trace b, dark grey line) and 120 minutes (trace c, black line) after complex 1 was dissolved in CD ₃ CN.
S-4	Figure S2. ¹ H-NMR spectra recorded between 258 and 313 K on a CD ₃ CN solution of complex 1 that was let to evolve for 4 hours after dissolution.
S-5	Figure S3. Time dependence of the proportion of form 1c since dissolution of complex 1 in deuterated acetonitrile.
S-6	Figure S4. Experimental zero-field Mössbauer spectra recorded at 78 K (hashed line) on an acetonitrile solution of complex 1 immediately or 4 hours after dissolution (middle and bottom traces, respectively).
S-7	Figure S5. ESI-MS spectra recorded shortly (a) and 4h (b) after dissolution of complex 1 in CH ₃ CN.
S-8	Figure S6. ¹ H-NMR spectra recorded immediately (trace a), 1 minute (trace b) and 17 minutes (trace c) after addition of 1.5 eq of NEt ₃ on a CD ₃ CN solution of complexes 1t and 1c in a 35:65 ratio.
S-9	Figure S7. Evolution of the UV-visible absorption spectra when 1.5 eq of NEt ₃ are added on 1t:1c solutions after (a) 50 s, (b) 20 min, (c) 40 min, (d) 60 min, (e) 80 min and (f) 100 min after dissolution of complex 1 .
S-10	Figure S8. UV-visible absorption spectra recorded immediately after the addition of 1.5 eq. of NEt ₃ on solutions of 1t and 1c complexes (dotted lines).
S-11	Figure S9. Time dependence of the molar extinction coefficient measured at 720 nm after the addition of 1.5 eq. of NEt ₃ on solutions of 1t and 1c complexes (dots).
S-12	Figure S10. Time dependence of the molar extinction coefficient measured at 720 nm on the spectra recorded immediately after the addition of 1.5 eq. of NEt ₃ on solutions of 1t and 1c complexes performed <i>t_{off}</i> after complex 1 was dissolved in CH ₃ CN (black dots, see Figure S8).
S-13	Figure S11. Time dependence of the absorption at 720 nm of the solution (red curve) after the addition of 0.5 eq of NEt ₃ on an equilibrated CH ₃ CN solution of complex 1 calculated according to the kinetic constants and <i>K_{app}</i> determined from UV-visible data: (<i>k_{1t}</i> + <i>k_{1c}</i>) = 0.03 min ⁻¹ , <i>K₁</i> = 1.8, (<i>k_{2t}</i> + <i>k_{2c}</i>) = 0.30 min ⁻¹ , <i>K₂</i> = 0.2, and <i>K_{app}</i> = 34.
S-14	Figure S12. Zero-field Mössbauer spectra recorded at 78 K after the addition of 1.5 eq. of NEt ₃ on an CH ₃ CN 1t:1c 35:65 solution (hashed marks) that was frozen shortly (spectrum A), 1.5 min (spectrum B) or 10 min (spectrum C) after the addition of the base.
S-15	Figure S13. ¹ H-NMR spectra recorded on an equilibrated CD ₃ CN solution of complex 1 (bottom trace, blue line) and after addition of 6 and 12 equivalents of D ₂ O (middle and top traces, red and black lines, respectively).
S-16	Comments on the 1t → 1c conversion relying on the coordination of a water molecule.
S-17	Table S1. Details on the dinuclear complexes for which the quadrupole splitting values are listed in Scheme 3.
S-20	Scheme S1. 1t → 1c and 2c → 2t disfavoured isomerisation mechanism through Berry rotation.

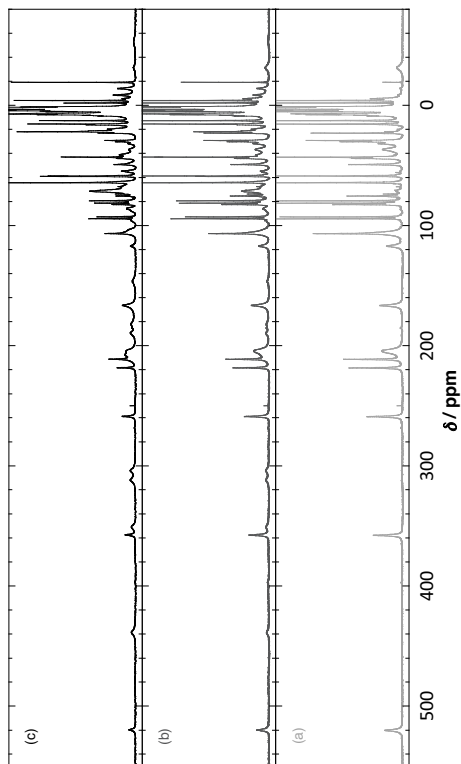


Figure S1. Full-scale $^1\text{H-NMR}$ spectra recorded immediately (trace a, light grey line), 20 minutes (trace b, dark grey line) and 120 minutes (trace c, black line) after complex **1** was dissolved in CD_3CN .

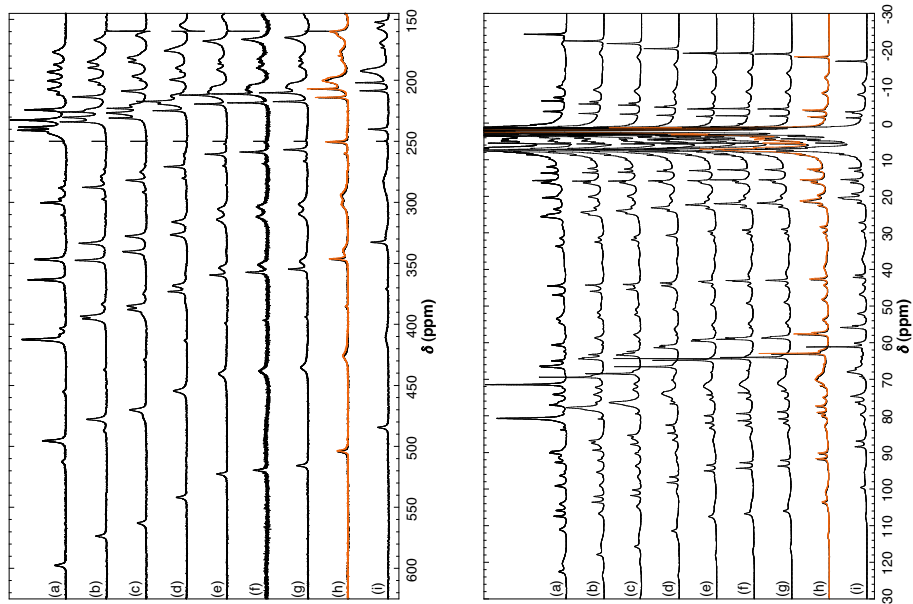


Figure S2. $^1\text{H-NMR}$ spectra recorded between 258 and 313 K on a CD_3CN solution of complex **1** that was let to evolve for 4 hours after dissolution. The spectra are displayed in two different chemical shift windows to evidence the changes in peak positions and linewidths. The labels (a) to (i) correspond to the following temperatures: 258, 268, 273, 283, 293, 295, 298, 303 and 313 K (black traces). Spectra were recorded in the following order: f/h/i/g/a/b/c/d/e/h that is 295/303/313/298/258/268/273/283/293/303 K. The first spectrum recorded at 303 K is drawn in pink while the last one corresponds to the black trace.

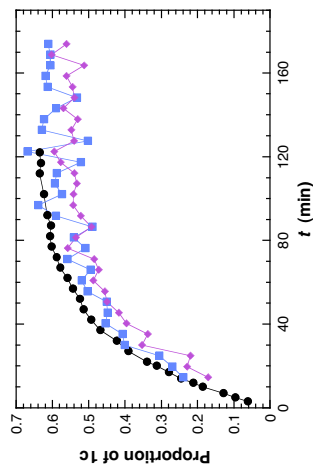


Figure S3. Time dependence of the proportion of form **1c** since dissolution of complex **1** in deuterated acetonitrile. The black dots are those of Figure 2 and are calculated as the area of the -19 ppm peak relatively to those at -2, -4 and -5.5 ppm. The blue squares (resp. violet diamonds) are calculated as the area of the 438 ppm peak (resp. the average of those at 310 and 304 ppm) relatively to those at 520 ppm (resp. 258 ppm). Each signal is assumed to correspond to a single proton.

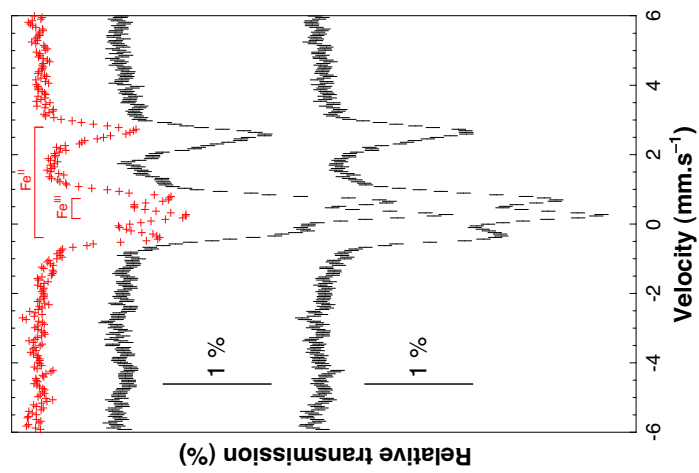


Figure S4. Experimental zero-field Mössbauer spectra recorded at 78 K (hashed line) on an acetonitrile solution of complex **1** immediately or 4 hours after dissolution (middle and bottom traces, respectively). The top trace (red crosses) is obtained by subtracting to the bottom spectrum the middle one weighted by 0.35. The quadrupole doublets attributed to the Fe^{II} and Fe^{III} centres are indicated.

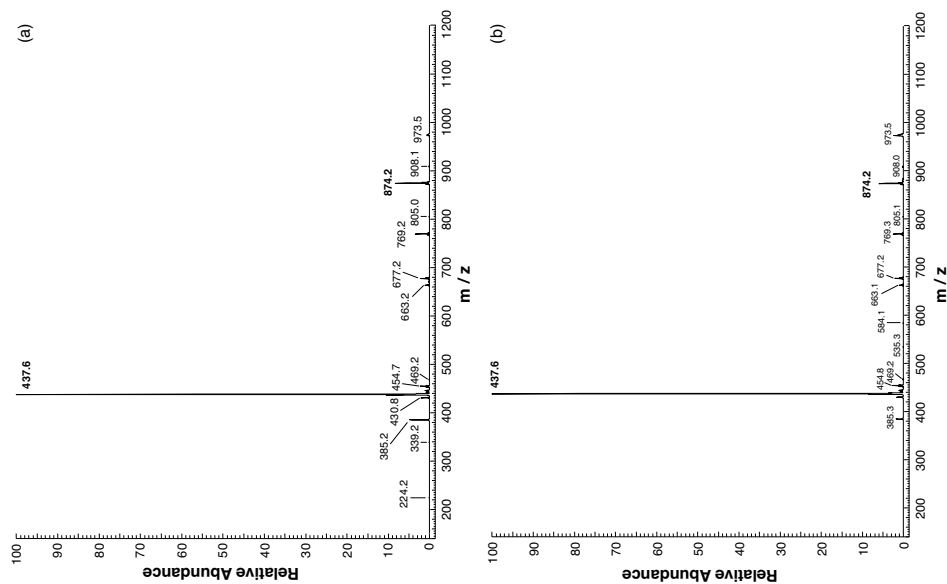


Figure S5. ESI-MS spectra recorded shortly (a) and 4h (b) after dissolution of complex **1** in CH₃CN. The peak at 437.6 is associated to the dicationic complex [Fe₂(L-BnNH₂)(mpdp)]²⁺, while that at 874.2 corresponds to the deprotonated species [Fe₂(L-BnNH)(mpdp)]⁺.

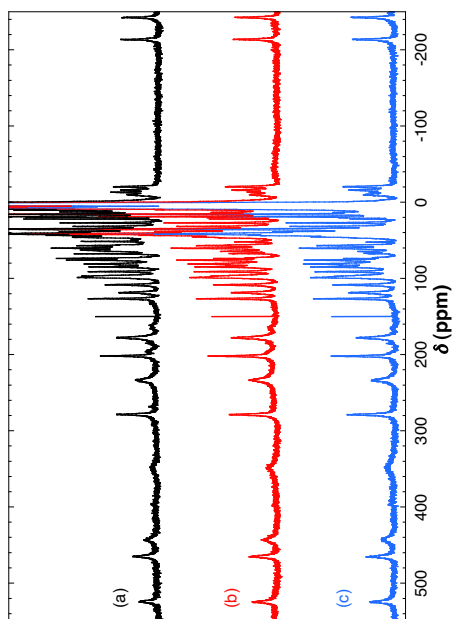


Figure S6. ¹H-NMR spectra recorded immediately (trace a), 1 minute (trace b) and 17 minutes (trace c) after addition of 1.5 eq of NEt₃ on a CD₃CN solution of complexes **1t** and **1c** in a 35:65 ratio.

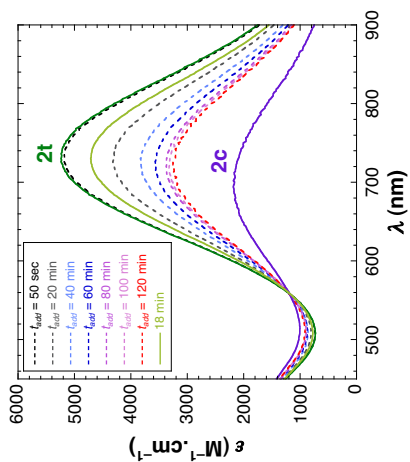


Figure S8. UV-visible absorption spectra recorded immediately after the addition of 1.5 eq. of NEt_3 on solutions of **1t** and **1c** complexes (dotted lines). t_{diss} indicates the moment of the addition of the base once complex **1** is dissolved. The dark green and dark purple lines correspond to the spectra of complexes **2t** and **2c** that can be deduced from this series. The light green line is the common spectrum recorded 18 minutes after the addition of NEt_3 , whatever the value of t_{diss} .

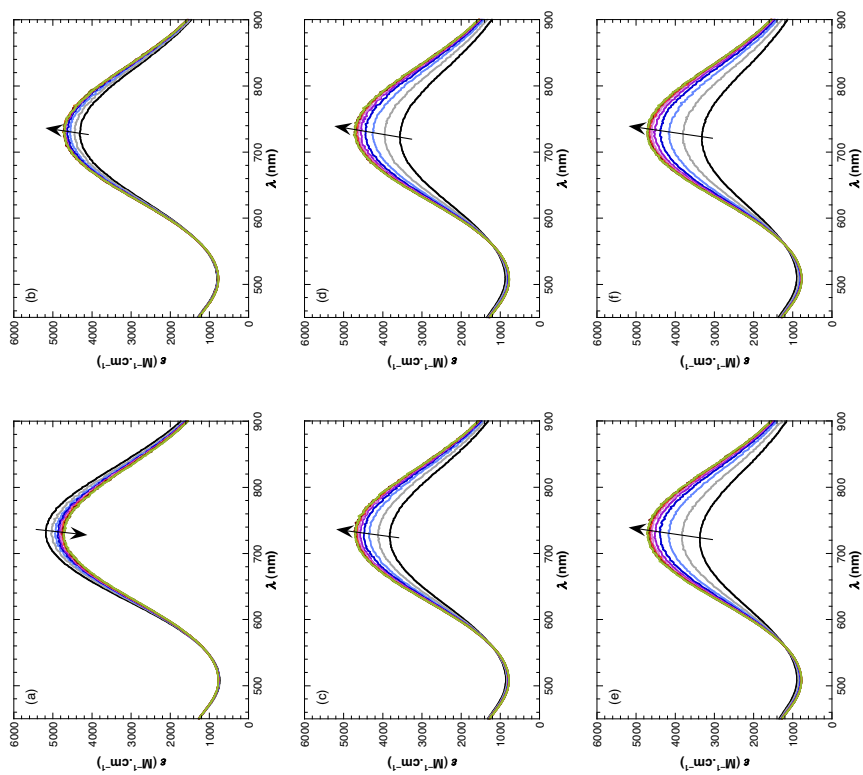


Figure S7. Evolution of the UV-visible absorption spectra when 1.5 eq of NEt_3 are added on **1t:1c** solutions after (a) 50 s, (b) 20 min, (c) 40 min, (d) 60 min, (e) 80 min and (f) 100 min after dissolution of complex **1**. Spectra recorded every 97 s are shown. The arrow indicates the decrease (a) or increase (b-f) of the intensity upon time.

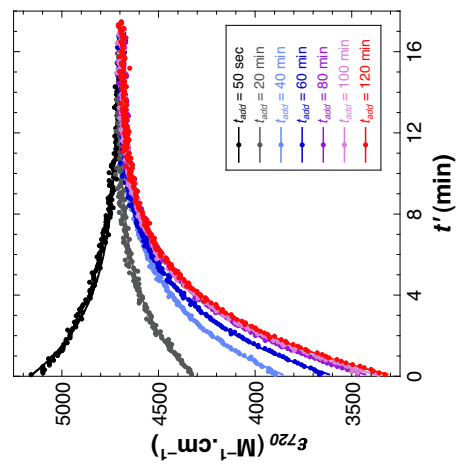


Figure S9. Time dependence of the molar extinction coefficient measured at 720 nm after the addition of 1.5 eq. of NEt_3 on solutions of **1t** and **1c** complexes (dots). The addition of base was performed t_{add} after complex **1** was dissolved in CH_3CN . The fits were performed according to Eq. 3a and lead to $(k_{21} + k_{22}) = 0.30(2) \text{ min}^{-1}$ (solid lines).

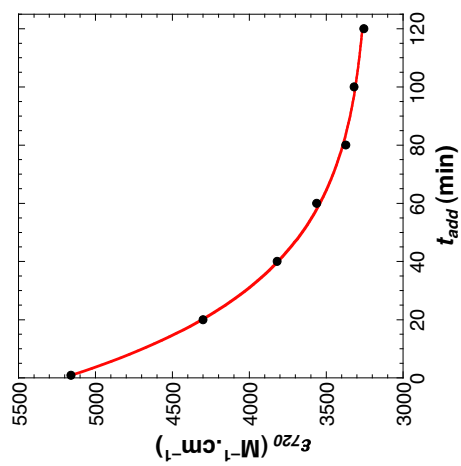


Figure S10. Time dependence of the molar extinction coefficient measured at 720 nm on the spectra recorded immediately after the addition of 1.5 eq. of NEt_3 on solutions of **1t** and **1c** complexes performed t_{add} after complex **1** was dissolved in CH_3CN (black dots, see Figure S7). The fit was performed according to Eq. 2a and lead to $(k_{1t} + k_{1c}) = 0.03(1) \text{ min}^{-1}$.

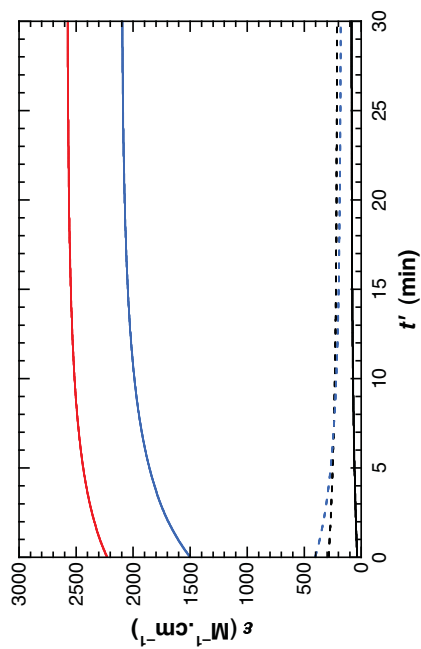


Figure S11. Time dependence of the absorption at 720 nm of the solution (red curve) after the addition of 0.5 eq of NEt_3 on an equilibrated CH_3CN solution of complex **1** calculated according to the kinetic constants and K_{app} determined from UV-visible data: $(k_{1t} + k_{1c}) = 0.03 \text{ min}^{-1}$, $K_1 = 1.8$, $(k_{2t} + k_{2c}) = 0.30 \text{ min}^{-1}$, $K_2 = 0.2$, and $K_{\text{app}} = 34$. The contribution to the total absorbance of the different species are drawn as follow: **1t** as solid black line, **1c** as dotted black line, **2t** as solid blue line, and **2c** as dotted blue line. The individual extinction molar coefficient values are taken according to Figures 4 and 6 ($\epsilon_{1t} = 469 \text{ M}^{-1} \cdot \text{cm}^{-1}$, $\epsilon_{1c} = 643 \text{ M}^{-1} \cdot \text{cm}^{-1}$, $\epsilon_{2t} = 5209 \text{ M}^{-1} \cdot \text{cm}^{-1}$, $\epsilon_{2c} = 2136 \text{ M}^{-1} \cdot \text{cm}^{-1}$). The total absorption is mainly due to complex **2t**. After 15 min, more than 90% of the variation of the contribution of **2t** is indeed achieved.

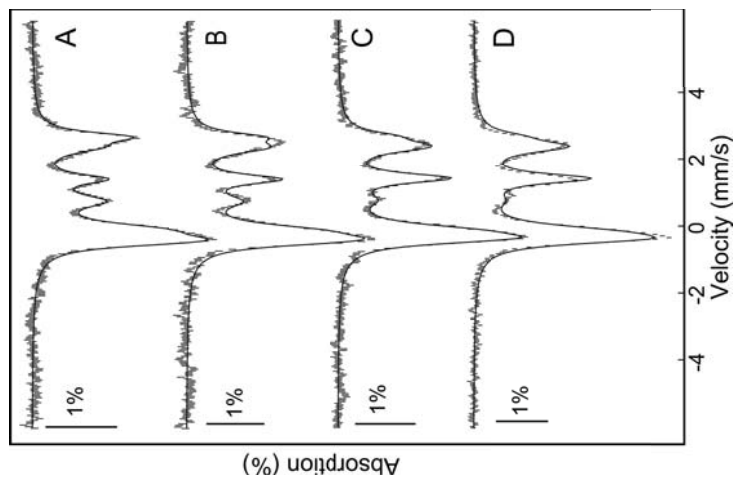


Figure S12. Zero-field Mössbauer spectra recorded at 78 K after the addition of 1.5 eq. of NEt_3 on an CH_3CN **1t:1c** 35:65 solution (hashed marks) that was frozen shortly (spectrum A), 1.5 min (spectrum B) or 10 min (spectrum C) after the addition of the base. For spectrum D, an additional 1.5 eq of NEt_3 was added to the solution corresponding to spectrum C and the resulting mixture let to evolve additional 10 min. The black solid lines correspond to the theoretical spectra calculated according to the nuclear parameters listed in Table 1. Only the relative contributions of the two complexes vary. The ratios **2t:2c** are equal to 45:55 in A, 61:39 in B, 77:23 in C and 84:16 in D.

Comments on the $1t \rightarrow 1c$ conversion relying on the coordination of a water molecule.

Spectra shown in Figure S13 were recorded on a 400 μL CD_3CN solution where 10 mg of complex **1** (9.15 μmoles) were dissolved. According to the 0.05% maximal content of $\text{D}_2\text{O} + \text{H}_2\text{O}$ present in commercial NMR high quality CD_3CN , one can deduce that ≈ 8.5 μmoles of water were initially introduced in the NMR tube. Under these conditions, a 35:65 **1t**:**1c** ratio was determined from the areas of the negative signals detected on the spectrum of the equilibrated solution (see text). If the conversion of complex **1t** is indeed the coordination of a water molecule to the Fe^{II} site to give the complex **1c** of formula $[\text{Fe}^{\text{II}}(\mu_2\text{-mpdp})\text{Fe}^{\text{II}}(\text{OH}_2)(\text{L-BnNH}_2)]^{2+}$, one gets :



Addition of small amounts of water will strongly displace the equilibrium. Indeed after the addition of 6 or 12 equivalents of D_2O (1 and 2 μL , respectively), complex **1** would be more than 95% under the form **1c**. The recorded $^1\text{H-NMR}$ spectra do not evidenced neither a modification of the distribution of the forms **1t** and **1c**, nor a change in the peak positions or profiles, thus invalidating the working hypothesis, that is the substitution of the aniline ligand by a water molecule.

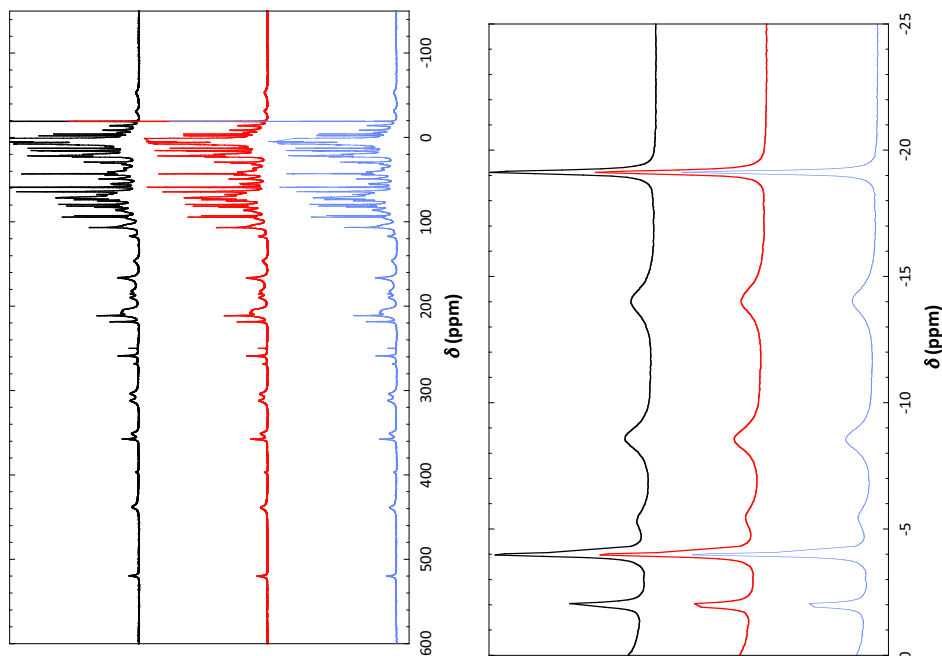
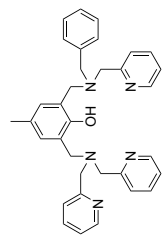
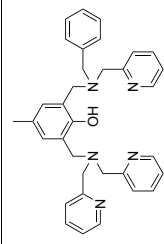
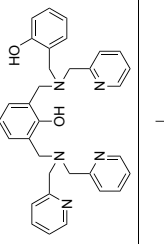
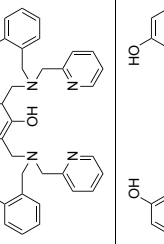
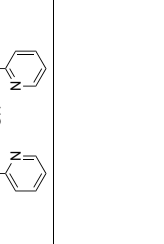
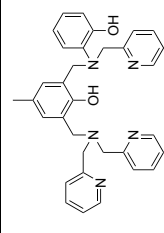


Figure S13. $^1\text{H-NMR}$ spectra recorded on an equilibrated CD_3CN solution of complex **1** (bottom trace, blue line) and after addition of 6 and 12 equivalents of D_2O (middle and top traces, red and black lines, respectively). The top part shows the full-scale spectra while a zoom on the 0 to 25 ppm domain is presented. The spectra shown were recorded 5 minutes after the addition of D_2O . Superimposable spectra were observed 12 hours after the addition.

Table S1. Details on the dinuclear complexes for which the quadrupole splitting values are listed in Scheme 3. These values were determined between 50 and 115 K except for one complex.

(a) 					
Ditopic ligand	Bridge	M	L	ΔE_Q (mm.s ⁻¹)	Ref.
	μ_2 -mpdp	Fe ^{III}	CH ₃ CN	3.14	[1]
			H ₂ O	2.41	

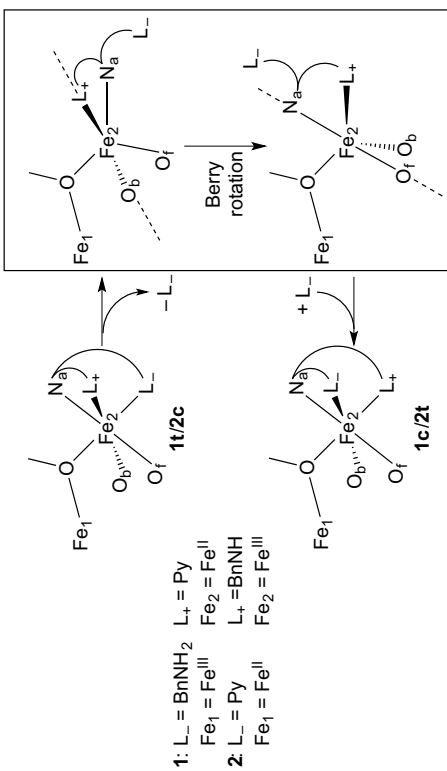
(c) 					
Ditopic ligand	Bridge	M	L	ΔE_Q (mm.s ⁻¹)	Ref.
	μ_2 -mpdp	Fe ^{III}	OH	1.51	[1]
			$(\mu\text{-O}_2\text{P(OPh)}_2)_2$	Fe ^{II}	BnO
Fe ^{III}	1.22	[2]			
Fe ^{II}	1.096	[3]			
Mn ^{II}	1.04	[4]			
	$(\mu\text{-OAc})_2$	Fe ^{II}	0.96	[5]	
		Fe ^{III}	1.093	[6]	
	$(\mu\text{-OAc})_2$	Fe ^{III}	1.09	[5]	
		Fe ^{III}	1.27	[7]	
	$(\mu\text{-O}_2\text{P(OPh)}_2)_2$	Fe ^{III}	BnO	1.17	[8]

(d) 						
Ditopic ligand	Bridge	M	L	ΔE_Q (mm.s ⁻¹)	Ref.	
	μ_2 -mpdp	Fe ^{II}	PhO	0.594	[2]	
			$(\mu\text{-OPr})_2$	Fe ^{III}	PhO	0.77 (at 298 K)
$(\mu\text{-OAc})_2$	Fe ^{III}	BnO			0.89	[7]
		$(\mu\text{-O}_2\text{P(OPh)}_2)_2$			0.65	[8]

- [1] S. Chardon-Noblat, O. Horner, B. Chabut, F. Avenier, N. Debaecker, P. Jones, J. Pécaut, L. Dubois, C. Jeandey, J.-L. Oddou, A. Deronzier, J.-M. Latour: Spectroscopic and Electrochemical Characterizations of an Aqua Ligand Exchange and Oxidatively Induced Deprotonation in Diiron Complexes. *Inorg. Chem.* **2004**, *43*, 1638-1648.
- [2] E. Lambert, B. Chabut, S. Chardon-Noblat, A. Deronzier, G. Chottard, A. Bousseksou, J.-P. Tuchagues, M. Bardet, J. Laugier, J.-M. Latour: Synthesis, Structural, Magnetic and Redox Properties of Asymmetric Diiron Complexes with a Single Terminally Bound Ligand. Relevance to the Purple Acid Phosphatase Enzymes. *J. Am. Chem. Soc.* **1997**, *119*, 9424-9437.
- [3] A. Neves, M. A. de Brito, V. Drago, K. Griesar, W. Haase: A new asymmetric N₂O₂-donor binucleating ligand and its first Fe^{II} complex as a model for the redox properties of uteroferrin. *Inorg. Chim. Acta* **1995**, *237*, 131-135.
- [4] P. Karsten, A. Neves, A. J. Bortoluzzi, M. Lanzmaister, V. Drago: Synthesis, structure, properties, and phosphatase-like activity of the first heterodinuclear Fe^{III}Mn^{II} complex with the unsymmetric ligand H₂BPBPMP as a model for the PAP in sweet potato. *Inorg. Chem.* **2002**, *41*, 4624-4626.
- [5] A. Neves, M. A. de Brito, I. Vencato, V. Drago, K. Griesar, W. Haase: Fe^{II}Fe^{III} and Fe^{II}Fe^{III} Complexes as Synthetic Analogues for the Oxidized and Reduced Forms of Purple Acid Phosphatases. *Inorg. Chem.* **1996**, *35*, 2360-2368.
- [6] A. Neves, M. A. de Brito, I. Vencato, V. Drago, K. Griesar, W. Haase, Y. P. Mascarenhas: Synthesis, crystal structure and properties of a new binuclear iron(III) complex as a model for the purple acid phosphatases. *Inorg. Chim. Acta* **1993**, *214*, 5-8.
- [7] A. Neves, S. M. D. Erthal, V. Drago, K. Griesar, W. Haase: A new N,O-donor binucleating ligand and its first iron(III) complex as a model for the purple acid phosphatases. *Inorg. Chim. Acta* **1992**, *197*, 121-124.

- [8] B. Krebs, K. Shepers, B. Bremer, G. Henkel, E. Althaus, W. Müller-Warmuth, K. Griesar, W. Haase: Model Compounds for the Oxidized Uteroferrin-Phosphate Complex with Novel Dinucleating Ligands Containing Phenolate and Pyridine Groups. *Inorg. Chem.* **1994**, *33*, 1907-1914.
- [9] V. D. Campbell, E. J. Parsons, W. T. Pennington: Diirion and Dicobalt Complexes of a Phenolate-Bridged Binucleating Ligand with Mixed Phenolate and Pyridine Podands. *Inorg. Chem.* **1993**, *32*, 1773-1778.

Scheme S1. **1t**→**1c** and **2c**→**2t** disfavoured isomerisation mechanism through Berry rotation. N_a stands for the tertiary amine. O_f and O_b are the carboxylate oxygen atoms of $mpdp^{2-}$ coordinated in front and in back of the plane formed by the two iron atoms and the bridging oxygen, respectively.



3.2 Discussion

Here after, as in the submitted paper, the complex $[\text{Fe}^{\text{III}}(\mu_2\text{-mpdp})\text{Fe}^{\text{II}}(\text{H}_2\text{NBn-L})]^{2+}$ with the geometry revealed by X-ray diffraction studies will be denoted **1t**. The letter **t** stands for trans and indicates that the aminobenzyl group is coordinated to the metal ion (here the Fe^{II} site) in *trans* position with respect to the bridging phenoxide. The new complex that is formed, denoted **1c** (significance of the letter c will be deduced, see below), has the following properties:

- (i) Electron-Spray Ionization Mass Spectroscopy (ESI-MS) only indicates the presence of the dicationic complex of formula $[\text{Fe}^{\text{III}}(\mu_2\text{-mpdp})\text{Fe}^{\text{II}}(\text{H}_2\text{NBn-L})]^{2+}$;
- (ii) The maximum of the absorption in the visible domain is observed at 583 nm with $\varepsilon_{583} = 1000 \text{ M}^{-1}\cdot\text{cm}^{-1}$ versus 564 nm $\varepsilon_{564} = 875 \text{ M}^{-1}\cdot\text{cm}^{-1}$ for **1t**;
- (iii) $^1\text{H-NMR}$ spectroscopy reveals that **1c** is a mixed valent diiron complex with **1t:1c** ratio of 35:65 at completion;
- (iv) Mössbauer spectroscopy confirms the mixed-valent state for species **1c**. Table 3.1 summarized the values for the isomeric shifts and the quadrupole splittings determined for both complexes; the ratio between the two forms is found similar to that from $^1\text{H-NMR}$;
- (v) Evolutions observed in UV-visible and NMR spectroscopies can be interpreted according to the following equilibrium (Eq. 3.1):



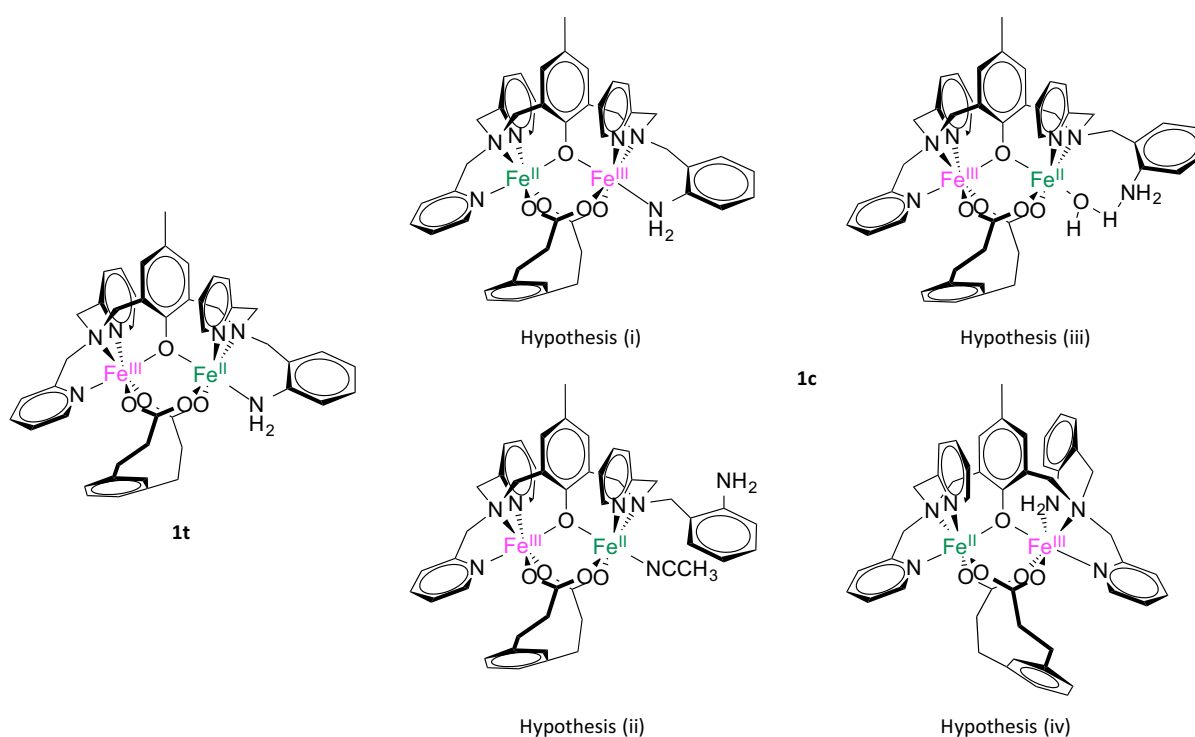
The following values were determined: $k_{1t} = 0.02(1) \text{ min}^{-1}$ and $k_{1c} = 0.01(1) \text{ min}^{-1}$.

Table 3.1. Mössbauer nuclear parameters from the simulations of two spectra recorded 1 min or 4 hours after dissolution of complex **1t** in CH_3CN .

Complex	Site	δ (mm/s)	ΔE_Q (mm/s)	% after 1 min	% after 4 hours
1t	Fe^{III}	0.46(1)	0.41(2)	89	33
	Fe^{II}	1.19(1)	2.67(2)		
1c	Fe^{III}	0.49(1)	0.52(2)	11	67
	Fe^{II}	1.14(1)	3.00(2)		

Different reactions can be hypothesized to rationalize these data:

- (i) A valence isomer $[\text{Fe}^{\text{II}}(\mu_2\text{-mpdp})\text{Fe}^{\text{III}}(\text{H}_2\text{NBn-L})]^{2+}$ where the valence of the iron ions have been inverted;
- (ii) Substitution of the aminobenzyl group by an acetonitrile molecule;
- (iii) Substitution of the aminobenzyl group by a water molecule. The water ligand may be stabilized by H-bonding with the non coordinated aniline;
- (iv) A coordination isomer where the pyridine and the aniline have interchanged their positions, the aminobenzyl group being *cis* to the bridging phenoxide in **1c** (and the pyridine in *trans*).



Scheme 3.1. Scheme of the starting complex **1t** (left) and of the resulting complex **1c** within hypotheses (i-iv).

The first three hypotheses can be rejected on the following arguments.

Hypothesis (i):

When one pyridine arm in Hbpmp is replaced by a non-coordinating group (benzyl or dichlorobenzyl), the X-ray structure of the $\text{M}^{\text{III}}\text{M}^{\text{II}}$ complexes with $\text{M} = \text{Fe}$ or Mn systematically revealed the M^{III} site coordinated by the bis-picolylamine branch. Only when the modification of the Hbpmp ligand includes the introduction of a coordinating anionic ligand such as phenol or hydroxybenzyl, the bis-picolylamine coordinates the Fe^{II} ion. In addition, the Inter Valence Charge Transfer Transition (IVCT) in this type of complexes was observed in the 1000-1400 nm range and

the corresponding energy thus extends from 7000 to 10000 cm^{-1} . Such high energy indicates, that the two valence isomers can hardly coexist.

Hypothesis (ii):

We have shown in the first section of this part that the isomer shift of the Fe^{II} site is indeed very sensitive to the environment. When acetonitrile is coordinated to the Fe^{II} site in $[(\text{L-Bn})\text{Fe}_2(\mu_2\text{-mpdp})(\text{NCCH}_3)]^{2+}$, the quadrupole splitting of the ferrous ion is determined at 3.14(2) mm/s. Since $\Delta E_Q = 3.00(2)$ mm/s for the ferrous site in **1c** and that both values differ by more than four times the standard deviation, coordination of acetonitrile is not probed by Mössbauer spectroscopy. Moreover, substitution of the aminobenzyl group by acetonitrile should lead to a $^1\text{H-NMR}$ spectrum close to that of $[(\text{L-Bn})\text{Fe}_2(\mu_2\text{-mpdp})(\text{NCCD}_3)]^{2+}$ and this is not observed.

Hypothesis (iii):

The quadrupole splitting of the ferrous site in $[(\text{L-Bn})\text{Fe}_2(\mu_2\text{-mpdp})(\text{OH}_2)]^{2+}$ is determined at 2.41 mm/s in acetonitrile solution. This value is well separated from the $\Delta E_Q = 3.00(2)$ mm/s of the ferrous site in **1c**. Accordingly, Mössbauer spectroscopy disfavored the coordination of a water molecule in place of the aniline.

The observed $^1\text{H-NMR}$ spectrum of **1c** also significantly differs from that of $[(\text{L-Bn})\text{Fe}_2(\mu_2\text{-mpdp})(\text{OD}_2)]^{2+}$. However, the NMR spectrum (as the Mössbauer parameters) may be modified if the coordinated water molecule is H-bonded to the aminobenzyl group.

Since the measurements have been performed in CD_3CN , the only source of water is the molecules initially present in the deuterated solvent. The contaminating amounts of HDO and D_2O in CD_3CN obviously vary from one experiment to the other and the upper limit that has been estimated corresponds to 1 equivalent of complex. If **1c** indeed originates from **1t** according to (Eq. 3.2), addition of extra equivalents of D_2O would undoubtedly result in a strong modification of the **1t:1c** ratio at completion.



The 35:65 **1t:1c** ratio determined at completion leads to an equilibrium constant K_1 of few hundreds of $\text{mol}^{-1}\cdot\text{L}$. Addition of 6 or 12 equivalents of D_2O would lead to a **1t:1c** ratio close to 90:10 or even higher. Recordings of the corresponding $^1\text{H-NMR}$ spectra, reveal no modifications neither in the intensity nor on the peak positions (Figure 3.1).

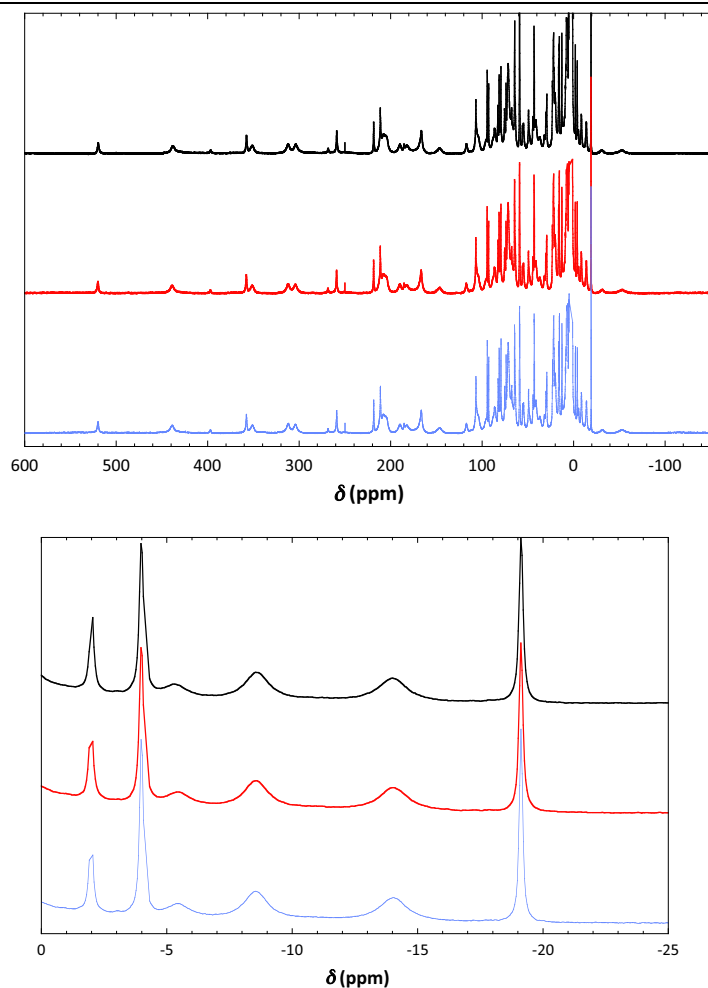
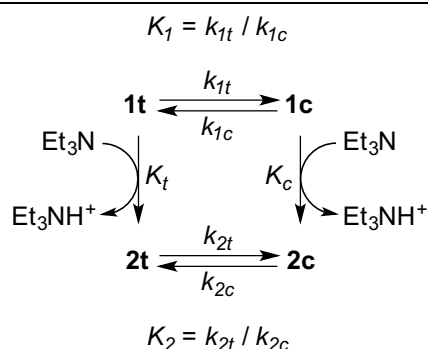


Figure 3.1. $^1\text{H-NMR}$ spectra recorded on an equilibrated CD_3CN solution of complex **1** (bottom trace, blue line) and after addition of 6 and 12 equivalents of D_2O (middle and top traces, red and black lines, respectively). The top part shows the full-scale spectra while a zoom on the 0 to -25 ppm domain is presented. The spectra shown were recorded 5 minutes after the addition of D_2O . Superimposable spectra were observed 12 hours after the addition.

Experimental data thus argue against hypothesis (i) to (iii). We are thus left with hypothesis (iv) that is an isomerization reaction. The letter **c** in **1c** indicates that the aminobenzyl group is coordinated to the metal ion in *cis* position with respect to the bridging phenoxide (and the pyridine in *trans*).

To further confirm this hypothesis, the behavior of the **1t:1c** mixtures upon addition of triethylamine were investigated. As presented in the submitted manuscript, spectroscopic data reveal that both complexes **1t** and **1c** are deprotonated upon addition of 1.5 equivalents of NEt_3 , thus generating complexes **2t** and **2c**. We are thus left with the square Scheme 3.2:



Scheme 3.2. Square scheme showing how the four complexes **1t**, **1c**, **2t** and **2c** are related.

The spectroscopic signatures of complexes **2t** and **2c** are fairly compatible with an anilide coordinated to the Fe^{III} site *trans* or *cis* to the μ -phenoxide in **2t** and **2c**, respectively.

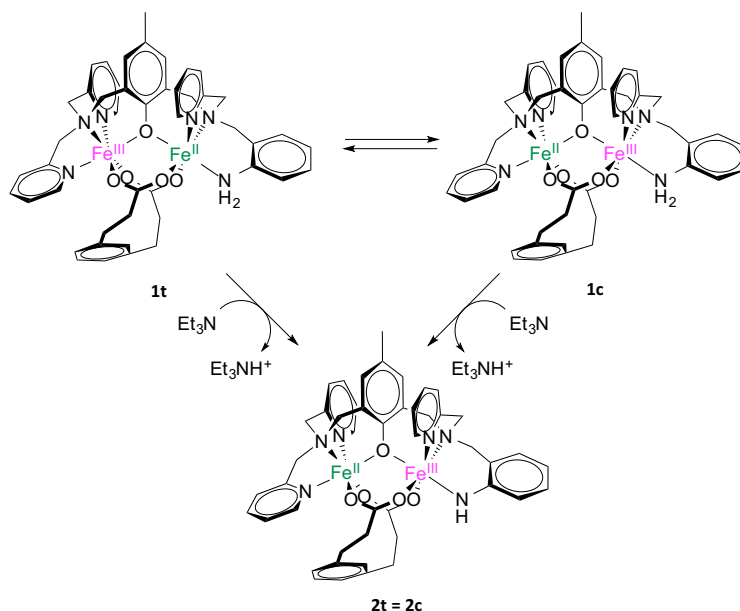
- (i) The maximum of the absorption in the visible domain is observed at 730 nm with $\epsilon_{730} = 5240 \text{ M}^{-1} \cdot \text{cm}^{-1}$ for **2t** and at 700 nm with $\epsilon_{700} = 2175 \text{ M}^{-1} \cdot \text{cm}^{-1}$ for **2c**;
- (ii) Mössbauer signatures of complexes **2t** and **2c** differ significantly. The parameters are given in Table 3.2. The variation upon time of the **2t**:**2c** ratio is fully in agreement with those observed by UV-visible absorption spectroscopy.

Table 3.2. Mössbauer nuclear parameters from the simulations of two spectra recorded 1 or 10 min after the addition of 1.5 eq of NEt₃ on a 35:65 **1t**:**1c** acetonitrile solution.

Complex	Site	δ (mm/s)	ΔE_Q (mm/s)	% 1 min after addition of NEt ₃	% 10 min after addition of NEt ₃
2t	Fe ^{III}	0.56(1)	1.75(2)	44	77
	Fe ^{II}	1.15(1)	2.55(2)		
2c	Fe ^{III}	0.39(1)	0.80(2)	56	23
	Fe ^{II}	1.16(1)	3.15(2)		

The **2t**:**2c** ratio at completion is found close to 85:15, indicating that while isomer **1c** is favored among the protonated complexes, the isomer **2t** of the deprotonated anilide complex is more stable. The rate of the interconversion between species **2t** and **2c** has also been determined: $k_{2t} = 0.05(2) \text{ min}^{-1}$ and $k_{2c} = 0.25(2) \text{ min}^{-1}$.

At this stage, we may come back to the four hypotheses that were formulated for the nature of the isomer **1c**. What are the consequences of the addition of triethylamine in the framework of hypotheses (i) to (iii)?

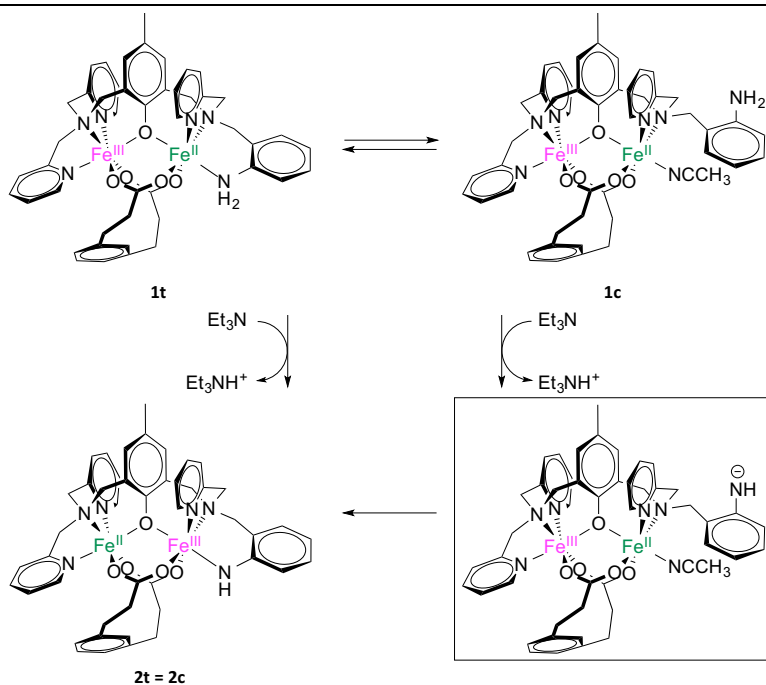
Hypothesis (i):

Scheme 3.3 Interconversion of **1t** to **1c** and the resulting anilide species **2t** and **2c** according to hypothesis (i)

If **1c** is a valence isomer, the aminobenzyl group would be coordinated to the ferric site. Deprotonation would thus lead directly (that is without intramolecular electron transfer) to the anilide ligand coordinated to the Fe^{III} site in *trans* position versus the bridging phenoxide. Isomer **1t** would also lead to the same complex with an intramolecular electron transfer. Hence, a single isomer would result from the deprotonation of the two valence isomers **1t** and **1c** (Scheme 3.3). This contradicts the experimental data.

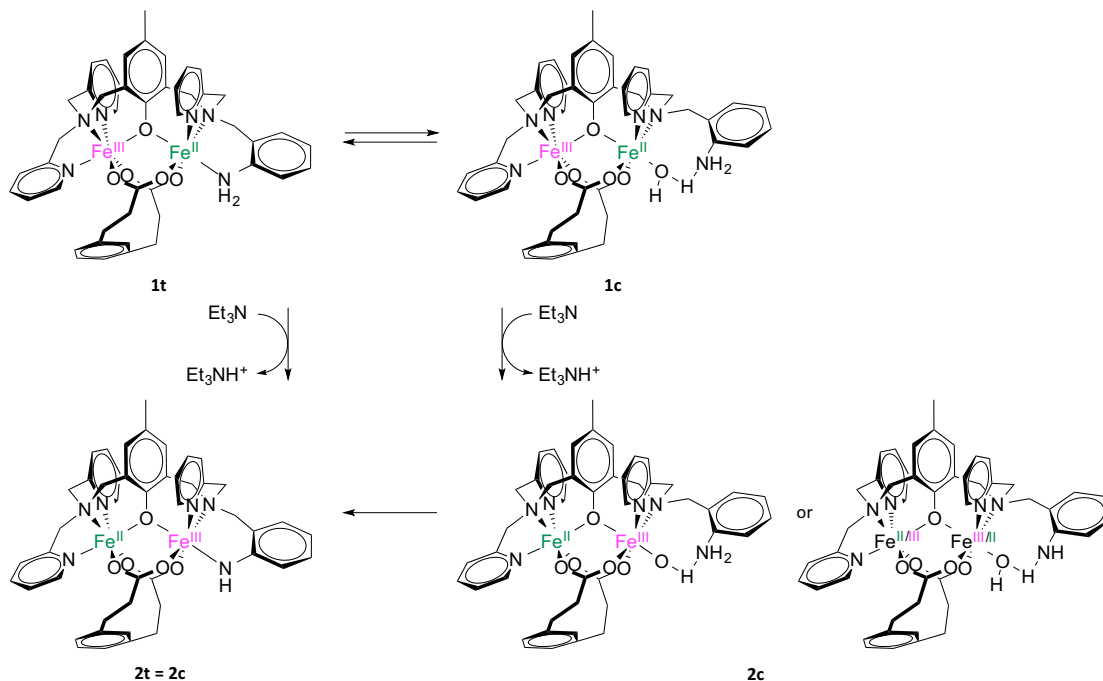
Hypothesis (ii):

1c would present a free aminobenzyl group and an acetonitrile molecule coordinated in *trans* position to the ferrous ion. Deprotonation of **1c** would thus firstly lead to a non coordinated anilide ligand, the acetonitrile molecule remaining coordinated to the Fe^{II} . Such a species wouldn't present an intense charge transfer band in the visible domain (maximum at 700 nm, $\epsilon_{700} = 2175 \text{ M}^{-1} \cdot \text{cm}^{-1}$). So species **2c** that is detected must result from a coordination of the initially free anilide arm. If the reaction is the substitution of the *trans* CH_3CN , the resulting isomer is identical to that generated from **1t**. The "free" anilide arm must then coordinates in *cis* position while the leaving CH_3CN ligand is in *trans* (Scheme 3.4). This seems a too intricate movement within the coordination sphere of the metal. Moreover, this sophisticated dance would precede an isomerization process. This is highly disfavored.



Scheme 3.4. Interconversion of 1t to 1c and the resulting anilide species 2t and 2c according to hypothesis (ii). The framed one with a free anilide arm can't be isolated.

Hypothesis (iii):

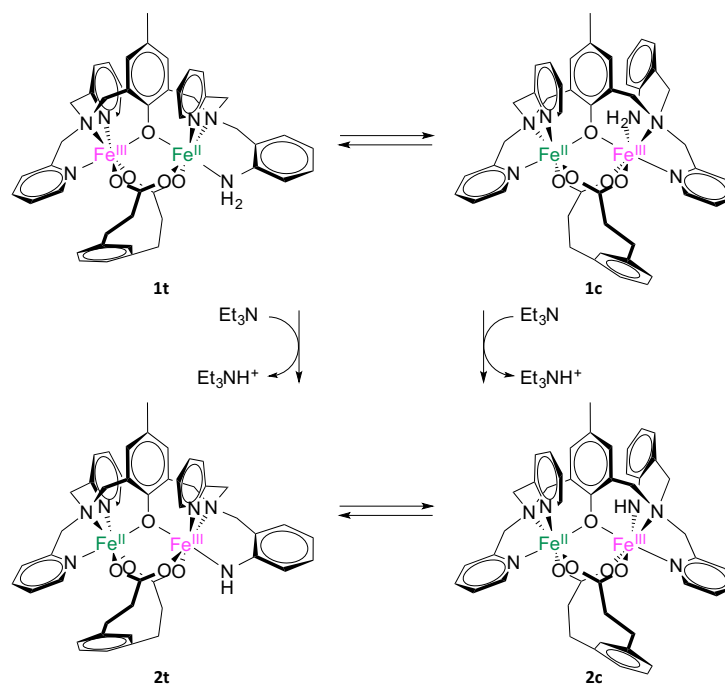


Scheme 3.5. Interconversion of 1t to 1c and the resulting anilide species (2t/2c) according to hypothesis (iii).

1c would present a coordinated water molecule on the ferrous ion in *trans* position to the bridging phenoxide. The water molecule would be in addition H-bonded to the aniline arm. Addition of NEt₃ can thus lead to the deprotonation of either the aminobenzyl group (leading to an anilide H-bonded to the water molecule) or the water molecule (leading to an hydroxide ion H-

bonded with the aminobenzyl arm). Due to the H-bond, the quadrupole splitting of the Fe^{III} ion with a *trans*-hydroxide must be strongly reduced (0.80 mm/s measured for the form **2c** versus 1.51 mm/s in [(L-Bn)Fe^{III}₂(μ₂-mpdp)(OH)]²⁺). It is worth noticing that the 90:10 mixture of [(L-Bn)Fe^{III}₂(μ₂-mpdp)(OH)]²⁺ and [(L-Bn)Fe^{III}₂(μ₂-mpdp)(OH₂)]³⁺ present a band at 598 nm but no evidence of an intense absorption around 700 nm. Consequently, a Fe^{III}-OH⁻-H₂NBn topology is disfavored. If deprotonation leads to a complex with the Fe^{II/III}-OH⁻-HNBn motif, Mössbauer and UV-visible data can hardly be understood. The detected **2c** species must result from a recoordination of the anilide arm while the leaving water molecule is in *trans* position (Scheme 3.5). We are thus facing a problem identical to that met within hypothesis (ii), the water replacing CH₃CN. For identical reasons, we disfavored this hypothesis.

In conclusion, none of the hypotheses (i) to (iii) are able to rationalize the spectroscopic data recorded both on the protonated and the deprotonated species. Only isomerization reactions in both protonated states allow deciphering the collection of experimental features. This can be summarized in Scheme 3.6.



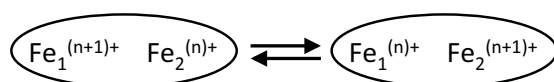
Scheme 3.6. Isomerization reactions proposed for the two complexes [Fe^{III}(μ₂-mpdp)Fe^{II}(H₂NBn-L)]²⁺ (**1t** and **1c**) and [Fe^{II}(μ₂-mpdp)Fe^{III}(HNBn-L)]⁺ (**2t** and **2c**).

It is proposed in the submitted manuscript that the conversions **1t** → **1c** and **2c** → **2t** process through an identical mechanism.

4 Studies of the proton-coupled electron transfer reaction

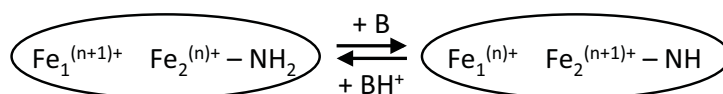
In continuation to the examples shown in the introduction, the mixed valent aniline complex discussed so far provides us a nice base to study the interdependent transfer mechanisms through electrochemistry. The study of these transfer mechanisms plays a vital role in clearly understanding the behavior of the different ligand groups and their effects on the iron ions in the complex.

In the aniline complex, the two metal centers i.e. Fe_1 and Fe_2 are held together by a bridging phenoxide (refer the X-ray structure shown in Figure 2.1 in Section 2)⁽¹⁴⁾. The valence inversion of the iron ions could be summarized as shown in Scheme 4.1.



Scheme 4.1. Inversion of the iron valences.

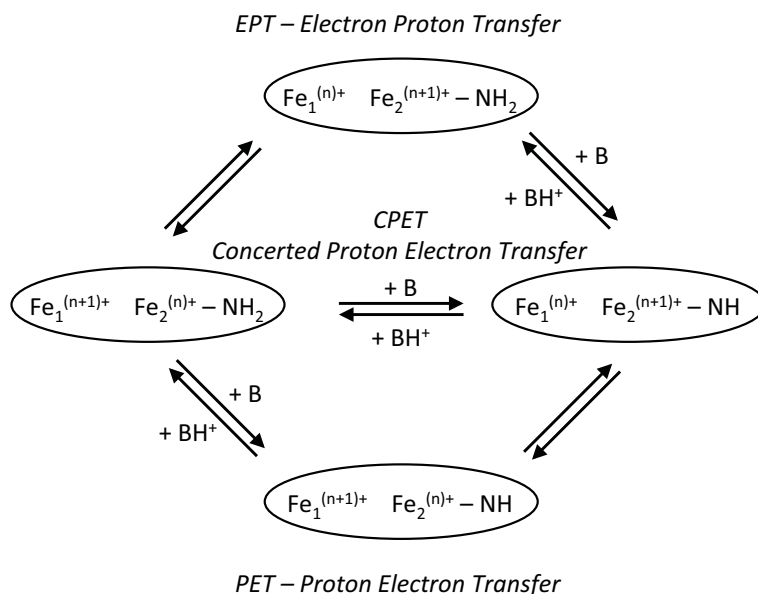
We have shown that a valence inversion occurs upon deprotonation of the aniline complex. Deprotonation of the aniline ligand bound to the Fe^{II} ion leads to the formation of an anilide coordinated to the Fe^{III} ion. A single example in synthetic chemistry of such a valence inversion triggered by a proton transfer on a terminal ligand has been previously demonstrated by Mayer *et al.* in Ru–Os complexes, but no detailed investigations were reported⁽¹⁹⁾. Hemerythrin⁽²⁰⁾, which was briefly presented in the introduction, is the other example of a pH-controlled valence inversion⁽¹⁰⁾. In Scheme 4.2, the external base that serves as an acceptor for the proton delivered by the ligand L-BnNH₂ is denoted “B”.



Scheme 4.2. Iron valence inversion with the aniline (left) and anilide (right) group in the presence of base (B) and its conjugated acid (BH⁺).

The base induces the deprotonation of the protic ligand thereby triggering the valence inversion, in which an electron is transferred from the right-hand side to the left-hand side metal center. The main aim of the work presented here focuses on the analysis of the kinetics studies. This allows distinguishing between the different possible pathways (Scheme 4.3): the stepwise pathways in which (i) the protonation and electron transfer takes place successively (PET pathway), or (ii) the electron transfer is followed by a proton transfer (EPT pathway), and (iii) a

concerted proton – electron transfer (CPET) pathway in which the two events takes place simultaneously.



Scheme 4.3. The two sequential pathways (EPT at the top and PET at the bottom) versus the concerted one (CPET in the middle)

Such mechanism analysis requires the determination of the rate constants of the PCET reaction and this is the first of its kind in which the rate constants aid in establishing the reaction mechanism. This work has been published in *the Journal of American Chemical Society* as a communication entitled “Proton – Coupled Intervalence Charge Transfer: Concerted Processes” *J. Am. Chem. Soc.* **2012**, *134*, 1906-1908. The proof for this transfer mechanism has been obtained by recording and analyzing cyclic voltammetry experiments performed on the aniline complex in acetonitrile (CH₃CN) solution and by measuring the H/D kinetic isotope effect.

The publication is given hereafter (text and Supporting Information). A short discussion follows in order to emphasize the strategy that has been developed.

4.1 Published work

Proton-Coupled Intervalence Charge Transfer: Concerted Processes

Ramachandran Balasubramanian,[†] Geneviève Blondin,[‡] Juan Carlos Canales,[†] Cyrille Costentin,[†] Jean-Marc Latour,[‡] Marc Robert,[†] and Jean-Michel Savéant^{*,†}

[†]Université Paris Diderot, Sorbonne Paris Cité, Laboratoire d'Electrochimie Moléculaire, Unité Mixte de Recherche Université - CNRS 7591, Bâtiment Lavoisier, 15 rue Jean de Baïf, 75205 Paris Cedex 13, France

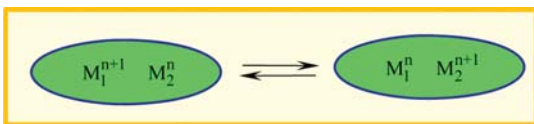
[‡]UJF-Grenoble 1/CEA-DSV-iRTSV/CNRS, Laboratoire de Chimie et Biologie des Métaux-pmb, UMR 5249, Grenoble F-38054, France

S Supporting Information

ABSTRACT: The kinetics of proton-induced intervalence charge transfer (IVCT) may be measured electrochemically by generating one of the members of the IVCT couple in situ and following its conversion by means of the electrochemical signature of the other member of the couple. In the case of the diiron complex taken as an example, the reaction kinetics analysis, including the H/D isotope effect, clearly points to the prevalence of the concerted proton–intervalence charge transfer pathway over the stepwise pathways. A route is thus open toward systematic kinetic studies of proton-induced IVCT aiming at uncovering the main reactivity parameters and the factors that control the occurrence of concerted versus stepwise pathways.

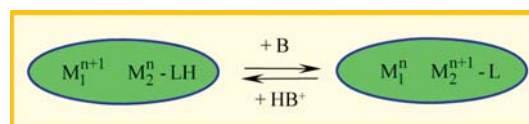
For almost four decades,¹ intervalence charge transfer (IVCT) has attracted continuously renewed experimental and theoretical attention,² being illustrated by organic systems³ and mostly by transition-metal complex systems.^{4–8} In the latter case, these systems involve two metal centers that may be identical or not, although systems comprising more than two metal centers have also been considered. The metal centers are held together by a common ligand and may or may not be connected by a more or less conducting ligand. The various situations are symbolized by the general diagram shown in Scheme 1.

Scheme 1



Electron transfer can be triggered by proton transfer. Examples of such electron transfer have been reported for dinuclear complexes upon deprotonation of a bridging ligand.^{9–11} In addition, such symmetric dinuclear mixed-valent systems may present localized or delocalized valences depending on pH. A single example of IVCT triggered by a proton transfer on a terminal ligand (Scheme 2) has been reported to date.¹² B is an external base that serves as an acceptor for the proton delivered by the protonated ligand LH, thus triggering the IVCT, in which an electron is transferred from the right-

Scheme 2



hand to the left-hand metal center. The reaction in Scheme 2 is thus a typical proton-coupled electron transfer (PCET) process. The system is a bistable construct wherein the passage from one state to the other may be triggered by a change in pH.

PCET reactions are currently under active scrutiny from both experimental and theoretical viewpoints.¹³ Mechanism analysis based on the kinetics of the reaction has mostly focused on the distinction between stepwise pathways in which protonation and electron transfer take place successively [initial proton transfer followed by electron transfer (PET pathway) or vice versa (EPT pathway)] and a concerted proton–electron transfer (CPET) pathway in which the two events take place in concert. The advantage of the CPET pathway over the stepwise pathways is that it avoids going through high-energy intermediates. This is a way of exploiting the driving force advantage offered by the coupling between proton and electron transfers, an advantage that becomes effective if the kinetic price that may have to be paid is not too high. A delineation of the various pathways in the present case of proton-coupled IVCT is summarized in Scheme 3. Such a mechanism analysis requires the determination of the rate constant of the PCET reaction, which has not been the case for the systems in which proton transfer triggers IVCT as reported to date.

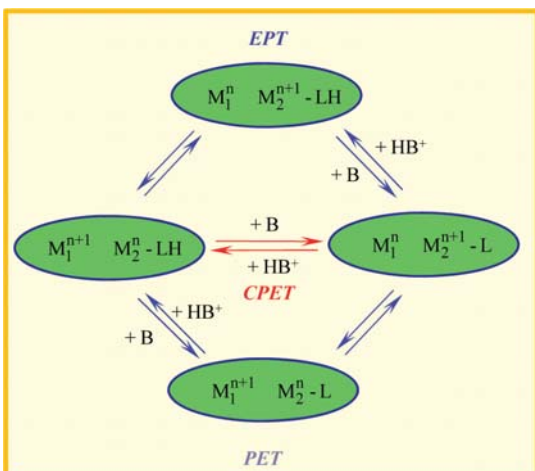
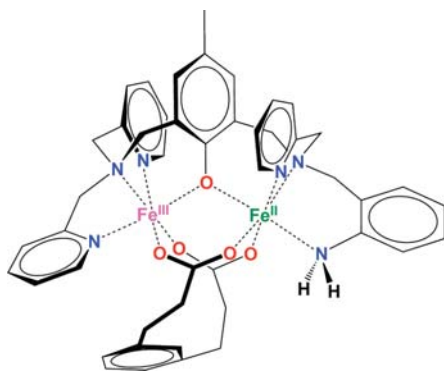
The purpose of the present communication is to describe a method that allows such rate constant determinations to aid in establishing the reaction mechanism. The main thrust in this connection is the distinction between the concerted and stepwise pathways. The method is based on the recording and analysis of the cyclic voltammetric responses of the complexes involved. It is illustrated by the diiron complex depicted in Scheme 4, where, with reference to Schemes 2 and 3, $M_1 = M_2 = \text{Fe}$, $n = \text{II}$, and the ligand L is defined in Scheme 4.¹⁴

The first step of the analysis deals with the description of the thermodynamic framework in the form of a Pourbaix diagram (variation of the apparent standard potentials of the system, E^0 ,

Received: August 10, 2011

Published: January 18, 2012

Scheme 3

Scheme 4. $\text{Fe}^{\text{III}}\text{Fe}^{\text{II}}\text{LH}^{\text{a}}$ 

^aOnly the H atoms at the site where proton transfer occurs are shown.

with pH) as reported in Figure 1, which shows the diagram itself and the various cyclic experiments that allowed its establishment. The four cyclic voltammograms (CVs) allowed the derivation of the four characteristic standard potentials; the most negative one is approximate since the corresponding wave is not reversible. The $\text{p}K$ of $\text{Fe}^{\text{III}}\text{Fe}^{\text{II}}\text{LH}$ was obtained from the variation of its UV-vis spectrum upon addition of NEt_3 (Figure 1f,g) according to the expression

$$\frac{A - A_{n=0}}{A_{n \rightarrow \infty} - A_{n=0}} = \frac{n + 1 - \sqrt{(n + 1)^2 - 4n(1 - K)}}{2(1 - K)}$$

in which n is the number of NEt_3 equivalents and K is related to the $\text{p}K$ of interest as

$$K = 10^{\text{p}K_{\text{Fe}^{\text{III}}\text{Fe}^{\text{II}}\text{LH}} - \text{p}K_{\text{Et}_3\text{NH}^+}}$$

K was thus found to be 0.1, which, in combination with $\text{p}K_{\text{Et}_3\text{NH}^+} = 18.6$,¹⁵ gave $\text{p}K_{\text{Fe}^{\text{III}}\text{Fe}^{\text{II}}\text{LH}} = 17.6$. These E^0 and $\text{p}K$ data allowed the Pourbaix diagram shown in Figure 1 to be drawn, thus leading to $\text{p}K_{\text{Fe}^{\text{III}}\text{Fe}^{\text{II}}\text{LH}} = 9.9$ and $\text{p}K_{\text{Fe}^{\text{III}}\text{Fe}^{\text{II}}\text{LH}} \approx 27.9$ [see the Supporting Information (SI) for details].

Once the thermodynamic scene had been set, we employed the following electrochemical method to determine the rate constants of the proton-coupled IVCT on the basis of the reactions depicted in the scheme shown in Figure 2a. Starting with the initial complex $\text{Fe}^{\text{III}}\text{Fe}^{\text{III}}\text{LH}$ in the presence of a mixture of B (i.e., NEt_3) and its corresponding acid BH^+ , the potential

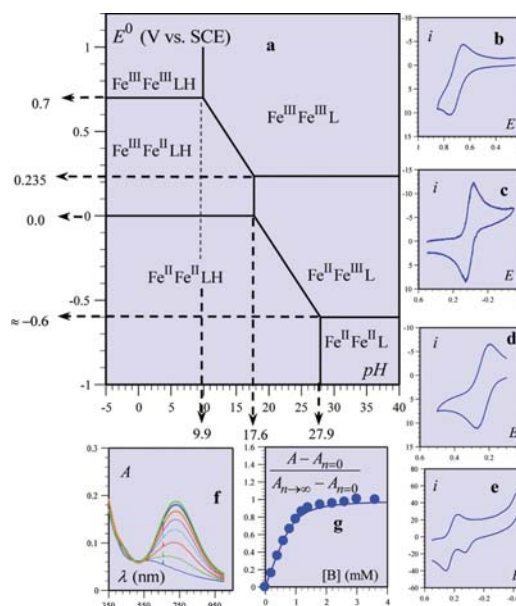


Figure 1. (a) Pourbaix diagram. (b–e) CVs of 0.65 mM $\text{Fe}^{\text{III}}\text{Fe}^{\text{II}}\text{LH}$ complex in $\text{CH}_3\text{CN} + 0.1 \text{ M NBu}_4\text{BF}_4$ on a 3 mm diameter glassy carbon disk electrode at scan rates (ν) of (b–d) 0.1 and (e) 0.5 V/s: (b) oxidation; (c) reduction; (d) oxidation in the presence of 10 equiv of NEt_3 ; (e) reduction in the presence of 10 equiv of NEt_3 . (f) Increase in the UV-vis band of the $\text{Fe}^{\text{III}}\text{Fe}^{\text{III}}\text{L}$ complex upon addition of NEt_3 to $\text{Fe}^{\text{III}}\text{Fe}^{\text{II}}\text{LH}$. (g) Variation of the normalized peak absorbance with the number of NEt_3 equivalents, n .

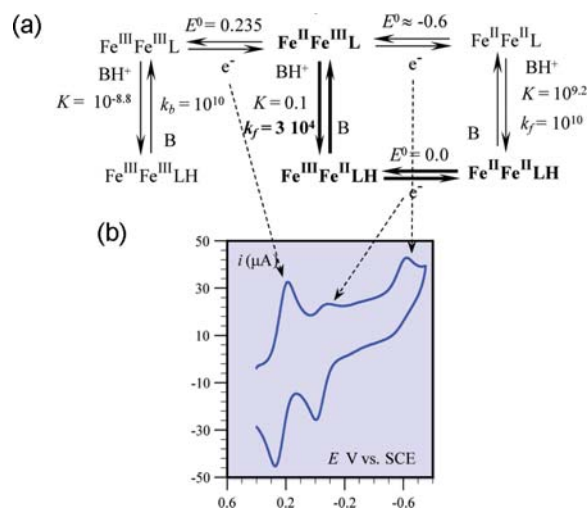


Figure 2. (a) Reaction scheme for determining the rate constants of proton-coupled IVCT. Standard potentials (E^0) are given in V vs SCE and forward (k_f) and backward (k_b) rate constants in $\text{M}^{-1} \text{ s}^{-1}$. K 's are equilibrium constants. (b) CV of 0.65 mM $\text{Fe}^{\text{III}}\text{Fe}^{\text{II}}\text{LH}$ complex in $\text{CH}_3\text{CN} + 0.1 \text{ M NBu}_4\text{BF}_4$ on a 3 mm diameter glassy carbon disk electrode at $\nu = 1 \text{ V/s}$ in the presence of a mixture of NEt_3 (4 mM) and Et_3NH^+ (2 mM) after a pre-electrolysis at 0.4 V to convert the initial complex into $\text{Fe}^{\text{III}}\text{Fe}^{\text{III}}\text{L}$.

of the working electrode was set at 0.4 V vs SCE for an in situ pre-electrolysis (10 s), at the end of which $\text{Fe}^{\text{III}}\text{Fe}^{\text{III}}\text{L}$ was the only complex present in the solution surrounding the electrode, together with a preset mixture of B and BH^+ . At the first cathodic peak (Figure 2b), $\text{Fe}^{\text{III}}\text{Fe}^{\text{III}}\text{L}$ was reduced at ca. 0.235 V to give $\text{Fe}^{\text{II}}\text{Fe}^{\text{III}}\text{L}$, which, thanks to the BH^+ present, was

partly converted into $\text{Fe}^{\text{III}}\text{Fe}^{\text{II}}\text{LH}$ according to the reaction of interest. Addition of BH^+ in these experiments was necessary to ensure that its concentration was constant throughout the diffusion–convection layer. $\text{Fe}^{\text{III}}\text{Fe}^{\text{II}}\text{LH}$ was reduced at ca. 0.0 V, whereas the remainder of $\text{Fe}^{\text{II}}\text{Fe}^{\text{III}}\text{L}$ was reduced at a much more negative potential (ca. -0.6 V). The second wave on the voltammogram involved a typical chemical reaction preceding electron transfer (CE) process¹⁶ (bold arrows and symbols in Figure 2a) in which the electroactive species, $\text{Fe}^{\text{III}}\text{Fe}^{\text{II}}\text{LH}$, was reduced at the electrode and continuously regenerated by the transformation of $\text{Fe}^{\text{II}}\text{Fe}^{\text{III}}\text{L}$ with an efficiency that depended on the scan rate (ν). The second wave decreased with increasing NEt_3 concentration at a given ν (Figure 3a) and with increasing

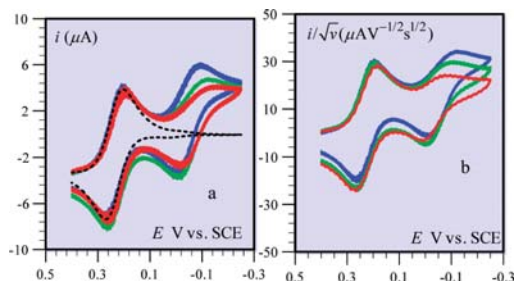


Figure 3. CVs of 0.65 mM $\text{Fe}^{\text{III}}\text{Fe}^{\text{II}}\text{LH}$ complex after a 10 s pre-electrolysis at 0.4 V in the presence of 2 mM Et_3NH^+ . (a) Variation with the NEt_3 concentration at $\nu = 0.05$ V/s: 4 mM (blue); 8 mM (green); 12 mM (red). Dotted line: simulation of the first wave. (b) Variation with ν at $[\text{NEt}_3] = 8$ mM: 0.05 V/s (blue); 0.2 V/s (green); 1 V/s (red). The current at the starting potential was set to zero for the sake of an easier comparison.

ν at a given NEt_3 concentration (Figure 3b), as expected for a CE mechanism.¹⁶ The third wave was consistently observed to vary in the opposite manner.

With knowledge of the equilibrium constant of the reaction (see the above thermodynamic analysis), the second wave of the voltammograms could be simulated^{17,18} according to the CE mechanism (bold arrows and symbols in Figure 2a) and compared to the experimental data after subtraction of the current due to the first wave, corresponding to $\text{Fe}^{\text{III}}\text{Fe}^{\text{III}}\text{L}$ reduction (its simulation is represented as a dashed line in Figure 3a). The rate constant of the PCET reaction for conversion of $\text{Fe}^{\text{II}}\text{Fe}^{\text{III}}\text{L}$ into $\text{Fe}^{\text{III}}\text{Fe}^{\text{II}}\text{LH}$ was found to be $\log(k_f) = 4.5 \pm 0.1$. Examples of simulations are given in Figure 4 (other simulations and details are available in the SI).

The results gathered to this point are compatible with the CPET pathway but also with the two stepwise pathways, PET and EPT, as shown in Schemes 3 and 5. To discriminate between these mechanisms, the same experiments were repeated with another base, pyrrolidine ($\text{p}K = 19.6$)^{15b} (see the SI), which gave $\log(k_f) = 4.0 \pm 0.1$. Relating the decrease in the rate constant to the 1 pK unit decrease of the driving force entails a value of the symmetry factor $\alpha = (\text{d} \log k_f / \text{d} \log K) \approx 0.5 \pm 0.05$.¹⁹ This value is compatible with the CPET mechanism insofar it is characterized by a quadratic activation driving force law,²⁰ which can be linearized over the small range of driving forces considered here. Such a value of the symmetry factor is not compatible with either of the two stepwise pathways for the following reasons. With simple amines such as those used here, the rate constants of the protonation and deprotonation reactions are expected to be at the diffusion limit in the thermodynamically favorable direction,²¹ as sketched in

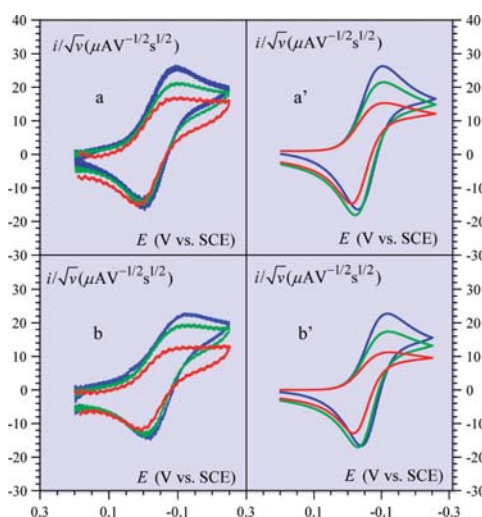
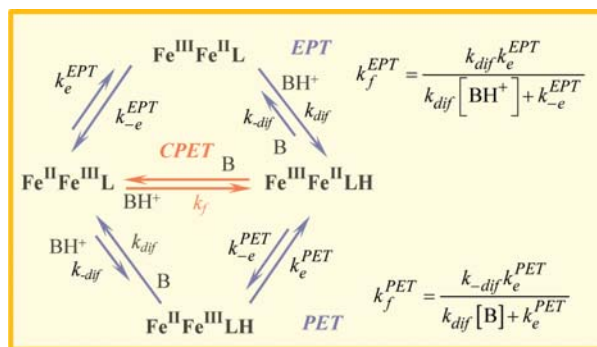


Figure 4. CVs of 0.65 mM $\text{Fe}^{\text{III}}\text{Fe}^{\text{II}}\text{LH}$ complex under the same conditions as in Figure 3 after subtraction of the simulated first wave. ν (V/s): 0.05 (blue) 0.2 (green) 1 (red). $[\text{Et}_3\text{NH}^+] = 2$ mM. (a, a') $[\text{NEt}_3] = 4$ mM; (b, b') $[\text{NEt}_3] = 8$ mM. (a, b) experimental; (a', b') simulated (see the text).

Scheme 5



Scheme 5. The resulting expressions for k_f for the two stepwise mechanisms are given in Scheme 5. It is seen that α is predicted to be 1 for the PET pathway and 0 for the EPT pathway, thus ruling out these two possibilities.^{19b}

If the reaction does follow the CPET pathway, an H/D kinetic isotope effect (KIE) would be expected. That this is indeed the case is shown in Figure 5, where experiments with NEt_3 as a base performed in the presence of 1% MeOH were repeated in the presence of 1% MeOD. It is a purely kinetic effect because the equilibrium constant K had the same value in the presence of either 1% MeOH or 1% MeOD, as checked by UV–vis experiments (see the SI). A quantitative estimation of the effect (KIE = 2 ± 0.2)²² was obtained by means of simulations (see the SI). A clear confirmation that the proton-coupled IVCT reaction follows the concerted pathway is thus provided.^{22b} No significant KIE would be expected with the stepwise pathways since, as already noted, the rate constants of the protonation and deprotonation reactions would be at the diffusion limit in the thermodynamically favorable direction.

In summary, we have shown that the kinetics of proton-induced IVCT may be measured electrochemically by generating one of the members of the IVCT couple in situ and following its conversion by means of the electrochemical signature of the other member of the couple.

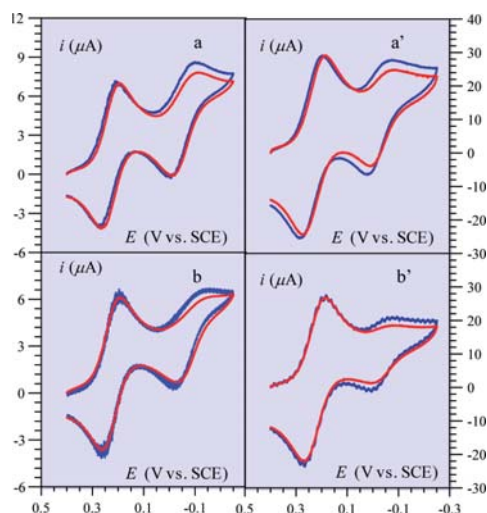


Figure 5. CVs of 0.65 mM $\text{Fe}^{\text{III}}/\text{Fe}^{\text{II}}\text{LH}$ complex under the same conditions as in Figure 3 in the presence of 1% MeOH (blue) or 1% MeOD (red). $[\text{Et}_3\text{NH}^+] = 2$ mM. (a, a') $[\text{NEt}_3] = 4$ mM; (b, b') $[\text{NEt}_3] = 12$ mM. (a, b) $\nu = 0.05$ V/s; (a', b') $\nu = 1$ V/s.

In the case of the diiron complex used as an example in the present study, application of the method to the determination of the H/D isotope effect and variation of the rate constant with the driving force clearly points to the prevalence of the concerted proton–intervalence charge transfer pathway over the stepwise pathways.

A route is thus open toward a systematic kinetic study of proton-induced IVCT aimed at uncovering the main reactivity parameters and the factors that control the occurrence of concerted versus stepwise pathways. Work is in progress to investigate the dependence of the CPET intervalence kinetics upon temperature in order to evaluate reorganization and proton tunneling factors.

■ ASSOCIATED CONTENT

● Supporting Information

Experimental details and additional simulations. This material is available free of charge via the Internet at <http://pubs.acs.org>.

■ AUTHOR INFORMATION

Corresponding Author

saveant@univ-paris-diderot.fr

■ ACKNOWLEDGMENTS

Partial financial support from the Agence Nationale de la Recherche (ANR 2010 BLAN 703) is gratefully acknowledged.

■ REFERENCES

- (1) Creutz, C.; Taube, H. *J. Am. Chem. Soc.* **1973**, *95*, 1086.
- (2) Reimers, J. R.; Wallace, B. B. *Philos. Trans. R. Soc. London, Ser. A* **2008**, *366*, 15.
- (3) Nelsen, S. F. *Adv. Phys. Org. Chem.* **2006**, *41*, 183.
- (4) Ceccon, A.; Santi, S.; Orian, L.; Bisello, A. *Coord. Chem. Rev.* **2004**, *248*, 683.
- (5) Evangelio, E.; Ruiz-Molina, D. *Eur. J. Inorg. Chem.* **2005**, 2957.
- (6) (a) D'Alessandro, D. M.; Keene, F. R. *Chem. Rev.* **2006**, *106*, 2270. (b) D'Alessandro, D. M.; Keene, F. R. *Chem. Soc. Rev.* **2006**, *35*, 424.
- (7) Kaim, W.; Sarkar, B. *Coord. Chem. Rev.* **2007**, *251*, 584.
- (8) Aguirre-Etcheverry, P.; O'Hare, D. *Chem. Rev.* **2010**, *110*, 4839.

(9) (a) Haga, M. A.; Ano, T.; Kano, K.; Yamabe, S. *Inorg. Chem.* **1991**, *30*, 3843. (b) Haga, M. A.; Ali, M. M.; Koseki, S.; Fujimoto, K.; Yoshimura, A.; Nozaki, K.; Ohno, T.; Nakajima, K.; Stufkens, D. J. *Inorg. Chem.* **1996**, *35*, 3335.

(10) Rocha, R. C.; Toma, H. E. *Inorg. Chem. Commun.* **2001**, *4*, 230.

(11) Baitalik, S.; Dutta, S.; Biswas, P.; Florke, U.; Bothe, E.; Nag, K. *Eur. J. Inorg. Chem.* **2010**, 570.

(12) Neyhart, G. A.; Meyer, T. J. *Inorg. Chem.* **1986**, *25*, 4807.

(13) *Chemical Reviews* special issue on PCET: *Chem. Rev.* **2010**, *110*, issue 12.

(14) The synthesis and characteristics of the complex (including an X-ray crystal structure) as well as the demonstration that it undergoes IVCT upon deprotonation are the subject of a separate publication: Gouré, E.; Thiabaud, G.; Carboni, M.; Gon, N.; Dubourdeaux, P.; Garcia-Serres, R.; Clémancey, M.; Oddou, J.-L.; Robin, A. Y.; Jacquamet, L.; Dubois, L.; Blondin, G.; Latour, J.-M. *Inorg. Chem.* **2011**, *50*, 6408.

(15) (a) Two values of $\text{p}K_{\text{Et}_3\text{NH}^+}$ are given in ref 15b: 18.7 and 18.5. We therefore used the value 18.6 ± 0.1 , giving $\text{p}K_{\text{Fe}^{\text{III}}/\text{Fe}^{\text{II}}\text{LH}} = 17.6 \pm 0.1$.

(b) Izutsu, K. *Acid–Base Dissociation Constants in Dipolar Aprotic Solvents*; Blackwell: Boston, 1990; pp 17–35.

(16) Savéant, J.-M. *Elements of Molecular and Biomolecular Electrochemistry: An Electrochemical Approach to Electron Transfer Chemistry*; Wiley: Hoboken, NJ, 2006; Chapter 2.

(17) Using the Digielch software: Rudolph, M. J. *Electroanal. Chem.* **2003**, *543*, 23.

(18) The protonation reactions in the fully oxidized and fully reduced states are thermodynamically very unfavorable and very favorable, respectively. Their rate constants were consequently considered to be at the diffusion limit in the favorable direction. The standard rate constant for the first electrode reaction ($\text{Fe}^{\text{III}}\text{Fe}^{\text{III}}\text{L}/\text{Fe}^{\text{II}}\text{Fe}^{\text{III}}\text{L}$) was taken as equal to 0.1 cm/s to take into account the slight electrochemical irreversibility of the corresponding wave; the value for the second electrode reaction ($\text{Fe}^{\text{III}}\text{Fe}^{\text{II}}\text{LH}/\text{Fe}^{\text{II}}\text{Fe}^{\text{II}}\text{LH}$) was taken at 1 cm/s. The solution electron transfer reaction, $\text{Fe}^{\text{III}}\text{Fe}^{\text{II}}\text{LH} + \text{Fe}^{\text{II}}\text{Fe}^{\text{III}}\text{L} \rightleftharpoons \text{Fe}^{\text{III}}\text{Fe}^{\text{III}}\text{L} + \text{Fe}^{\text{II}}\text{Fe}^{\text{II}}\text{LH}$, has little effect; its rate constant was considered to be at the diffusion limit in the favorable direction. The diffusion coefficients were taken as equal to 10^{-5} for all of complexes and $5 \times 10^{-5} \text{ cm}^2 \text{ s}^{-1}$ for NEt_3 and Et_3NH^+ . Finite diffusion with a convection layer of 0.01 cm was employed to take into account natural convection in order to get a correct description of the pre-electrolysis procedure.

(19) (a) A larger variation of the driving force could not be achieved because the use of a stronger base led to a CE current that was too small to be measured reliably. (b) In spite of the modest variation of the driving force that could be achieved, the value of α is clearly not compatible with the stepwise pathways.

(20) (a) The quadratic models developed for homogeneous^{20b} and electrochemical^{20c} CPET reactions may be extended to the present intervalence CPET reaction. (b) Hammes-Schiffer, S.; Stuchebrukhov, A. I. *Chem. Rev.* **2010**, *110*, 6939. (c) Costentin, C.; Robert, M.; Savéant, J.-M. *Acc. Chem. Res.* **2010**, *43*, 1019.

(21) *Proton Transfer Reactions*; Caldin, E., Gold, V., Eds.; Wiley: New York, 1975.

(22) (a) Although the accuracy of the determination of k_f was 20%, performing the 1% MeOH and 1% MeOD experiments consecutively resulted in better precision, leading to an absolute error of ± 0.2 in the H/D KIE. (b) A value of 2 is commonly found for the H/D KIE in electrochemical CPET reactions.^{20c}

Supporting Information

Proton-Coupled Intervalence Charge Transfer. Concerted Processes.

Ramachandran Balasubramanian, Geneviève Blondin, Juan Carlos Canales, Cyrille Costentin, Jean-Marc Latour, Marc Robert and Jean-Michel Savéant

Table of Content.

1. Experimental Details
2. Construction of the Pourbaix diagram
3. Data with pyrrolidine as a base
4. Additional data for KIE
5. Determination of the equilibrium constant K in deuterated medium:
6. Simulations

1. Experimental Details

Chemicals. Acetonitrile (Fluka, > 99.5 %, stored on molecular sieves), the supporting electrolyte NBU_4PF_6 (Fluka, puriss.), NEt_3 (Prolabo, HPLC grade), HNEt_3Cl (Aldrich, 98%), pyrrolidine (Aldrich, 99%), HClO_4 (Prolabo, Normapur), methanol and CD_3OD (Eurisco-top, 100%) were used as received.

Cyclic voltammetry. The working electrode was a 3-mm diameter glassy carbon (GC) electrode disk (Tokai) carefully polished and ultrasonically rinsed in absolute ethanol before use. The counter-electrode was a platinum wire and the reference electrode an aqueous SCE electrode. All experiments were carried out under argon at 23°C , the double-wall jacketed cell being thermostated by circulation of water. Cyclic voltammograms were obtained by use of a Metrohm AUTOLAB instrument.

UV-vis. Spectra were recorded on a Specord S600 spectrophotometer (Analytik Jena) at room temperature with a 0.5 cm quartz cuvette.

2. Construction of the Pourbaix diagram (fig 1S):

CV recorded in absence of base allows the determination of the $\text{Fe}^{\text{III}}\text{Fe}^{\text{III}}\text{LH}/\text{Fe}^{\text{III}}\text{Fe}^{\text{II}}\text{LH}$ and $\text{Fe}^{\text{III}}\text{Fe}^{\text{II}}\text{LH}/\text{Fe}^{\text{II}}\text{Fe}^{\text{II}}\text{LH}$ standard potential thus giving rise to horizontal lines **1** and **2** in the Pourbaix diagram.

CV recorded in large excess of base (NEt_3) allows the determination of the $\text{Fe}^{\text{III}}\text{Fe}^{\text{III}}\text{L}/\text{Fe}^{\text{II}}\text{Fe}^{\text{III}}\text{L}$ and estimation of the $\text{Fe}^{\text{II}}\text{Fe}^{\text{III}}\text{L}/\text{Fe}^{\text{II}}\text{Fe}^{\text{II}}\text{L}$ standard potential thus giving rise to horizontal lines **3** and **4** in the Pourbaix diagram.

UV-vis determination of the pK_a of the $\text{Fe}^{\text{III}}\text{Fe}^{\text{II}}\text{LH}/\text{Fe}^{\text{II}}\text{Fe}^{\text{III}}\text{L}$ gives rise to the vertical line **5** joining lines 2 and 3.

Diagonal lines **6** and **7** joining lines **1** and **3** and **2** and **4** respectively corresponds to $1 e^- - 1 H^+$ processes thus corresponding to a $RT/F \ln(10)$ slope. Drawing those lines from **2-5** and **3-5** corners allows the determination of both $pK_{\text{Fe}^{\text{III}}\text{Fe}^{\text{III}}\text{LH}} = 9.9$ and $pK_{\text{Fe}^{\text{II}}\text{Fe}^{\text{II}}\text{LH}} = 27.9$.

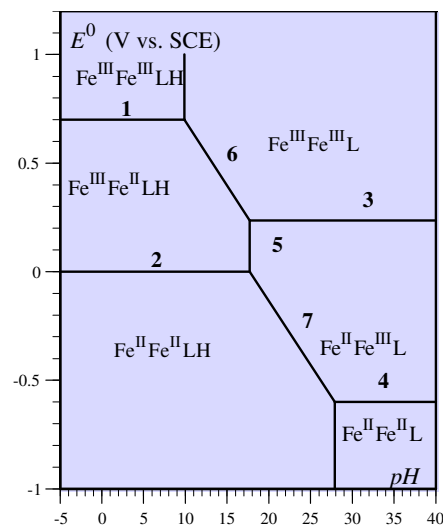


Fig. 1S. Pourbaix diagram.

3. Data with pyrrolidine as a base:

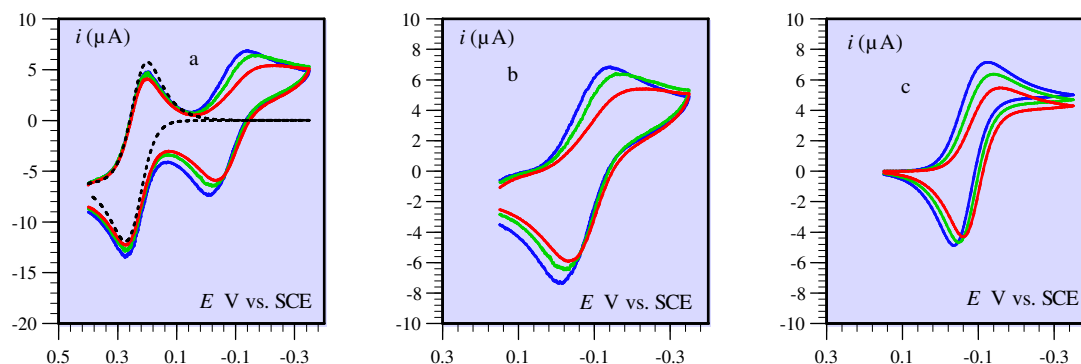


Fig. 2S. Cyclic voltammetry of 1 mM $\text{Fe}^{\text{III}}\text{Fe}^{\text{II}}\text{LH}$ complex after a 10 s pre-electrolysis at 0.4 V in presence of 2 mM ^+HB (B = pyrrolidine; ^+HB is obtained by mixing HClO_4 and an equal amount of B). $v = 0.05 \text{ V/s}$. a: experiments (except dotted black line: first wave simulation), b: second wave after subtraction of the first wave. c: simulation with $k_f = 10^4 \text{ M}^{-1}\text{s}^{-1}$. Blue: $[\text{B}] = 2 \text{ mM}$; Green: $[\text{B}] = 3 \text{ mM}$; Red: $[\text{B}] = 5 \text{ mM}$.

2S

4. Additional data for KIE :

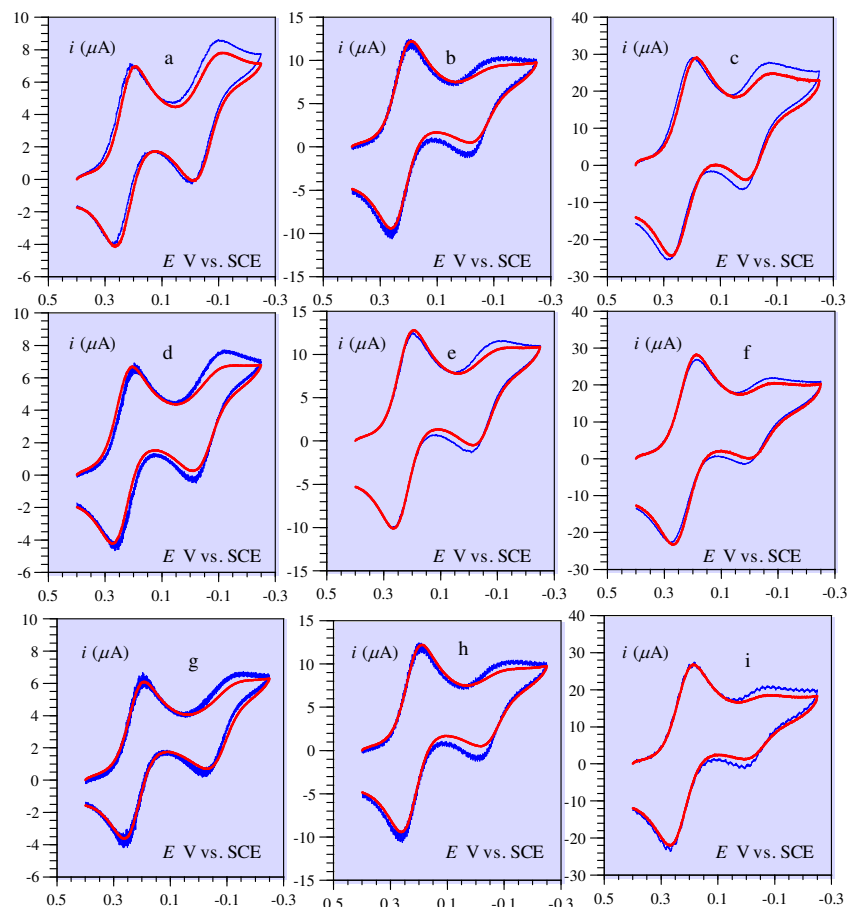


Fig. 3S. Cyclic voltammetry of 0.65 mM $\text{Fe}^{\text{III}}\text{Fe}^{\text{II}}\text{LH}$ complex after a 10 s pre-electrolysis at 0.4 V in presence of 2 mM $^+\text{HNEt}_3$. Blue: in presence of 1% MeOH. Red: in presence of 1% MeOD. a, b, c: $[\text{NET}_3] = 4$ mM; d, e, f: $[\text{NET}_3] = 8$ mM; g, h, i: $[\text{NET}_3] = 12$ mM. a, d, g: $v = 0.05$ V/s. b, e, h: $v = 0.2$ V/s. c, f, i: $v = 1$ V/s. Current at the starting potential was set to zero for the sake of an easier comparison.

5. Determination of the equilibrium constant K in deuterated medium:

The constant K in deuterated medium is obtained from the variation of its UV-Vis spectrum upon addition of NEt_3 (figure 4S) in presence of 1% MeOD using the following equation:
$$\frac{A - A_{n=0}}{A_{n \rightarrow \infty} - A_{n=0}} = \left[n + 1 - \sqrt{(n+1)^2 - 4n(1-K)} \right] / [2(1-K)]$$

where n is the number of triethylamine equivalents. K is found equal to 0.1 as in the case of hydrogenated medium.

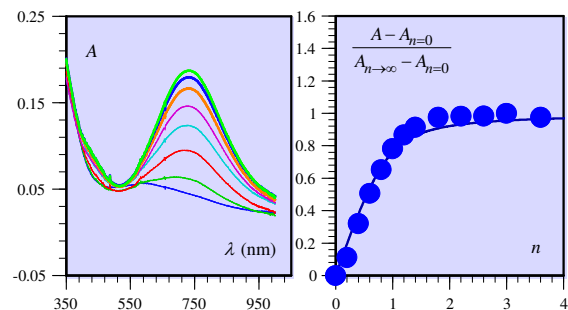
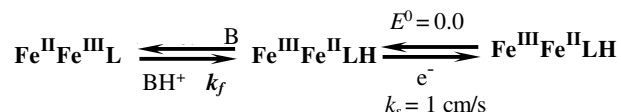


Fig 4S. left: Increase of the UV-Vis band of the $\text{Fe}^{\text{II}}\text{Fe}^{\text{III}}\text{L}$ complex upon addition of NEt_3 in presence of 1% MeOD. Right: variation of the normalized peak absorbance with the number of NEt_3 equivalents, n .

6. Simulations

The second waves of the voltammograms shown in figures 3, 2S and 5S have been simulated according to the CE mechanism depicted in the scheme below. The rate constant k_f was used as the only adjustable variable in the simulation. Initial concentrations of the various species were calculated according to the introduced concentrations of complex and the equilibrium constant. The diffusion coefficients were taken as equal $10^{-5} \text{ cm}^2\text{s}^{-1}$ and $5 \times 10^{-5} \text{ cm}^2\text{s}^{-1}$ for of all complexes on the one hand and B and ^+HB on the other. Finite diffusion with a convection layer of 0.01 cm was considered to take into account natural convection in order to get a correct description of the pre-electrolysis procedure (finite diffusion procedure is an option available in Digilch CV-properties).



Below, simulations are compared to experimental data (figure 5S) and k_f were estimated for both hydrogenated and deuterated media. The second waves observed in figures 3, 2S and 5S are extracted from the whole voltammograms through subtraction of the simulated first wave. Simulation of this first wave was obtained from the reaction shown below starting with $\text{Fe}^{\text{II}}\text{Fe}^{\text{III}}\text{L}$ species. The diffusion coefficients were taken as equal $10^{-5} \text{ cm}^2\text{s}^{-1}$. Finite diffusion with a convection layer of 0.01 cm was considered to take into account natural convection. Simulation of the 10 seconds pre-electrolysis at 0.4 V was obtained by performing a first scan (at 0.01 V/s) between 0.5 V and 0.4 V. Simulation fits well with the experimental first wave (see figure 3a).

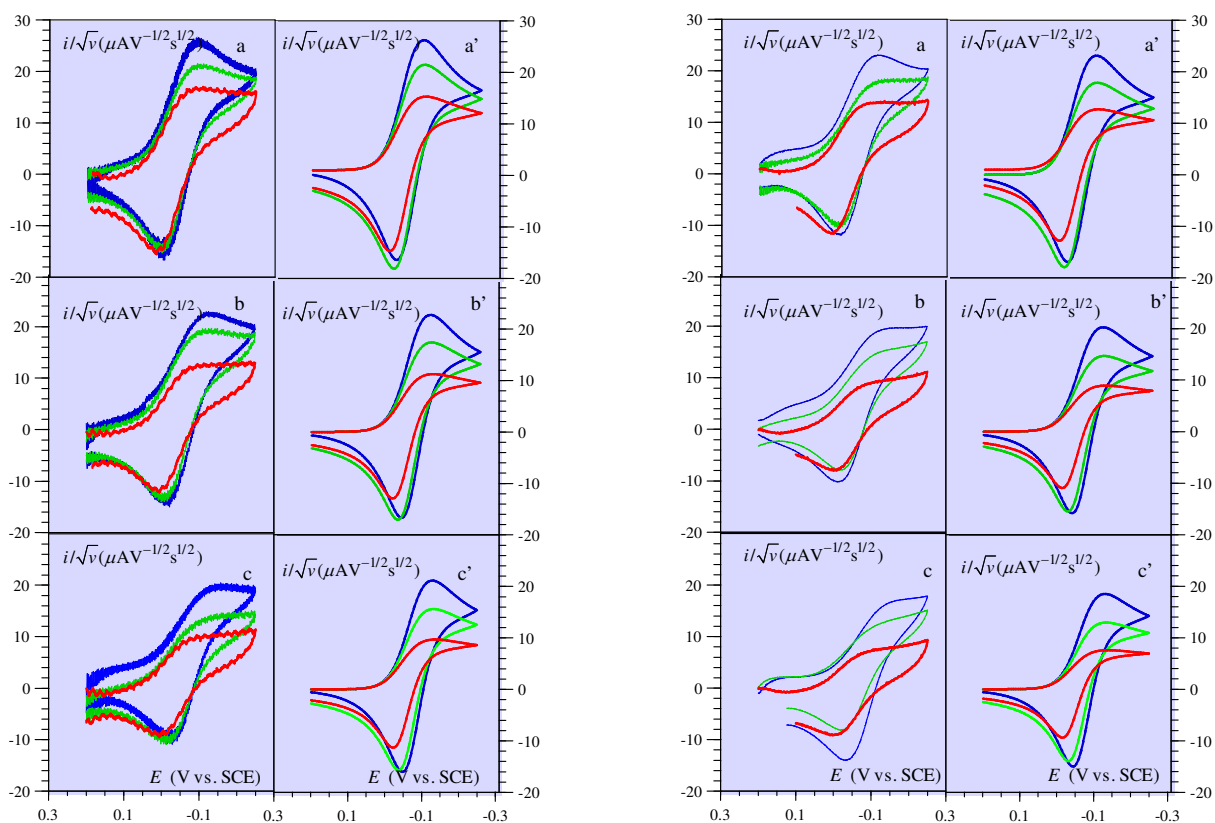
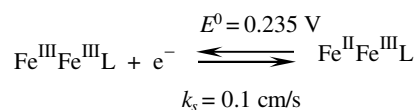
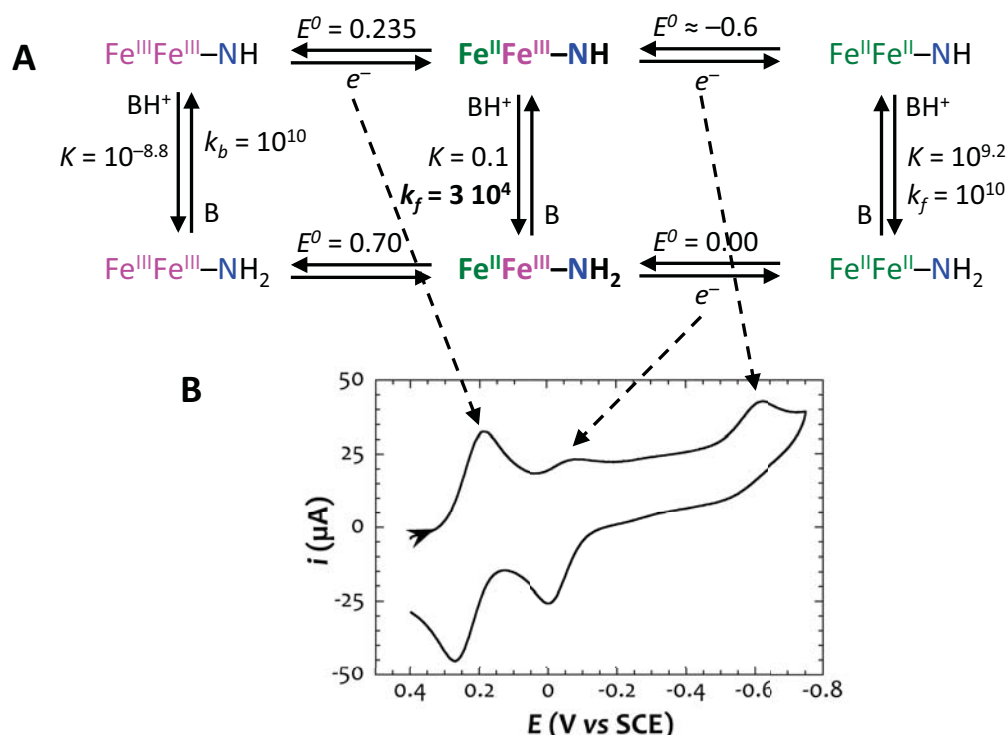


Fig. 5S. Cyclic voltammetry of 0.65 mM $\text{Fe}^{\text{III}}\text{Fe}^{\text{II}}\text{LH}$ complex in the same conditions as in figure 3 after subtraction of the simulated first wave. Left: in the presence of 1% MeOH; right: in the presence of 1% MeOD. Scan rates (V/s): 0.05 (blue) 0.2 (green) 1 (red). $[\text{HNEt}_3]=2 \text{ mM}$. a, a': $[\text{NEt}_3] = 4 \text{ mM}$, b, b': $[\text{NEt}_3] = 8 \text{ mM}$. b, b': $[\text{NEt}_3] = 12 \text{ mM}$. a, b, c: experimental, a', b', c': simulated: left: $k_f = 3 \cdot 10^4 \text{ M}^{-1}\text{s}^{-1}$. Right: $k_f = 1.5 \cdot 10^4 \text{ M}^{-1}\text{s}^{-1}$.

4.2 Strategy developed

A strategy has been developed by the group of Pr. Cyrille Costentin in the Laboratoire d'Electrochimie Moléculaire in University Paris-Diderot (Paris 7) to measure electrochemically the kinetics of the proton-induced intervalence charge transfer by generating one of the mixed valent complex in situ, namely the deprotonated species $[\text{Fe}^{\text{II}}(\mu_2\text{-mpdp})\text{Fe}^{\text{III}}(\text{HNBn-L})]^+$, and following the electrochemical signature of the other mixed valent species, namely the protonated form $[\text{Fe}^{\text{III}}(\mu_2\text{-mpdp})\text{Fe}^{\text{II}}(\text{H}_2\text{NBn-L})]^{2+}$.

Let us first list the different complexes that can be generated in solution. Obviously, the two mixed valent forms that will be further denoted $\text{Fe}^{\text{III}}\text{Fe}^{\text{II}}\text{-NH}_2$ and $\text{Fe}^{\text{II}}\text{Fe}^{\text{III}}\text{-NH}$. Preliminary studies by cyclic voltammetry have evidenced that $\text{Fe}^{\text{III}}\text{Fe}^{\text{II}}\text{-NH}_2$ can be reversibly oxidized in the bisferric complex $\text{Fe}^{\text{III}}\text{Fe}^{\text{III}}\text{-NH}_2$ at 0.70 V vs SCE and reversibly reduced in the bisferrous complex $\text{Fe}^{\text{II}}\text{Fe}^{\text{II}}\text{-NH}_2$ at 0.0 V vs SCE. Similar experiments performed on the deprotonated mixed valent complex $\text{Fe}^{\text{II}}\text{Fe}^{\text{III}}\text{-NH}$ show a reversible oxidation wave at 0.24 V vs SCE and an irreversible reduction process at -0.60 V vs SCE. These data are summarized in Scheme 4.4.

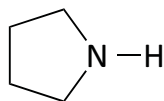


Scheme 4.4. (A) Reaction scheme for determining the rate constants of proton-coupled IVCT. Standard potentials (E^0) are given in V vs SCE. Values for the equilibrium constants K as for forward (k_f) and backward (k_b) rate constants (in $\text{M}^{-1} \text{s}^{-1}$) are given when the BH^+/B couple is $\text{Et}_3\text{NH}^+/\text{NEt}_3$. (B) CV of 0.65 mM $\text{Fe}^{\text{III}}\text{Fe}^{\text{II}}\text{NH}_2$ complex in CH_3CN + 0.1 mM NBu_4BF_4 on a 3 mm diameter glassy carbon disk electrode at $\nu = 1$ V/s in the presence of a mixture of NEt_3 (4 mM) and Et_3NH^+ (2 mM) after a pre-electrolysis at 0.4 V to convert the initial complex into $\text{Fe}^{\text{III}}\text{Fe}^{\text{III}}\text{NH}$.

The cyclic voltammogram experiments were conducted on a solution where the $[\text{Fe}^{\text{III}}\text{Fe}^{\text{II}}-\text{NH}_2](\text{ClO}_4)_2$ powder is dissolved in the presence of NEt_3 and its corresponding acid Et_3NH^+ , so that the two mixed valent species are formed. Performing a pre-electrolysis at 0.40 V vs SCE leads to the formation of the bis-ferric $\text{Fe}^{\text{III}}\text{Fe}^{\text{III}}-\text{NH}$ complex. According to the value indicated in Scheme 4.4A, it is indeed the only diiron species present in the solution surrounding the electrode along with the base NEt_3 and the conjugated acid Et_3NH^+ . The CV scanning was performed toward reduction which is denoted by an arrow in the Scheme 4.4B. The first cathodic peak at 0.24 V corresponds to the reduction of $\text{Fe}^{\text{III}}\text{Fe}^{\text{III}}-\text{NH}$ into $\text{Fe}^{\text{II}}\text{Fe}^{\text{III}}-\text{NH}$ that further partly gets converted into $\text{Fe}^{\text{III}}\text{Fe}^{\text{II}}-\text{NH}_2$ in the presence of Et_3NH^+ . It is important to note that the two mixed valent complex $\text{Fe}^{\text{II}}\text{Fe}^{\text{III}}-\text{NH}$ and $\text{Fe}^{\text{III}}\text{Fe}^{\text{II}}-\text{NH}_2$ are coexisting in the immediate surrounding of the working electrode, their relative proportions being dictated by the equilibrium constant $K = 0.1$ (the deprotonated form is the major species). The mixed valent aniline species $\text{Fe}^{\text{III}}\text{Fe}^{\text{II}}-\text{NH}_2$ is reduced at 0.0 V as observed in the CV. The remaining mixed valent anilide species is reduced at a much more negative potential (-0.60 V). In this reaction scheme, the point of interest focuses on the conversion of $\text{Fe}^{\text{II}}\text{Fe}^{\text{III}}-\text{NH}$ into $\text{Fe}^{\text{III}}\text{Fe}^{\text{II}}-\text{NH}_2$. The electroactive species $\text{Fe}^{\text{III}}\text{Fe}^{\text{II}}-\text{NH}_2$ while it is getting reduced at 0.0 V, is constantly regenerated by the protonation of $\text{Fe}^{\text{II}}\text{Fe}^{\text{III}}-\text{NH}$. Indeed, while between 0.24 and 0.0 V, there is an equilibrium between the two mixed valent species $\text{Fe}^{\text{II}}\text{Fe}^{\text{III}}-\text{NH}$ and $\text{Fe}^{\text{III}}\text{Fe}^{\text{II}}-\text{NH}_2$, the reduction of the protonated form disrupts this equilibrium. Consequently, to recover the equilibrium, the $\text{Fe}^{\text{II}}\text{Fe}^{\text{III}}-\text{NH}$ complex gets protonated and more $\text{Fe}^{\text{III}}\text{Fe}^{\text{II}}-\text{NH}_2$ is thus generated at the working electrode. The effect of this transformation can be evidenced by the behavior of the second reduction wave at 0.0 V, which follows a CE mechanism. The intensity of the second wave decreases when increasing either the scan rate (ν) or the NEt_3 concentration. These variations disfavor the formation of the protonated mixed valent form $\text{Fe}^{\text{III}}\text{Fe}^{\text{II}}-\text{NH}_2$ that gets reduced at 0.0 V. After subtraction of the first wave contribution, the second wave could be satisfyingly simulated with the help of Digielch software⁽²¹⁾ (see Supporting Information of Section 4.1). The simulations of the CVs recorded at different scan rates and NEt_3 concentration lead to the determination of the rate constant of the PCET reaction corresponding to the conversion of $\text{Fe}^{\text{II}}\text{Fe}^{\text{III}}-\text{NH}$ into $\text{Fe}^{\text{III}}\text{Fe}^{\text{II}}-\text{NH}_2$: $\log(k_f) = 4.5 \pm 0.1$.

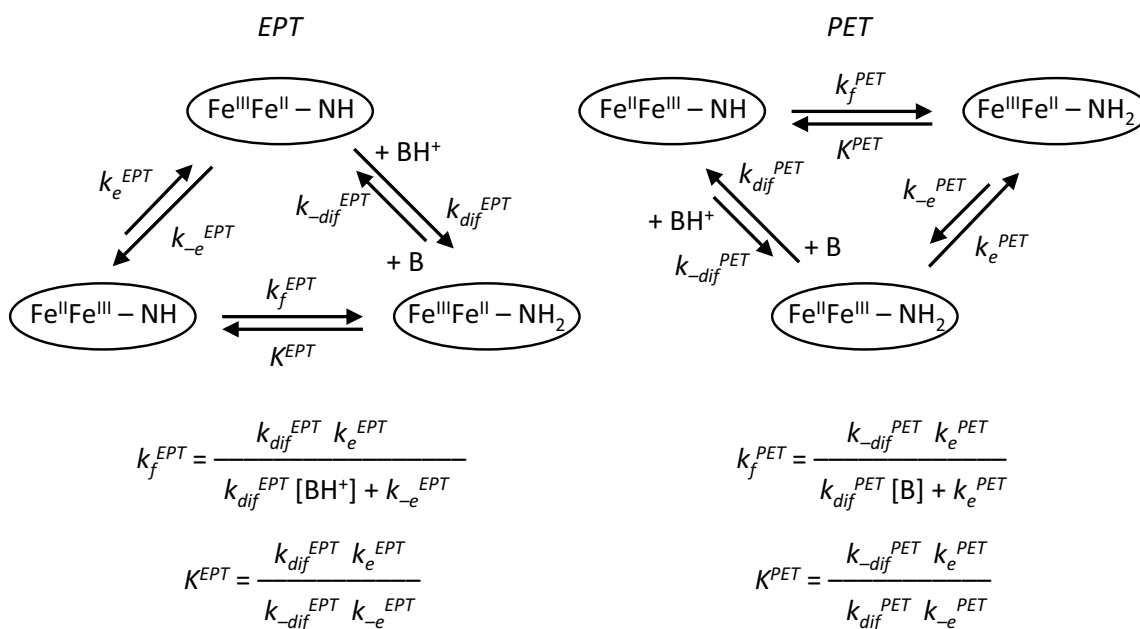
To discriminate between the two mechanisms, the experiments were repeated with another base, pyrrolidine (Scheme 4.5). The pK_a of pyrrolidinium is 19.6, that is 1 unit higher than that of

Et_3NH^+ ($pK_a = 18.6$). Using this base, simulations of the cyclic voltammograms yield a value of $\log(k_f) = 4.0 \pm 0.1$. This decrease in the rate constant upon 1 pK_a unit decrease in the driving force gives the value of the symmetry factor $\alpha = \partial[\log(k_f)] / \partial[\log(K)] \approx 0.5 \pm 0.05$ (much larger variation could not be achieved because using a stronger base will eventually decrease the CE current which will be very difficult to measure).



Scheme 4.5. Scheme of pyrrolidine.

From the symmetry factor value $\alpha = 0.5 \pm 0.05$, it is indeed possible to determine the pathway of the PCET. To understand in depth, let's look at a scheme that includes the rate constant terms for each conversion (electron transfer and proton transfer). For the two sequential pathways, it is possible to determine the dependence of the overall rate constant over the driving force. The rate constants and the equilibrium constants for the $\text{Fe}^{\text{II}}\text{Fe}^{\text{III}}-\text{NH} \rightarrow \text{Fe}^{\text{III}}\text{Fe}^{\text{II}}-\text{NH}_2$ conversion can be formulated for the EPT and PET sequential pathways as a function of the rate constants of the electron transfer step and the proton transfer step (Scheme 4.6).



Scheme 4.6. The rate constant k_f and the equilibrium constant K formulated for the conversion $\text{Fe}^{\text{II}}\text{Fe}^{\text{III}}-\text{NH} \rightarrow \text{Fe}^{\text{III}}\text{Fe}^{\text{II}}-\text{NH}_2$, for the two sequential pathways as a function of the rate constants for the electron transfer and proton transfer steps.

The question is: what is the pertinent rate constant to determine the dependence of the kinetics *versus* the thermodynamics for the overall conversion? The rate-limiting constant is among the protonation or deprotonation process, rather than in the electron transfer step. In

addition, it may be anticipated that for the EPT pathway, the protonation is strongly favored likewise deprotonation for the PET pathway. It is worth noticing that the proton transfer occurs between two nitrogen atoms, either the aminobenzyl group of the mixed valent complex $\text{Fe}^{\text{III}}\text{Fe}^{\text{II}}\text{-NH}_2$ or the exogeneous triethylammonium or pyrrolidinium. This allows hypothesizing that the proton transfer occurs at the diffusion limit in the thermodynamically favored direction. This justifies the k_{dif} and $k_{-\text{dif}}$ constants indicated in Scheme 4.6. Consequently, in the EPT pathway, the rate constants of the proton transfer step satisfy $k_{-\text{dif}}^{\text{EPT}} \ll k_{\text{dif}}^{\text{EPT}}$, thereby making $k_{-\text{dif}}^{\text{EPT}}$ associated to the deprotonation of the mixed valent aniline complex to the intermediate mixed valent anilide $\text{Fe}^{\text{III}}\text{Fe}^{\text{II}}\text{-L}$ species as the rate limiting step. This allows the determination of the two partial derivatives:

$$\frac{\partial(\log[k_f^{\text{EPT}}])}{\partial(\log[k_{-\text{dif}}^{\text{EPT}}])} = 0 \quad \frac{\partial(\log[K^{\text{EPT}}])}{\partial(\log[k_{-\text{dif}}^{\text{EPT}}])} = -1$$

that in turn lead to a symmetry factor α of 0.

Similarly for PET, we get $k_{-\text{dif}}^{\text{PET}} \ll k_{\text{dif}}^{\text{PET}}$ by which $k_{-\text{dif}}^{\text{PET}}$ that corresponds to the protonation of the mixed valent anilide complex into the intermediate mixed valent $\text{Fe}^{\text{II}}\text{Fe}^{\text{III}}\text{-LH}$ species becomes the rate limiting step. The two following partial derivatives may thus be established:

$$\frac{\partial(\log[k_f^{\text{PET}}])}{\partial(\log[k_{-\text{dif}}^{\text{PET}}])} = 1 \quad \frac{\partial(\log[K^{\text{PET}}])}{\partial(\log[k_{-\text{dif}}^{\text{PET}}])} = 1$$

that in turn lead to a symmetry factor α of 1.

The value of the symmetry factor α obtained as 0 for EPT and 1 for PET is not compatible with the experimental value of 0.5. Hence, the conversion of the anilide to aniline species should occur through a CPET pathway, which is further supported by the kinetic isotopic effect (KIE).

Thus, the demonstration shows that a pH-driven intervalence charge transfer mechanism between the two species $\text{X}^{\text{q}+}$ and $\text{XH}^{(\text{q}+1)+}$ can be assessed electrochemically by generating one of the members in situ ($\text{X}^{\text{q}+}$) and investigating its conversion into the other species of the couple ($\text{XH}^{(\text{q}+1)+}$) by monitoring the electrochemical signature of the latter.

5 References

- [1] W. Kanda, W. Moneta, M. Bardet, E. Bernard, N. Debaecker, J. Laugier, A. Bousseksou, S. Chardon-Noblat, J.-M. Latour: A Model of Semimet Hemerythrin; NMR Spectroscopic Evidence of Valence Localization in Bis(μ -carboxylato)(μ -phenolato)diiron(II,III) Complexes in Solution. *Angew. Chem., Int. Ed. Engl.* **1995**, *34*, 588-590.
- [2] E. Bernard, W. Moneta, J. Laugier, S. Chardon-Noblat, A. Deronzier, J.-P. Tuchagues, J.-M. Latour: A Mixed-Valent Fe(II)Fe(III) Complex with an Unsymmetrical Terminal Phenoxo Ligand as Model for the Active Site of Purple Acid Phosphatases. *Angew. Chem., Int. Ed. Engl.* **1994**, *33*, 887-889.
- [3] E. Lambert, B. Chabut, S. Chardon-Noblat, A. Deronzier, G. Chottard, A. Bousseksou, J.-P. Tuchagues, J. Laugier, M. Bardet, J.-M. Latour: Synthesis, Structural, Magnetic and Redox Properties of Asymmetric Diiron Complexes with a Single Terminally Bound Ligand. Relevance to the Purple Acid Phosphatase Enzymes. *J. Am. Chem. Soc.* **1997**, *119*, 9424-9437.
- [4] A. Neves, M. A. de Brito, V. Drago, K. Griesar, W. Haase: A new asymmetric N₅O₂-donor binucleating ligand and its first Fe^{II}Fe^{III} complex as a model for the redox properties of uteroferrin. *Inorg. Chim. Acta* **1995**, *237*, 131-135.
- [5] S. Chardon-Noblat, O. Horner, B. Chabut, F. Avenier, N. Debaecker, P. Jones, J. Pécaut, L. Dubois, C. Jeandey, J.-L. Oddou, A. Deronzier, J.-M. Latour: Spectroscopic and Electrochemical Characterizations of an Aqua Ligand Exchange and Oxidatively Induced Deprotonation in Diiron Complexes. *Inorg. Chem.* **2004**, *43*, 1638-1648.
- [6] A. S. Borovik, V. Papaefthymiou, L. F. Taylor, O. P. Anderson, L. Que Jr.: Models for Iron-Oxo Proteins. Structures and Properties of Fe^{II}Fe^{III}, Zn^{II}Fe^{III}, and Fe^{II}Ga^{III} Complexes with (μ -Phenoxo)bis(μ -carboxylato)dimetal Cores. *J. Am. Chem. Soc.* **1989**, *111*, 6183-6195.
- [7] A. S. Borovik, L. Que Jr.: Models for the Fe^{II}Fe^{II} and Fe^{III}Fe^{II} Forms of Iron-Oxo Proteins. *J. Am. Chem. Soc.* **1988**, *110*, 2345-2347.
- [8] M. Suzuki, A. Uehara, H. Oshio, K. Endo, M. Yanaga, S. Kida, K. Saito: Syntheses and Characterization of Dinuclear Iron(II,II) and Iron(II,III) Complexes with a Dinucleating ligand, 2,6-Bis[bis(2-pyridylmethyl)-aminomethyl]-4-methylphenolate. *Bull. Chem. Soc. Jpn.* **1987**, *60*, 3547-3555.
- [9] A. Neves, A. J. Bortoluzzi, R. Jovito, R. A. Peralta, B. de Souza, B. Szpoganicz, A. C. Joussef, H. Terenzi, P. C. Serevino, F. L. Fischer, G. Schenk, M. J. Riley, S. J. Smith, L. R. Gahan: Catalytic Promiscuity: Catecholase-like Activity and Hydrolytic DNA Cleavage Promoted by a Mixed-Valence Fe^{III}Fe^{II} Complex. *J. Braz. Chem. Soc.* **2010**, *21*, 1201-1212.
- [10] J. M. McCormick, R. C. Reem, E. I. Solomon: Chemical and Spectroscopic Studies of the Mixed-Valent Derivatives of the Non-Heme Iron Protein Hemerythrin. *J. Am. Chem. Soc.* **1991**, *113*, 9066-9079.
- [11] L.-J. Ming, H. G. Jang, L. Que Jr.: 2D NMR Studies of Paramagnetic Diiron Complexes. *Inorg. Chem.* **1992**, *31*, 359-364.

- [12] P. Gütlich, E. Bill, A. X. Trautwein: *Mössbauer Spectroscopy and Transition Metal Chemistry. Fundamentals and Applications*; Springer Verlag: Berlin Heidelberg, 2011.
- [13] P. Gütlich: *Mössbauer Spectroscopy – Principles and Applications*. 2006.
- [14] E. Gouré, G. Thiabaud, M. Carboni, N. Gon, P. Dubourdeaux, R. Garcia-Serres, M. Clémancey, J.-L. Oddou, A. Y. Robin, L. Jacquamet, L. Dubois, G. Blondin, J.-M. Latour: Reversible (De)protonation-Induced Valence Inversion in Mixed-Valent Diiron(II,III) Complexes. *Inorg. Chem.* **2011**, *50*, 6408-6410.
- [15] O. Schlager, K. Wiegardt, B. Nuber: Trivalent Transition Metal Complexes $[M^{III}(L-3H)]$ (M = Fe, Co) of the Triply Deprotonated Hexadentate Ligand 1,4,7-Tris(*o*-aminobenzyl)-1,4,7-triazacyclononane (L). Crystal Structure of $[Mn^{IV}(L-3H)]BPh_4$. *Inorg. Chem.* **1995**, *34*, 6456-6462.
- [16] C. E. Dubé, D. W. Wright, W. H. Armstrong: Multiple Reversible Protonations of the Adamantane-Shaped $\{Mn_4O_6\}^{4+}$ Core: Detection of Protonation Stereoisomers at the $\{Mn_4O_4(OH)_2\}^{2+}$ Level. *J. Am. Chem. Soc.* **1996**, *118*, 10910-10911.
- [17] P. Karsten, A. Neves, A. J. Bortoluzzi, M. Lanznaster, V. Drago: Synthesis, structure, properties, and phosphatase-like activity of the first heterodinuclear $Fe^{III}Mn^{II}$ complex with the unsymmetric ligand $H_2BPBPMP$ as a model for the PAP in sweet potato. *Inorg. Chem.* **2002**, *41*, 4624-4626.
- [18] F. Avenier, E. Gouré, P. Dubourdeaux, O. Sénèque, J.-L. Oddou, J. Pécaut, S. Chardon-Noblat, A. Deronzier, J.-M. Latour: Multiple Aromatic Amination Mediated by a Diiron Complex. *Angew. Chem. Int. Ed.* **2008**, *47*, 715-717.
- [19] G. A. Neyhart, T. J. Meyer: pH-induced intramolecular electron transfer. *Inorg. Chem.* **1986**, *25*, 4807-4808.
- [20] R. E. Stenkamp: Dioxygen and hemerythrin. *Chem. Rev.* **1994**, *94*, 715-726.
- [21] M. Rudolph: Digital simulations on unequally spaced grids. Part 2. Using the box method by discretisation on a transformed equally spaced grid. *J. Electroanal. Chem.* **2003**, *543*, 23-29.



PART 2

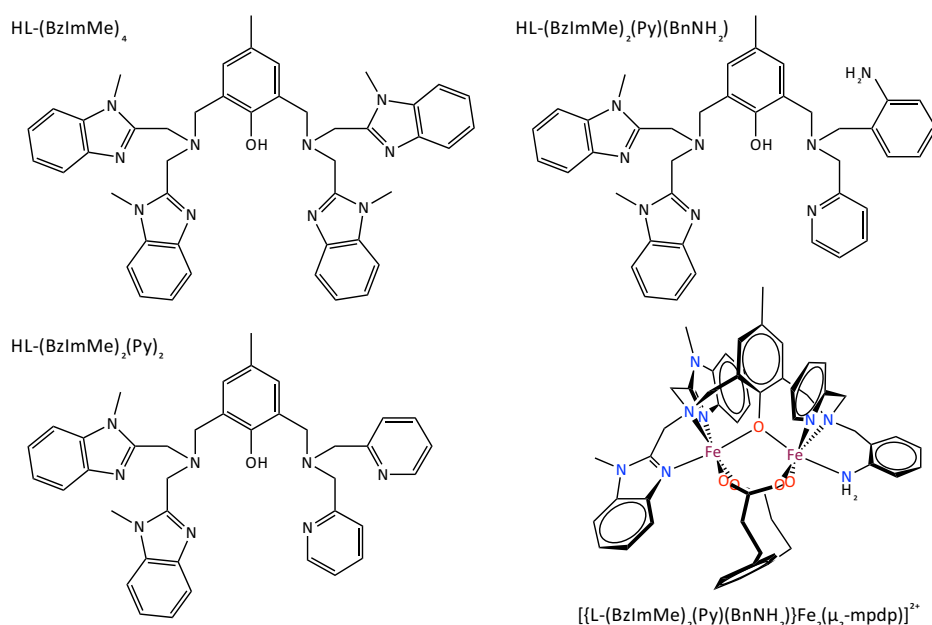


A Proton-coupled electron transfer:
How it is influenced by the redox potential and
the acidity of the partners

1 Overview

A main objective of the ANR project was to evaluate the influence of the pK_a of the protic group and the influences of the respective redox potentials of the two Fe^{II}/Fe^{III} couples on the thermodynamics and kinetics of the proton coupled electron transfer reaction. To achieve this goal, the modification of the original ligand with two branches $[Py_2]$ and $[Py/Aniline]$ (Py = pyridine) was undertaken aiming on one hand at replacing the aniline in the $[Py/Aniline]$ branch by a benzimidazole (BzImH) resulting in the $[Py/BzImH]$ branch and on another hand to replace the pyridine by a 1-methylbenzimidazole (BzImMe) in the bispicolylamine $[Py_2]$ branch to give a bis-1-methylbenzimidazole $[(BzImMe)_2]$ branch. Several combinations of the various branches have been implemented as described below.

We first attempted to substitute the two pyridine rings that were coordinated to the Fe^{III} site by two 1-methylbenzimidazole groups. These ligands were supposed to stabilize the +III oxidation state of the metal. Unfortunately the synthesis of the bis-((1-methylbenzimidazol-2-yl)methyl)amine was quite difficult. The condensation of the *N*-methyl-*o*-phenylenediamine with the iminodiacetic acid occurs between two solids and the reaction must be achieved in a very narrow window of temperatures (see experimental section for details). The main difficulty is the purification of the compound. The purification through the formation of the hydrochloride compound that has been very recently attempted seems promising.

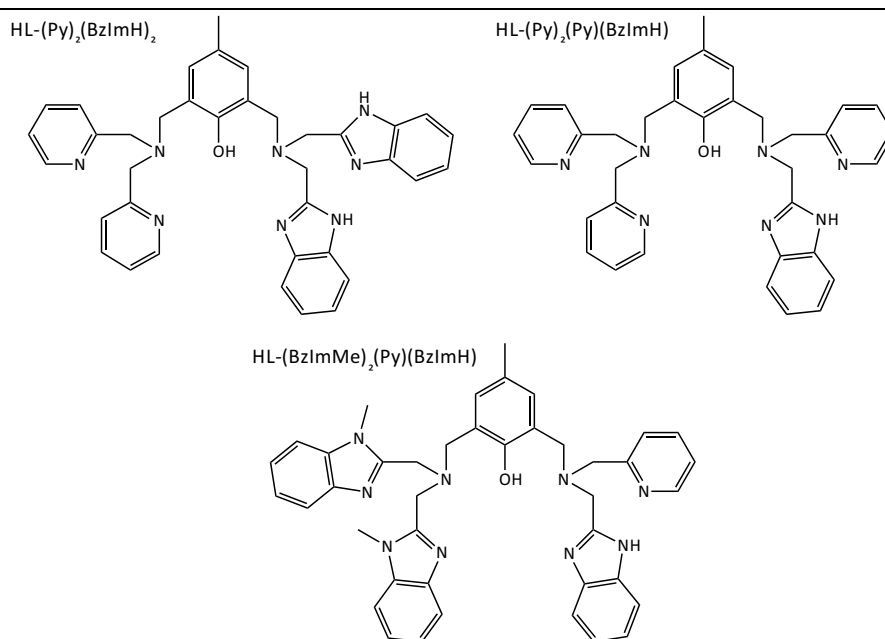


Scheme 1. Scheme of the three binucleating ligands with the bis((1-methylbenzimidazol-2-yl)methyl)amine branch (left side). Scheme of the new aniline complex with the ligand $HL-(BzImMe)_2(Py)(BnNH_2)$ (bottom right).

Two reference mixed valent $\text{Fe}^{\text{II}}\text{Fe}^{\text{III}}$ complexes were synthesized: $[\{\text{L}-(\text{BzImMe})_4\}\text{Fe}_2(\mu_2\text{-mpdp})]^{2+}$ and $[\{\text{L}-(\text{BzImMe})_2(\text{Py})_2\}\text{Fe}_2(\mu_2\text{-mpdp})]^{2+}$ (the corresponding binucleating ligands are respectively shown on the top left and bottom left part of Scheme 1). An X-ray structure was obtained for the dissymmetric complex with two 1-methylbenzimidazole rings on one side and two pyridines on the other. Unexpectedly, the bispicolylamine branch coordinates the Fe^{III} ion and the two methylbenzimidazole groups the Fe^{II} ion. Spectroscopic characterizations using ^1H -MNR, Mössbauer and UV-visible absorption spectroscopies were performed. Redox potentials were also determined thanks to cyclic voltammetry. The mixed valent complex to be synthesized for a comparison with $[\text{Fe}^{\text{III}}(\mu_2\text{-mpdp})\text{Fe}^{\text{II}}(\text{H}_2\text{NBn-L})]^{2+}$ is $[\{\text{L}-(\text{BzImMe})_2(\text{Py})(\text{BnNH}_2)\}\text{Fe}_2(\mu_2\text{-mpdp})]^{2+}$ (see right part of Scheme 1 for a drawing of the binucleating ligand and a draft of the complex). The complex was synthesized but was contaminated by an impurity issued from the early stages of the synthesis of the binucleating ligand. The amine character of the contaminant renders all purification processes (chromatography, ...) inoperative. We are currently restarting all the synthetic procedure with the hope that using a highly purified bis-((1-methylbenzimidazol-2-yl)methyl)amine will give a pure ligand.

All the characterizations performed so far on these three complexes are gathered in the draft n°1 given in the next pages. The manuscript is entitled “pH-driven valence inversion in mixed-valent diiron(II,III) complexes. Redox potential influence on the proton-coupled electron transfer”. Before submission, the paper will undoubtedly be complemented according to the new results gathered especially on the new aniline complex.

The second modification of the aniline complex $[\text{Fe}^{\text{III}}(\mu_2\text{-mpdp})\text{Fe}^{\text{II}}(\text{H}_2\text{NBn-L})]^{2+}$ involves replacement of the aniline group by a benzimidazole. Apart from the expected change in pK_a , the removable proton in the benzimidazole complex, is not on the iron binding nitrogen, a property that is likely to influence the PCET. Scheme 2 presents the three binucleating ligands that have been synthesized.



Scheme 2. Scheme of the binucleating ligands incorporating one or two benzimidazole rings. The complex synthesized with HL-(Py)₂(Py)(BzImH) will allow a direct comparison with [Fe^{II}(μ₂-mpdp)Fe^{III}(H₂NBn-L)]²⁺ investigated in Part 1. That with HL-(BzImMe)₂(Py)(BzImH) will be compared with the one issued from HL-(BzImMe)₂(Py)(BnNH₂) (see Scheme 1).

The mixed valent complex $[\{L-(Py)_2(BzImH)_2\}Fe_2(\mu_2\text{-mpdp})]^{2+}$ was synthesized by Michaël Carboni during his PhD and preliminary characterizations were given in his manuscript, including a X-ray structure. The two other mixed valent complexes, namely $[\{L-(Py)_2(Py)(BzImH)\}Fe_2(\mu_2\text{-mpdp})]^{2+}$ and $[\{L-(BzImMe)_2(Py)(BzImH)\}Fe_2(\mu_2\text{-mpdp})]^{2+}$, were isolated. Characterizations by ¹H-NMR, Mössbauer and UV-visible absorption spectroscopies were performed on acetonitrile solutions. The addition of NEt₃ was also investigated resorting on the same techniques. Preliminary measurements by cyclic voltammetry were also recorded. These results are gathered in the draft of a second paper given here after. The title is “pH-driven valence inversion in mixed-valent diiron(II,III) complexes. Influence of the protic ligand on the proton-coupled electron transfer”. Complementary experiments by cyclic voltammetry are planned to investigate the proton-coupled electron transfer.

2 Draft n°1

“pH-driven valence inversion in mixed-valent diiron(II,III) complexes. Redox potential influence on the proton-coupled electron transfer”

pH-driven valence inversion in mixed-valent diiron(II,III) complexes. Redox potential influence on the proton-coupled electron transfer.

Eric Gouré,^a Patrick Dubourdeaux,^a Martin Clémancey,^a Nathalie Gon,^a Ramachandran Balasubramanian,^a Colette Lebrun,^b Jacques Pécaut,^b Geneviève Blondin^{a,} and Jean-Marc Latour^{a,*}*

(a) Univ. Grenoble Alpes, LCBM, 38054 Grenoble, France, CEA/DSV/iRTSV/CBM/pmb, 38054 Grenoble, France, CNRS UMR5249, LCBM, 38054 Grenoble, France

(b) Univ. Grenoble Alpes, RICC, 38054 Grenoble, France, CEA/DSM/INAC/SCIB/RICC, 38054 Grenoble, France, UMR E 3, RICC, 38054 Grenoble, France

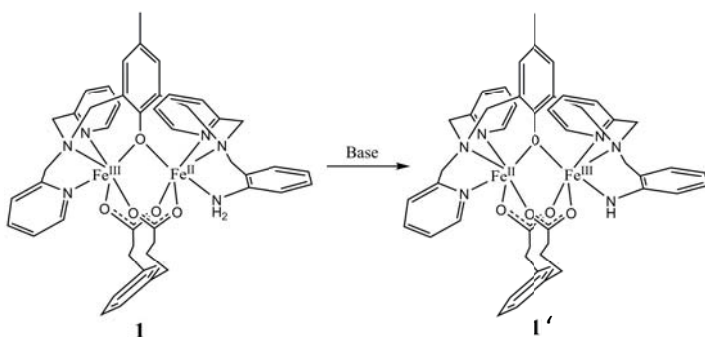
genevieve.blondin@cea.fr; jean-marc.latour@cea.fr

KEYWORDS (Word Style “BG_Keywords”). If you are submitting your paper to a journal that requires keywords, provide significant keywords to aid the reader in literature retrieval.

ABSTRACT (Word Style “BD_Abstract”). All manuscripts must be accompanied by an abstract. The abstract should briefly state the problem or purpose of the research, indicate the theoretical or experimental plan used, summarize the principal findings, and point out major conclusions. Abstract length is one paragraph.

INTRODUCTION

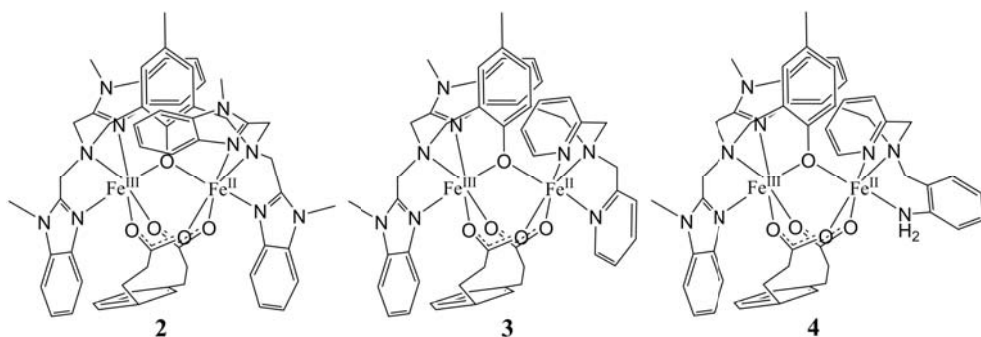
Intervalence charge transfer (IVCT) has attracted continuous interest among inorganic chemists for several decades.¹ In most cases, it occurs through a ligand bridging two metals in different oxidation states, these metals being identical or not.²⁻⁵ We recently reported that such an IVCT can be induced in a mixed-valent $\text{Fe}_2^{\text{II,III}}$ complex **1** by deprotonation of an aniline ligand bound to the ferrous site,⁶ as illustrated in Scheme 1.



Scheme 1

A similar process has been described only in an heterodinuclear RuOs complex⁷ and in the semimet forms of the dioxygen carrier hemerythrin, albeit in the latter case the system switches between a ferrous pentacoordinate site and an hydroxo-bound ferric center.⁸ The thermodynamic and kinetic aspects of the reaction were investigated by spectroscopic and electrochemical techniques.⁹ Moreover, thorough electrochemical experiments showed that this process could be described as a concerted proton-electron transfer. Owing to the singularity of this system it appeared of interest to investigate further how the reaction is influenced by the redox potential difference of the two Fe sites and the pK_a of the group that is deprotonated. The modularity of the ligand constitution and its sequential synthesis¹⁰ (Scheme S1) allow to vary the complexing branch of each metal. In the present work, we

used it to vary the redox potential of the ferric site in the starting aniline complex by replacing the bis((pyridyl-2-yl)methyl)amine branch by a bis((1-methylbenzimidazol-2-yl)methyl)amine in complex **4** (Scheme 2). To fully assess the effect of this substitution on the properties of complex **4**, we also prepared the symmetric complex with two bis((1-methylbenzimidazol-2-yl)methyl)amine branches **2** and the asymmetrical complex **3** incorporating the two kinds of complexing branches (Scheme 2). This article describes the syntheses, the structural and spectroscopic properties of **2-4** and the deprotonated form of the latter **4'** together with their electrochemical study.



Scheme 2. Mixed-valent diiron complexes studied in this work.

RESULTS AND DISCUSSION

Syntheses of the ligands and complexes. The three ligands used in the present work were synthesized according to the already described procedure¹⁰ (Scheme S1) adapted for inserting the desired bis((pyridyl-2-yl)methyl)amine, bis((1-methylbenzimidazol-2-yl)methyl)amine and ((2-pyridyl-2-yl)methyl)-(1-amino-2-methylphenyl)amine branch.⁶ Complexes **2-4** were prepared by usual procedures.^{11,12} They were all characterized by ElectroSpray Ionization-Mass Spectrometry (ESI-MS) and spectroscopic techniques (see below).

Characterization of complexes 2 and 3. Solid state studies.

X-ray structure of 3(ClO₄)₂. Figure 1 shows the structure of the dicationic complex **3**. The crystal parameters are listed in Table 1, and important bond lengths and angles are given in Table 2. The two iron ions are bridged by the oxygen atom of the phenoxide of the deprotonated ditopic ligand and by the two carboxylates of benzene-1,3-dipropionate (mpdp²⁻). The coordination spheres of the two metal ions are completed by three nitrogen atoms of the ditopic ligand, one is a tertiary amine function and the two others are either from the pyridine or the benzimidazole rings. The presence of the two perchlorate anions per diiron complex is in agreement with a mixed valent Fe^{II}Fe^{III} composition. The average of the metal-ligand distances for Fe2 is smaller than that for Fe1 (2.16 vs 2.06 Å, respectively), indicating that the Fe^{III} site is in the bispicolylamine cavity while the Fe^{II} ion is coordinated by the two methylbenzimidazoles. This is counterintuitive since the methylbenzimidazole is a better electron donor than pyridine and was expected to favor the +III oxidation state. The metal-ligand bond lengths compare well with those determined on similar complexes with either four pyridine rings,¹³ [(bpmmp)Fe₂(μ-OPr)₂]²⁺, or with four *N*-methylimidazole groups,¹⁴ [(bimp)Fe₂(μ-O₂CPh)₂]²⁺.

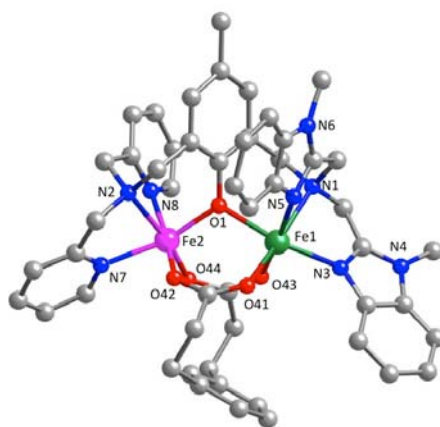


Figure 1. X-ray structure of **3**.

Table 1. Summary of crystal data and structure refinement for compound **3**(ClO₄)₂.

chemical formula	C ₅₁ H ₅₁ Cl ₂ Fe ₂ N ₈ O ₁₃
formula weight	1166.60
crystal system	triclinic
space group	<i>P</i> -1
<i>a</i> (Å)	10.0771(11)
<i>b</i> (Å)	13.4513(16)
<i>c</i> (Å)	20.341(2)
α (deg)	86.427(8)
β (deg)	84.643(9)
γ (deg)	70.346(10)
<i>V</i> (Å ³)	2583.8(5)
<i>Z</i>	2
<i>D</i> _{calcd} (g cm ⁻³)	1.499
λ (Å), μ (mm ⁻¹)	0.71073, 0.738
<i>T</i> (K)	150(2)
θ range (deg)	3.282 to 24.713
reflns collected	18131
unique reflns	8743
data/restraints/parameters	8743/0/688
<i>R</i> ₁ , <i>wR</i> ₂ (<i>I</i> > 2 σ (<i>I</i>))	0.0715, 0.1393

Table 2. Selected bond lengths (Å) and angle (°) in **3**(ClO₄)₂.

Fe1–O1	2.127(5)	Fe2–O1	1.944(5)
Fe1–O41	2.065(5)	Fe2–O42	1.956(5)
Fe1–O43	2.134(5)	Fe2–O44	1.948(5)
Fe1–N1	2.310(6)	Fe2–N2	2.221(6)
Fe1–N3	2.132(6)	Fe2–N7	2.138(6)
Fe1–N5	2.174(5)	Fe2–N8	2.175(6)
Fe1 ... Fe2	3.443	Fe1–O1–Fe2	115.5(2)

Mössbauer spectroscopy. Figure 2 reproduces the spectra recorded at 80 K and zero-field on solid-state samples of complexes **2** and **3**. Each spectrum comprises four components and can be satisfyingly reproduced by two quadrupole doublets of equal area. The isomer shift and quadrupole splitting values deduced from the simulation (Table 3) are in the range expected for one high-spin ferric and one high-spin ferrous ions. These spectra thus indicate that the valences of the two Fe ions are localized in these conditions. These parameters should be informative on the location of the valences in the asymmetric complex **3**. Comparison of the parameters of **3** with those of the two symmetric analogs **2** (with methylbenzimidazole donors) and [(bpmp)Fe₂(μ-OPr)₂]²⁺ (with pyridine donors)¹³ reveal that the parameters of the ferrous ion are closer to that of [(bpmp)Fe₂(μ-OPr)₂]²⁺ while those of the ferric ion are closer to those of **2**. This suggests that in the powder, the location of the valences of the two Fe ions is inverted with respect to that found in the X-ray crystal structure. However, it must be noticed that for Hbpmp based mixed valent complexes, the quadrupole splittings of both iron sites may differ by ±0.2 mm.s⁻¹ depending on the bis-carboxylato bridge and on the counterion. Therefore the present assignment may be taken as tentative only.

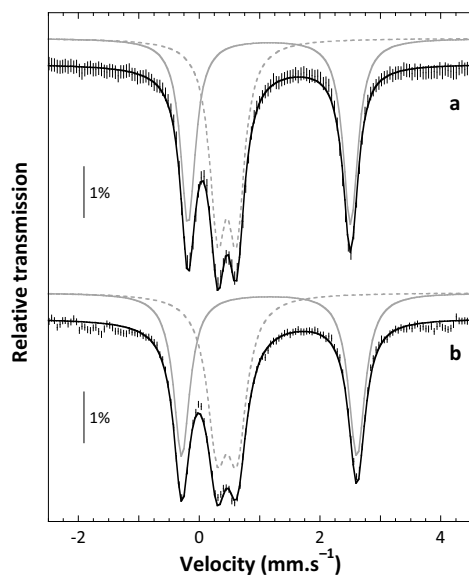


Figure 2. Mössbauer spectra (hashed lines) of complexes **2** (a) and **3** (b) recorded at 80 K and zero-field. The theoretical spectra are shown as the solid black lines. The Fe^{II} and Fe^{III} contributions are shown above the spectra as the solid gray and dashed gray lines, respectively.

Table 3. Isomer shifts and quadrupole splittings for complexes **2** and **3** and related species.

Complex		δ (mm.s ⁻¹)	ΔE_Q (mm.s ⁻¹)	Γ_{fwhm} (mm.s ⁻¹)	Relative area (%)
2	Fe ^{II}	1.16	2.69	0.30	50
	Fe ^{III}	0.46	0.31	0.32	50
3	Fe ^{II}	1.16	2.90	0.33	50
	Fe ^{III}	0.46	0.33	0.39	50
[(bpm)Fe ₂ (μ -OPr) ₂] ²⁺	Fe ^{II}	1.13	2.91	0.29	48
	Fe ^{III}	0.48	0.54	0.30	52

Solution studies

¹H-NMR spectroscopy. Figure 3 reproduces the ¹H-NMR spectra of complexes **2** and **3** recorded in CD₃CN solutions. They expand over a large chemical shift domain, 340 and 370 ppm for **2** and **3**, respectively. This is reminiscent of what was observed for the complexes [(bpmp)Fe₂(μ-OPr)₂]²⁺ ¹³ and [(bimp)Fe₂(μ-OAc)₂]²⁺ ¹⁴ whose spectra extend over 390 and 350 ppm, respectively. According to the peak assignments that were achieved for these two complexes, the thin peaks observed above 150 ppm can be attributed to protons of the six methylene groups of the binucleating ligand, two bound to the phenoxide (N-CH₂-Ph) and four bound to the amine donor (N-CH₂-Amine). A single of these protons appear in this range, the other resonating more up-field. For the latter complexes, only three peaks are observed for these groups owing to the symmetry of the ligand and to an intervalence exchange between the two equivalent mixed valent forms Fe^{II}Fe^{III} and Fe^{III}Fe^{II} that is fast on the ¹H-NMR time scale. In addition, for [(bpmp)Fe₂(μ-OPr)₂]²⁺ ¹³ two additional resonances are observed which are associated to the four *ortho*-pyridinyl protons; these resonances are broad owing to the short distance of these protons to the Fe ions. Extensive ¹H-NMR studies have led to assign the methylene resonances in decreasing chemical shifts to the (N-CH₂-Ph) and then the two (N-CH₂-Amine) groups.

The spectrum of complex **2** is very similar to that of [(bimp)Fe₂(μ-OAc)₂]²⁺ ¹⁴ with only three signals in the 400-150 ppm domain, in accord with a fast intervalence exchange. Also by analogy with [(bpmp)Fe₂(μ-OPr)₂]²⁺ ¹³ the peak at 337.5 ppm can be attributed to the (N-CH₂-Ph) group and the two signals at 198.5 and 170.1 ppm to the two (N-CH₂-Amine) groups. For complex **3**, owing to the asymmetry of the ligand, the methylene groups are non equivalent and indeed six narrow peaks are observed above 140 ppm. In addition two broad signals are detected at 198.1 and 152.6 ppm that can be attributed to the two *ortho*-pyridinyl protons. As for **2**, the observed positions are indicative of a delocalized mixed valent

complex on the NMR time scale. A tentative assignment of the methylene protons of **3** can be proposed from an analysis of their positions in the symmetrical complexes **2** and $[(\text{bpmp})\text{Fe}_2(\mu\text{-OPr})_2]^{2+}$. These protons occur at higher chemical shifts in the latter compound than in **2** (396, 265 and 198 vs 337.5, 198.5 and 170.1 ppm): therefore the signals at 361.7, 235.7 and 180.3 ppm are attributed to methylene groups of the bis((pyridyl-2-yl)methyl)amine branch whereas those at 355.8, 208.6 and 163.1 ppm would originate from the CH_2 groups of the bis((1-methylbenzimidazol-2-yl)-methyl)amine arm. The first signal out of the three within each of the two series would be assigned to the $\text{N-CH}_2\text{-Ph}$ group.

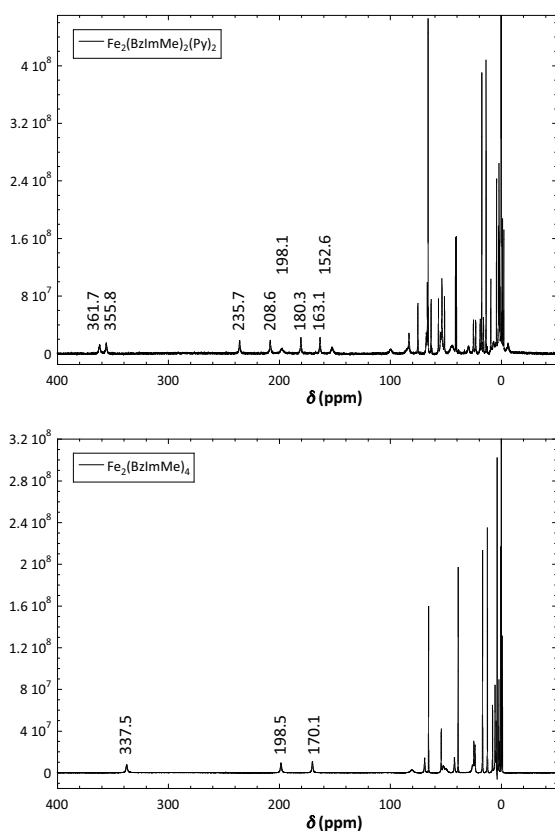


Figure 3. $^1\text{H-NMR}$ spectra of complexes **2** (bottom) and **3** (top) in CD_3CN solution.

UV-visible absorption spectroscopy. Figure 4 reproduces the UV-visible absorption spectra recorded on 0.3 mM acetonitrile solutions of complexes **2** and **3**. The more intense bands are respectively observed at $\lambda_{\text{max}} = 560$ and 575 nm with molar extinction coefficient values of

740 and 595 mol⁻¹.L.cm⁻¹. This is reminiscent of the phenoxide-to-Fe^{III} charge transfer transition observed in [(bpmp)Fe₂(μ-OPr)₂]²⁺ at λ_{max} = 554 nm with ε = 950 mol⁻¹.L.cm⁻¹ ¹³ and that at λ_{max} = 523 nm with ε = 660 mol⁻¹.L.cm⁻¹ detected for [(bimp)Fe₂(μ-OAc)₂]²⁺. ¹⁴

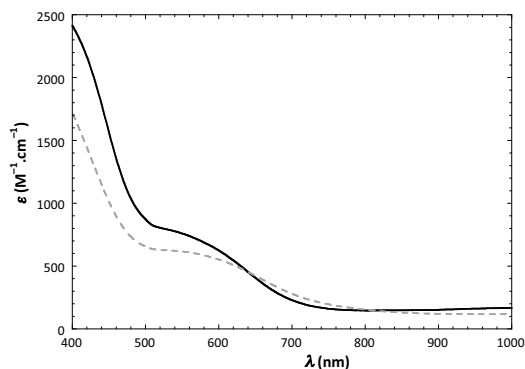


Figure 4. UV-visible absorption spectra of complexes **2** (solid black line) and **3** (gray dashed line) recorded on 0.3 mM acetonitrile solutions.

Electrochemistry. Cyclic voltammograms were recorded on millimolar acetonitrile solutions of complexes **2** and **3**. They are shown on Figure 5. For both complexes, one reversible oxidation process is observed at $E_{ox}^{1/2} = 0.52$ V ($E_{ap} = 0.55$ V, $E_{cp} = 0.48$ V, $\Delta E = 0.07$ V) for **2** and at $E_{ox}^{1/2} = 0.58$ V ($E_{ap} = 0.63$ V, $E_{cp} = 0.54$ V, $\Delta E = 0.09$ V) for **3**. A reduction process is also detected at $E_{red}^{1/2} = -0.18$ V ($E_{ap} = -0.14$ V, $E_{cp} = -0.21$ V, $\Delta E = 0.07$ V) for **2** and at $E_{red}^{1/2} = -0.12$ V ($E_{ap} = -0.08$ V, $E_{cp} = -0.15$ V, $\Delta E = 0.07$ V) for **3**. These can be attributed to one electron processes, namely the oxidation of the mixed valent complexes into the bis-ferric species and to their reduction into the bis-ferrous systems. These redox potentials indicate a 700 mV stabilization domain for both mixed valent complexes, that is a value close to that observed for similar mixed valent complexes.^{10,11,15} The two symmetric complexes [(bpmp)Fe₂(μ-OPr)₂]²⁺ ¹³ and [(bimp)Fe₂(μ-OAc)₂]²⁺ ¹⁴ present similar one-electron transfers at 0.69 and 0.44 V in oxidation and at -0.01 and -0.22 V in reduction. Redox potentials can be ordered according to Hbpmp > HL-(BzImMe)₂(Py)₂ > HL-

$(\text{BzImMe})_4 > \text{Hbimp}$. This indicates a greater stabilization of the Fe^{III} state when methylbenzimidazoles vs pyridines are present: substitution of a bis((1-methylbenzimidazol-2-yl)methyl)amine (in **2**) by a bis((pyridyl-2-yl)methyl)amine (in **3**) in a complexing branch leads to a 60 mV increase in the potentials of the two redox couples. The valence location in **3** as determined from the X-ray structure is thus surprising.

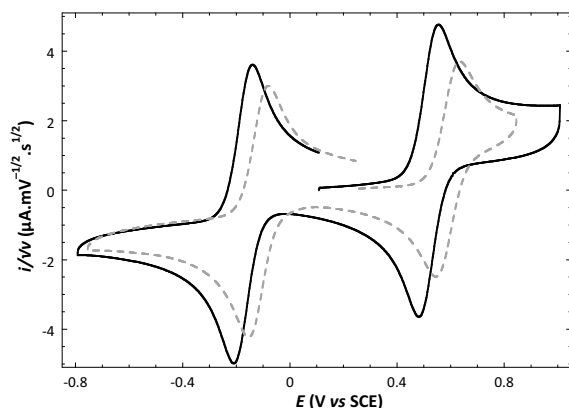


Figure 5. Cyclic voltammograms recorded on acetonitrile solutions of complexes **2** (black solid line) and **3** (gray dashed line).

Characterization of complex **4**.

¹H-NMR spectroscopy. Figure 6 (top) illustrates the ¹H-NMR spectrum of complex **4**. This spectrum departs from those of **2** and **3** by the drastically enlarged spectral range that extends over ca 500 ppm instead of 340-370 ppm. Such a high spectral range is commonly observed for complexes bearing significantly different complexing branches i.e. either with a non-bonding benzyl group or a strongly binding phenoxide,^{10,12} and was observed for **1**.⁶ This extended spectral range is indicative of a higher localization of the valences of the two Fe ions on the ¹H-NMR time scale. A second notable feature is the high number of signals (> 16) present in the 500-140 ppm range. This high number of resonances can not be due to the

asymmetric nature of the ligand since **3** presents about half that number in the corresponding range. It is therefore indicative of the occurrence of two isomers as observed for the original aniline complex **1** where the aniline group can occupy either the *trans* or the *cis* position with respect to the bridging phenoxide.¹⁶ Indeed, the spectrum of **4** bears a significant resemblance with that of **1** except for a slightly smaller spectral range that is quite in line with the shorter range observed for **2** vs **3** when a bis((1-methylbenzimidazol-2-yl)methyl)amine is replaced by a bis((pyridyl-2-yl)methyl)amine. A notable difference between **4** and **1** resides in the different kinetics of isomerization. Indeed, for **1** it takes *ca* 2h to reach the equilibrated *cis-trans* mixture upon dissolution of the *trans* isomer, whereas for **4** the equilibrated mixture is detected immediately after dissolution.

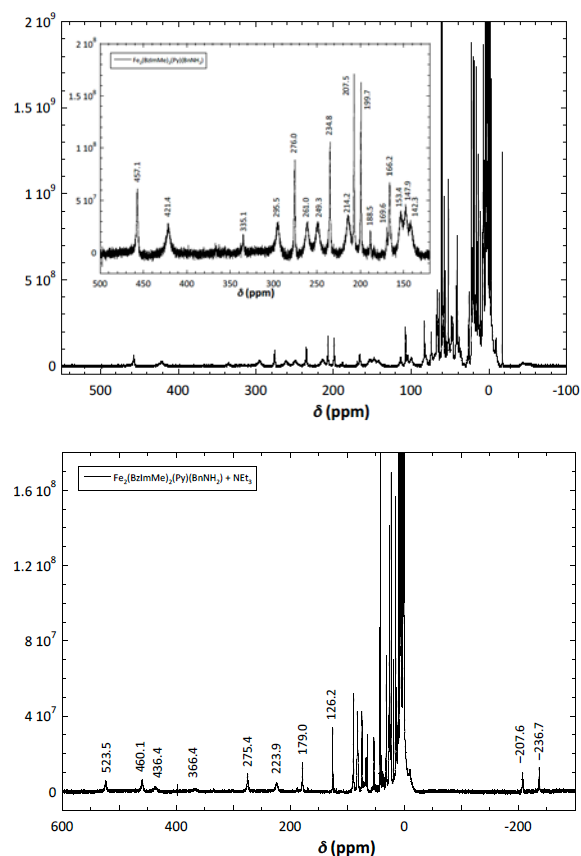


Figure 6. ¹H-NMR spectra of complexes **4** before (top) and **4'** after (bottom) addition of 3 eq. NEt₃ in CD₃CN solution.

UV-visible absorption spectroscopy. The UV-visible spectrum of **4** presents a broad unfeatured absorption plateau near $\lambda = 588$ nm. By analogy with **2** and **3** this band can be assigned to the phenoxide-to-Fe^{III} charge transfer transition characteristic of these kinds of complexes.^{10,13} Interestingly, this spectrum does not show any evolution over a period of several hours, thus confirming the ¹H-NMR observation that the isomers are formed very rapidly upon dissolution or are present in the powder. It is not thus possible to distinguish them and assign their individual UV-visible spectra.

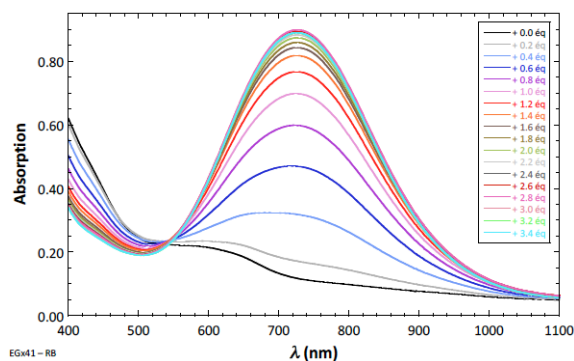


Figure 7. UV-visible monitoring of the deprotonation of complex **4** by addition of NEt_3 in acetonitrile solution.

Mössbauer spectroscopy. The Mössbauer spectra of **4** were recorded in the solid state and in acetonitrile solution and are depicted in Figure 8a,b. They can be accounted for by considering the presence of two doublets of equal intensity, the parameters of which deduced from the simulation correspond to a high-spin Fe^{II} and a high-spin Fe^{III} ion (Table 4). At first sight, this is at odds with the results of $^1\text{H-NMR}$ spectroscopy which revealed the presence of two isomers. However, the Mössbauer spectra recorded in both conditions exhibit rather broad lines, especially for the Fe^{II} site ($\Gamma_{\text{fwhm}} > 0.5 \text{ mm}\cdot\text{s}^{-1}$), which can be due to the presence of two closely similar species, the contributions of which are not resolved. The similarity of the parameters of **4** with those of the two isomers of **1** is consistent with this possibility.

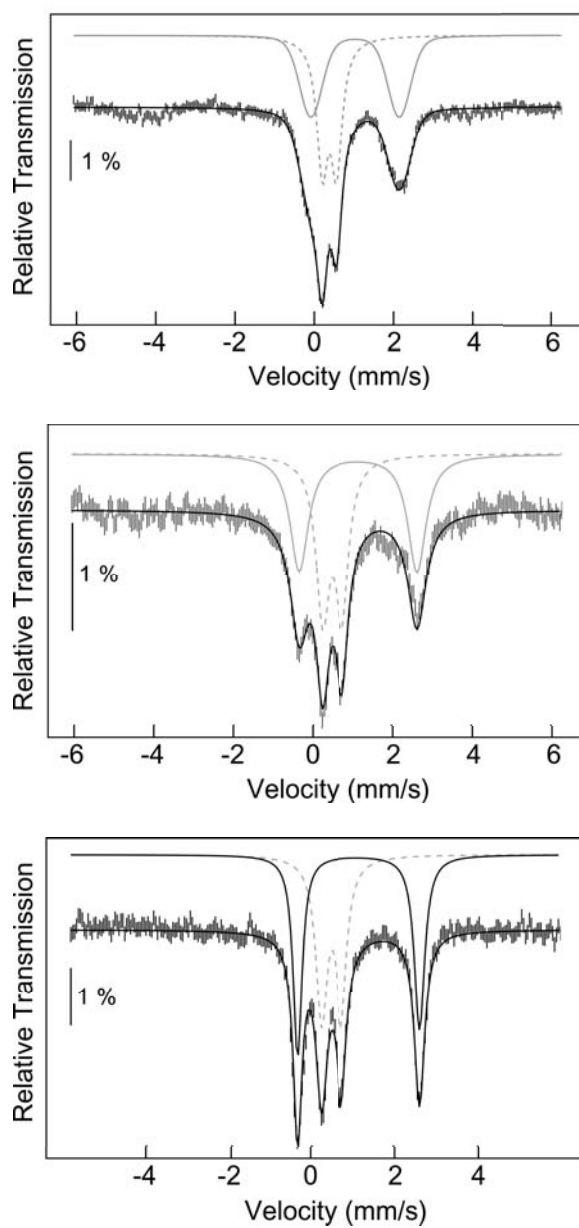


Figure 8. Mössbauer spectra of **4** recorded at 80 K in the solid state (top), in acetonitrile before (middle) and after of **4'** after addition of triethylamine (bottom) to a solution of **4**. The contribution of a ferric impurity (7 %) was subtracted from the three spectra. The solid and dashed lines underneath the spectra illustrate the contributions of the ferrous and ferric site, respectively, as deduced from the simulations.

Table 4. Isomer shifts and quadrupole splittings for complex **4** in solid and solution state and after deprotonation by NEt₃.

Complex		δ (mm.s ⁻¹)	ΔE_Q (mm.s ⁻¹)	Γ_{fwhm} (mm.s ⁻¹)	Relative area (%)
4 (solid state)	Fe ^{II}	1.07	2.19	0.73	50
	Fe ^{III}	0.43	0.37	0.37	50
4 (acetonitrile)	Fe ^{II}	1.14	2.98	0.50/0.67	50
	Fe ^{III}	0.50	0.49	0.40	50
4' (acetonitrile)	Fe ^{II}	1.14	2.97	0.26/0.30	50
	Fe ^{III}	0.48	0.51	0.33	50

Deprotonation of complex **4**.

Addition of triethylamine to an acetonitrile solution of **4** causes a drastic color change from violet-blue to green as the deprotonated complex **4'** is formed. As illustrated in Figure 7, this corresponds to the appearance of an intense band at $\lambda_{max} = 725$ nm which is at slightly higher energy ($E = 13793$ cm⁻¹) than the transition observed for complex **1'** ($\lambda_{max} = 730$ nm, $E = 13699$ cm⁻¹) obtained by deprotonation of **1**.⁶ This energy difference results mostly from the effect of the substitution of a bis((pyridyl-2-yl)methyl)amine by a bis((1-methylbenzimidazol-2-yl)methyl)amine in the complexing branch on the energy of the Fe^{III} orbitals.

Figure 6 (bottom) shows the ¹H-NMR spectrum of **4'** formed by addition of triethylamine to a CD₃CN solution of **4**. When compared to the spectrum of **4**, two main differences appear clearly. First, the spectral range has even increased to *ca* 760 ppm from 524 to -237 ppm. This is in agreement with a localization of the valences of the Fe ions. Moreover the occurrence of two highly upfield shifted resonances at -207.6 and -237.6 ppm is the signature of an anilide ligand bound to a ferric ion in a *trans* position with respect to the

bridging phenoxide, these resonances being associated to the *ortho* and *para* anilide protons. Similar resonances were observed in the original deprotonated aniline complex **1**^{6,16} as well as in the corresponding phenoxide.¹⁰ Second, the number of resonances is drastically reduced to eight in the 550-100 ppm range that is similar to the spectrum of **3**. This observation indicates that a single isomer of the anilide complex is present in solution as opposed to the situation noted for **4**, **1** and **1'** where two isomers coexist. This shows that the substitution of a bis((pyridyl-2-yl)methyl)amine by a bis((1-methylbenzimidazol-2-yl)methyl)amine in the complexing branch has a significant and distinct effect on the respective stabilities of the two isomers in the protonated and deprotonated forms.

The Mössbauer spectrum of **4'** is depicted on Figure 8. It is clearly composed of four lines of equal intensity that can be decomposed in two doublets associated to a high-spin ferrous and a high-spin ferric site. Examination of the parameters listed in Table 4 clearly shows that the deprotonation has not occurred: indeed the only difference with the spectrum of **4** in acetonitrile is in the line widths which are drastically reduced. Careful deprotonation under UV-visible or ¹H-NMR monitoring will be undertaken to solve the problem.

Electrochemistry of complex 4.

Preliminary electrochemical experiments of **4** have been performed to characterize its redox properties and its reduction behavior. Two redox couples are detected in cyclic voltammetry corresponding to one-electron transfers to form the diferrous ($E_{red}^{1/2}$ ca -0.23 V) and the diferric ($E_{ox}^{1/2}$ ca 0.46 V) form. The stability domain of the mixed-valent is thus close to 0.7 V in line with the other compounds in this study. Addition of increasing amounts of triethylamine causes a decrease of the oxidation couple together with the appearance of a new reversible couple at 0.11 V. At the same time an irreversible oxidation wave is formed at ca 0.8 V. This could correspond to the oxidation of triethylamine, showing that it is not totally

consumed by the deprotonation reaction. This hypothesis would explain the difficulty encountered for preparation of the Mössbauer sample of **4'**. However, more experiments are needed to ascertain it. Whatever the nature of this wave, these experiments show that upon deprotonation of the aniline, the oxidation of the Fe^{II} center is facilitated by ca 0.35 V. This effect is comparable to that observed for the same process in **1** (ca 0.45 V) and about the double of that linked to deprotonation of a benzimidazole ligand.¹⁷

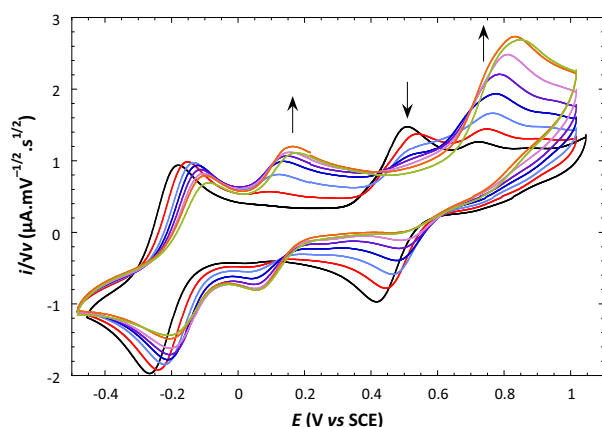


Figure 9. Cyclic voltammetric curves of **4** recorded on millimolar solutions in acetonitrile with addition of increasing amounts of triethylamine: 0.16 (black), 0.33 (red), 0.49 (light blue), 0.66 (dark blue), 0.82 (violet), 0.99 (mauve), 1.15 (orange) and 1.32 (green) equivalent of base.

SUMMARY

In this work we have prepared **4** that is an analog of **1** with a different arm complexing the ferric ion. We showed with related complexes **2** and **3** that the modification introduced, replacement of two pyridines in **1** by two 1-methylbenzimidazoles in **4**, lowers the redox potential of the system by ca 60 mV. A second difference concerns the isomerization processes observed to be slow in **1** but which are not detected in **4**. Although the presence of similar isomers was detected in ¹H-NMR, it is possible that the different structural constraints

within the ligand are responsible for this difference. Most importantly, the electronic structure of the two complexes are very similar and especially the localization of the valences of the two Fe ions. This feature will make possible the study of the deprotonation-induced electron transfer to assess the redox potential influence.

EXPERIMENTAL SECTION

General methods.

Materials: Acetonitrile for spectroscopic measurements was distilled under argon over CaH₂ and stored within an inert atmosphere glovebox. All other reagents were of reagent grade quality and used as received.

Physicochemical studies: ¹H-NMR spectra were recorded in deuterated acetonitrile on a Bruker AC 200 with a 5 mm indirect detection as described previously.¹⁰ Mass spectra were obtained in the electrospray ionization mode on a LCQ-Finnigan Thermoquest spectrometer equipped with an octupolar analyser and an ion trap. Electronic absorption spectra were recorded in acetonitrile (0.18 mM solution with 1 cm optical length cuvettes) on a Varian Cary® 50 spectrometer. Mössbauer spectra were recorded on 2-4 mM solutions of ⁵⁷Fe-fully enriched complexes. The experiments were performed using a horizontal transmission cryostat (Oxford Instruments) and a 50 mCi source of ⁵⁷Co(Rh) as previously described.⁶ All velocity scales and isomer shifts are referred to metallic iron foil at room temperature.

bis((1-methylbenzimidazol-2-yl)methyl)amine. Dechlorhydratation of the *N*-methyl-*o*-phenylenediamine was performed at first. 4 g (20.5 mmole) of the *N*-methyl-*o*-phenylenediamine dihydrochloride was dissolved in 40 mL of CH₂Cl₂. 6 mL of a saturated aqueous solution of NaHCO₃ were added to the flask. Small quantities of NaHCO₃ were added until the end of CO₂ release. The solution was then carefully filtered, stirred 30 min with Na₂SO₄, and evaporated. Six washings with 5 mL of CH₂Cl₂ were performed and the

resulting solution was evaporated using the rotating evaporator. 2.46 g (20.1 mmole) of the *N*-methyl-*o*-phenylenediamine were collected as a red highlighted dark liquid ($\rho = 98\%$). It was introduced as it is in a flask with 965 mg (7.25 mmole) of finely grinded iminodiacetic acid and maintained under circulating argon. The flask with a Y-shape condensation column at the top was placed into an oil bath preliminary heated at 192°C. After 90 min, the mixture was allowed to cool at room temperature. Chromatography on silica was performed to separate the desired product from the starting diamine. Firstly CH₂Cl₂ was used as the eluent that was slowly added by 2 and 4% of CH₃OH. The bis((1-methylbenzimidazol-2-yl)methyl)amine was obtained as a whitish orange powder of 90 to 95% purity.

Binucleating ligands.

The syntheses of the two asymmetrical ligands were realized according to the published synthetic scheme that involves successive condensation of the two desired secondary amines to the chloromethylphenol derivatives. The general procedure for the condensation is described below. 1 mmol of the chloro derivative is dissolved in 10 mL of THF and added to a 10 mL THF solution of 1 mmol of the secondary amine containing an excess of triethylamine (600 μ L, 4.3 mmol). After one hour, the mixture is filtered and the filtrate is evaporated. The oil is dissolved in 3-20 mL dichloromethane, dried on Na₂SO₄ and evaporated to give the final product ($\rho \approx 90\%$).

2,6-bis[bis(((1-methylbenzimidazol-2-yl)methyl)amino)methyl]-4-methylphenol. Under argon, 200 mg (0.59 mmole) of bis((1-methylbenzimidazol-2-yl)methyl)amine (90% purity) was dissolved in 18 mL of THF with 560 μ L (4 mmole) of NEt₃. The solution was added to 66 mg (0.32 mmole) of 2,6-bis(chloromethyl)-*p*-cresol dissolved in 2 mL of THF. The mixture was gently stirred under argon for 30 h at least with regular ¹H-NMR control. A white precipitate of triethylamine hydrochloride formed. The orange solution was then filtered, washed with THF and evaporated to dryness. The solid product was dissolved in

12 mL of CH₂Cl₂, washed twice with 8 mL of saturated NH₄Cl aqueous solution, and then three times with 8 mL of H₂O before drying on Na₂SO₄. Evaporation of the solution leads to 187 mg (0.25 mmole) of a whitish orange solid ($\rho = 85 \%$).

2-(bis((1-methylbenzimidazol-2-yl)methyl)aminomethyl)-6-(N-(2-amino)benzyl-N-(2-picolyl)aminomethyl)-4-methylphenol. The last step of the ligand synthesis aims at reducing the nitro group by tin in presence of hydrochloric acid. The synthetic protocole is adapted from the previously published one for 2-(bis(2-picolyl)aminomethyl)-6-(N-(2-amino)benzyl-N-(2-picolyl)aminomethyl)-4-methylphenol.⁶

Syntheses of complexes 2-4. The general procedure is as follows. 0.18 mmol of the binucleating ligand and 0.18 mmol of the dicarboxylate salt Na₂mpdp are dissolved in 5 - 10 mL of degassed solvent (MeOH for **1**, CH₃CN for **2** and **3**). When CH₃CN is used, some Na₂SO₄ is added to trap residual water. To this solution was added dropwise 0.36 mmol of ferrous perchlorate dissolved in 8 mL of degassed MeOH. The solution was stirred under argon for 1h-1h30 at room temperature and if required filtrated under Ar. Dioxygen was bubbled in the solution (ca 15 min). After 1 day, a small quantity of precipitate was formed and the solution was kept at ca 6 °C. The precipitate was carefully filtered and dried under vacuum. ($\rho \approx 60\%$)

References

- (1) Creutz, C.; Taube, H. *J. Am. Chem. Soc.* **1973**, *95*, 1086.
- (2) Ceccon, A.; Santi, S.; Orian, L.; Bisello, A. *Coord. Chem. Rev.* **2004**, *248*, 683.
- (3) D'Alessandro, D.; Keene, F. R. *Chem. Rev.* **2006**, *106*, 2270.
- (4) Kaim, W.; Sarkar, B. *Coord. Chem. Rev.* **2007**, *251*, 584.
- (5) Aguirre-Etcheverry, P.; O'Hare, D. *Chem. Rev.* **2010**, *110*, 4839.

- (6) Gouré, E.; Thiabaud, G.; Carboni, M.; Gon, N.; Dubourdeaux, P.; Garcia-Serres, R.; Clémancey, M.; Oddou, J.-L.; Robin, A. Y.; Jacquamet, L.; Dubois, L.; Blondin, G.; Latour, J.-M. *Inorg. Chem.* **2011**, *50*, 6408.
- (7) Neyhart, G. A.; Meyer, T. J. *Inorg. Chem.* **1986**, *25*, 4807.
- (8) McCormick, J. M.; Reem, R. C.; Solomon, E. I. *J. Am. Chem. Soc.* **1991**, *113*, 9066.
- (9) Balasubramanian, R.; Blondin, G.; Canales, J. C.; Costentin, C.; Latour, J.-M.; Robert, M.; Savéant, J.-M. *J. Am. Chem. Soc.* **2012**, *134*, 1906.
- (10) Lambert, E.; Chabut, B.; Chardon-Noblat, S.; Deronzier, A.; Chottard, G.; Bousseksou, A.; Tuchagues, J.-P.; Laugier, J.; Bardet, M.; Latour, J.-M. *J. Am. Chem. Soc.* **1997**, *119*, 9424.
- (11) Chardon-Noblat, S.; Horner, O.; Chabut, B.; Avenier, F.; Debaecker, N.; Jones, P.; Pécaut, J.; Dubois, L.; Jeandey, C.; Oddou, J.-L.; Deronzier, A.; Latour, J.-M. *Inorg. Chem.* **2004**, *43*, 1638.
- (12) Kanda, W.; Moneta, W.; Bardet, M.; Bernard, E.; Debaecker, N.; Laugier, J.; Bousseksou, A.; Chardon-Noblat, S.; Latour, J.-M. *Angew. Chem., Int. Ed. Engl.* **1995**, *34*, 588.
- (13) Borovik, A. S.; Papaefthymiou, V.; Taylor, L. F.; Anderson, O. P.; Que Jr., L. *J. Am. Chem. Soc.* **1989**, *111*, 6183.
- (14) Mashuta, M. S.; Webb, R. J.; McCusker, J. K.; Schmitt, E. A.; Oberhausen, K. J.; Richardson, J. F.; Buchanan, R. M.; Hendrickson, D. N. *J. Am. Chem. Soc.* **1992**, *114*, 3815.
- (15) Suzuki, M.; Oshio, H.; Uehara, A.; Endo, K.; Yanaga, M.; Kida, S.; Saito, K. *Bull. Chem. Soc. Jpn.* **1988**, *61*, 3907.
- (16) Gouré, E.; Carboni, M.; Dubourdeaux, P.; Clémancey, M.; Balasubramanian, R.; Lebrun, C.; Bayle, P.-A.; Blondin, G.; Latour, J.-M. *Chem. Eur. J.* **2013**, Submitted.
- (17) Gouré, E.; Carboni, M.; Dubourdeaux, P.; Clémancey, M.; Gon, N.; Balasubramanian, R.; Lebrun, C.; Pécaut, J.; Blondin, G.; Latour, J.-M. *Inorg. Chem.* **2013**, To be submitted.

Supplementary information for the manuscript

pH-driven valence inversion in mixed-valent diiron(II,III) complexes.

Redox potential influence on the proton-coupled electron transfer.

Eric Gouré,^a Patrick Dubourdeaux,^a Martin Clémancey,^a Nathalie Gon,^a Ramachandran Balasubramanian,^a Colette Lebrun,^b Jacques Pécaut,^b Geneviève Blondin^{a,} and Jean-Marc Latour^{a,*}*

(a) Univ. Grenoble Alpes, LCBM, 38054 Grenoble, France, CEA/DSV/iRTSV/CBM/pmb, 38054 Grenoble, France, CNRS UMR5249, LCBM, 38054 Grenoble, France

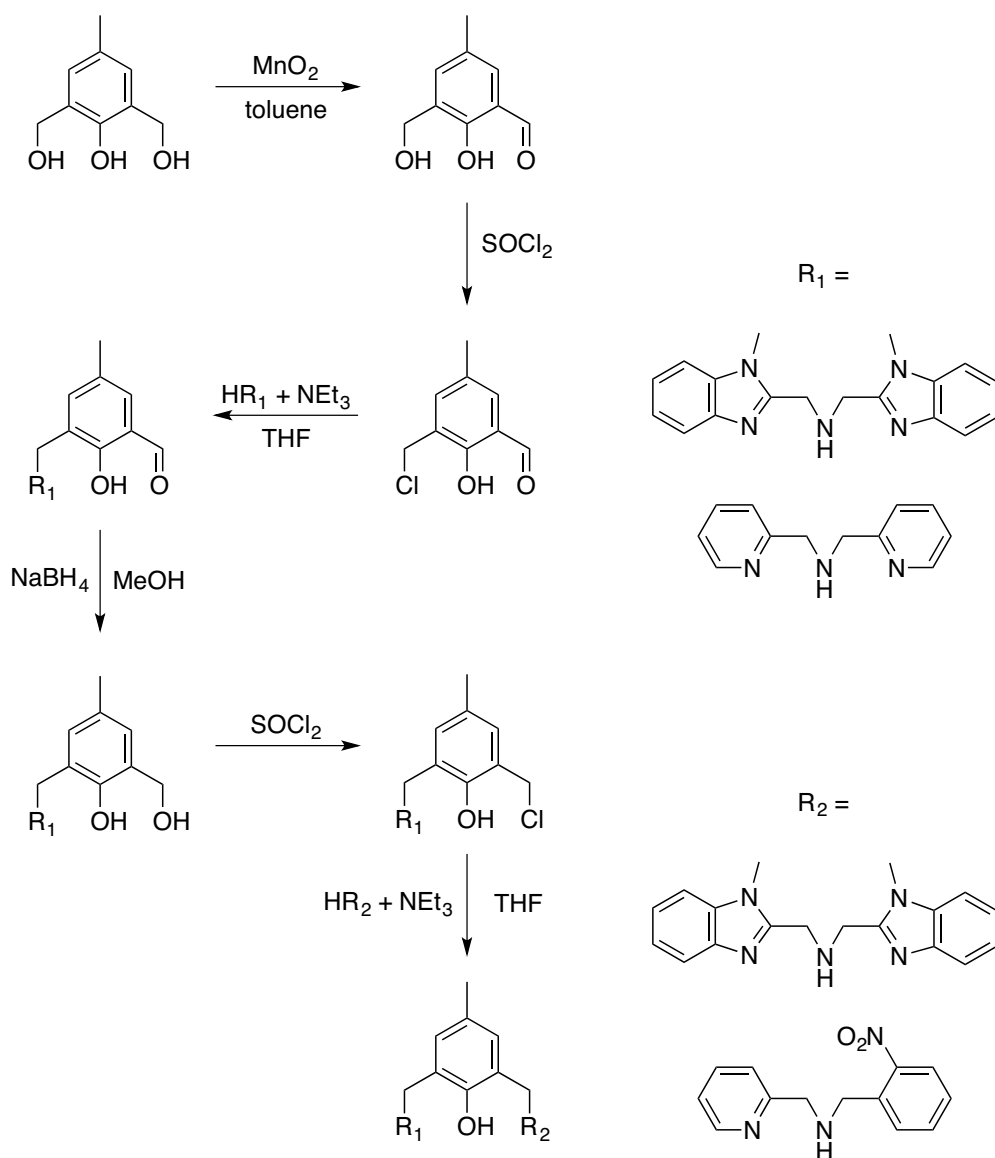
(b) Univ. Grenoble Alpes, RICC, 38054 Grenoble, France, CEA/DSM/INAC/SCIB/RICC, 38054 Grenoble, France, UMR E 3, RICC, 38054 Grenoble, France

genevieve.blondin@cea.fr; jean-marc.latour@cea.fr

List of supplementary figures, comments, tables and schemes

Scheme S1. General scheme of ligand synthesis

Scheme S1. General scheme of ligand synthesis



3 Draft n°2

“pH-driven valence inversion in mixed-valent diiron(II,III) complexes. Influence of the protic ligand on the proton-coupled electron transfer”

pH-driven valence inversion in mixed-valent diiron(II,III) complexes. Influence of the protic ligand on the proton-coupled electron transfer.

Eric Gouré,^a Michaël Carboni,^a Patrick Dubourdeaux,^a Martin Clémancey,^a Nathalie Gon,^a Ramachandran Balasubramanian,^a Colette Lebrun,^b Jacques Pécaut,^b Geneviève Blondin^{a,} and Jean-Marc Latour^{a,*}*

(a) Univ. Grenoble Alpes, LCBM, 38054 Grenoble, France, CEA/DSV/iRTSV/CBM/pmb, 38054 Grenoble, France, CNRS UMR5249, LCBM, 38054 Grenoble, France

(b) Univ. Grenoble Alpes, RICC, 38054 Grenoble, France, CEA/DSM/INAC/SCIB/RICC, 38054 Grenoble, France, UMR E 3, RICC, 38054 Grenoble, France

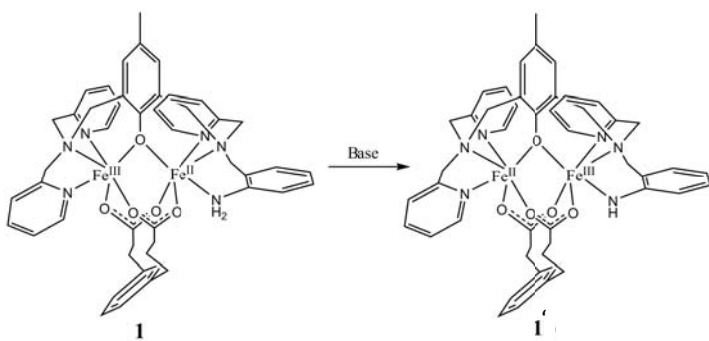
genevieve.blondin@cea.fr; jean-marc.latour@cea.fr

KEYWORDS (Word Style “BG_Keywords”). If you are submitting your paper to a journal that requires keywords, provide significant keywords to aid the reader in literature retrieval.

ABSTRACT (Word Style “BD_Abstract”). All manuscripts must be accompanied by an abstract. The abstract should briefly state the problem or purpose of the research, indicate the theoretical or experimental plan used, summarize the principal findings, and point out major conclusions. Abstract length is one paragraph.

INTRODUCTION

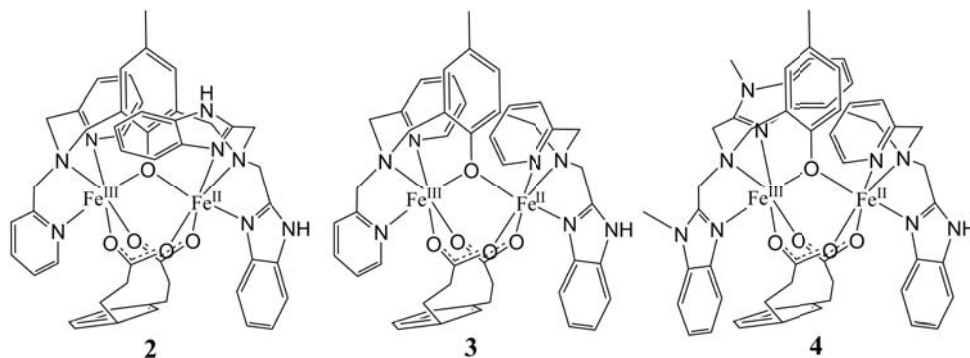
It is well established from Pearson theory that oxidation of a metal ion makes it a harder acid and that similarly deprotonation of a ligand makes it a harder base. As a consequence it has been often observed that deprotonation of a ligand within a complex is connected to oxidation of the metal. This link has been recently thoroughly studied by Mayer and coworkers in their seminal work on proton coupled electron transfers.¹⁻³ In this work they established the thermodynamic cycles of mononuclear iron bi-imidazole complexes. We recently reported that the deprotonation of an aniline ligand can induce the oxidation of a ferrous center. This process occurs within a dinuclear mixed-valent $\text{Fe}^{\text{III}}\text{Fe}^{\text{II}}$ complex **1** and the oxidation of the Fe^{II} center is compensated by the reduction of the Fe^{III} center leading to an overall intervalence transfer as shown in Scheme 1.⁴ This reaction can be viewed as a proton-coupled electron transfer (PCET).



Scheme 1

A similar process has been described only in an heterodinuclear RuOs complex⁵ and in the semimet forms of the dioxygen carrier hemerythrin, albeit in the latter case the system switches between a ferrous pentacoordinate site and an hydroxo-bound ferric center.⁶ The thermodynamic and kinetic aspects of the deprotonation reaction of **1** were investigated by spectroscopic and electrochemical techniques. A thorough electrochemical study of its redox

properties and isotope labeling experiments have revealed that the deprotonation-induced intervalence transfer is indeed a concerted proton-electron transfer (CPET).⁷ Owing to the peculiarity of this system, it appeared of interest to assess how the redox potentials of the iron centers and the acidity of the protic ligand influence this singular PCET. The modularity of the ligand constitution and its sequential synthesis⁸ (Scheme S1) allow to vary the complexing branch of each metal. In this article we changed the nature of the protic ligand replacing the aniline by a benzimidazole. This allowed us to prepare complex **3** that differs from **1** by the aniline/benzimidazole replacement and complex **4** that derives from **3** by the additional replacement of the bis((pyridyl-2-yl)methyl)amine branch by a bis((1-methylbenzimidazol-2-yl)methyl)amine. In addition, as a reference complex, we prepared complex **2** that features two protic groups in a bis((benzimidazol-2-yl)methyl)amine branch, the other branch being constituted by a bis((pyridyl-2-yl)methyl)amine (Scheme 2).



Scheme 2. Mixed-valent diiron complexes studied in this work.

RESULTS

Syntheses of the ligands and complexes. The three ligands used in the present work were synthesized according to the already described procedure (Scheme S1) adapted for inserting the desired bis((pyridyl-2-yl)methyl)amine, bis((1-methylbenzimidazol-2-yl)methyl)amine and *N*-(pyridyl-2-yl)methyl-*N*-(benzimidazol-2-yl)methylamine and bis((benzimidazol-2-yl)methyl)amine branches. Complexes **2-4** were prepared by usual procedures.^{9,10} They were

all characterized by ElectroSpray Ionization-Mass Spectrometry (ESI-MS) and spectroscopic techniques (see below).

X-ray structure of $2(ClO_4)_2 \cdot 2CH_3CN$. Figure 1 displays the X-ray structure of the dicationic complex **2**. The crystal parameters are listed in Table 1, and important bond lengths and angles are given in Table 2. The two iron ions are bridged by the phenoxide oxygen O1 and the two carboxylato groups of the *m*-phenyl-dipropionate ligand (mpdp²⁻). The coordination of Fe1 and Fe2 is complemented by the three nitrogen atoms of the bispicolylamine branch or those of the bis((benzimidazol-2-yl)methyl)amine branch, respectively. The overall N₃O₃ coordination around Fe1 and Fe2 corresponds to a rhombically distorted octahedron. Examination of the metal-ligand distances listed in Table 2 shows that they average 2.122 Å around Fe1 and 2.069 Å around Fe2. These values are close to those observed in [(bpmp)Fe₂(μ-OPr)₂]²⁺ (**5**)¹¹ (2.131 and 2.057 Å) or in [(bimp)Fe₂(μ-OBz)₂]²⁺ (**7**)¹² (2.145 and 2.063 Å). They indicate two different valences for the iron ions, namely a Fe^{II} and a Fe^{III}, that can be assigned to Fe1 and Fe2, respectively. The mixed valent character is fully consistent with the presence of two perchlorate anions per diiron units. This location of the valences is consistent with the better donating character of the benzimidazole compared to that of the pyridine.

The two benzimidazole rings are hydrogen bonded to the perchlorate anions. Three out of the four oxygen atoms for the two perchlorate anions are disordered. Only oxygen O11 on Cl1 and O21 on Cl2 present 100% occupancy. H7N on the N7 atom is located at 2.167 Å from the O21 while H8N on the N8 atom is separated by 2.192 Å (resp. 2.056 Å) from O14 (resp. O14B) with 81.8% site occupancy (resp. 18.2%). These hydrogen bonds give a slight benzimidazolide character to the ligands, thus further stabilizing the +III oxidation state of Fe2.

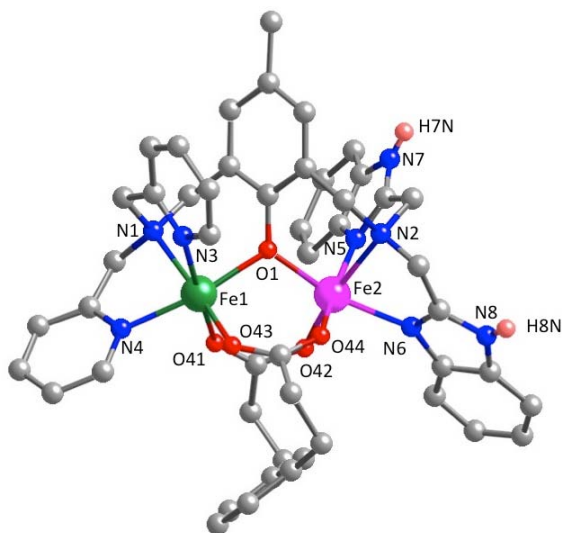


Figure 1. X-ray structure of the dicationic species **2**. Only the hydrogen atoms bond to the nitrogen atoms of the benzimidazole rings are shown.

Table 1. Summary of crystal data and structure refinement for compound **2**(ClO₄)₂•2CH₃CN.

chemical formula	C ₅₃ H ₅₃ Cl ₂ Fe ₂ N ₁₀ O ₁₃
formula weight	1220.65
crystal system	triclinic
space group	<i>P</i> -1
<i>a</i> (Å)	12.3827(9)
<i>b</i> (Å)	13.2351(7)
<i>c</i> (Å)	18.8207(11)
α (deg)	74.765(5)
β (deg)	71.367(6)
γ (deg)	71.904(5)
<i>V</i> (Å ³)	2732.0(3)
<i>Z</i>	2
<i>D</i> _{calcd} (g cm ⁻³)	1.484
λ (Å), μ (mm ⁻¹)	0.71073, 0.703
<i>T</i> (K)	150(2)
θ range (deg)	3.34 to 28.28
reflns collected	28892
unique reflns	13554
data/restraints/parameters	13554/12/987
<i>R</i> ₁ , <i>wR</i> ₂ (<i>I</i> > 2 σ (<i>I</i>))	0.0528, 0.0974

Table 2. Selection of bond lengths (Å) and angle (deg) for compound **2**(ClO₄)₂•2CH₃CN.

Fe1–O1	2.0745(18)	Fe2–O1	1.9588(17)
Fe1–O41	2.1413(17)	Fe2–O42	1.9531(18)
Fe1–O43	2.0014(7)	Fe2–O44	2.0102(18)
Fe1–N1	2.208(2)	Fe2–N2	2.267(2)
Fe1–N3	2.176(2)	Fe2–N5	2.115(2)
Fe1–N4	2.128(2)	Fe2–N6	2.109(2)
Fe1···Fe2	3.388	Fe1–O1–Fe2	114.27(8)

¹H-NMR Spectroscopy. Figure 2 reproduces the ¹H-NMR spectra in the range 450-130 ppm recorded on CD₃CN millimolar solutions of complexes **2-4**. The domain from 130 to –20 ppm is shown in Figure S1 of the Supporting Information. These spectra can be analyzed by comparison with the previously published spectra of the symmetric complexes [(bpmp)Fe₂(μ-OPr)₂]²⁺ (**5**),¹¹ [(bimp)Fe₂(μ-OAc)₂]²⁺ (**7**)¹² and [(L-BzImMe₄)Fe₂(μ₂-mpdp)]²⁺ (**8**),¹³ and the asymmetric one [(L-(BzImMe)₂(Py)₂)Fe₂(μ₂-mpdp)]²⁺ (**9**).¹³

The first notable feature of the spectra of **2-4** is their range, 366 ppm for **2**, 432 ppm for **3** and 379 ppm for **4**, which are similar to those observed for **5**, **7**, **8** and **9**, 390, 350, 340 and 366 ppm, respectively. This relatively narrow spectral ranges are associated with an intervalence exchange between the two equivalent mixed valent forms Fe^{II}Fe^{III} and Fe^{III}Fe^{II} that is fast on the ¹H-NMR time scale. This is supported by the number of peaks detected for complexes **5**, **7** and **8** based on symmetrical ligands that is about half the number of protons of the molecule. The similar chemical shift window observed for complexes **2-4** suggests a similar behavior in spite of the asymmetry of the ligand. Indeed, it has been previously observed within this family of complexes that a high asymmetry in the coordination of the iron centers induced a localization of the valences that led to a wider ¹H-NMR spectral range.⁸ For instance, the ¹H-NMR spectrum of [(L-Bn)Fe₂(μ₂-mpdp)(S)]²⁺ (S = CH₃CN or

H₂O) spreads over more than 600 ppm.^{9,10} So, the less than 450 ppm spectral window is a strong indication of an intramolecular electron transfer within the Fe pair that is fast on the ¹H-NMR time scale.

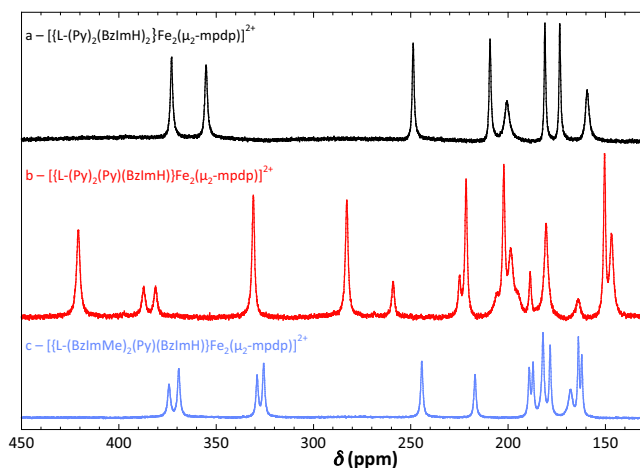


Figure 2. 450-130 ppm domain of the ¹H-NMR spectra of complexes **2** (top black trace), **3** (middle red trace) and **4** (bottom blue trace) recorded on CD₃CN solutions for **2** and **3** and on a CD₃CN:*d*₇-DMF (400:150 v:v) solution for **3**.

For complexes **7** and **8**, owing to the symmetry of the ligand and to the valence delocalization, only three peaks are detected above 130 ppm which are associated to methylenic protons bound to the phenoxide (N-CH₂-Ph) or to the two aromatic amines (N-CH₂-Amine) of each branch. In **5**, two additional signals are detected in this region that correspond to two *ortho*-pyridinic protons.¹¹ They present a larger linewidth than the previously mentioned CH₂ proton signals owing to their short distances to the Fe ions. We will resort on these features to analyze the signals detected above 130 ppm for complexes **2-4**. Owing to the complexity of the spectra a precise assignment of a resonance to a single

proton of the methylene group is precluded at this stage but $^1\text{H-NMR}$ monitoring of the deprotonation reaction will provide insights into these assignments (see below).

Table 3. Chemical shift values (in ppm) in complexes **2-5** and **7-9** for methylenic protons directed toward the iron centers, *ortho*-pyridinic protons when present, and the methyl group in *para* position of the bridging phenoxide.

		N-CH ₂ -Ph ^a	N-CH ₂ -Amine ^a	<i>o</i> -Py	CH ₃ -Ph ^a	ref
5		377	262 184	197.5 152.4	72.1	¹¹
7		342	214 175		65.7	¹²
8		337.5	198.5 170.1		65.5	¹³
9		361.7 / 355.8	235.7 / 208.6 180.3 / 163.1	198.1 152.6	66.0	¹³
2		372.9 / 355.1	248.9 / 209.3 180.9 / 173.7	200.7 159.2	68.9	This work
3	isomer 1 (75%)	420.7 / 331.2	283.1 / 221.8 259.0 / 224.8	198.9 180.3 ?	71.4	This work
	isomer 2 (25%)	387.1 / 381.1	202.5 / 150.2 188.7 / 146.6	205.5 195.3 164.0	54.9	
4	isomer 1 (55%)	369.1 / 325.7	244.5 / 178.5 181.9 / 164.0	167.8	67.2	This work
	isomer 2 (45%)	374.1 / 329.1	217.0 / 189.2 187.3 / 162.1	≈184	65.3	

^a Ph stands for the central phenoxide ring while Amine is the pyridine, benzimidazole or 1-methylbenzimidazole arm.

Table 3 lists the chemical shift values associated to the more downfield shifted methylenic protons. For **5**, **7** and **8**, the most downfield shifted proton is associated to the methylene group linked to the phenoxide (noted N-CH₂-Ph), while the two narrow peaks at lower chemical shift belong to the methylene groups linked to the aromatic amine (noted N-CH₂-

Amine).¹¹⁻¹³ For **9**, a chemical asymmetry exists and each of these three signals is split in two components.¹³ The same phenomenon is observed for **2** and six peaks are indeed detected. The ¹H-NMR signatures of complexes **3** and **4** are more intricate because of the increased number of peaks detected even in the 450–130 ppm domain. For both complexes, based on the peak intensities, a close inspection of the spectrum (see Figure 2) reveals two different sets of resonances, for both the methylenic and *ortho*-pyridinic protons. In addition, it is worth noticing that two signals originate from the methyl group in *para* position of the phenoxide bridge for **3** and **4** (see Figure S1 and Table 3) with the same intensity ratio as the methylenic protons. These combined features strongly suggest that two different isomers coexist in solution for **3** and **4**. We have previously evidenced that in acetonitrile solution the aminobenzyl group of **1** can be either *trans* or *cis* to the bridging phenoxide, the *cis* isomer being favored.¹⁴ Similarly, we thus propose that the benzimidazole ligand in **3** and **4** may either coordinate the iron in *cis* or *trans* position with respect to the bridging phenoxide. The resonances for each isomer are listed in Table 3. The population ratios will be close to 75:25 for **3** and 55:45 for **4**. However it is difficult to assess if these values correspond to the *cis:trans* ratio or to the reverse.

Addition of triethylamine. UV-visible absorption spectroscopic monitoring. Addition of base on the three complexes **2-4** was investigated. The goal was to generate the benzimidazolide. At first, the reaction was monitored using UV-visible absorption spectroscopy. A typical experiment is shown in Figure 3 where the spectra recorded on a CH₃CN solution of complex **4** upon addition of NEt₃ are reproduced. The corresponding titration experiments performed for complexes **2** and **3** are given in Figures S2 and S3 in the Supporting Information.

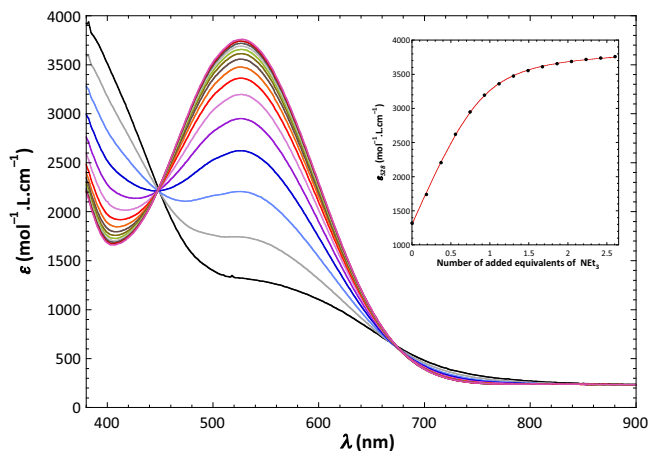


Figure 3. Evolution of UV-visible absorption spectra recorded upon addition of aliquots of 0.3 eq of NEt_3 on a 0.4 mM acetonitrile solution of **4**.

A single band at 550 nm with a molar extinction coefficient value of $1285 \text{ M}^{-1}.\text{cm}^{-1}$ is observed in the starting spectrum of **4**. Upon addition of NEt_3 an intense band at 528 nm develops with a molar extinction coefficient close to $3800 \text{ M}^{-1}.\text{cm}^{-1}$ and the transformation occurs with an isosbestic point at 448 nm. Similar behaviors are observed for complexes **2** and **3**. The initial spectra exhibit a single band at 540 nm with $\epsilon_{540} = 1020 \text{ M}^{-1}.\text{cm}^{-1}$ and at 545 nm with $\epsilon_{545} = 1080 \text{ M}^{-1}.\text{cm}^{-1}$ for complexes **2** and **3**, respectively. Addition of NEt_3 induces the increase of an intense absorption respectively at 533 ($\epsilon_{533} \approx 3800 \text{ M}^{-1}.\text{cm}^{-1}$) and 528 nm ($\epsilon_{528} \approx 3800 \text{ M}^{-1}.\text{cm}^{-1}$) with a single isosbestic point at 705 nm for **2** and two at 403 and 682 nm for **3**. The similar λ_{max} - and ϵ -values for the spectra of species **2-4** are fully consistent with phenoxide-to- Fe^{III} charge transfer transitions as usually observed within this family of complexes.^{8,10,11} The two isomers for **3** and **4** evidenced by $^1\text{H-NMR}$ spectroscopy differ by the coordination of the benzimidazole and the pyridine groups on one iron site. We showed that for **1** where the spectra of the two isomers can be kinetically resolved that the

pyridine/aniline exchange on the ferrous site causes only minor spectral modifications on the $\text{PhO}^- \rightarrow \text{Fe}^{\text{III}}$ charge transfer transition.¹⁴ It is likely that these changes would be too small even if occurring on the Fe^{III} site. Action of NEt_3 leads to identical features whatever the starting complex indicating a common origin. Accordingly, we propose that NEt_3 indeed induces the deprotonation of the benzimidazole ligand and that the intense band at ≈ 530 nm would originate mainly from a benzimidazolide-to- Fe^{III} charge transfer transition. We will further denote **2'-4'** the generated complexes. A contribution of the $\text{PhO}^- \rightarrow \text{Fe}^{\text{III}}$ charge transfer to this transition is likely but is not expected to be dominating owing to the moderate values of their molar extinction coefficient. This assignment is supported by the observation that the original anilide complex **1'**, the deprotonated form of complex **1** (see Scheme 1), exhibits absorptions that are significantly different both in energy ($\lambda_{\text{max}} = 730$ vs 530 nm, $E = 13700$ vs 18870 cm^{-1}) and in intensity ($\epsilon_{533} = 5250$ vs 3800 $\text{M}^{-1}.\text{cm}^{-1}$).^{4,14}

The observed variations upon the addition of NEt_3 of the extinction coefficient value can be satisfyingly reproduced using Eq. 1 that is derived according to the deprotonation reaction of the complexes **2-4** by the added base characterized by the equilibrium constants $K_{1,3}$ (see Figures 3, S2 and S3). In Eq. 1, a stands for the addition index, δn for the number of molecules of NEt_3 in each aliquot and n_0 for the starting number of molecules of the complex **2-4**.

$$\epsilon_{\text{obs}}(a) = \epsilon_{\text{CxH}} + (\epsilon_{\text{Cx}} - \epsilon_{\text{CxH}}) \frac{K \left(1 + a \frac{\delta n}{n_0}\right) - \sqrt{K^2 \left(1 - a \frac{\delta n}{n_0}\right)^2 + 4 K a \frac{\delta n}{n_0}}}{2(K-1)} \quad (\text{Eq. 1})$$

The best fit gives $K_1 = 11.5 \pm 1.5$, $K_2 = 9.7 \pm 1.0$ and $K_3 = 9.1 \pm 0.7$. The acidic strengths of the three complexes **2-4** are comparable consistently with the identical nature of the deprotonated ligand.

¹H-NMR spectroscopy. Figure 4 gathers the ¹H-NMR spectra recorded after addition of ≈3 eq of NEt₃ on CD₃CN solutions of complexes **2-4**. The missing 105 to –30 ppm domain is reproduced in Figure S4 of the Supporting Information. The observed spectra are relevant of mixed valent diiron complexes. One major difference with the ¹H-NMR spectra shown in Figure 2 and recorded prior the addition of NEt₃ is the enhanced spectral window measured here: from 490 to –23 ppm, 530 to –27 ppm and 515 to –25 ppm for **2'**, **3'** and **4'**, respectively. This is a strong indication that the iron valences have become localized on the ¹H-NMR time scale.⁸ This trap of the iron valences is in full agreement with the deprotonation of the benzimidazole ligand, the generated benzimidazolide stabilizing the +III oxidation state for the iron, as evidenced by the LMCT transition observed in UV-visible absorption spectroscopy (see above).

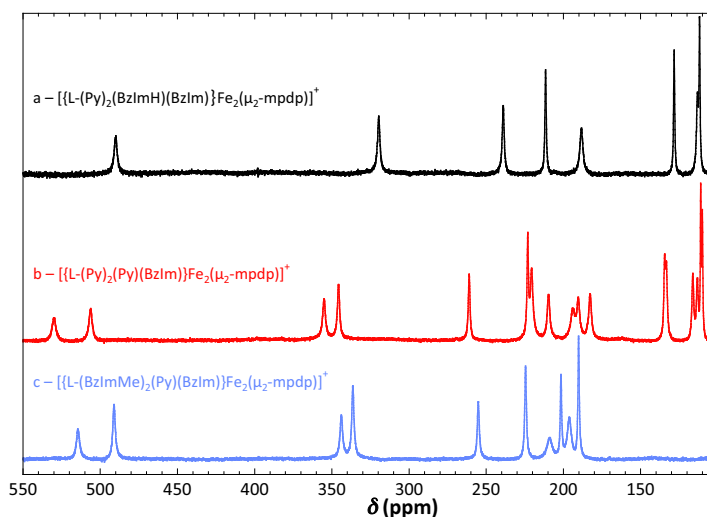


Figure 4. 550-105 ppm domain of the ¹H-NMR spectra of complexes **2'** (top black trace), **3'** (middle red trace) and **4'** (bottom blue trace) recorded on CD₃CN solutions for **2-4** after the addition of 3 to 4 equivalents of NEt₃.

The spectrum of **2'** exhibits only eight peaks in the 550-105 ppm domain what is reminiscent of those of [(L-PhO)Fe₂(μ₂-mpdp)]⁺ and of [(L-BnO)Fe₂(μ₂-mpdp)]⁺ where the terminal phenoxide binds the Fe^{III} site.^{8,9} By analogy with these compounds, the three most downfield shifted signals at 490.0, 319.7 and 239.0 ppm can be assigned to methylenic protons that are on the Fe^{III} side that is from Ph-CH₂-N-(CH₂-BzImH)(CH₂-BzIm⁻), N-(CH₂-BzIm⁻) and N-(CH₂-BzImH) groups, respectively. Interestingly, the first two signals are clearly split in two components in complexes **3'** and **4'**. The same holds for the signal issued from the methyl group in *para* position of the bridging phenoxide. The peak at 56.2 ppm for **2'** is split in two at 59.6 and 54.8 ppm for **3'** and at 58.8 and 54.8 ppm for **4'** (see Figure S4 in the Supporting Information). In addition the relative intensities of the signals within each pair of resonances within one complex are similar. This clearly indicates that two forms also exist for **3'** and **4'** after deprotonation as was observed for **1'**. Accordingly, we propose that the two forms evidenced by ¹H-NMR in **3'** and **4'** are the *cis* and *trans* isomers, depending on the coordination of the benzimidazolide with respect to the phenoxide bridge. It may appear surprising that a single isomer is detected for **2'** in ¹H-NMR. As a matter of fact, the existence of a *cis* and a *trans* isomer cannot be ruled out, but owing to the presence of the monodeprotonated bis((benzimidazol-2-yl)methyl)amine branch the two forms in **2'** would differ only by the localization of a single benzimidazole NH proton. It is likely that the exchange of the proton between the benzimidazole and the benzimidazolide may occur rapidly on the NMR time scale thus averaging the two sets of peaks of the isomers.

¹H-NMR spectroscopic monitoring of the deprotonation. Titration experiments were run on **2-4** and monitored by ¹H-NMR spectroscopy. Figure 5 shows the series of spectra in the 550–60 ppm range recorded on a CD₃CN solutions of **2** and **4** with increasing amounts of triethylamine. Spectra in the domain ranging from 100 to –100 ppm are shown in Figures S5

and S6 in the Supporting Information. The experiment was also performed on complex **3** but the DMF required to dissolve the complex unfortunately leads to a broadening of the peaks.

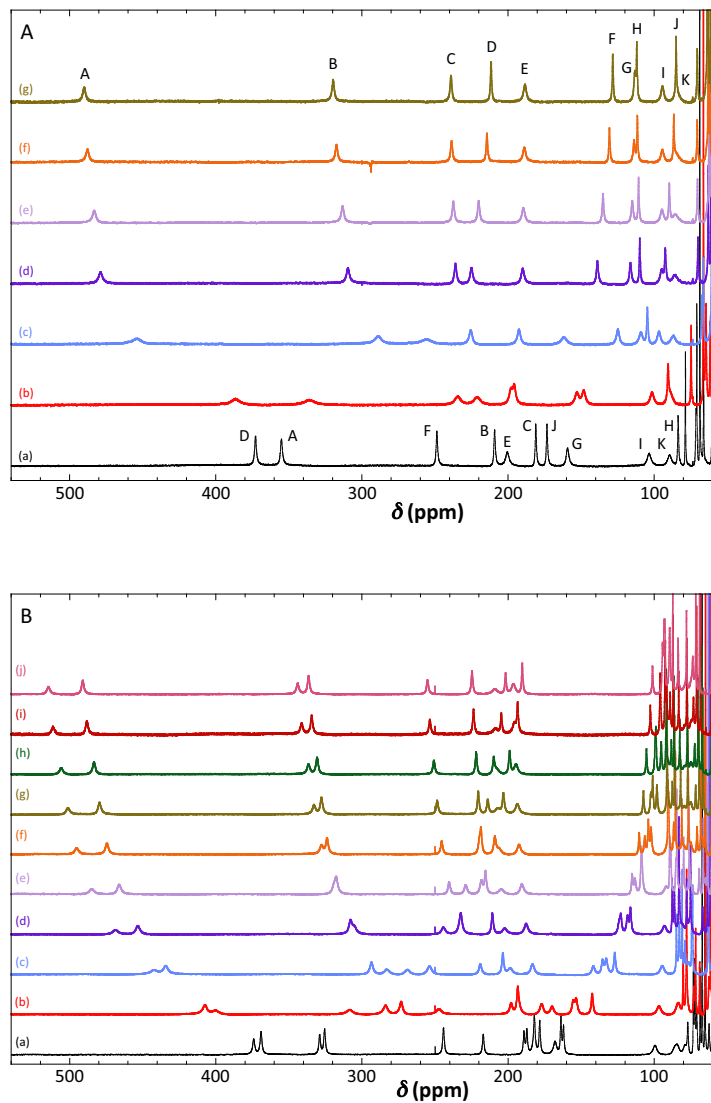


Figure 5. Series of ¹H-NMR spectra recorded on a CD₃CN solution of complexes **2** (top) and **4** (bottom) with increasing amounts of NEt₃; For **2**: (a) 0, (b) 0.26, (c) 0.79, (d) 1.32, (e) 1.59, (f) 2.11 and (g) 2.64 eq. For **4**: (a) 0, (b) 0.56, (c) 0.83, (d) 1.11, (e) 1.39, (f) 1.67, (g) 1.95, (h) 2.22, (i) 2.78 and (j) 3.34 eq.

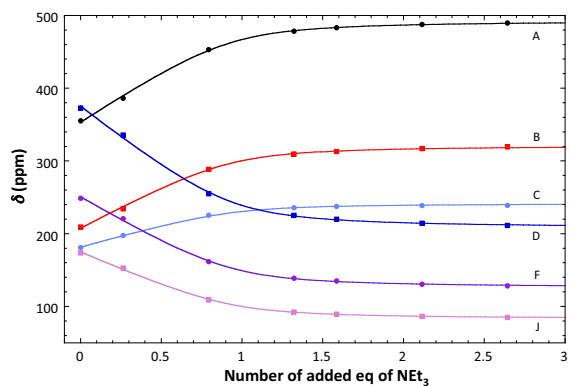


Figure 6. Dependence upon the addition of NEt_3 of the position of the signals A-D, F and J of complex **2**. Experimental points are shown as color dots while the solid lines are the best fit obtained according to Eq 1 adapted with δ in place of ϵ .

The evolutions upon the addition of base of the positions of the A-D, F and J signals of complex **2** are shown in Figure 6. Their variations can be perfectly reproduced by assuming that the observed position is the average of those observed in **2** and **2'** weighted by the proportion of the two species. This equation is the transcription of Eq 1 with δ in place of ϵ . The six curves lead to a unique value of the equilibrium constant K_1 associated to the deprotonation of **2** by NEt_3 : $K_1 = 18.5 \pm 5$. This value is consistent with that determined from the evolution of the UV-visible absorption spectra. The determination of a single value for K_1 allows us to validate the proposed signal assignments which are based on symmetric evolution of the resonances associated to related methylene groups. Signals A and D, which are the most downfield shifted in **2**, are associated to the $\text{N-CH}_2\text{-Ph}$ groups with signal A belonging to that on the bis((benzimidazol-2-yl)methyl)amine side and D that on the bis(pyridyl-2-yl-methyl)amine side. These assignments stem from the fact that in **2'** the valences are localized with the Fe^{III} ion on the side of the monodeprotonated bis((benzimidazol-2-yl)methyl)amine what identifies A. Signals B and C originate from the

N-CH₂-BzImH groups, since they move downfield upon deprotonation of the benzimidazole group in agreement with being located close to the Fe^{III} ion. Signals F and J are thus associated to the N-CH₂-Py groups of the bis(pyridyl-2-yl-methyl)amine branch. The peak assignment for complex **2** is summarized in Figure S7 of the Supporting Information.

A similar study can be performed for complex **4**. However, it is more intricate owing to the existence of two forms both before and after addition of NEt₃.

Mössbauer spectroscopy. Zero-field Mössbauer spectra were recorded at 80 K on acetonitrile solutions of complexes **2-4**, DMF being added to solubilize **3**. The left column of Figure 7 presents the spectra prior to the addition of triethylamine. Four lines can be distinguished and the spectra can indeed be reproduced with two equally intense quadrupole doublets. The isomer shift and quadrupole splitting values deduced from the simulation of the spectra are listed in Table 4. They are in full agreement with the presence of high-spin Fe^{II} and high-spin Fe^{III} sites. For complexes **3** and **4** the spectra can be simulated upon taking into account a single Fe^{II}Fe^{III} species whereas two isomers have been detected by ¹H-NMR spectroscopy. Benzimidazole and pyridine are both neutral amine ligands that coordinate through a nitrogen atom. In addition, the metallacycle formed upon coordination is a 5-membered one whatever the ligand. This can explain why the two isomers would present highly similar parameters in Mössbauer spectroscopy. The two isomers of **1** were distinguished by Mössbauer spectroscopy but in this case the two amines were less similar, the aminobenzyl ligand giving rise to a 6-membered metallacycle on the Fe^{II} ion as opposed to the 5-membered one with the (pyridyl-2-yl)methyl arm.¹⁴

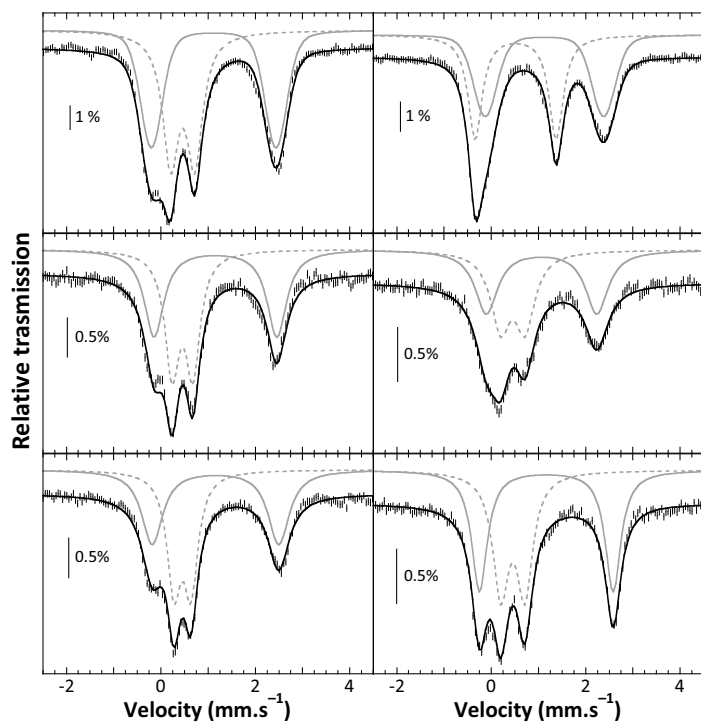


Figure 7. Experimental (hashed lines) zero-field and 80 K Mössbauer spectra recorded on solutions of complexes **2** (top), **3** (middle) and **4** (bottom) prior (left column) and after (right column) the addition of 3 eq of NEt_3 . Simulations are shown as solid black lines. Contributions of the Fe^{II} and Fe^{III} ions are reproduced above the spectra as solid and dotted grey lines, respectively.

Table 4. Nuclear parameters for complexes **2-4** and **2'-4'** from the simulation of the Mössbauer spectra presented in Figure 7.

Complex	Site	δ (mm.s ⁻¹)	ΔE_Q (mm.s ⁻¹)	Γ_{fwhm} (mm.s ⁻¹) ^a	Relative Area (%)
2	Fe ^{II}	1.12	2.64	-0.53	50
	Fe ^{III}	0.47	0.51	0.41	50
3	Fe ^{II}	1.16	2.60	0.50	50
	Fe ^{III}	0.46	0.44	0.37	50
4	Fe ^{II}	1.16	2.68	0.54	50
	Fe ^{III}	0.46	0.36	0.36	50
2'	Fe ^{II}	1.13	2.51	-0.54	50
	Fe ^{III}	0.52	1.72	0.36	50
3'	Fe ^{II}	1.07	2.34	0.58	50
	Fe ^{III}	0.46	0.52	0.50	50
4'	Fe ^{II}	1.17	2.83	0.40	50
	Fe ^{III}	0.46	0.51	0.41	50

^a Negative value indicates convolution with a pseudo-Voigt profile.

Spectra recorded under similar conditions after the addition of 3 eq. of NEt₃ on complexes **2-4** are displayed on the right column of Figure 7. Four lines can clearly be identified in the spectrum of **4'**. Three lines are evidenced in the spectra of species **2'** and **3'**, with the low velocity line presenting a shoulder. The three spectra can be satisfyingly reproduced by two quadrupole doublets of identical area (see Table 4), in full agreement with a Fe^{II}Fe^{III} composition. The three deprotonated species differ by the quadrupole splitting value determined on the Fe^{III} site: 1.72 mm.s⁻¹ for **2'** versus 0.52 and 0.51 mm.s⁻¹ for **3'** and **4'**, respectively. According to the previous studies on phenoxide⁸ and anilide^{4,14} complexes, this large ΔE_Q value strongly suggests that an anionic ligand is coordinated to the Fe^{III} ion in *trans* position with respect to the bridging phenoxide. Thus, only the *trans* isomer of **2'** with the

benzimidazole arm on the Fe^{III} site *trans* to the phenoxide bridge is formed upon deprotonation. Conversely, only the *cis* isomer is detected by Mössbauer spectroscopy for **3'** and **4'** whereas two forms were evidenced by ¹H-NMR spectroscopy.

Cyclic voltammetry. The cyclic voltammograms were recorded on millimolar acetonitrile solutions of complexes **2-4**, with addition of DMF to get complete dissolution of **3**. For all complexes two reversible one-electron transfers are observed, one in oxidation and one in reduction (see Table 5). The potential difference between the two redox waves is very similar for the three complexes. This ≈ 0.7 V separation value is commonly observed in mixed valent Hbpmf-derived diiron complexes.^{8,10,11,15} Substitution of one pyridine ligand in **5** by a benzimidazole group (**3**) leads to a ≈ 0.1 V decrease in potentials. The second substitution of a pyridine ligand is less efficient owing to the ≈ 0.05 V diminution observed between **3** and **2**. It may be noticed that the redox potentials of complex **2** are very similar to that of **6** where four benzimidazole groups are present. Complexes **4**, **8** and **9** share a common bis-1-methylbenzimidazole amine arm. The redox potentials of **4** are in between those of **8** and **9**, in agreement with the presence of two 1-methylbenzimidazoles and two pyridines in **8** and **9**, respectively *versus* the mixed benzimidazole-pyridine arm in **4**. Redox potentials of **2** and **4** are very similar. The dependence of the redox waves upon the scan rate has been investigated (see Figure S8). The separation between the anodic and cathodic peaks increases upon increasing scan rate thus evidencing a slow electron transfer for both processes whatever the complex.

Table 5. Redox potentials (in V vs SCE) measured for complexes **2-4** and a few related systems.

Complex	$E_{red}^{1/2}$	$E_{ox}^{1/2}$	ΔE	ref
2	-0.14	0.58	0.72	this work
3	-0.09	0.63	0.72	this work
4	-0.14	0.56	0.70	this work
5	-0.01	0.69	0.70	11
6	-0.12	0.56	0.68	15
7	-0.22	0.44	0.66	12
8	-0.18	0.52	0.70	13
9	-0.12	0.58	0.70	13

Progressive addition of triethylamine to the three complexes was performed and their CV recorded. They all behave in the same manner and Figure 8 illustrates that of **4** (see also Figures S11 and S12 in the Supporting Information). Upon addition of NEt_3 , the oxidation wave at 0.56 V decreases and a new oxidative process at 0.37 V concomitantly increases. This is in agreement with the deprotonation of the benzimidazole ligand and the formation a benzimidazolide complex (**4'**) that expectedly is oxidized at a less positive potential. By contrast, upon reaction with NEt_3 , the cathodic process is mostly unaffected. Such a behavior was already observed for the hydroxide $[(\text{L-Bn})\text{Fe}_2(\mu_2\text{-mpdp})(\text{OH})]^+$ complex.¹⁰ This suggests that the bis-ferrous deprotonated species is not stable and becomes rapidly reprotonated.

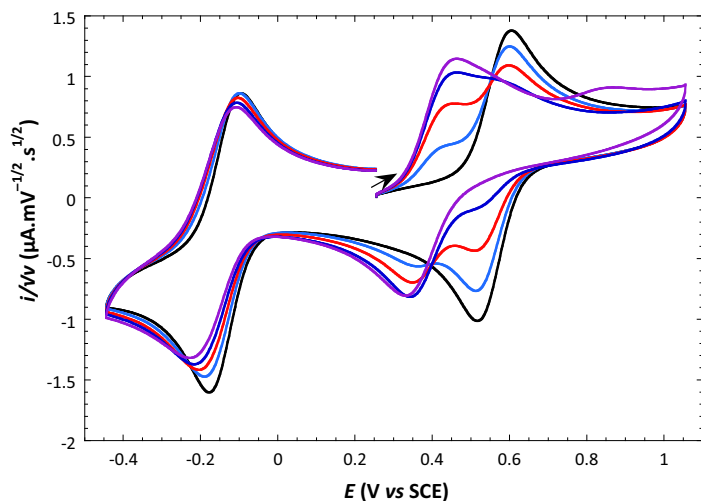


Figure 8. CV recorded at $100 \text{ mV}\cdot\text{s}^{-1}$ upon addition of NEt_3 on an acetonitrile solution of **4**. The black, light blue, red, dark blue and purple traces correspond to the addition of 0, 0.28, 0.56, 0.83 and 1.11 eq of base, respectively. The oxidation wave at 0.87 V is associated to the oxidation of free NEt_3 .

DISCUSSION

Valence (de)localization within the mixed-valent complexes. As illustrated in Scheme 1 the original process evidenced on compound **1** was the valence inversion induced by the deprotonation of the aniline bound to Fe^{II} . Indeed, in **1** $^1\text{H-NMR}$ showed that the valences of the two Fe were localized with the ferrous center bound to the aniline.⁴ It was later found that **1** can exist as two position isomers, with the aniline occupying either the *cis* or the *trans* position with respect to the bridging phenoxide.¹⁴ But the exchange of pyridine and aniline ligands within the Fe^{II} coordination sphere did not change the localization of the valences.

The conclusion that in **1** the valences of two Fe ions were localized was based on the X-ray structure and confirmed by $^1\text{H-NMR}$ which revealed a spectral range of ca 550 ppm. Indeed, it was noticed that the $\text{Fe}^{\text{II}}\text{Fe}^{\text{III}}$ complexes of the symmetrical Hbpmp ligand (complex **5**) extend over ca 390 ppm, and that replacing one pyridine of the ligand by an other group

resulted in a drastic enlargement of the spectrum.⁸⁻¹⁰ Indeed, whatever the nature of the new group, phenoxide or solvent molecule when the pyridine was replaced by a non-bonding group, the chemical shift domain extended over ca 600 ppm.

It was assumed that replacing the aniline by a benzimidazole would not bring a too important change and that the new complex would still be localized. The ¹H-NMR studies reported above for complex **4** strongly suggests that the reverse is true and that the valences are delocalized. The same conclusion applies to **2** and **3**.

Benzimidazole deprotonation. ¹H-NMR and Mössbauer spectroscopies and electrochemical studies have evidenced that triethylamine treatment of **2-4** induces the deprotonation of a benzimidazole group. **3** and **4** exhibit closely similar behaviors. ¹H-NMR reveals the presence of two isomers as for **1'**, and this was already the case for the protonated form. However, the occurrence of a single isomer was sufficient to account for the Mössbauer spectra of **3'** and **4'**, as well as **3** and **4**. One may argue that the presence of a second isomer can be hidden by the broadness of the Mössbauer lines. This explanation might work for **3** and **4**, the two isomers having similar nuclear parameters, as found for **1**. It does not hold, however, for **3'** and **4'**. Indeed, in the deprotonated species the position of the anion (deprotonated ligand) with respect to the bridging phenoxide strongly influences the quadrupole splitting of the ferric site to which it is bound. Very large quadrupole splittings are characteristic of the *trans* isomer: 1.77 mm.s⁻¹ for **1'** for example. In this respect, it is worth noting that the Mössbauer spectrum of **2'** strongly departs from those of **3'** and **4'** by the presence of a line at ca 1.3 mm.s⁻¹ corresponding to the high velocity line of the quadrupole doublet of the ferric site that possesses a very large quadrupole splitting 1.72 mm.s⁻¹. This value suggests that in **2'** the *trans* isomer of the benzimidazolide is formed. In addition, this shows that no *trans* isomer is present in the Mössbauer spectrum of **3'** and **4'**. The absence of an isomer in the Mössbauer spectrum may be due to the different recording conditions: room temperature for ¹H-NMR

and frozen solution at 80 K for Mössbauer spectroscopy. Indeed, it is quite possible that during the cooling of the Mössbauer samples, the equilibrium between the two isomers be displaced in favor of the most stable one. This did not occur in the case of **1**, but the kinetics of isomerization of both **1** and **1'** were slow, 120 and 20 min respectively. For **3** and **4** there was no evidence in either UV-visible or ¹H-NMR for any slow process, which suggests that the isomerizations are fast.

As far as redox properties are concerned, the electrochemical studies have revealed again that **3** and **4** behave in a very similar manner (Figures 8 and S12). In particular, the deprotonation of the benzimidazole facilitates the oxidation of the Fe^{II} center by the same amount 0.19 V. This is less than half the effect linked to deprotonation of the aniline in **1** (ca 0.45 V). This reduced effect is in agreement with the negative charge of the benzimidazolidate ligand delocalized on the two nitrogen atoms of the imidazole ring compared to the location on the single coordinated nitrogen atom of the anilide.

EXPERIMENTAL SECTION

General methods.

Materials: Acetonitrile for spectroscopic measurements was distilled under argon over CaH₂ and stored within an inert atmosphere glovebox. All other reagents were of reagent grade quality and used as received.

Physicochemical studies: ¹H-NMR spectra were recorded in deuterated acetonitrile on a Bruker AC 200 with a 5 mm indirect detection as described previously.¹⁶ Mass spectra were obtained in the electrospray ionization mode on a LCQ-Finnigan Thermoquest spectrometer equipped with an octupolar analyser and an ion trap. Electronic absorption spectra were recorded in acetonitrile (0.18 mM solution with 1 cm optical length cuvettes) on a Varian Cary® 50 spectrometer. Mössbauer spectra were recorded on 2-4 mM solutions of ⁵⁷Fe-fully

enriched complexes. The experiments were performed using a horizontal transmission cryostat (Oxford Instruments) and a 50 mCi source of $^{57}\text{Co}(\text{Rh})$ as previously described.⁴ All velocity scales and isomer shifts are referred to metallic iron foil at room temperature.

Syntheses. 2-chloromethylbenzimidazole. 1 g of 2-hydroxymethylbenzimidazole ($M=148.16 \text{ g}\cdot\text{mol}^{-1}$, 6.75 mmol) is dissolved in 10 mL CH_2Cl_2 . An excess of SOCl_2 (3 mL, 41 mmol) is added and the mixture is stirred for 18 hrs. A white solid is formed that is filtered and washed with 20 mL of CH_2Cl_2 . 1.12 g of 2-chloromethylbenzimidazole are obtained ($M=166.61 \text{ g}\cdot\text{mol}^{-1}$, 6.72 mmol, $\rho = 100\%$).

N-(pyridyl-2-yl)methyl-N-(benzimidazol-2-yl)methylamine. 1 g of 2-chloromethylbenzimidazole ($M=166.61 \text{ g}\cdot\text{mol}^{-1}$, 6.0 mmol) dissolved in 10 mL of THF is added to 649 mg of 2-picolyamine ($M=108.14 \text{ g}\cdot\text{mol}^{-1}$, 6.0 mmol) dissolved in 20 mL of THF with 2 mL of triethylamine ($M=101.19 \text{ g}\cdot\text{mol}^{-1}$, 14.3 mmol). The solution is stirred. After 3 days, a white suspension and a colorless solution is obtained. The mixture is filtered and the solid is washed with THF (20 mL). A first purification by a SiO_2 column eluted with ethyl acetate (only impurities migrate) and with methanol gives the product and few impurities. Further purification is obtained by forming the chlorhydratation (ethanol/HCl) and crystallization in hot isopropanol yields 300 mg of the chlorhydrated amine ($M=311.21 \text{ g}\cdot\text{mol}^{-1}$, 0.96 mmol, $\rho = 16\%$).

Binucleating ligands.

The syntheses of the three ligands were realized according to the published synthetic scheme that involves successive condensation of the two desired secondary amines to the chloromethylphenol derivatives. The syntheses of the 2-chloromethyl-6-bis((pyridyl-2-methyl)amino)methyl-4-methylphenol and the 2-chloromethyl-6-bis((1-methylbenzimidazol-2-yl-methyl)amino)methyl-4-methylphenol have been previously described.^{8,13} The general procedure for the condensation is described below. 1 mmol of the chloro derivative is

dissolved in 10 mL of THF and added to a 10 mL THF solution of 1 mmol of the secondary amine containing an excess of triethylamine (600 μ L, 4.3 mmol). After one hour, the mixture is filtered and the filtrate is evaporated. The oil is dissolved in 3-20 mL dichloromethane, dried on Na₂SO₄ and evaporated to give the final product ($\rho \approx 90\%$).

Syntheses of complexes 2-4. The general procedure is as follows. 0.18 mmol of the binucleating ligand and 0.18 mmol of the dicarboxylate salt Na₂mpdp are dissolved in 5-10 mL of degassed solvent (MeOH for **2**, CH₃CN for **3** and **4**). When CH₃CN is used, some Na₂SO₄ is added to trap residual water. To this solution was added dropwise 0.36 mmol of ferrous perchlorate dissolved in 8 mL of degassed MeOH. The solution was stirred under argon for 1h-1h30 at room temperature and if required filtrated under Ar. Dioxygen was bubbled in the solution (ca 15 min). After 1 day, a small quantity of precipitate was formed and the solution was kept at ca 6 °C. The precipitate was carefully filtered and dried under vacuum. ($\rho \approx 60\%$)

ESI-MS. **3**: m/z = 450.1 [(L-(Py)₂(Py)(BzImH))Fe₂(μ_2 -mpdp)]²⁺ (100%). **4**: m/z = 503.1 [(L-(BzImMe)₂(Py)(BzImH))Fe₂(μ_2 -mpdp)]²⁺ (100%).

Crystals of 2(ClO₄)₂•2CH₃CN. A solution of diethylether was allowed to slowly diffuse into a 5 mL CH₃CN solution containing 5 mg of complex **2**.

REFERENCES

- (1) Roth, J. P.; Lovell, S.; Mayer, J. M. *J. Am. Chem. Soc.* **2000**, *122*, 5486.
- (2) Warren, J. J.; Mayer, J. M. *J. Am. Chem. Soc.* **2011**, *133*, 8544.
- (3) Saouma, C. T.; Kaminsky, W.; Mayer, J. M. *J. Am. Chem. Soc.* **2012**, *134*, 7293.
- (4) Gouré, E.; Thiabaud, G.; Carboni, M.; Gon, N.; Dubourdeaux, P.; Garcia-Serres, R.; Clémancey, M.; Oddou, J.-L.; Robin, A. Y.; Jacquamet, L.; Dubois, L.; Blondin, G.; Latour, J.-M. *Inorg. Chem.* **2011**, *50*, 6408.
- (5) Neyhart, G. A.; Meyer, T. J. *Inorg. Chem.* **1986**, *25*, 4807.

- (6) McCormick, J. M.; Reem, R. C.; Solomon, E. I. *J. Am. Chem. Soc.* **1991**, *113*, 9066.
- (7) Balasubramanian, R.; Blondin, G.; Canales, J. C.; Costentin, C.; Latour, J.-M.; Robert, M.; Savéant, J.-M. *J. Am. Chem. Soc.* **2012**, *134*, 1906.
- (8) Lambert, E.; Chabut, B.; Chardon-Noblat, S.; Deronzier, A.; Chottard, G.; Bousseksou, A.; Tuchagues, J.-P.; Laugier, J.; Bardet, M.; Latour, J.-M. *J. Am. Chem. Soc.* **1997**, *119*, 9424.
- (9) Kanda, W.; Moneta, W.; Bardet, M.; Bernard, E.; Debaecker, N.; Laugier, J.; Bousseksou, A.; Chardon-Noblat, S.; Latour, J.-M. *Angew. Chem., Int. Ed. Engl.* **1995**, *34*, 588.
- (10) Chardon-Noblat, S.; Horner, O.; Chabut, B.; Avenier, F.; Debaecker, N.; Jones, P.; Pécaut, J.; Dubois, L.; Jeandey, C.; Oddou, J.-L.; Deronzier, A.; Latour, J.-M. *Inorg. Chem.* **2004**, *43*, 1638.
- (11) Borovik, A. S.; Papaefthymiou, V.; Taylor, L. F.; Anderson, O. P.; Que Jr., L. *J. Am. Chem. Soc.* **1989**, *111*, 6183.
- (12) Mashuta, M. S.; Webb, R. J.; McCusker, J. K.; Schmitt, E. A.; Oberhausen, K. J.; Richardson, J. F.; Buchanan, R. M.; Hendrickson, D. N. *J. Am. Chem. Soc.* **1992**, *114*, 3815.
- (13) Gouré, E.; Dubourdeaux, P.; Clémancey, M.; Gon, N.; Balasubramanian, R.; Lebrun, C.; Pécaut, J.; Blondin, G.; Latour, J.-M. *Inorg. Chem.* **2013**, To be submitted.
- (14) Gouré, E.; Carboni, M.; Dubourdeaux, P.; Clémancey, M.; Balasubramanian, R.; Lebrun, C.; Bayle, P.-A.; Blondin, G.; Latour, J.-M. *Chem. Eur. J.* **2013**, Submitted.
- (15) Suzuki, M.; Oshio, H.; Uehara, A.; Endo, K.; Yanaga, M.; Kida, S.; Saito, K. *Bull. Chem. Soc. Jpn.* **1988**, *61*, 3907.
- (16) Lambert, E.; Chabut, B.; Chardon-Noblat, S.; Deronzier, A.; Chottard, G.; Bousseksou, A.; Tuchagues, J.-P.; Laugier, J.; Bardet, M.; Latour, J.-M. *J. Am. Chem. Soc.* **1997**, *119*, 9424.

Supplementary information for the manuscript

**pH-driven valence inversion in mixed-valent diiron(II,III) complexes.
Influence on the protic ligand on the proton-coupled electron transfer.**

*Eric Gouré,^a Michaël Carboni,^a Patrick Dubourdeaux,^a Martin Clémancey,^a Nathalie Gon,^a
Ramachandran Balasubramanian,^a Colette Lebrun,^b Jacques Pécaut,^b Geneviève Blondin^{a,*}
and Jean-Marc Latour^{a,*}*

(a) Univ. Grenoble Alpes, LCBM, 38054 Grenoble, France, CEA/DSV/iRTSV/CBM/pmb,
38054 Grenoble, France, CNRS UMR5249, LCBM, 38054 Grenoble, France

(b) Univ. Grenoble Alpes, RICC, 38054 Grenoble, France, CEA/DSM/INAC/SCIB/RICC,
38054 Grenoble, France, UMR E 3, RICC, 38054 Grenoble, France

genevieve.blondin@cea.fr; jean-marc.latour@cea.fr

List of supplementary figures, comments, tables and schemes

	Scheme S1. General scheme of ligand synthesis
	Figure S1. ¹ H-NMR spectra of complexes 1-3 in the 130 to –20 ppm domain.
	Figure S2. Titration of complex 2 with NEt ₃ . Each added aliquot corresponds to 0.24 eq of base. 0 and 2.45 eq of NEt ₃ were added for curves (a) and (k), respectively. The insert shows the variations at 532 nm (dots) and the best fit (red curve) according to Eq. 1.
	Figure S3. Titration of complex 3 with NEt ₃ . Each added aliquot corresponds to 0.18 eq of base. 0 and 2.71 eq of NEt ₃ were added for curves (a) and (p), respectively. The insert shows the variations at 528 nm (dots) and the best fit (red curve) according to Eq. 1.
	Figure S4. ¹ H-NMR spectra of complexes 2'-4' in the 105 to –30 ppm domain.
	Figure S5. Evolution of the ¹ H-NMR spectra of 2 upon addition of NEt ₃ . (a) 0, (b) 0.26, (c) 0.79, (d) 1.32, (e) 1.59, (f) 2.11 and (g) 2.64 eq.
	Figure S6. Evolution of the ¹ H-NMR spectra of 4 upon the addition of NEt ₃ . For 4 :(a) 0, (b) 0.56, (c) 0.83, (d) 1.11, (e) 1.39, (f) 1.67, (g) 1.95, (h) 2.22, (i) 2.78 and (j) 3.34 eq.
	Figure S7. Tentative assignment of the signals detected on the 400–140 ppm range of the ¹ H-NMR spectrum of complex 2 . This assignment relies on the monitoring of the addition of NEt ₃ on a CD ₃ CN solution of complex 2 (see Figures 5A and 6).
	Figure S8. Dependence on the scan rate of the cyclovoltammograms of 2 .
	Figure S9. Dependence on the scan rate of the cyclovoltammograms of 3 .
	Figure S10. Dependence on the scan rate of the cyclovoltammograms of 4 .
	Figure S11. Evolution of the cyclovoltammograms of 2 upon the addition of NEt ₃ . The black, light blue, red, dark blue, purple, violet, maroon and green traces correspond to the addition of increasing amounts of base. The oxidation wave at 0.95 V is associated to the oxidation of free NEt ₃ .
	Figure S12. Evolution of the cyclovoltammograms of 3 upon the addition of NEt ₃ . The black, light blue, red, dark blue, purple and violet traces correspond to the addition of 0, 0.25, 0.50, 0.75, 1.00 and 1.25 eq of base, respectively. The oxidation wave at 0.85 V is associated to the oxidation of free NEt ₃ .

Scheme S1. General scheme of ligand syntheses

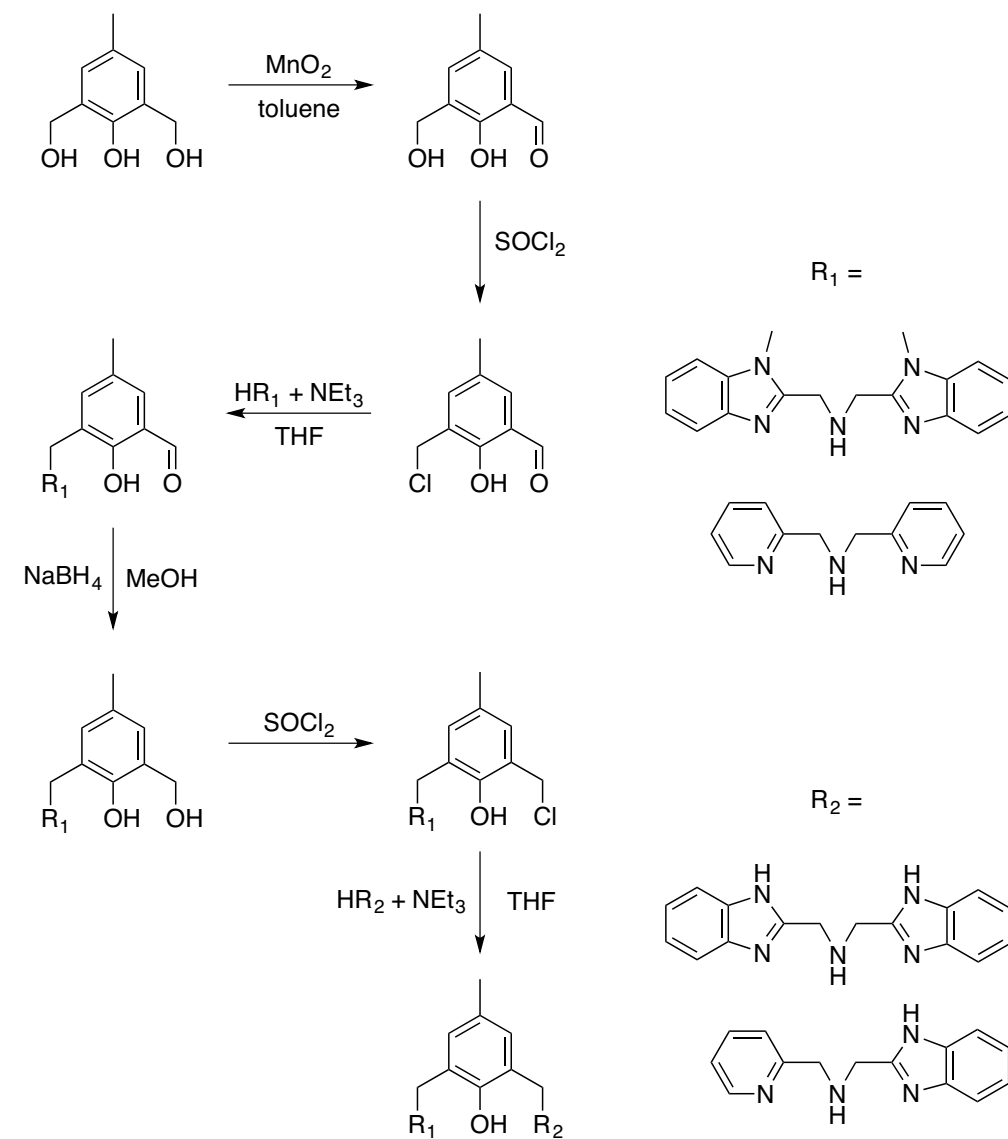


Figure S1. $^1\text{H-NMR}$ spectra of complexes **2-4** in the 130 to -20 ppm domain.

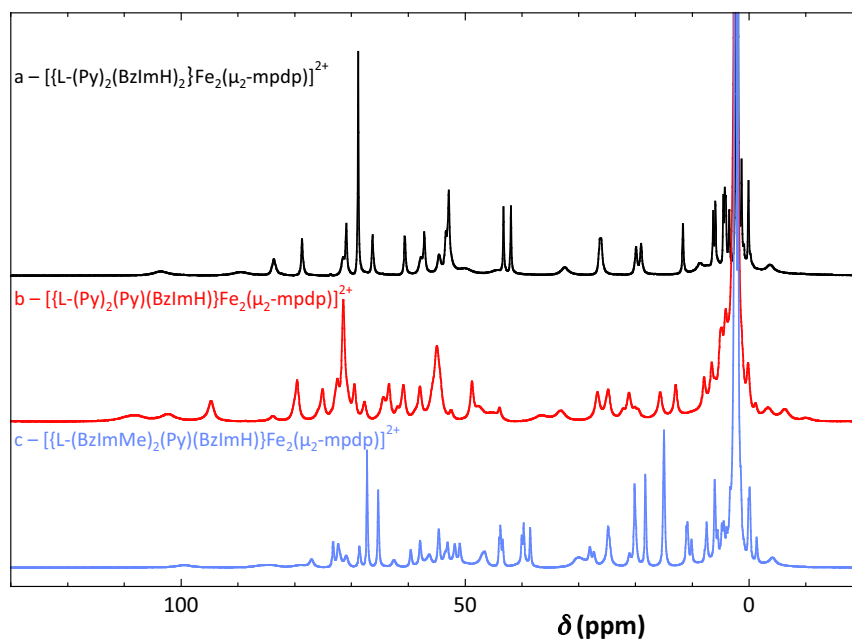


Figure S2. Titration of complex **2** with NEt_3 . Each added aliquot corresponds to 0.24 eq of base. 0 and 2.45 eq of NEt_3 were added for curves (a) and (k), respectively. The insert shows the variations at 532 nm (dots) and the best fit (red curve) according to Eq. 1.

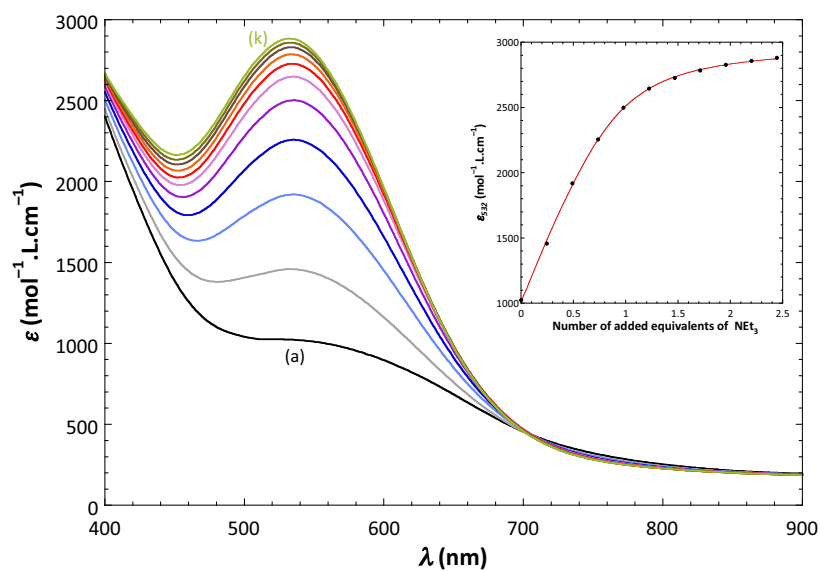


Figure S3. Titration of complex **3** with NEt_3 . Each added aliquot corresponds to 0.18 eq of base. 0 and 2.71 eq of NEt_3 were added for curves (a) and (p), respectively. The insert shows the variations at 528 nm (dots) and the best fit (red curve) according to Eq. 1.

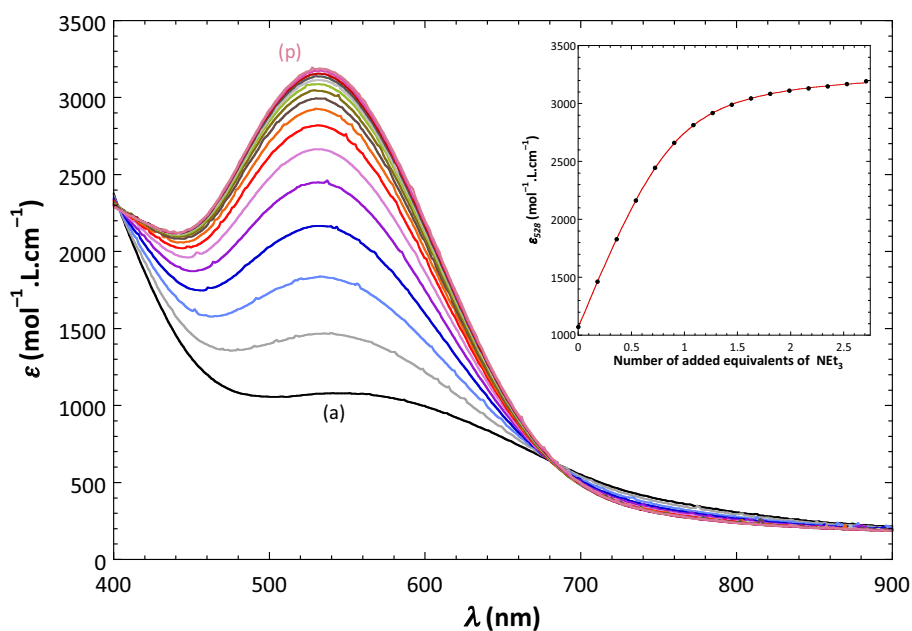


Figure S4. $^1\text{H-NMR}$ spectra of complexes **2'**-**4'** in the 105 to -30 ppm domain.

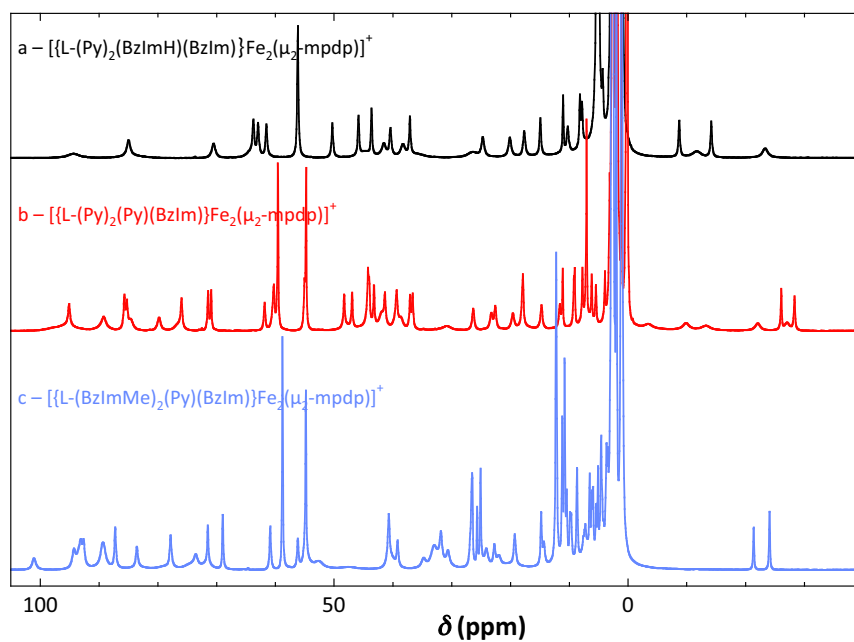


Figure S5. Evolution of the ^1H -NMR spectra of **2** upon addition of NEt_3 . (a) 0, (b) 0.26, (c) 0.79, (d) 1.32, (e) 1.59, (f) 2.11 and (g) 2.64 eq.

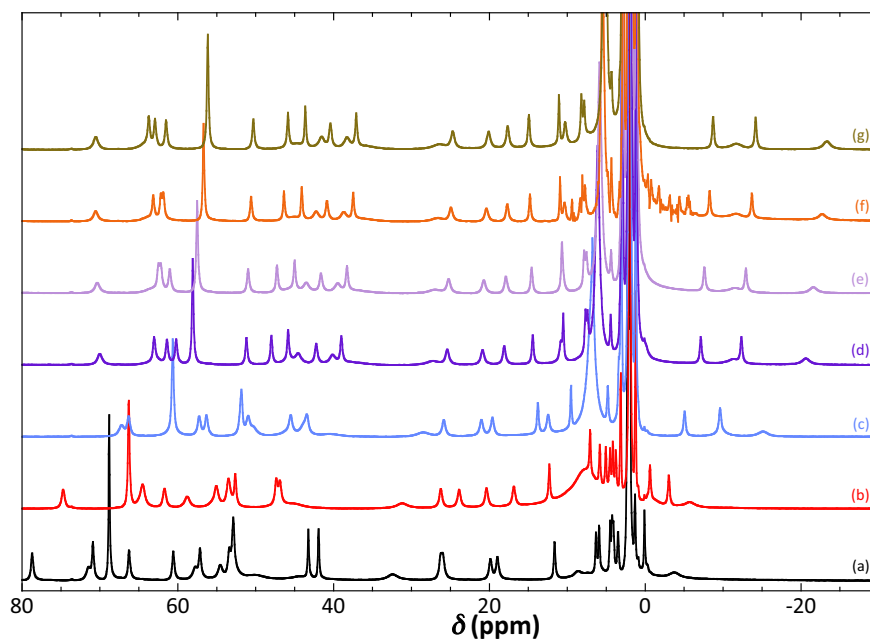


Figure S6. Evolution of the ^1H -NMR spectra of **4** upon the addition of NEt_3 . For **3**: (a) 0, (b) 0.56, (c) 0.83, (d) 1.11, (e) 1.39, (f) 1.67, (g) 1.95, (h) 2.22, (i) 2.78 and (j) 3.34 eq.

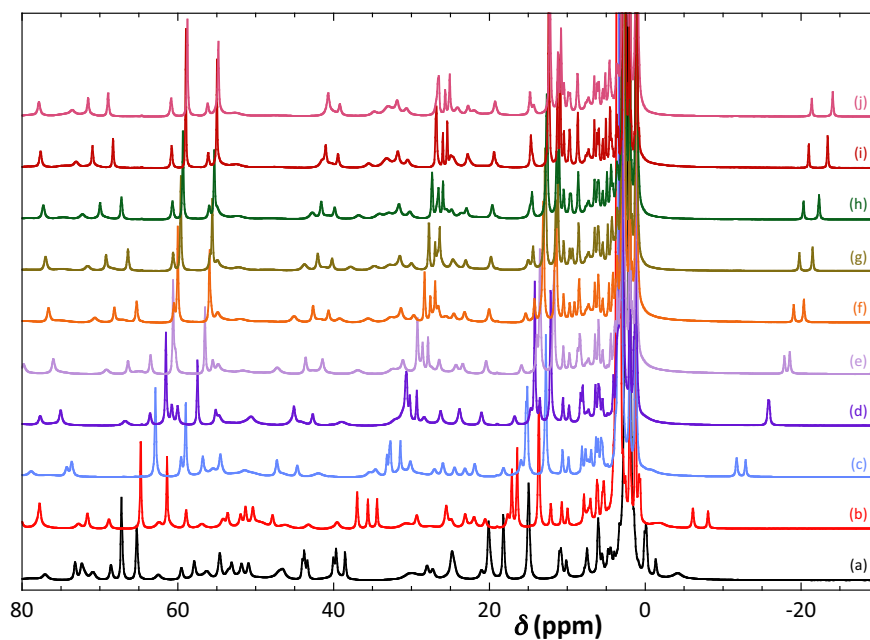


Figure S7. Tentative assignment of the signals detected on the 400–140 ppm range of the ^1H -NMR spectrum of complex **2**. This assignment relies on the monitoring of the addition of NEt_3 on a CD_3CN solution of complex **2** (see Figures 5A and 6).

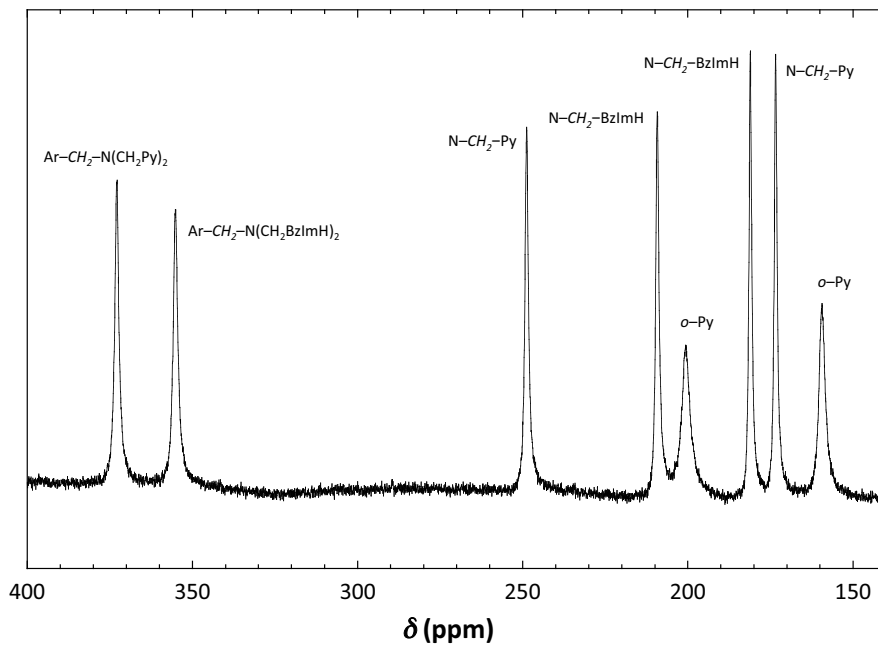


Figure S8. Dependence on the scan rate of the cyclic voltammograms of **2**.

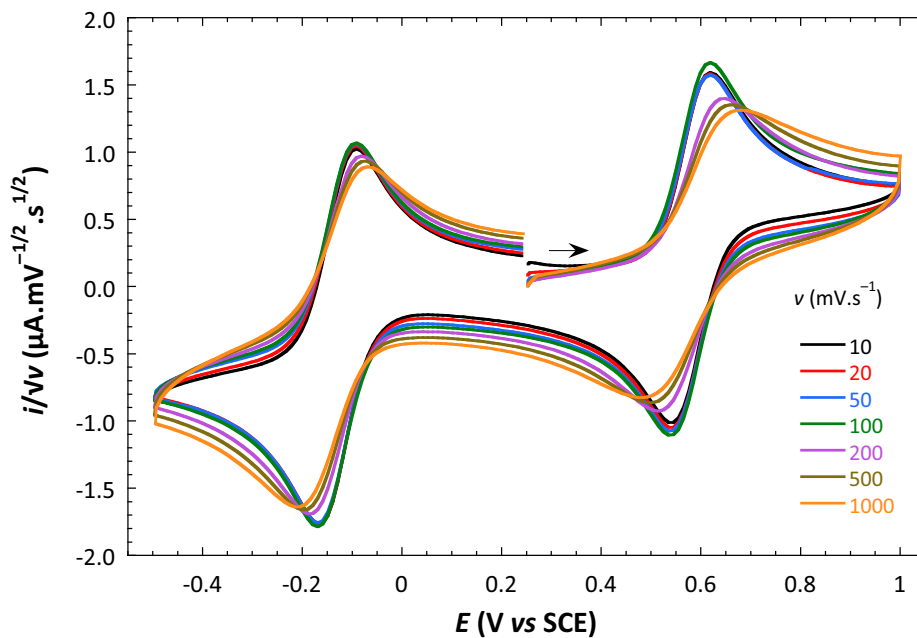


Figure S9. Dependence on the scan rate of the cyclic voltammograms of **3**.

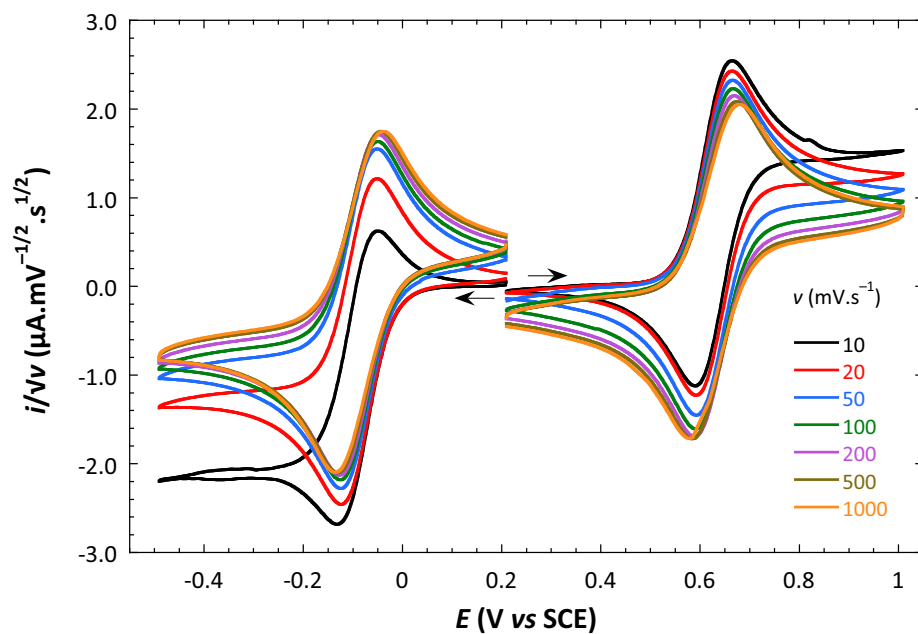


Figure S10. Dependence on the scan rate of the cyclic voltammograms of **4**.

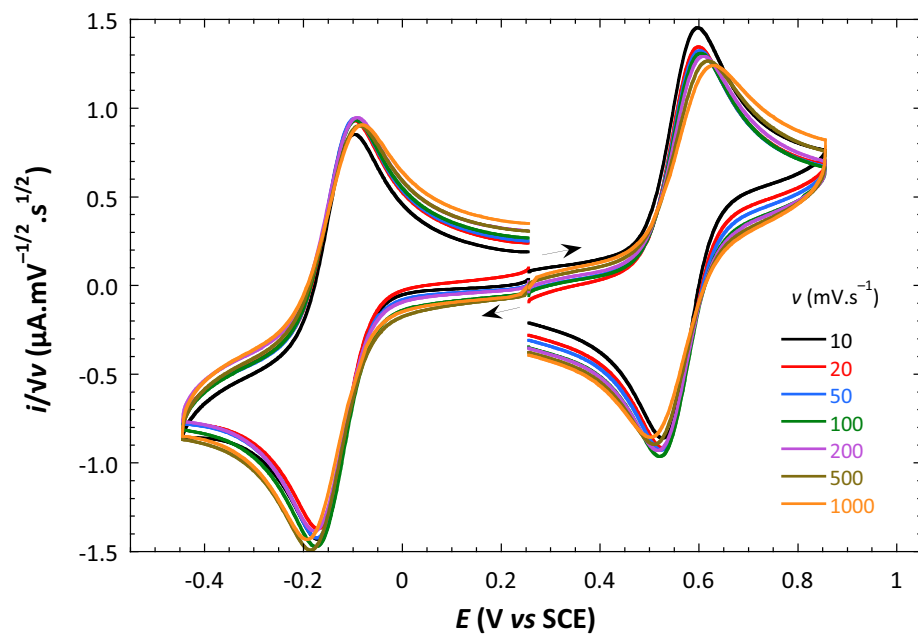


Figure S11. Evolution of the cyclic voltammograms of **2** upon the addition of NEt_3 . The black, light blue, red, dark blue, purple, violet, maroon and green traces correspond to the addition of increasing amounts of base. The oxidation wave at 0.95 V is associated to the oxidation of free NEt_3 .

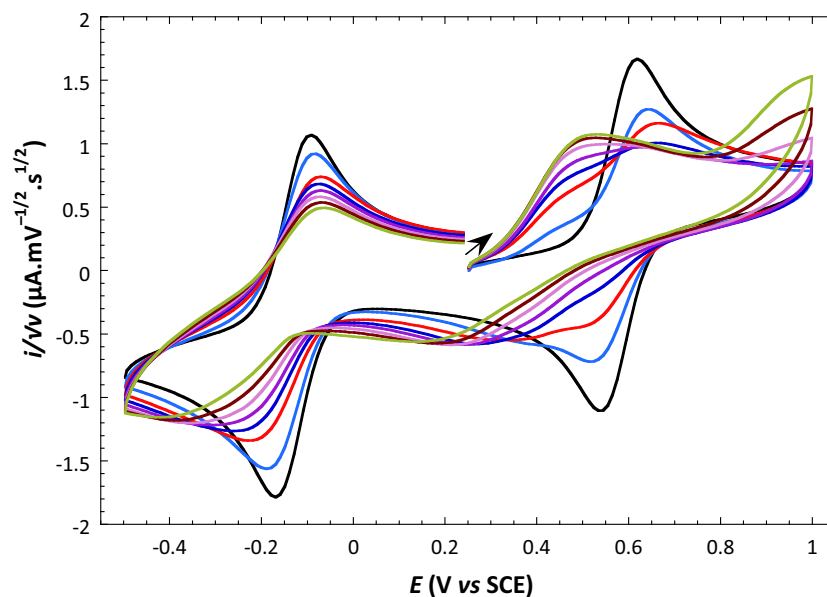
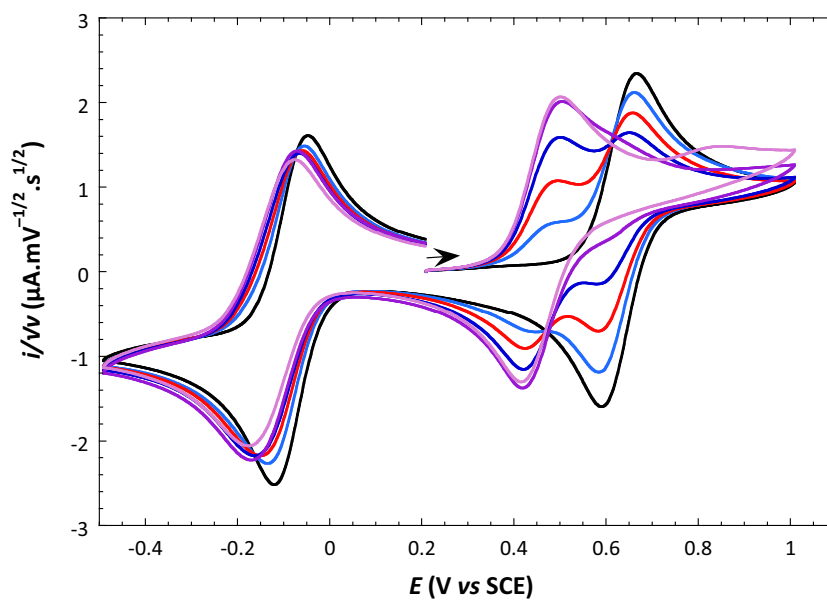


Figure S12. Evolution of the cyclic voltammograms of **3** upon the addition of NEt_3 . The black, light blue, red, dark blue, purple and violet traces correspond to the addition of 0, 0.25, 0.50, 0.75, 1.00 and 1.25 eq of base, respectively. The oxidation wave at 0.85 V is associated to the oxidation of free NEt_3 .





CONCLUSION



Proton coupled electron transfer is of great interest and its occurrence in mixed valent diiron systems was the key objective of the project Bi3Pro funded by ANR. My PhD was highly focused to reveal the mechanisms involved in a particular mixed valent diiron complex of the form $[\text{Fe}^{\text{III}}(\mu_2\text{-mpdp})\text{Fe}^{\text{II}}(\text{H}_2\text{NBn-L})]^{2+}$ that was developed by Jean-Marc LATOUR's group in LCBM/CEA-Grenoble.

My PhD started with the electrochemical investigation of the above said diiron complex. The results obtained allowed us to frame and develop a strategy to study the transfer of proton and electron induced by a pH change. As a result of the strategy, the final outcome supports the concerted pathway which is nothing but the proton and the electron transferring simultaneously in the presence of base and its conjugated acid. This conclusion was further supported by the simulations performed at various experimental conditions.

These complexes also showed signatures of evolution while performing the UV-Vis experiments in acetonitrile solution. This evolution was further analyzed and a hypothesis was framed according to the results obtained which supports the occurrence of isomerization processes. The most likely hypothesis would be that initially upon dissolution in acetonitrile the aniline complex exists in a form where aniline is in *trans* position to the phenoxide and slowly converts to *cis*-form upon time (=2hrs), both forms existing after 2hrs in a ratio 35:65 (*trans*:*cis*). Deprotonation of this mixture leads to the *cis* and *trans* form of the anilide species resulting in a dominating *trans* in a ratio 17:83 (*cis*: *trans*) respectively. Evidence of UV-Vis, $^1\text{H-NMR}$ and Mossbauer supports these findings and allows us to rule out other hypothesis from the desired one.

The results obtained on the aniline complex led us to modify the existing complex by substituting different groups and study the influence of *pKa* of the protic group and the influences of the respective redox potentials of the two $\text{Fe}^{\text{III}}/\text{Fe}^{\text{II}}$

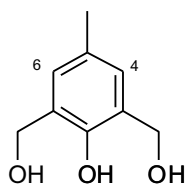
couples on the thermodynamics and kinetics of the PCET reaction. To facilitate these studies, modifications of the original ligands were performed and the characterizations performed by the various spectroscopic techniques. The results grouped in the draft n°1, showed that the introduction of two methylbenzimidazoles in the place of two pyridines lowers the redox potential by ca 60mV and also speeds up isomerization probably due to structural constrains within the ligand. The results gathered in draft n°2 where benzimidazole (protic group) was introduced to the different complexes shows similar behaviours to the other members. In particular, the introduction of benzimidazole facilitates the oxidation of the Fe^{II} centre which is less than half of the effect link to the deprotonation of the aniline complex. Thus, the future perspective would fall into further exploration on the study of deprotonation-induced electron transfer to open access to the redox potential influence. This work thus paves clear understanding of the reactions mechanism and allows us to better understand the biological relevancies. This kind of work allows us to study the most intricate biological mechanism by mimicking them chemically and to explore the usage of different sophisticated techniques to analyze the same.



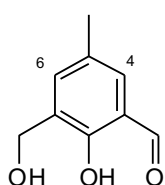
ANNEX 1



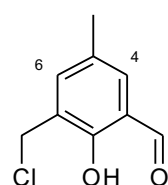
Ligand syntheses



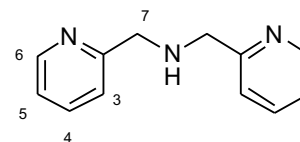
1



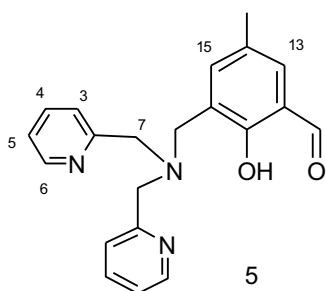
2



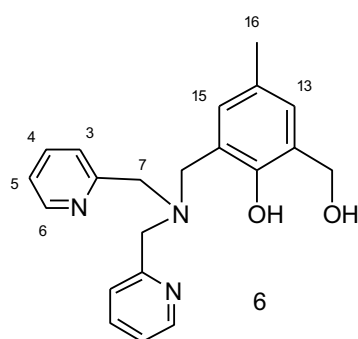
3



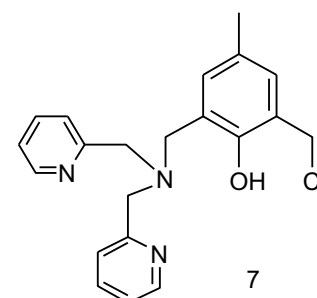
4



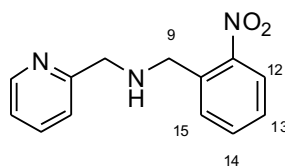
5



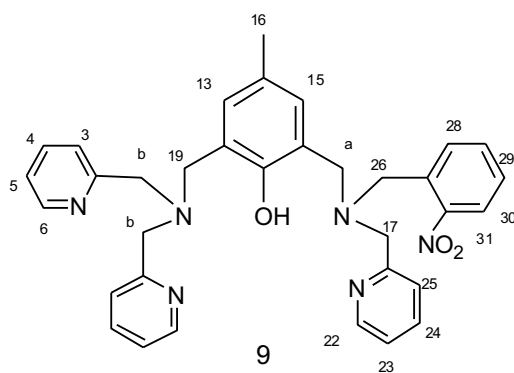
6



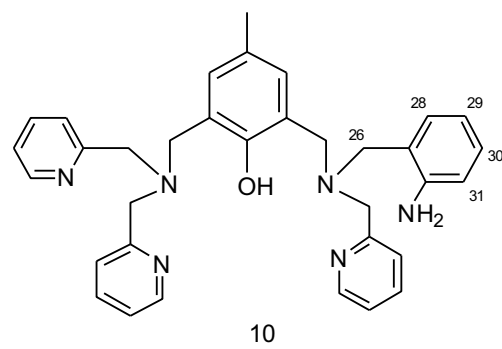
7



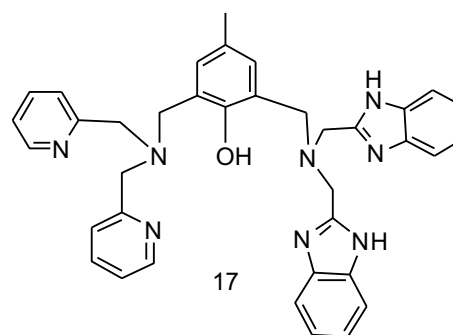
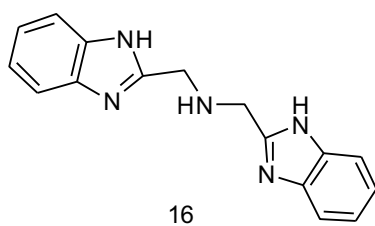
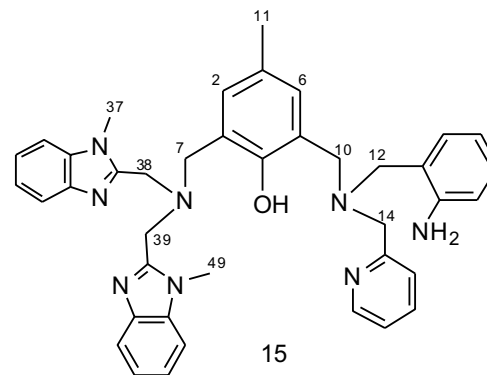
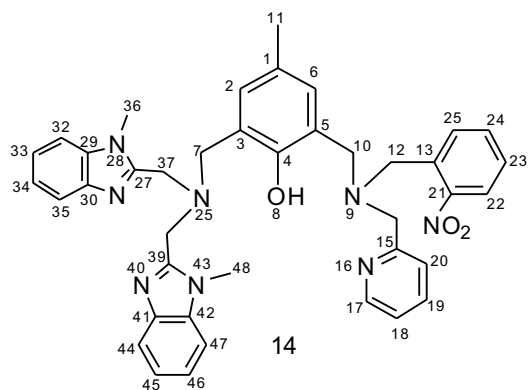
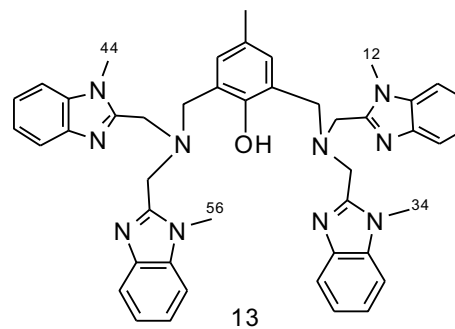
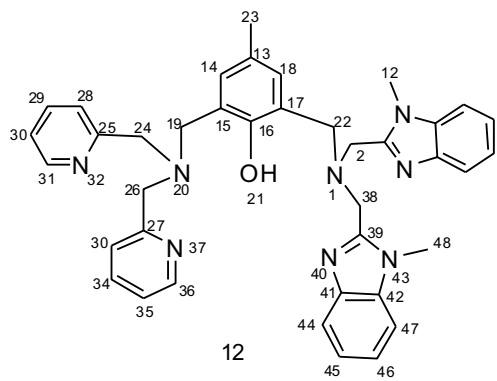
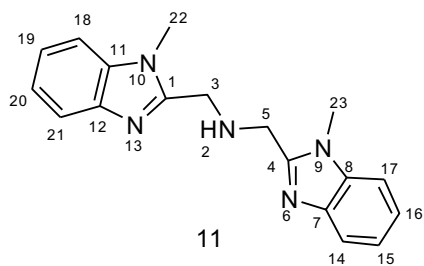
8



9



10



* The number under each compound (1-17) in the above scheme is mentioned in the synthetic procedures at each level.

1 2-hydroxymethyl-6-carboxaldehyde-p-cresol (2)

12.5 g (74.4 mmole) of triol **1** ($M = 168.19 \text{ g}\cdot\text{mol}^{-1}$) were dissolved in 2.5 L of toluene, then 16.25 g (187 mmole) of MnO_2 ($M = 86.94 \text{ g}\cdot\text{mol}^{-1}$) were added and the mixture was stirred for 4 days. Two similar reactions were performed in parallel with the same quantity of the reactants. After stirring, the mixture was filtered under vacuum pump which yields yellow solution leaving behind the excess MnO_2 in the filter which needs further washing with toluene. The whole 5 L yellow solution (from the two reactions) was evaporated in the rotavapor until it forms a high voluminous dry yellow solid substance. The obtained yellow solid contains both mono and di-aldehyde group which was subjected to further purification by column chromatography to extract the pure mono-aldehyde derivative of the triol. Silica gel column was prepared with 150 g of silica in toluene. Upon eluting the column with toluene we get the impurities first then followed by the di-aldehyde derivative followed by the mono. Initially toluene was used as the eluent and when the di-aldehyde compounds starts to descend we elute the column with dichloromethane which was then followed with few percentage of methanol for the final product. Each extraction was carefully scrutinized by the TLC in the eluent CH_2Cl_2 and methanol in the ratio 99:1 respectively. Upon obtaining the correct fraction of the desired mono-aldehyde we dissolve it in minimum toluene and allow it to crystallize overnight. Yellow needle like crystals were obtained and are filtered using a vacuum filter.

$m = 4.85 \text{ g}$; Yield = 57%; MW = $166 \text{ g}\cdot\text{mol}^{-1}$; Product: solid yellow needle like crystals

$^1\text{H NMR}$ (CDCl_3), δ (ppm): 2.33 (s, 3H, CH_3); 4.74 (d, 2H, $\text{CH}_2\text{-OH}$); 7.30 (s, 1H, CH-6); 7.40 (s, 1H, CH-4); 9.86 (s, 1H, CH=O); 11.18 (s, 2H, OH).

2 2-chloromethyl-6-carboxaldehyde-p-cresol (3)

2.8 g (16.8 mmole) of monoaldehyde **2** ($M = 166.18 \text{ g}\cdot\text{mol}^{-1}$) was dissolved in 5 mL CH_2Cl_2 , 3 mL (41.1 mmole) of thionyl chloride (SOCl_2) ($d = 1.631 \text{ g}\cdot\text{mL}^{-1}$; $M = 118.96 \text{ g}\cdot\text{mol}^{-1}$) in 5 mL CH_2Cl_2 was added drop by drop. After stirring for 1 hr at room temperature the mixture was evaporated forming white solid powder. The product was washed several times with the mixture of hexane and DCM in order to remove the excess of SOCl_2 .

$m = 2.35 \text{ g}$; Yield: 92%; MW = $184.62 \text{ g}\cdot\text{mol}^{-1}$; Product: White solid powder

^1H NMR (CDCl_3), δ (ppm): 2.33 (s, 3H, CH_3); 4.65 (d, 2H, $\text{CH}_2\text{-Cl}$); 7.32 (s, 1H, CH-6); 7.44 (s, 1H, CH-4); 9.84 (s, 1H, CH=O); 11.23 (s, 1H, OH)

3 bis-(2-picoly) amine (4)

2.7 g (25 mmole) of 2-picolyamine ($M = 108.14 \text{ g}\cdot\text{mol}^{-1}$) and 2.68 g (25 mmole) of pyridine-2-carboxaldehyde ($M = 107.11 \text{ g}\cdot\text{mol}^{-1}$) were dissolved in 40 mL of methanol. The solution was stirred for 1 hr at room temperature in the presence of argon. The mixture was cooled down to -50°C with the help of liquid N_2 and ethyl acetate mixture. Under maintaining constant temperature NaBH_4 was added in small quantities and the mixture was stirred for 15 min at -50°C . The mixture was allowed to warm up gradually at room temperature and stirred over night. The mixture was evaporated at 20°C giving a solid orange precipitate which was dissolved in CH_2Cl_2 and washed with NH_4Cl and the aqueous phase was rinsed 3 x 20 mL CH_2Cl_2 and stirred with Na_2SO_4 for 30 min. Upon filtering the mixture and evaporation we obtained oil like product.

$m = 4.094 \text{ g}$; Yield: 84%; $\text{MW} = 199.26 \text{ g}\cdot\text{mol}^{-1}$; Product: Orange oil

^1H NMR (CDCl_3), δ (ppm): 3.94 (s, 4H, $\text{CH}_2\text{-7}$); 7.11 (ddd, 2H, CH-5); 7.32 (d, 2H, CH-3); 7.59 (d, 2H, CH-4); 8.52 (ddd, 2H, CH-6)

4 2-(*N,N*-bis(2-picoly)-aminomethyl)-6-carboxaldehyde-*p*-cresol (5)

2.51 g (13.5 mmole) of **3** ($M = 184.62 \text{ g}\cdot\text{mol}^{-1}$) was dissolved in 60 mL THF (clear pale yellow) and 2.87 g (14.4 mmole) of **4** ($M = 199.26 \text{ g}\cdot\text{mol}^{-1}$) in 15 mL THF with 7.5 mL (75.6 mmole) of NEt_3 ($d = 0.726 \text{ g}\cdot\text{mL}^{-1}$; $M = 101.19 \text{ g}\cdot\text{mol}^{-1}$) (yellowish orange solution) was prepared separately the later solution was added drop by drop to the first which results is a coagulated precipitate which make it hard to stir. The mixture was stirred overnight which yields clear orange solution with precipitate. The mixture was filtered and the filtrate was washed thoroughly by THF. Evaporating the solution at 35°C produces orange oil. The oil was dissolved in 30 mL CH_2Cl_2 and 60 mL H_2O to which conc. HCl was added drop by drop to lower the $\text{pH} = 2\text{-}3$ ($\approx 6 \text{ mL}$). Phase separation was done using the decantation flask and the aqueous phase was washed with 3 x 30 mL CH_2Cl_2 to remove the excess of product **3** and the water phase was evaporated at 45°C to get orange oil.

Saturated solution of NaHCO_3 plus powder was added to the solution of the oil in CH_2Cl_2 till it forms bubble gum like structure and the pH was raised to 7-8. The phase was separated again and the bubble gum formed was washed with 3 x 30 mL of CH_2Cl_2 . The solution was stirred with Na_2SO_4 for 30 min and evaporated to dryness at 30°C .

$m = 4.74$ g; Yield: 62%; $\text{MW} = 347.42$ $\text{g}\cdot\text{mol}^{-1}$; Product: Orange solid

^1H NMR (CDCl_3), δ (ppm): 2.17 (s, 3H, CH_3); 3.70 (s, 2H, CH_2 -9); 3.80 (s, 4H, CH -7); 7.08 (t, 2H, CH -5); 7.12, 7.35 (2d, 2H, CH -13 and CH -15); 7.91 (d, 2H, CH -3); 7.55 (dt, 2H, CH -4); 8.47 (dd, 2H, CH -6); 10.36 (s, 1H, $\text{CH}=\text{O}$).

5 2-(*N,N*-bis(2-picoly)-aminomethyl)-6-hydroxymethyl-*p*-cresol (6)

4.3 g (12.4 mmole) of **5** ($M = 347.42$ $\text{g}\cdot\text{mol}^{-1}$) was dissolved in 100 mL methanol to which 1.29 g (34.1 mmole) of NaBH_4 ($M = 37.83$ $\text{g}\cdot\text{mol}^{-1}$) was added resulting in pale yellowish solution which was stirred for 15 min at room temperature. The solution was refluxed for 30 min leading to the change in color from pale yellow to orange. Conc. HCl was added to lower the pH to 2-3 and the solvent was evaporated at 45°C which yields yellowish orange semi-solid oil like product which is insoluble in 15 mL CH_2Cl_2 and few drops of sat. NaHCO_3 solution was added drop by drop to arrive at a pH = 7. The aqueous (white) and organic (orange) phase was separated and the organic phase was washed with 3 x 15 mL of water and resultant was stirred with Na_2SO_4 to remove excess water. Evaporation at 35°C produces oil like product.

$m = 2.01$ g; Yield: 49 %; $\text{MW} = 349.43$ $\text{g}\cdot\text{mol}^{-1}$; Product: Orange thick oil

^1H NMR (CDCl_3), δ (ppm): 2.21 (s, 3H, CH_3); 3.74 (s, 2H, CH_2 -9); 3.85 (s, 4H, CH -7); 4.71 (s, 2H, CH_2 -OH) ; 6.81 and 6.93 (2d, 2H, CH -13 and CH -15); 7.16 (td, 2H, CH -15); 7.30 (d, 2H, CH -3); 7.62 (dt, 2H, CH -4); 8.55 (dd, 2H, CH -6); 10.70 (s, 1H, OH).

6 2-(*N,N*-bis(2-picoly)-aminomethyl)-6-chloromethyl-*p*-cresol (7)

2.7 g (7.7 mmole) of **6** ($M = 349.43$ $\text{g}\cdot\text{mol}^{-1}$) to which 19.4 mL (266 mmole) of SOCl_2 ($d = 1.631$ $\text{g}\cdot\text{mL}^{-1}$; $M = 118.96$ $\text{g}\cdot\text{mol}^{-1}$) was added and stirred for 3 hrs at room temperature. After 3 hrs of stirring, it gives us caramel colored solution. By evaporation we obtained dark brown colored

powder. The powder was washed nicely with the mixture of 20 mL CH₂Cl₂ and 20 mL Hexane and evaporated. This was repeated 5 to 7 times till we get rid of the pungent odor. Upon evaporation, the flask with the product was left in the desiccator overnight for drying.

m = 3.583 g; Yield: 68.5%; MW = 367.88 g.mol⁻¹; Product: Light brown colored powder.

¹H NMR (CD₃CN), δ (ppm): 2.0 (s, 3H, CH₃); 3.75 (s, 2H, CH₂-Cl); 4.20 (s, 4H, CH-7); 4.50 (s, 2H, CH₂-9); 6.74 and 6.86 (2d, 2H, CH-13 and CH-15); 7.68 (td, 2H, CH-5); 8.19 (d, 2H, CH-3); 8.56 (dt, 2H, CH-4); 8.59 (dd, 2H, CH-6).

7 *N*-(2-nitro) benzyl-*N*-(2-picolyl) amine (8)

756 mg (5.0 mmole) of 2-nitrobenzaldehyde (M = 151.12 g.mol⁻¹) were dissolved in 10 mL methanol, then 541 mg (5.0 mmole) of 2-picolylamine (M = 108.14 g.mol⁻¹) in 5 mL methanol were added drop wise. After stirring 5 h, 250 mg (6.6 mmole) of NaBH₄ (M = 37.83 g.mol⁻¹) were added slowly and the mixture was stirred for 10 hrs. After stripping the solution to dryness, the resulting oil was dissolved in dichloromethane. The solution was washed with an ammonium chloride saturated aqueous solution and then dried over Na₂SO₄. Evaporation of the dichloromethane furnished orange oil.

m = 0.95 g; Yield: 94 %; MW = 243.27 g.mol⁻¹; Product: Reddish orange oil.

¹H NMR (CD₃CN), δ (ppm): 4.01 (s, 2H, CH₂-7); 4.19 (s, 2H, CH₂-9); 7.17 to 8.50 (m, 8H, aromatic protons).

8 2-(bis(2-picolyl)-aminomethyl)-6-(*N*-(2-nitro)benzyl-*N*-(2-picolyl)-aminomethyl-*p*-cresol (9)

430 mg (1.17 mmole) of **7** (M = 367.88 g.mol⁻¹), 277 mg (1.14 mmole) of **8** (M = 243.27 g.mol⁻¹) and 800 μL of triethylamine (5.74 mmole) (d = 0.726 g.mL⁻¹; M = 101.19 g.mol⁻¹) were dissolved in 15 mL of THF. The mixture was stirred at room temperature for 3 days and then filtered. After stripping the solution to dryness, the resulting oil was dissolved in dichloromethane. The solution was washed with a solution at pH 7 and then dried over Na₂SO₄. Evaporation of the dichloromethane gives brown oil like product.

m = 1.22 mg; Yield: 95 %; MW = 574.68 g.mol⁻¹; Product: Orange oil

¹H NMR (CD₃CN), δ (ppm): 2.23 (s, 3H, CH₃-16); 3.74 (s, 2H, CH₂-a); 3.76 (s, 2H, CH₂-19); 3.89 (s, 2H, CH₂-17); 3.82 (s, 4H, CH₂-b); 4.00 (s, 2H, CH₂-26); 6.87 (dd, 1H, CH-28); 6.90 (s, 1H, CH-13); 6.98 (s, 1H, CH-15); 7.0- 7.2 (m, 3H, CH-5, CH-23); 7.58 (d, 1H, CH-25); 7.70 (d, 2H, CH₃) ; 7.70 (td, 2H, CH-4); 7.83 (td, 1H, CH-24); 8.44 (ddd, 1H, CH-22); 8.52 (ddd, 2H, CH-6).

9 2-(bis(2-picolyl)-aminomethyl)-6-(*N*-(2-amino)benzyl-*N*-(2-picolyl)-aminomethyl-*p*-cresol, HL-BnNH₂ (10)

318 mg (0.55 mmole) of **9** (HL-BnNO₂, M = 574.68 g.mol⁻¹) were dissolved in 18 mL of methanol producing a bright orange solution. 6.8 mL (about 80 mmole) of hydrochloric acid (d = 1.2 g.mL⁻¹; M = 36.46 g.mol⁻¹) were then added. The mixture was stirred vigorously and 100 mg (0.8 mmole) of tin powder (Sn) (M = 118.71 g.mol⁻¹) were added in small amounts, leading to a light orange solution. After additional stirring for one hour, the excess hydrochloric acid was neutralized by adding NH₄OH until the solution pH reached 7. A dense white precipitate was filtered off and the resulting yellow solution was evaporated to dryness. The resulting residue was taken in 20 mL of chloroform and a white precipitate formed was filtered again. This operation was repeated twice until no precipitate appeared anymore. After evaporating the chloroform orange oil was obtained.

m = 336.4 mg; Yield: 90%; MW = 544.70 g.mol⁻¹; Product: Orange oil

¹H NMR (CD₃OD), δ (ppm): 2.24 (s, 3H, CH₃); 3.94 (s, 2H, CH₂-26); 3.94 (s, 2H, CH₂-9); 4.03 (s, 2H, CH₂-17); 4.12 (s, 2H, CH₂-19); 4.19 (s, 4H, CH₂-7); 6.66 (dd, 1H, CH-28); 6.67 (s, 1H, CH-13); 6.70 (s, 1H, CH-15); 7.0- 7.3 (m, 3H, CH-5, CH-23); 7.41 (d, 1H, CH-25); 7.64 (d, 2H, CH-3); 7.75 (td, 2H, CH-4); 7.76 (td, 1H, CH-24); 8.55 (ddd, 1H, CH-22); 8.57 (ddd, 2H, CH-6).

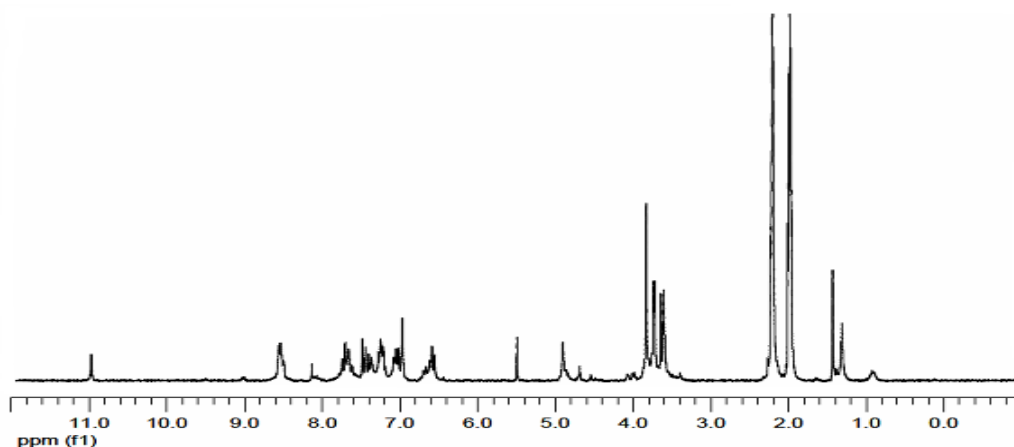


Figure 1. $^1\text{H-NMR}$ spectra of the final ligand HL-BnNH₂ (10)

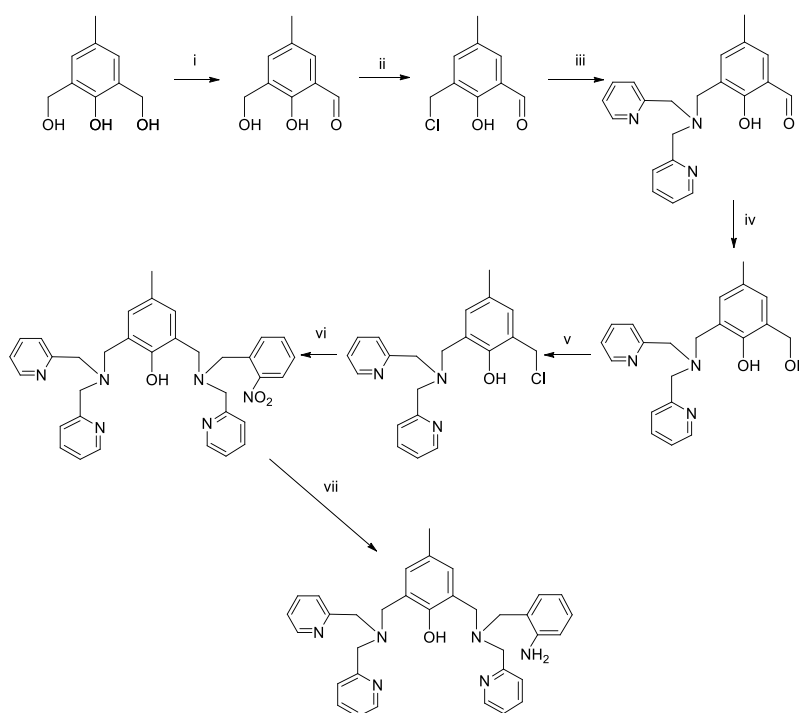


Figure 2. Schematic representation of the multiple steps sequence explained above for the synthesis of HL-BnNH₂ (10).

10 bis((1-methyl-benzimidazol-2-yl)methyl)amine, HN(CH₂BzImMe)₂ (11)

Initially dechlorination was performed on *N*-methyl-*o*-phenylenediamine.2HCl whose MW = 160 g.mol⁻¹, for which 4 g (0.25 mmole) of amine was dissolved in 40 mL CH₂Cl₂ to which 6 mL of NaHCO₃ was added. Small amounts of NaHCO₃ salt were added to the mixture to release the gas and to form bubble gum like compound. The bubble gum white product was repeatedly washed with CH₂Cl₂ and the filtrate was dried with Na₂SO₄ and evaporated. The yield for this reaction accounts for 98% of pure dechlorinated amine as a dark brown colored oil. 2.46 g (20 mmole)

methyl-o-phenylenediamine to which nicely grinded 965 mg (72.5 mmole) iminodiacetic acid was added and the mixture was heated in the oil bath at 192° C under Ar surmounted in a Y tube set up. The mixture was maintained at a constant temperature for 90 min and allowed it to cool down at room temperature overnight. The obtained ratio 69:31 from the NMR reveals the presence of the starting amine and the impurities contributing 23% on the total product. To remove the impurities column chromatography has been performed on silica gel with CH₂Cl₂ as eluent with consecutive addition of methanol.

m = 1.678 mg; Yield: 49% (after the chromatography); MW = 305.38 g.mol⁻¹; Product: Brown thick oil

¹H NMR (CD₂Cl₂), δ (ppm): 2.06 (s, 1H, NH); 3.77 (s, 3H, CH₃-2); 4.07 (s, 2H, CH₂-2); 4.16 (s, 2H, CH₂-2); 7.13 (td, 1H, CH-2); 7.28 (td, 1H, CH-2); 7.51 (dd, 1H, CH-2).

11 2-((bis((1-methyl-benzimidazol-2-yl)methyl)amino)methyl)-6-((bis((pyridyl-2-yl)methyl)amino)methyl)-4-methylphenol, HL-(BzImMe)₂(Py)₂ (12)

132 mg (0.43 mmole) of **11** (MW = 305.38 g.mol⁻¹) in 6 mL THF to which 0.50 mL of NEt₃ was added. The mixture was stirred under Ar gas to which 158 mg (0.43 mmole) of **7** (MW = 367.88 g/mol) dissolved in 6 mL THF was added. The mixture was not soluble completely and stirred for 1 hr. ¹H-NMR was performed to check the completion of the reaction. The mixture was filtered in a pipette stuffed with cotton and the filtered solution was evaporated to form yellow collagen like product. It is further dissolved in 2 mL of CH₂Cl₂ and the organic phase was washed with NH₄Cl solution (2 x 2 mL) followed by water (3 x 4 mL). The organic phase was dried up with Na₂SO₄ and evaporated.

m = 108 mg; Yield: 52%; MW = 636.80 g.mol⁻¹; Product: caramel colored powder

¹H NMR (CD₂Cl₂), δ (ppm): 2.13 (s, 3H, CH₃); 3.74 (s, 3H, CH₃-2); 3.96-4.01 (s, 2H, CH₂-4); 4.13 (s, 2H, CH₂); 4.20 (s, 2H, CH₂-12); 6.29 (s, 1H, -OH); 6.88 (s, 1H, CH-2(phenol)); 7.13-8.59 (m, 16H, H_{ar}).

12 2,6-bis((bis((1-methyl-benzimidazol-2-yl)methyl)amino)methyl)-4-methylphenol, HL-(BzImMe)₄ (13)

33 mg (0.16 mmole) of 2,6-bis(chloromethyl)-4-methyl-phenol (MW = 205.08 g.mol⁻¹) (which is readily available in the market) was dissolved in 2 mL THF (sol 1). In parallel 100 mg (0.32 mmole) of **11** (MW = 305.38 g.mol⁻¹) was dissolved in 9 mL THF with 280 μL of NEt₃ (d = 0.726 g.mL⁻¹; M = 101.19 g.mol⁻¹) was prepared (sol 2). Sol 2 was added to the sol 1 and the mixture was stirred under Ar for 2 days and frequent NMR monitoring was performed. We obtain yellow solution with white precipitate. Upon filtering, the suspension was washed thoroughly with THF and filtrate was evaporated to dryness. Again it is dissolved in 2 mL CH₂Cl₂ and the washed 2 x 8 mL of NH₄Cl followed by water.

m = 87.78 mg; Yield: 66 %; MW = 742.93 g.mol⁻¹; Product: Yellow solid

¹H NMR (CD₂Cl₂), δ (ppm): 2.13 (s, 3H, CH₃); 3.69 (s, 3H, (CH₃)-4); 3.96-4.01 (s, 2H, (CH₂)-2); 4.13 (s, 2H, CH₂); 4.20 (s, 2H, CH₂-12); 6.57 (s, 1H, -OH); 6.88 (s, 1H, CH-2(phenol)); 7.13-7.62 (dd, 1H, H_{ar}).

13 2-(((bis((1-methyl-benzimidazol-2-yl)methyl)amino)methyl)-4-methyl-6-(((2-nitrobenzyl)(pyridilmethyl)amino)methyl)phenol, HL-(MeBzIm)₂(Py)(NO₂) (14)

430 mg (1.0 mmole) of the chloro derivative (MW= 438.50 g.mol⁻¹) issued from the condensation of **11** (MW= 305.38 g.mol⁻¹) with **3** (MW= 184.62 g.mol⁻¹), 277 mg (1.0 mmole) of **8** (M = 243.27 g.mol⁻¹) and 682 μL of triethylamine (4.90 mmole) (d = 0.726 g.mL⁻¹; M = 101.19 g.mol⁻¹) were dissolved in 12 mL of THF. The mixture was stirred at room temperature for 3 days and then filtered. After stripping the solution to dryness, the resulting oil was dissolved in dichloromethane. The solution was washed with a solution at pH 7 and then dried over Na₂SO₄. Evaporation of the dichloromethane gives brown oil like product.

m = 603.5 mg; Yield: 85 %; MW = 680.80 g.mol⁻¹; Product : Orange oil

¹H NMR (CD₂Cl₂), δ (ppm): 2.13 (s, 3H, CH₃); 3.64 (s, 2H, CH₂-12); 3.77 (s, 2H, CH₂-10); 3.86 (s, 3H, CH₃-36, 48); 3.88 (s, 2H, CH₂-7); 3.99 (s, 2H, CH₂-14); 4.19 (ds, 2H, CH₂-37, 38); 5.25 (s, 1H, CH-OH); 6.88 (s, 1H, CH-H_{ar}-2, 6); 7.13 – 8.59 (ddd, 1H, H_{ar}).

14 2-(((2-aminobenzyl)(pyridin-2-yl-methyl)amino)methyl)-6-((bis((1-methyl-benzimidazol-2-yl)methyl)amino)methyl)-4-methylphenol, HL-(MeBzIm)₂(Py)(NH₂) (15)

318 mg (0.55 mmole) of **14** ($M = 680.80 \text{ g.mol}^{-1}$) were dissolved in 18 mL of methanol producing a bright orange solution. 6.8 mL (about 80 mmole) of hydrochloric acid ($d = 1.2 \text{ g.mL}^{-1}$; $M = 36.46 \text{ g.mol}^{-1}$) were then added. The mixture was stirred vigorously and 100 mg (0.8 mmole) of tin powder (Sn) ($M = 118.71 \text{ g.mol}^{-1}$) were added in small amounts, leading to a light orange solution. After additional stirring for one hour, the excess hydrochloric acid was neutralized by adding NH_4OH until the solution pH reached 7. A dense white precipitate was filtered off and the resulting yellow solution was evaporated to dryness. The resulting residue was taken in 20 mL of chloroform and a white precipitate formed was filtered again. This operation was repeated twice until no precipitate appeared anymore. After evaporating the chloroform orange oil was obtained. The drying of oil in dessicator gives us caramel colored crystalline powder.

$m = 22.6 \text{ mg}$; Yield: 70%; MW = $650.81 \text{ g.mol}^{-1}$; Product: caramel colored crystalline powder

$^1\text{H NMR}$ (CD_2Cl_2), δ (ppm): 2.13 (s, 3H, CH_3 -11); 3.29 (s, 2H, CH_2 -12); 3.55 (s, 2H, CH_2 -10); 3.86 (s, 3H, CH_3 -37, 49); 4.04 (s, 2H, CH_2 -7, 10); 3.94 (s, 2H, CH_2 -14); 4.13 (ds, 2H, CH_2 -38, 39, 14); 4.65 (s, 2H, NH_2); 6.01 (s, 1H, CH-OH); 6.88 (s, 1H, CH- H_{ar} -2,6); 6.58 – 8.59 (ddd, 1H, H_{ar}).

15 2-(bis-(2-picolyl)-aminomethyl)-6-(bis(2-benzimidazole)-aminomethyl)-p-cresol, HL-(BzImH)₂(Py)₂ (17)

150 mg of **16** (MW= $277.30 \text{ g.mol}^{-1}$) (0.54 mmole) available commercially was dissolved in 10 mL of THF to which a mixture of 0.8 mL of NEt_3 ($d = 0.726 \text{ g.mL}^{-1}$; $M = 101.19 \text{ g.mol}^{-1}$) with 240 mg of **7** (0.65 mmole) ($M = 367.88 \text{ g.mol}^{-1}$) was added. The mixture was stirred overnight and washed with THF and evaporated to dryness. The obtained product was dissolved again in 40 mL of CH_2Cl_2 and washed with 2 x 20 mL of $\text{NH}_4\text{Cl}_{\text{sat}}$. The organic phase obtained was stirred with Na_2SO_4 and evaporated.

$m = 292.5 \text{ mg}$; Yield: 75%; MW = $608.75 \text{ g.mol}^{-1}$; Product: Brown powder

$^1\text{H NMR}$ (CD_3CN), δ (ppm): 2,34 (s, 3H, CH_3); 3,66 (s, 2H, CH_2); 3,70 (s, 2H, CH_2); 3,94 (s, 4H, CH_2); 3,82 (s, 4H, CH_2 -12); 4,40 (s, 4H, CH_2); 6,91 (d, 1H, H_{ar}); 7,01 (d, 1H, H_{ar}); 7,23-8,46 (m, 16H).



ANNEX 2



Complex syntheses

1 $[\text{Fe}^{\text{III}}(\mu_2\text{-mpdp})\text{Fe}^{\text{II}}(\text{H}_2\text{NBn-L})](\text{ClO}_4)_2$

100 mg (0.18 mmole) of the ligand HL-BnNH₂ (MW = 544.70 g/mol) (10) and 49.3 mg (0.18 mmole) of the dicarboxylate disodium salt Na₂mpdp (MW = 266.20 g/mol) were dissolved in 10 mL of degassed methanol dried overnight on sodium sulfate. To this solution was added drop wise a solution of 132 mg (0.36 mmole) ferrous perchlorate (dried overnight under vacuum) in 8 mL of degassed methanol dried overnight on sodium sulfate. The reaction mixture was stirred under argon for 1h30 during which time a small amount of precipitate formed. The dark greenish solution was filtered under argon and then exposed to dry air for 10 min under stirring. The resulting dark bluish-grey solution was kept under argon at 5 °C until a precipitate started appearing and then at -20 °C for a week during which time a large amount of precipitate had formed. The supernatant solution was eliminated and the solid was washed twice with 1 mL of dry and degassed methanol and dried under vacuum

m = 133.26 mg; Yield: 69%; MW = 1073 g/mol; Product: Green powder

ESI-MS, positive mode: m/z 437.7 $[\text{Fe}^{\text{II}}\text{Fe}^{\text{III}}(\text{L-BnNH}_2)(\text{mpdp})]^{2+}$ (100%), 973.6 $\{[\text{Fe}^{\text{II}}\text{Fe}^{\text{III}}(\text{L-BnNH}_2)(\text{mpdp})](\text{ClO}_4)\}^+$ (34%), 875.2 $[\text{Fe}^{\text{II}}\text{Fe}^{\text{III}}(\text{L-BnNH}_2)(\text{mpdp})]^+$ (22%)

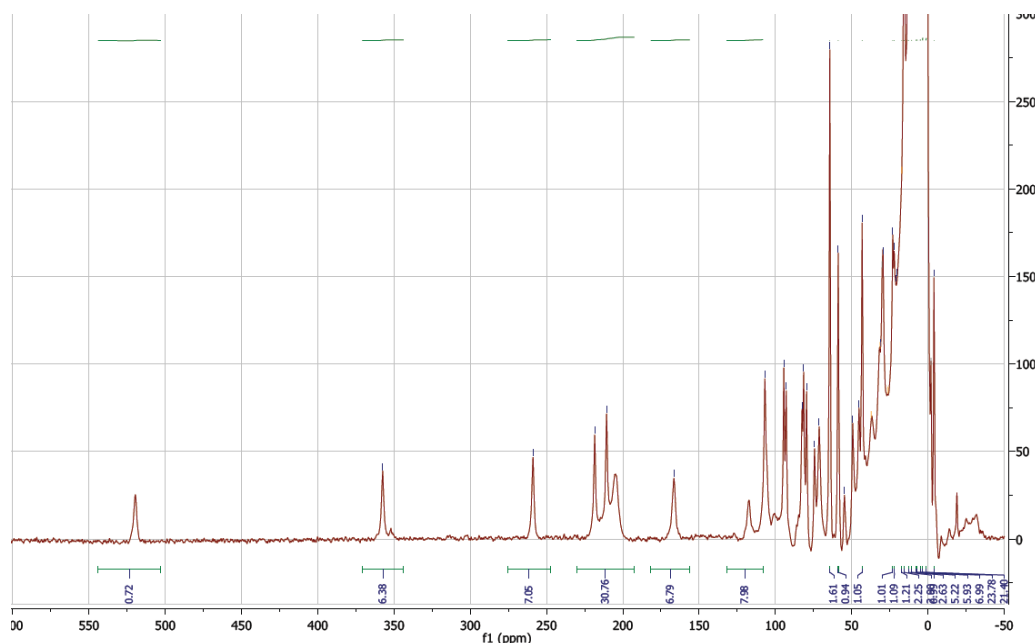


Figure 1. $^1\text{H-NMR}$ spectra of the complex $[\text{Fe}^{\text{III}}(\mu_2\text{-mpdp})\text{Fe}^{\text{II}}(\text{H}_2\text{NBn-L})](\text{ClO}_4)_2$.

2 $[\{L-(BzImH)_2(Py)_2\}Fe^{III}(\mu_2-mpdp)Fe^{II}](ClO_4)_2$

100 mg (0.16 mmole) of the ligand HL-(BzImH)₂(Py)₂ (MW = 608.75 g/mol) and 42.6 mg (0.16 mmole) of the dicarboxylate disodium salt Na₂mpdp (MW = 266.20 g/mol) were dissolved in 20 mL of degassed methanol dried overnight on sodium sulfate. To this solution was added drop wise a solution of 117.32 mg (0.32 mmole) ferrous perchlorate (dried overnight under vacuum) in 8 mL of degassed methanol dried overnight on sodium sulfate. Upon addition of perchlorate salt the solution turns dark brown color and it is stirred for 1 hr at room temperature. After stirring O₂ gas was bubble which makes the solution turn dark blue in color. After 24 hrs we observe precipitation in the solution which is left in the freezer to facilitate more precipitation of complex. The precipitate was filtered carefully and dried under vacuum.

m = 118.35 mg; Yield: 65%; MW = 1138 g/mol; Product: Dark blue.

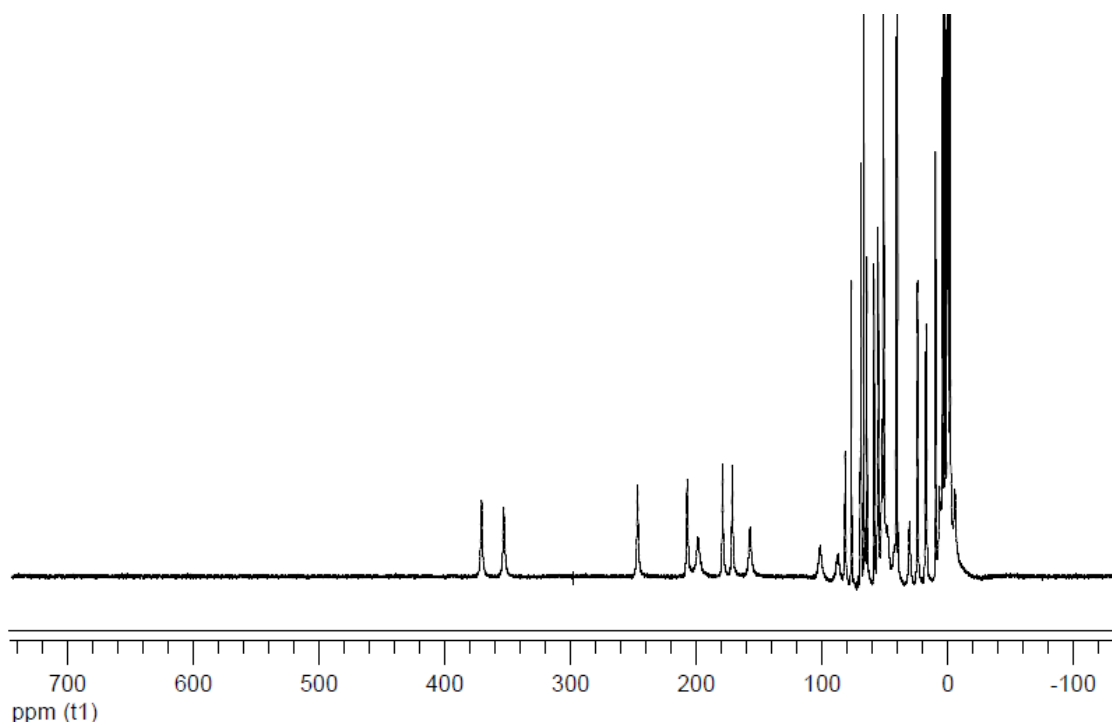


Figure 2. ¹H-NMR spectra of the complex $[\{L-(BzImH)_2(Py)_2\}Fe^{III}(\mu_2-mpdp)Fe^{II}](ClO_4)_2$

3 $[\{L-(BzImMe)_4\}Fe^{III}(\mu_2-mpdp)Fe^{II}](ClO_4)_2$

113 mg (0.15 mmole) of HL-(BzImMe)₄ **13** (MW = 742.93 g/mol) with 45 mg Na₂mpdp (MW = 266.20 g/mol) (0.17 mmole) was degassed along with 5 mL of CH₃CN with Na₂SO₄ suspension. The reactants are mixed with degassed 158 mg (0.44 mmole) of Fe(ClO₄)₂·6H₂O drop by drop and the

mixture was stirred for 1 hr doing so, allows the precipitate to settle down. After stirring, O₂ gas was bubble and the solution appears to be dark green in color. After 24 hrs we observe precipitation in the solution which is left in the freezer to facilitate more precipitation of complex. The precipitate was filtered carefully using a cotton stuffed pipette and dried under vacuum. The cotton was washed with limited methanol in order to remove the left over and the solution was left for recrystallization.

m = 101.48 mg; Yield: 58%; MW = 1166.59 g/mol; Product: dark black powder

ESI-MS, positive mode: m/z 536.8 [(L-(BzImMe)₄)Fe^{II}Fe^{III}(mpdp)]²⁺ (100%), 1172.3 {[(L-(BzImMe)₄)Fe^{II}Fe^{III}(mpdp)](ClO₄⁻)⁺ (5%).

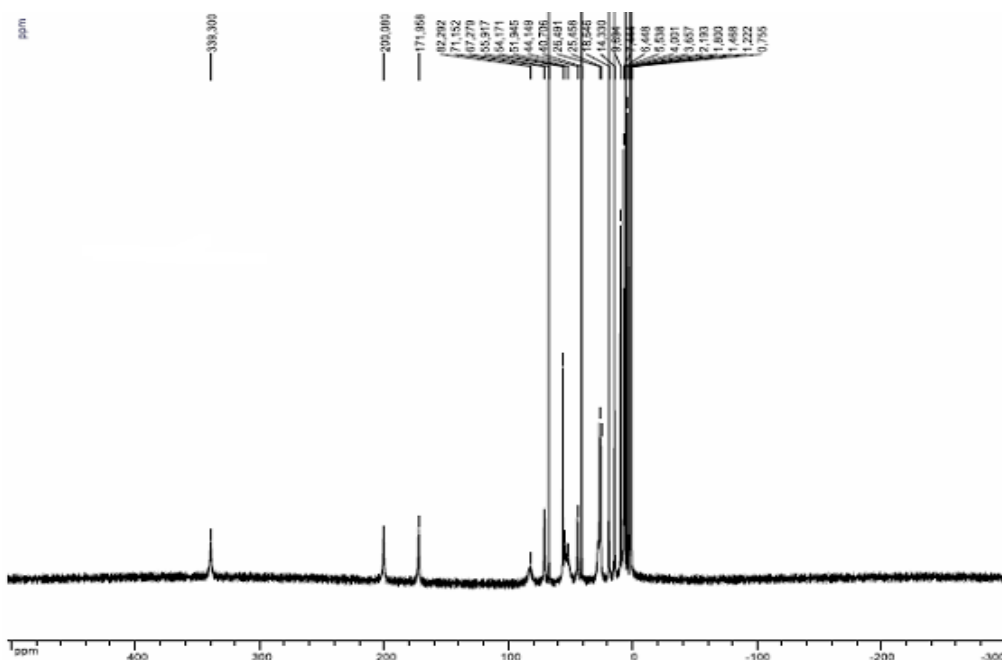


Figure 3. ¹H-NMR spectra of the complex [(L-(BzImMe)₄)Fe^{II}(μ₂-mpdp)Fe^{III}](ClO₄)₂.

4 [(L-(BzImMe)₂(Py)₂)Fe^{III}(μ₂-mpdp)Fe^{II}](ClO₄)₂

113 mg (0.18 mmole) of HL-(BzImMe)₂(Py)₂ (MW = 636.80 g/mol) (12) with 45 mg (0.17 mmole) Na₂mpdp (MW = 266.20 g/mol) was degassed along with 5 mL of CH₃CN with Na₂SO₄ suspension. The reactants are mixed with degassed 158 mg (0.36 mmole) of Fe(ClO₄)₂·6H₂O drop by drop and the mixture was stirred for 1 hr doing so, allows the precipitate to settle down. After stirring, O₂ gas was bubble and the solution appears to be dark green in color. After 24 hrs we observe precipitation in the solution which is left in the freezer to facilitate more precipitation of complex.

The precipitate was filtered carefully using a cotton stuffed pipette and dried under vacuum. The cotton was washed with limited methanol in order to remove the left over and the solution was left for recrystallization.

m = 132.79 mg; Yield: 58%; MW = 1272 g/mol; Product: Green powder

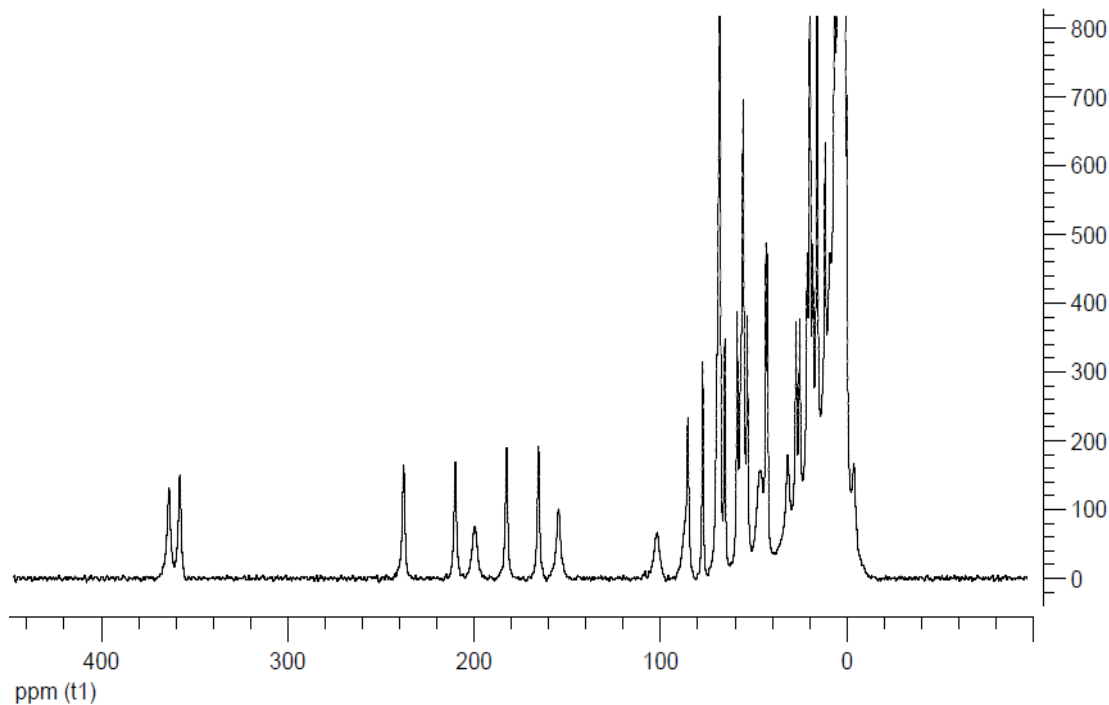


Figure 4. $^1\text{H-NMR}$ spectra of the complex $[\{\text{L-(BzImMe)}_2(\text{Py})_2\}\text{Fe}^{\text{III}}(\mu_2\text{-mpdp})\text{Fe}^{\text{II}}](\text{ClO}_4)_2$

5 $[\{\text{L-(BzImMe)}_2(\text{Py})(\text{BnNH}_2)\}\text{Fe}^{\text{III}}(\mu_2\text{-mpdp})\text{Fe}^{\text{II}}](\text{ClO}_4)_2$

112 mg (0.18 mmole) of HL-(BzImMe)₂(Py)(BnNH₂) **15** (MW = 650.83 g/mol) with 45 mg (0.17 mmole) Na₂mpdp (MW = 266.20 g/mol) was degassed along with 5 mL of MeOH with Na₂SO₄ suspension. The reactants are mixed with degassed 158 mg (0.36 mmole) of Fe(ClO₄)₂·6H₂O drop by drop and the mixture was stirred for 1 hr doing so, allows the precipitate to settle down. After stirring, O₂ gas was bubble and the solution appears to be dark green in color. After 24 hrs we observe precipitation in the solution which is left in the freezer to facilitate more precipitation of complex. The precipitate was filtered carefully using a cotton stuffed pipette and dried under vacuum. The cotton was washed with limited methanol in order to remove the left over and the solution was left for recrystallization.

m = 108.32 mg; Yield: 54%; MW = 1180 g/mol; Product: Dark blackish green powder

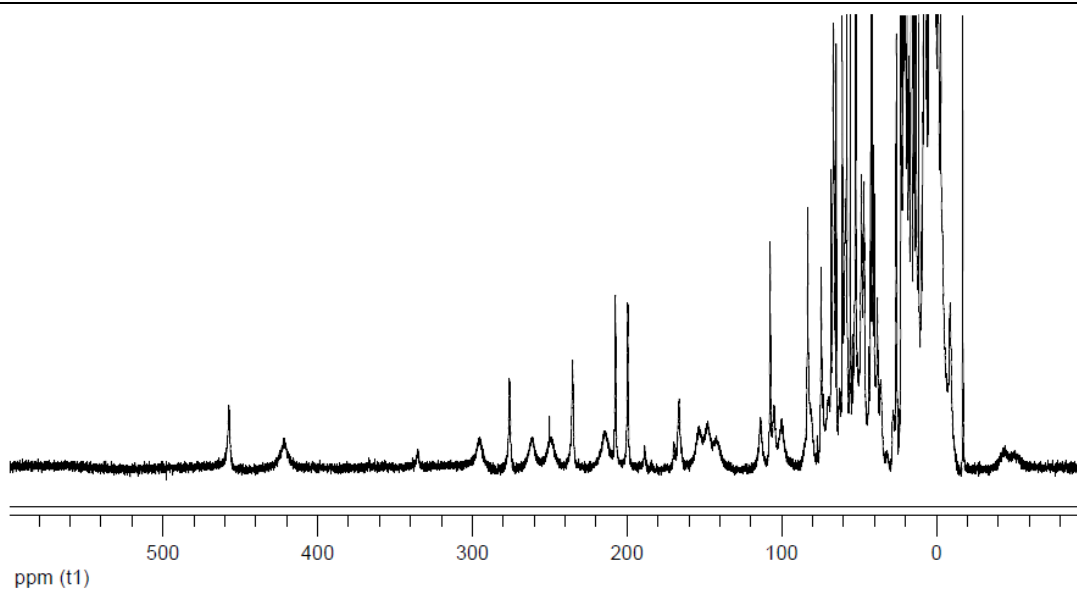


Figure 5. ¹H-NMR spectra of the complex $[\{L-(\text{BzImMe})_2(\text{Py})(\text{BnNH}_2)\text{Fe}^{\text{III}}(\mu_2\text{-mpdp})\text{Fe}^{\text{II}}\}](\text{ClO}_4)_2$.

Résumé de la thèse

Le sujet de la thèse concerne l'étude de l'inversion de valence dans des complexes $\text{Fe}^{\text{II}}\text{Fe}^{\text{III}}$ induite par la déprotonation d'un ligand de Fe^{II} . L'intérêt de cette étude vient de ce que le processus considéré peut être décrit comme un transfert d'électron induit par un transfert de proton. Les transferts de protons et d'électrons sont au cœur de nombreuses réactions catalytiques ou biologiques et la compréhension des mécanismes de leur mise œuvre, séquentielle ou couplée, est un enjeu très actuel.

La première partie de la thèse est consacrée à la caractérisation du premier système présentant cette propriété originale. Il est fondé sur un complexe binucléaire $\text{Fe}^{\text{II}}\text{Fe}^{\text{III}}$ dont les deux ions Fe sont pontés par un dicarboxylate et un phénolate. Le Fe^{III} est lié par un groupe bis-2-picolylamine et le Fe^{II} par un groupe similaire dans lequel une pyridine a été remplacée par une aniline. C'est la déprotonation de ce groupe aniline lié au Fe^{II} qui provoque l'inversion de valence, l'anilate formé étant lié au Fe^{III} .

Le complexe aniline est isolé avec le groupe aniline en position *-trans* par rapport au phénolate pontant mais il possède la particularité de ne pas être stable en solution et de s'isomériser, le groupe aniline passant en position *-cis* par échange avec une pyridine. Le même phénomène est observé pour le complexe anilate formé par déprotonation. Ce phénomène a été étudié en combinant les spectroscopies UV-visible, RMN du proton et Mössbauer et les caractéristiques thermodynamiques et cinétiques de l'isomérisation ont été déterminées.

La relation entre le transfert d'électron et le transfert de proton a été étudiée par des techniques électrochimiques. Des études approfondies par cyclovoltamétrie et marquage isotopique ont montré que dans ce système les transferts d'électron et de proton sont concertés.

La deuxième partie de la thèse est consacrée à l'étude des facteurs qui sont susceptibles d'influencer le transfert d'électron, c'est-à-dire les potentiels rédox des deux sites à Fe, et le transfert de proton, c'est-à-dire le pK_a du ligand protique. Pour ce faire, de nouveaux complexes ont été préparés en modifiant soit le ligand protique, l'aniline étant remplacée par un benzimidazole, soit le groupe complexant le Fe, remplacement de la bis-2-picolylamine par la bis-(2-méthyl-N-méthylbenzimidazole)amine. Des complexes présentant ces modifications mais dépourvus du ligand acide ont été synthétisés pour étudier les effets de ces modifications sur les propriétés rédox des ions Fe.

L'étude de l'influence des propriétés rédox a été menée dans un premier temps. La substitution du groupe complexant le Fe^{III} n'a pas de conséquence importante au plan structural pour le complexe protoné qui existe toujours sous la forme de deux isomères. Par contre, après déprotonation un seul isomère existe. Les propriétés spectroscopiques sont peu altérées ce qui montre que la structure électronique du système n'est pas bouleversée.

L'étude de l'influence des propriétés acides a été menée ensuite. Deux complexes ont été étudiés qui diffèrent par la nature du groupe complexant le Fe^{III} . La substitution de l'aniline par le benzimidazole ne change pas de façon notable les propriétés structurales du système mais on note cependant que les valences des deux ions sont moins localisées. La déprotonation du benzimidazole est observée et conduit à un chromophore sensiblement différent du précédent illustrant les différences de ligand.

L'étude électrochimique préliminaire révèle un comportement similaire au premier complexe étudié.

Summary of the PhD

The thesis matter concerns the valence inversion in $\text{Fe}^{\text{II}}\text{Fe}^{\text{III}}$ induced by deprotonation of a Fe^{II} ligand. This study is of strong interest owing to the fact this process can be described as an electron transfer induced by a proton transfer. Protons and electrons transfers play essential roles in numerous catalytic or biologic reactions and therefore understanding whether they occur in a sequential or concerted manner is presently a major endeavor.

The first part of the thesis is devoted to the characterization of the first system possessing this original property. It is based on binuclear complex $\text{Fe}^{\text{II}}\text{Fe}^{\text{III}}$ where the two Fe ions are bridged by a dicarboxylate and a phenoxide. The ferric ion is bound by a bis-2-picolyamine group and the ferrous ion by a similar group where a pyridine has been replaced by aniline. Deprotonation of this Fe^{II} bound aniline induces the valence inversion, the resulting anilide being bound to the Fe^{III} ion.

The aniline complex was isolated with the aniline in *trans* position with respect to the bridging phenoxide, but it is not stable in solution and isomerizes, the aniline group moving to a *cis* position upon exchange with a pyridine. The same phenomenon was observed for the anilide complex obtained through deprotonation. This phenomenon was studied by combining UV-visible, ^1H -RMN and Mössbauer spectroscopies, and the thermodynamic and kinetic characteristics of the isomerization were determined. The link between the electron transfer and the proton transfer were studied by electrochemical techniques. Thorough studies by cyclic voltammetry and isotopic labeling showed that in this system the electron and proton transfers are concerted.

The second section of the thesis was aimed at studying the factors susceptible to influence the electron transfer, namely the redox potentials of the two Fe sites, and the proton transfer, namely the pKa of the protic ligand. To achieve it, new complexes were prepared by modifying either the protic ligand, the aniline being replaced by a benzimidazole, or the Fe binding group, substitution of bis-2-picolyamine by bis-(2-methyl-N-methylbenzimidazole)amine. Model complexes incorporating these changes but deprived of the protic ligand were also obtained to assess their influence on the redox properties of the Fe ions.

The study of the influence of redox properties was considered first. The substitution of the group complexing Fe^{III} has not a strong influence on the structure of the protonated complex which still exists as two isomers. By contrast, after deprotonation a single isomer exists. The spectroscopic properties are mostly unchanged which shows that the electronic structure of the system is not altered significantly.

The study of the influence of the acidity was then conducted. Two complexes differing by the nature of the Fe^{III} bound group were considered. Replacing aniline by benzimidazole does not change significantly the structural properties of the system, but the valences of the Fe ions are less localized than in the original complex. The deprotonation of benzimidazole occurs and leads to a chromophore that differs from the preceding, revealing the difference in ligands. However, a preliminary electrochemical study reveals a behavior similar to that of the original complex.